

RUN II HANDBOOK

TABLE OF CONTENTS

1. INTRODUCTION AND SUMMARY.....	1.1
1.1 Tevatron Performance in Run Ib.....	1.3
1.2 Run II Performance Goals	1.6
1.2.1 Protons	1.6
1.2.2 Antiprotons	1.7
1.2.3 Luminosity Lifetime and Stacking Rate	1.8
1.3 Subsystem Performance Requirements.....	1.10
1.3.1 Linac/Booster.....	1.10
1.3.2 Antiproton Source.....	1.10
1.3.3 Recycler.....	1.10
1.3.4 Main Injector.....	1.11
1.3.5 Tevatron/Switchyard.....	1.11
1.4 Accelerator Improvement Plan.....	1.12
2. BOOSTER PERFORMANCE AND PROJECTIONS.....	2.1
2.1 Transverse Emittance vs. Intensity.....	2.1
2.2 Longitudinal Emittance vs. Intensity.....	2.2
2.3 Aperture	2.3
2.4 Damper Requirements	2.4
2.5 Booster Extraction to the Main Injector.....	2.5
2.6 Booster Losses.....	2.5
2.7 Booster Shielding.....	2.6
3. ANTIPROTON SOURCE PERFORMANCE AND PROJECTIONS.....	3.1
3.1 Current Performance and Required Improvements.....	3.1
3.1.1 Antiproton Source Performance.....	3.2
3.1.2 Antiproton Source Limitations and Required Improvements	3.5
3.2 Target Station Upgrades.....	3.6
3.2.1 Beam Sweeping System.....	3.6
3.2.2 Lithium Lens for Proton Beam.....	3.8
3.2.3 Pre-Target SEM	3.8
3.2.4 Lithium Collection Lens.....	3.8
3.2.5 Single-Turn Pulsed Magnet.....	3.10
3.2.6 Beam Dump.....	3.10
3.2.7 Radiation Safety Issues.....	3.10
3.2.8 Injection Line Transverse Aperture Increase.....	3.10
3.3 Debuncher Stochastic Cooling.....	3.11
3.3.1 Performance of the existing 2-4 GHz system.....	3.11
3.3.2 Overview of the new 4-8 GHz cooling systems.....	3.13
3.4 Stack-Tail System Upgrade	3.14
3.4.1 Overview.....	3.14
3.4.2 Lattice Modifications.....	3.15
3.4.3 Stack Tail Cooling System.....	3.22
3.4.4 Core cooling systems.....	3.29
3.5 Unstacking Scenario.....	3.36
4. Recycler (see TM-1991)	

5. MAIN INJECTOR PERFORMANCE GOALS	5.1
5.1 Project Overview.....	5.1
5.1.1 Role In The Fermilab III Program	5.2
5.1.2 Performance	5.3
5.1.3 Operational Modes	5.5
5.2 Lattice and Performance Simulations.....	5.7
5.2.1 Sources of errors.....	5.9
5.2.2 Closed orbit and betatron function errors	5.11
5.2.3 Tune versus amplitude and dynamic aperture results	5.13
5.3 Aperture	5.15
5.4 Transverse Emittance.....	5.15
5.5 Longitudinal Considerations and Emittance Projections.....	5.16
5.5.1 Proton Acceleration and Coalescing	5.16
5.5.2 Antiproton Acceleration	5.16
5.5.3 Antiproton Deceleration	5.16
5.5.4 Transition Crossing.....	5.17
5.6 Impedance and instabilities	5.23
5.6.1 Impedance budget and the microwave instability.....	5.23
5.6.2 Chromaticity and slow head-tail instability.....	5.24
5.6.3 Resistive wall instability.....	5.25
5.6.4 Coupled bunch instabilities	5.25
5.6.5 Transient beam loading.....	5.25
5.7 Damper requirements	5.26
5.7.1 Transverse dampers.....	5.26
5.7.2 Longitudinal dampers.....	5.28
5.8 RF Systems and Beam Loading Compensation.....	5.28
5.9 Intensity and Transmission Efficiency.....	5.30
5.10 Resonant Extraction.....	5.32
5.10.1 Half-Integer Resonant Extraction.....	5.32
5.10.2 Extraction Elements	5.33
5.10.3 Spill Regulation Elements	5.34
6. Tevatron Performance and Projections.....	6.1
6.1 Performance During Run Ib and Run II Goals	6.6
6.1.1 Comparison of Parameters for Run I and Run II.....	6.6
6.1.2 Transverse emittance.....	6.7
6.1.3 Longitudinal Emittance	6.9
6.2 Luminosity Leveling.....	6.9
6.3 Integrated Luminosity and Store Lifetime	6.11
6.3.1 Experience in Run Ib	6.11
6.3.2 Predictions for Run II	6.15
6.3.3 Intrabeam Scattering	6.18
6.4 Collider Fill Steps (Shot Setup).....	6.20
6.4.1 Tevatron at 150 GeV and Proton Injection.....	6.20
6.4.2 Antiproton Injection.....	6.21
6.4.3 Acceleration.....	6.22
6.4.4 Low Beta Squeeze	6.22
6.4.5 Beam Halo Scraping	6.23
6.4.6 Proton Removal	6.23
6.4.7 Low Beta Unsqueeze	6.23
6.4.8 Antiproton Deceleration	6.23
6.4.9 Antiproton Extraction.....	6.24
6.5 Run II Tevatron Lattice Issues.....	6.24
6.5.1 Dispersionless Interaction Region.....	6.24
6.5.2 Individually Powering the Tune Quads in E and F sectors.....	6.27

6.5.3 Roman Pots at D0.....	6.27
6.5.4 Interaction Point Orbit Control	6.28
6.5.5 Differential Coupling Feed-down Circuit	6.29
6.6 Injection of 36 proton and antiproton bunches.....	6.35
6.6.1 Injection at F0	6.35
6.6.2 Injection Sequence	6.37
6.6.3 Tevatron Injection Kickers.....	6.39
6.6.4 Short Batch Proton Injection Kicker.....	6.40
6.6.5 Injection Bumper Magnet	6.45
6.7 Energy of 1 TeV	6.46
6.8 Collective Effects and Damper Requirements.....	6.48
6.8.1 Potential well distortion	6.48
6.8.2 Landau damping.....	6.48
6.8.3 Single bunch instabilities.....	6.49
6.8.4 Single beam, multi-bunch instabilities.....	6.50
6.8.5 Longitudinal Coupled-Bunch Instabilities.....	6.50
6.8.6 Tevatron Dampers.....	6.51
6.9 Beam-beam tune shift for 36×36 operations.....	6.53
6.10 Beam Halo Scraping.....	6.61
6.11 Antiproton Recycling from the Tevatron	6.65
6.11.1 Proton Removal.....	6.65
6.11.2 Antiproton Deceleration.....	6.67
6.12 Instrumentation.....	6.68
6.12.1 Initial Run II 36×36	6.69
6.12.2 Instrumentation for 132 ns Bunch Spacing.....	6.72
6.13 Warm Straight Section Allocation.....	6.73
6.13.1 List of devices by functionality	6.73
6.13.2 List of devices by straight sections	6.74
6.14 Operational Concerns	6.80
6.15 132 nsec Bunch Spacing.....	6.83
6.15.1 Kicker Considerations	6.83
6.15.2 Beam-Beam Considerations.....	6.84
6.16 High Temperature Superconducting Power Leads.....	6.100
6.17 Tev Spare Magnet Requirements.....	6.101
6.17.1 Tevatron Dipoles.....	6.102
6.17.2 Standard Tevatron Quadrupoles	6.106
6.17.3 Tevatron Spool Pieces	6.106
6.17.4 Low Beta Quadrupoles.....	6.107
6.18 C0 Collision Hall.....	6.107
6.19 Superconducting RF.....	6.111
6.19.1 Use of a Higher Frequency, higher voltage rf System.....	6.111
6.19.2 Effect of Crossing Angle and Bunch Length on Luminosity.....	6.111
6.19.3 Choice of Frequency and Voltage	6.112
6.19.4 Cavity Groups	6.112
6.19.5 Cryogenic Requirements.....	6.112
6.19.6 Power Amplifier	6.112
6.19.7 Steady State Beam Loading	6.113
6.19.8 Transient Beam Loading: Injection	6.114
6.19.9 Transient Beam Loading: Collisions	6.114
6.19.10 Effect of Higher Frequency rf on Intrabeam Scattering	6.115
6.19.11 Power Loss in the Beam Pipe	6.116
6.19.12 Summary of Cavity Specifications.....	6.116
6.20 Speculative Ideas.....	6.117
6.20.1 Electron Compression of Beam Beam Tune Shifts.....	6.117
6.20.2 Optical Stochastic Cooling.....	6.118
6.20.3 Electron Cooling in the Tevatron	6.118

7. OPERATING SCENARIOS	7.1
7.1 36 x 36 Collider Operations	7.1
7.1.1 Shot Setup	7.1
7.1.2 Accumulator to RR Antiproton Transfers	7.3
7.2 Beam Transfers and Synchronization	7.3
7.2.1 Proton transfers from Tevatron to MI	7.4
7.2.2 Antiproton deceleration.....	7.4
7.2.3 NUMI operation.....	7.4
7.2.4 120 GeV Fixed Target operation	7.4
7.2.5 Inject decelerated antiprotons from the MI via the MI-22 transfer line.....	7.4
7.2.6 Inject antiprotons from Accumulator via AP5 line	7.4
7.2.7 Inject protons from MI via MI-32 line.....	7.4
7.2.8 Extract protons to MI via MI-22 line.....	7.5
7.2.9 Extract antiprotons to MI via MI-32 line	7.5
7.2.10 Extract protons to the Accumulator via the AP5 line	7.5
7.2.11 Extract protons via MI-40 (dump).....	7.5
7.2.12 Transfer Synchronization.....	7.5
7.3 Transverse and Longitudinal Emittance Budget	7.6
7.3.1 Antiprotons - Transverse.....	7.6
7.3.2 Protons - Transverse.....	7.7
7.3.3 Antiprotons - Longitudinal.....	7.7
7.3.4 Protons - Longitudinal.....	7.8
7.4 Instrumentation and Controls Requirements	7.8
7.4.1 Software.....	7.8
7.4.2 Controls Upgrades.....	7.11
7.5 Main Injector Fixed-Target Operations	7.12

1. INTRODUCTION AND SUMMARY*

The Tevatron proton-antiproton Collider is the highest-energy particle collider currently operational anywhere in the world. To exploit this unique tool fully, and to meet the goals of the Fermilab high energy physics research program through the 1990's and into the twenty-first century, a phased upgrade of the Fermilab accelerator complex is underway. The initial Run II goal is to achieve a luminosity of $5 \times 10^{31} \text{ cm}^{-2} \text{ sec}^{-1}$ and an integrated luminosity of 2 fb^{-1} . It is thought that the ultimate potential of the initial Run II upgrades is to achieve luminosities up to $2 \times 10^{32} \text{ cm}^{-2} \text{ sec}^{-1}$. Some of this potential will be need to achieve the Run II goal for integrated luminosity in a reasonable length of time—say 2 years—after the initial luminosity goal is reached. The Run II luminosity goals are about a factor of 100 increase over the original $1.0 \times 10^{30} \text{ cm}^{-2} \text{ sec}^{-1}$ design goal of the Tevatron Collider, accompanied by creation of simultaneous high intensity fixed target capability at 120 GeV.

The first phase of the upgrade program, an increase in the Linac energy from 200 MeV to 400 MeV, was completed in 1993 and has supported Tevatron collider operations at luminosities in the range of $1.5\text{-}2.5 \times 10^{31} \text{ cm}^{-2} \text{ sec}^{-1}$ during Run Ib. The second phase of the upgrade involves the replacement of the existing Main Ring with a new accelerator, the Fermilab Main Injector, and the construction of a new antiproton storage ring, the Recycler, within a common tunnel. The Main Injector and Recycler together are expected to support a luminosity in excess of $1 \times 10^{32} \text{ cm}^{-2} \text{ sec}^{-1}$ in the Tevatron collider. Improved performance is based on enhanced antiproton production, storage, and recovery capabilities following initiation of Main Injector and Recycler operations. In addition the Main Injector is designed to provide a slow (or fast) resonantly extracted 120 GeV beam containing 3×10^{13} protons with a 2.9 (or 1.9) second cycle time.

The Fermilab Main Injector is a large aperture, rapid cycling, proton synchrotron designed specifically to address the fundamental limitations inherent in the present Main Ring. With the advent of the Tevatron at Fermilab the role of the Main Ring changed significantly from its original mission of delivering 400 GeV protons for fixed-target operations. The conversion of the Main Ring to a supporting role in the early 1980s introduced a completely new set of operational requirements that were never envisaged in the original Main Ring design. Accommodating the needs of antiproton production, bipolar injection into the Tevatron, and physical avoidance of the colliding detector experiments has inevitably resulted in reduced Main Ring performance characteristics. Possible enhancements to the physics program, such as test beams for detector development and high intensity/low energy proton beams for high energy physics research, are all precluded by the present operational and physical constraints in the Main Ring. The replacement of the Fermilab Main Ring by the Main Injector addresses all of these issues in an elegant and efficient manner.

The Recycler Ring, which will be installed in the Main Injector enclosure, will provide a factor of ~ 2 in luminosity beyond that projected with the Main Injector alone, as well as providing a platform from which an additional increases in luminosity could be achieved. The initial (Run II) performance goals established for the Recycler ring are a stacking rate of 2×10^{11} antiprotons/hour, a total storage capability of 3×10^{12} antiprotons, and a capability for re-cooling relatively large emittance antiprotons recovered from the Tevatron via the Main Injector.

This report presents the design and operating parameters of the Fermilab Main Injector, the Recycler, and the remainder of the Tevatron complex during the initial operating cycle of the Main

* Last revised on July 17, 1998.

Injector era--a cycle referred to as Collider Run II. It should be noted that while many of the improvements described in this report are expected to form a basis for even greater luminosities, up to $1 \times 10^{33} \text{ cm}^{-2}\text{sec}^{-1}$ in the long term. Some of these concepts and improvements are discussed in subsequent chapters, but a complete description of the nature and feasibility of these improvements is beyond the scope of the Run II Handbook.

Table 1.1 summarizes the operational performance of the last collider run, Run Ib, accompanied by operational goals for the complex in Run II. Normalized emittances containing 95% of the beam are quoted. The horizontal and vertical emittance goals are equal as are the proton and antiproton bunch length goals. The antiproton intensity shown in the center column of the table is more than sufficient to achieve the initial Run II goal of $5 \times 10^{31} \text{ cm}^{-2}\text{sec}^{-1}$, but is not expected to be the maximum that could be obtained with 36×36 operation. In particular, the Recycler was designed to stochastically cool enough antiprotons to obtain a luminosity of $2 \times 10^{32} \text{ cm}^{-2}\text{sec}^{-1}$. However, as the luminosity increases the number of interactions increases and adversely affects the particle detector trigger rates and the ability of the experimenters to interpret the data.

One way to reduce the number of interactions per crossing is to increase the number of bunches. The rightmost column illustrates operation with 121 bunches at 132 nsec spacing. The number of bunches is tentative (see the discussion in Chapter 6) but the 132 nsec spacing is set by the trigger hardware at the experiments. The bunch parameters in the rightmost column are identical to those for 36×36 operation, but more than 3 times the number of antiprotons (121/36 to be exact) are required. The luminosity is increased by less than a factor of 2 because of the luminosity penalty incurred by the introduction of the $136 \mu\text{rad}$ crossing angle. This mode of operation is attractive when the antiproton production rate and recycling efficiency are high and the number of interactions per crossing are a concern. A more detailed discussion of the considerations of luminosity, store length, store lifetime, and the number of interactions per crossing are shown in Chapter 6.

Table 1.1. Operational performance in Run I and goals for Run II. The leftmost column shows parameters typical of the last collider run, Run Ib. The middle column shows parameters exceeding the initial Run II with 36×36 operation, and the rightmost column illustrated the performance obtained with the same bunch parameters but filling 121 antiproton bunches at a 132 nsec bunch spacing instead of the 36 that will be used initially. Normalized emittances containing 95% of the beam are quoted. The horizontal and vertical emittances are assumed equal and proton and antiproton bunch lengths are assumed to be equal.

RUN	Ib (1993-95) (6x6)	Run II (36x36)	Run II (140x121)	
Protons/bunch	2.3×10^{11}	2.7×10^{11}	2.7×10^{11}	
Antiprotons/bunch*	5.5×10^{10}	3.0×10^{10}	3.0×10^{10}	
Total Antiprotons	3.3×10^{11}	1.1×10^{12}	3.6×10^{12}	
Pbar Production Rate	6.0×10^{10}	2.0×10^{11}	2.0×10^{11}	hr ⁻¹
Proton emittance	23π	20π	20π	mm-mrad
Antiproton emittance	13π	15π	15π	mm-mrad
β^*	35	35	35	cm
Energy	900	1000	1000	GeV
Antiproton Bunches	6	36	121	
Bunch length (rms)	0.60	0.37	0.37	m
Crossing Angle	0	0	136	μ rad
Typical Luminosity	0.16×10^{31}	0.86×10^{32}	1.61×10^{32}	cm ⁻² sec ⁻¹
Integrated Luminosity†	3.2	17.3	32.5	pb ⁻¹ /week
Bunch Spacing	~3500	396	132	nsec
Interactions/crossing	2.5	2.3	1.3	

*The antiproton intensities given are merely examples. Higher antiproton intensities yield proportionally higher luminosities. The initial Run II upgrades are expected to have the ultimate potential to achieve luminosities of 2×10^{32} with 36 antiproton bunch operation.

†The typical luminosity at the beginning of a store has traditionally translated to integrated luminosity with a 33% duty factor. Operation with antiproton recycling may be somewhat different.

1.1 Tevatron Performance in Run Ib

The Tevatron Collider operated in Run Ib with a typical luminosity at the beginning of a store of $\sim 1.6 \times 10^{31}$ cm⁻²sec⁻¹. In the absence of a crossing angle or position offset, the luminosity in the Tevatron is given by the expression:

$$L = \frac{fBN_p N_{\bar{p}}}{2\pi(\sigma_p^2 + \sigma_{\bar{p}}^2)} F(\sigma_l / \beta^*) \quad [1.1]$$

where f is the revolution frequency, B is the number of bunches in each beam, N_p ($N_{\bar{p}}$) is the number of protons (antiprotons) in a bunch, σ_p ($\sigma_{\bar{p}}$) is the rms proton (antiproton) beam size at the interaction point, and F is a form factor that depends on the ratio of the bunch length, σ_l , to the beta function at

the interaction point, β^* . The luminosity can be rewritten in a form that more directly displays its dependences on the limiting factors within the Tevatron complex:

$$L \propto \frac{3\mathcal{N}\xi(BN_{\bar{p}})}{\beta^* N_{IR} (1 + \frac{\epsilon_{N\bar{p}}}{\epsilon_{Np}})} F(\sigma_l / \beta^*) \quad [1.2]$$

Here ϵ_N represents the normalized transverse emittance containing 95% of the beam, N_{IR} is the number of interaction regions, and ξ is the total head-on beam-beam tune shift seen by the antiprotons:

$$\xi = \frac{r_o}{4\pi} \frac{N_p}{\epsilon_{N_p}} N_{IR} = .000733 \frac{N_p}{\epsilon_{N_p}} N_{IR} \quad [1.3]$$

where r_o is the classical radius of the proton. The numerical expression on the right of (1.3) is evaluated with N_p in units of 10^9 and ϵ_{N_p} in units of π mm-mrad.

Fundamental limitations are related to the quantities ξ and $(BN_{\bar{p}})$. The beam-beam tune shift that can be tolerated by the antiprotons is believed to be limited by the tune space available between resonances up to about tenth order; tune shifts as high as 0.024 have been found to be tolerable. The second quantity, $(BN_{\bar{p}})$, represents the total number of antiprotons in the collider. Note that for a given total number of antiprotons, the luminosity does not depend explicitly on the number of bunches.

The performance of the Tevatron Collider during Run Ib represents a significant improvement relative to the previous collider run and is attributable to completion of the Linac upgrade and other improvements within the complex. The Linac upgrade has led directly to increased proton bunch intensities delivered from the Booster and through the Main Ring. The direct results have been more intense proton bunches in collision (2.3×10^{11} vs. 1.2×10^{11}) and a significant increase in the number of protons targeted for antiproton production (3.3×10^{12} vs. 2.0×10^{12} every 2.4 seconds). The increase in targeted protons has supported an increase in the antiproton production rate (from about 4×10^{10} /hour to about 6×10^{10} /hour) and an increase in the intensity of antiproton bunches in collision (5.5×10^{10} vs. 3.1×10^{10}).

When operating with six bunches, as in Run Ib, there are twelve potential proton-antiproton collision points in the Tevatron. Ten of these are now avoided through the utilization of electrostatic separators. In Run Ib the antiproton tune shift at the maximum proton intensity was about 0.015, limited by the proton beam brightness. An antiproton tune shift of 0.024 was achieved prior to the utilization of separators when all the beam crossings contributed nearly equally to the beam-beam tune shift. We expect that increases of 50% or so in N_p/ϵ_N are possible before beam-beam limitations set in. Long range beam-beam effects were relatively small during Run Ib but will become increasing significant in Run II. One of the design goals for the Tevatron is to keep the effect of these long range interactions to be sufficiently small such that the collisions at the interaction points produce the bulk of the beam-beam tune shift.

Antiproton availability was the most important factor limiting luminosity in the past and will continue to be so in Run II. As demonstrated in Equation 1.2 and displayed explicitly in Figure 1.1, the luminosity in the Tevatron is proportional to the total antiproton intensity. The total number of antiprotons in the collider is determined by the product of the antiproton production rate, the typical store duration, and the transmission efficiency from the Antiproton Accumulator to storage in the Tevatron. A typical store length of 10 hours, an average stacking rate of 6×10^{10} /hour, and an antiproton transmission of 70% account for the observed average number of antiprotons in the Tevatron in Run Ib. However, it should be noted that the antiproton intensity and therefore the luminosity varied widely over the course of Run Ib.

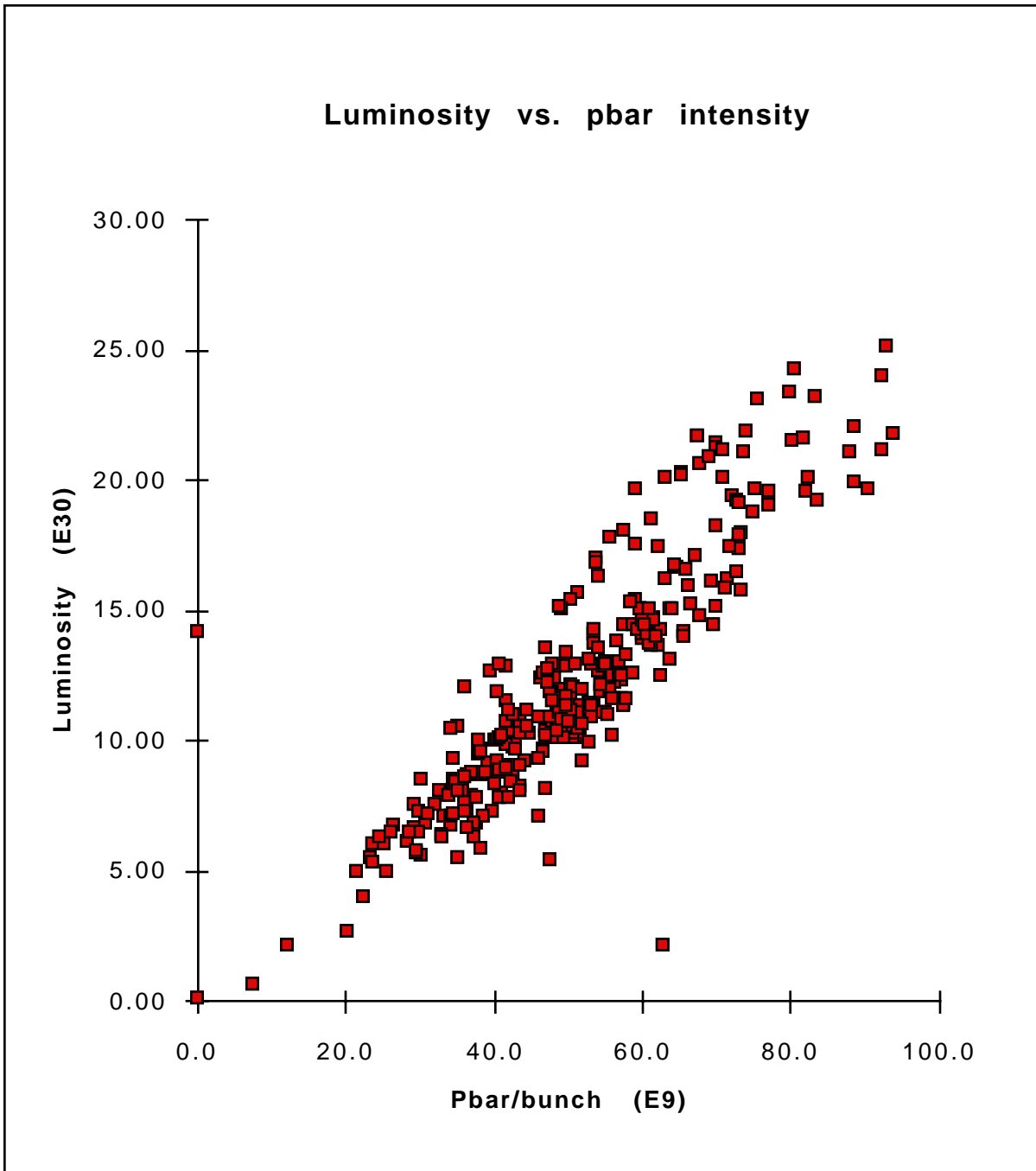


Figure 1.1. Luminosity observed in Run Ib vs. antiproton bunch intensity for all stores over the period July 23, 1994-July 9, 1995.

1.2 Run II Performance Goals

Performance goals for Collider Run II are presented in Table I.1. A luminosity goal of $5 \times 10^{31} \text{ cm}^{-2} \text{ sec}^{-1}$ has been established for this run, supported by the Main Injector and the Recycler rings. Two basic strategies are followed to attain the luminosity goal: using a proton beam brightness that produces an antiproton beam-beam tune shift close to the anticipated limit; and accumulating and delivering to the Tevatron as many antiprotons as possible through direct production and through

recovery at the end of collider stores. It is expected that the number of antiprotons available will gradually increase as Run II progresses because improvements in accumulating, transferring, and recycling antiprotons. The beta function at the interaction point, β^* , is assumed to remain at the present value of 35 cm. The bunch length shown in the table is based on the achievement of longitudinal emittances of 2 eV-sec in both the proton and antiproton beams. This emittance represents a significant improvement over the currently achieved 5 eV-sec. While the longitudinal emittance goal is aggressive, we expect improvements in the Main Injector for coalescing fewer proton bunches and from bypassing the coalescing of antiproton bunches. The antiproton bunch intensities listed in Table I.1 assume a recycling efficiency, defined as the fraction of antiprotons leaving the Recycler that are returned following completion of a store, of 50%.

1.2.1 Protons

The Proton Source at Fermilab is composed of the 400 MeV Linac (with accompanying H^- ion source and Cockcroft-Walton accelerator) and the 8 GeV Booster. The Linac/Booster is currently capable of delivering an intensity of 5×10^{10} protons per bunch with a transverse normalized emittance of less than 15π mm-mrad, and a longitudinal emittance of less than 0.1 eV-sec/bunch. Protons are delivered from the Booster in 84 bunches spaced by 18.9 nsec. A total intensity of 6×10^{10} protons per bunch has been specified for the Main Injector era--a 20% improvement over current performance. In this mode of operation the Booster will be delivering 5.0×10^{12} protons per batch to the Main Injector for acceleration to 120 GeV and delivery to the antiproton production target every 1.5 seconds. As described in Section 5.1, alternative scenarios are used during Main Injector fixed target operations.

The requirements on the Linac/Booster for proton loading of the Tevatron collider are similar. A pulse train of 5 to 7 bunches, containing $5-6 \times 10^{10}$ protons each, will be delivered from the Booster to the Main Injector. Transverse and longitudinal emittances of about 15π mm-mrad and 0.1 eV-sec/bunch are required. These bunches will be coalesced at 150 GeV in the Main Injector into a proton bunch containing 2.7×10^{11} protons with a longitudinal emittance of 2.0 eV-sec, the exact value depending on the number of bunches that are coalesced. It is expected that the number of bunches coalesced into a single proton bunch and the number of proton bunches that are formed simultaneously in the Main Injector will be determined operationally. There may be some advantage in transverse emittance from coalescing lower intensity bunches, but there will be a penalty in longitudinal emittance. With the new short batch kicker, Main Injector to Tevatron transfer will be able to coalesce from 1 to 4 batches. After coalescing, protons will be transferred to the Tevatron.

In principle the Proton Source and Main Injector will be able to produce proton beams bright enough to produce the maximum tolerable antiproton head-on beam-beam tune shift of 0.024 (cf. Equation 1.3). As can be seen from Equation 1.2, for fixed antiproton beam parameters and assuming operation in an antiproton beam-beam limited regime, luminosity increases as the proton emittance increases. However, diminishing returns set in once the proton emittance becomes much larger than the antiproton emittance. Figure 1.2 displays the proton emittance required to limit the antiproton head-on tune shift to 0.022 as a function of proton bunch intensity, assuming two head-on collisions per revolution. As can be seen from Equation 1.3, the required emittance increases linearly with proton intensity. The figure also shows the corresponding luminosity as the proton parameters are varied in this fashion with the antiproton parameters held fixed. The proton intensity and emittances chosen in Table 1.1 are a compromise between the desire to keep the emittance somewhat below the currently achieved level and to maximize luminosity. However, increases in proton emittance are

severely limited by the injection aperture and the long range beam-beam tune shift. It is not clear that emittances much beyond the nominal 20π mm-mrad are feasible. The final optimization of proton parameters will most likely follow empirical studies after commencement of operations.

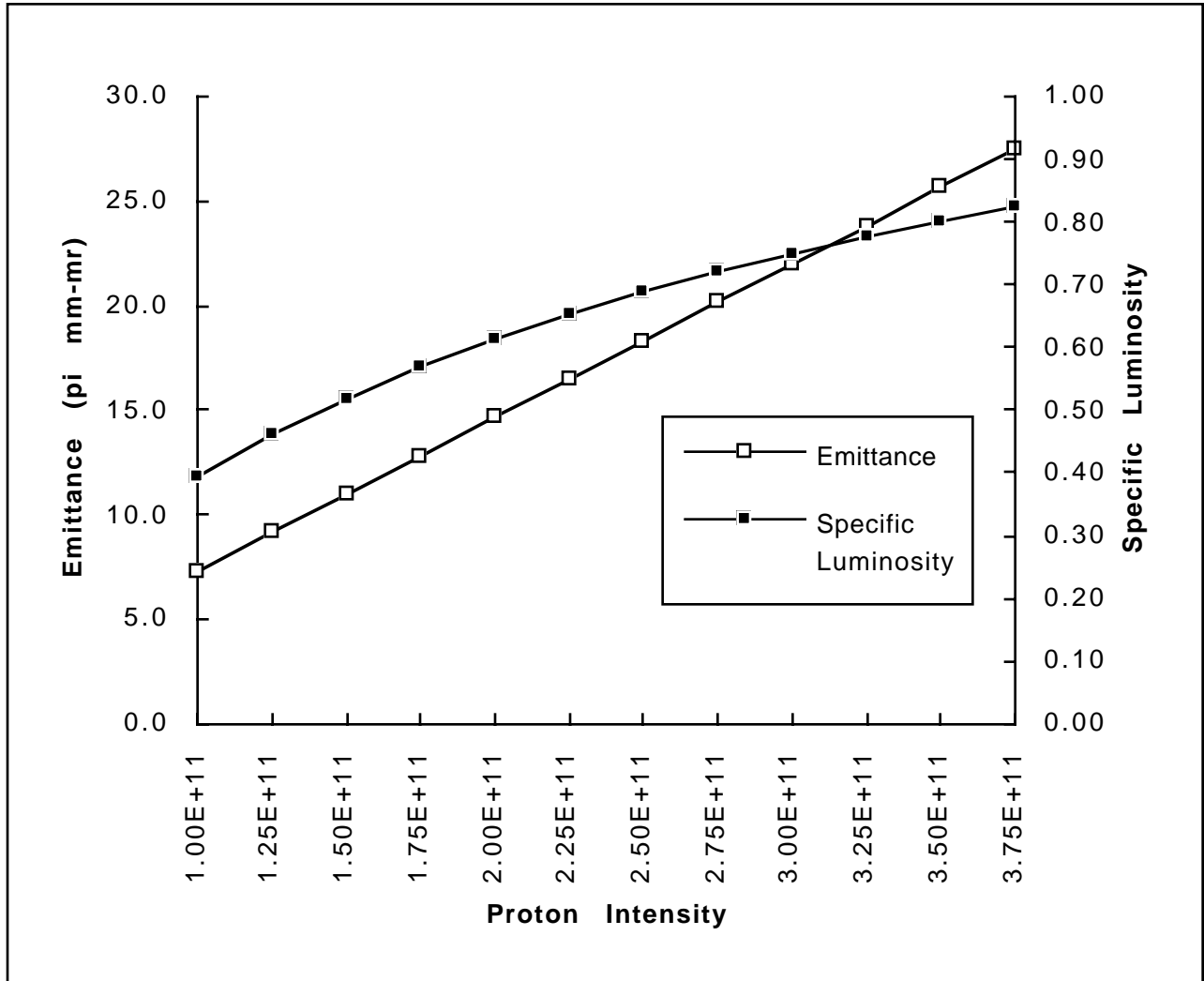


Figure 1.2. Proton emittance (mm-mrad) and luminosity per antiproton (arbitrary units) for the beam-beam limited situation. The head-on beam-beam tune shift seen by the antiprotons is .022 and the antiproton beam emittance 15π mm-mrad in this case. Long range beam-beam interactions are ignored.

1.2.2 Antiprotons

Luminosity in the Tevatron collider is proportional to the total antiproton intensity under current operating conditions. As described in Section I.1, antiproton availability represents the primary impediment to increased luminosity, both now and for the foreseeable future. The Antiproton Source is currently capable of supporting an accumulation rate of up to 7×10^{10} /hour at modest (less than 1×10^{12}) stack size, decreasing to 5×10^{10} /hour for stacks in excess of 1.5×10^{12} . The stacking rate is limited by apertures, cooling systems, and the number of protons on target. The Main Injector is designed to provide a 50% increase in the number of protons per pulse, from 3.3×10^{12} to 5.0×10^{12} ,

along with a 60% faster repetition rate, yielding a stacking rate in excess of 15×10^{10} /hour at large stacks. Planned improvements to the Debuncher and Accumulator stochastic cooling systems will support a stacking rate of 20×10^{10} /hour; a corresponding production rate may be possible if the Main Injector exceeds its design intensity or if modest improvements to the Debuncher acceptance are implemented. These planned improvements are sufficient to support the antiproton parameters listed in the middle column of Table I.1.

The Recycler can increase the number of antiprotons available at the beginning of each store by a factor of two. The Recycler accomplishes this by being able to store and cool as many as 3×10^{12} antiprotons, thus relieving the Accumulator stack-tail system of the responsibility of coping with antiproton stacks above 10^{12} , by recovering unspent antiprotons at the end of Tevatron Collider stores, and by improving reliability in the long term storage of antiprotons during stores while stacking.

In order to accumulate antiprotons in the Recycler ring stochastic cooling will be utilized. As described in Section IV stacks of up to about 3×10^{12} antiprotons can be created with the planned stochastic cooling systems. This performance is adequate to support the antiproton needs of Run II. A high stacking rate can be maintained by performing frequent transfers of antiprotons from the Accumulator to the Recycler. The frequency of such transfers will be determined operationally, but is nominally about once every 2.7 hours.

An important feature of the Recycler ring is the capability to re-cool antiprotons left over from the previous store. It is expected that about 75% of the initial complement of antiprotons will be available at the end of a typical Run II collider store. If two thirds of these can be decelerated and re-cooled, the number of antiprotons in collision in the Tevatron at the beginning of a store will be twice the number produced during the intervening store. This translates directly into a factor of two in weekly integrated luminosity.

The Main Injector, Antiproton Source, and Recycler are expected to provide the antiproton beam parameters specified in the right-most column of Table 1.1. Typically the Antiproton Source will produce and deliver to the Recycler 1.3×10^{12} antiprotons during a 8 hour collider store. These will be combined with an additional 1.5×10^{12} antiprotons recovered from the prior store, cooled, bunched and delivered to the Main Injector for acceleration and transfer to the Tevatron. The required transverse and longitudinal emittances of 10π mm-mr and 1.5 eV-sec in each of 36 bunches should be achievable.

1.2.3 Luminosity Lifetime and Stacking Rate

The store luminosity will continually decrease from its initial value as protons and antiprotons are consumed through interactions and as the bunch emittances increase. For the beam parameters expected for Run II, the initial luminosity lifetime is dominated by emittance growth due to intrabeam scattering, while after several hours the effect of antiproton loss due to luminosity becomes relatively more important. Figure 1.3 shows the time evolution of collider luminosity expected for the initial parameters of the 36×36 store listed in Table 1.1. This calculation is based upon a model that includes the effects of beam loss due to luminosity, intrabeam scattering, and noise induced transverse and longitudinal emittance growth. When compared with the observed evolution of high luminosity stores ($\sim 2 \times 10^{31} \text{ cm}^{-2} \text{ sec}^{-1}$) during Collider Run Ib the model agrees well.

The initial luminosity lifetime is 6.6 hours, but grows rapidly as the store progresses. The luminosity drops to half its initial value after 7 hours and to 1/e of its original value after about 12

hours. At the end of an 8-hour store 76% of the original antiproton beam remains in the Tevatron, but the transverse emittance is increased to 18π mm-mrad and the longitudinal emittance is increased to 2.66 eV-sec. Without the Recycler ring the remaining antiprotons would be disposed of, but with the Recycler they can be recovered for use in a later store.

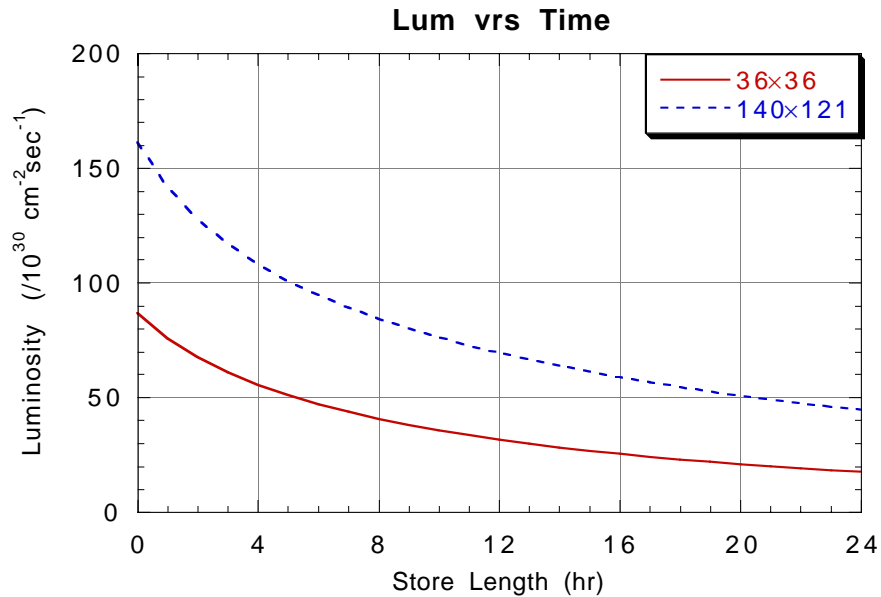


Figure 1.3. Predicted time evolution of luminosity for the two sets of store parameters listed in Table 1.1.

The Run Ib performance and Run II goals for antiproton production, transfer, and recycling are shown in Table 1.2. The Recycler stack size goals are taken from the Recycler Technical Design Report and correspond to the number of antiprotons required to achieve a luminosity of $2 \times 10^{32} \text{ cm}^{-2} \text{ sec}^{-1}$ with a 7 hour store time and a 1 hour shot set-up time. The initial antiproton intensity depends on the store length, the stacking rate, and the antiproton recovery efficiency. It is anticipated that the optimum initial antiproton intensity and store length will ultimately be established on the basis of operational experience. The improvements required to decrease the shot setup time to 1 hour are discussed in Chapter 7. The efficiencies given are for the nominal design emittances given in section 1.3. Degradation in efficiency is to be expected for larger than design emittances.

Table 1.2. Operational antiproton stacking requirements for the current collider conditions and for Run II.

Parameter	Run IB	Run II (Main Injector + Recycler)
Stacking Rate (E10/hr)	5	20
Antiproton at end of Store	73%	~75%
Deceleration Efficiency	---	80%
Acceleration Efficiency	75%	90%
Store Duration (hr)	12	7

Injection Time (hr)	2.5	≤1
Required Usable Stack (E10)	44	278
Antiprotons Recycled (E10)	0	148

1.3 Subsystem Performance Requirements

Performance requirements for the various accelerators within the complex are based upon the considerations discussed in Section 1.2 and are summarized below. Detailed descriptions of performance projections and required upgrades are contained in the remainder of this document.

1.3.1 Linac/Booster

- ◆ Antiproton Production
 - -5×10^{12} protons per pulse
 - $\leq 20\pi$ mm-mrad transverse emittance
 - Longitudinal emittance ≤ 0.2 eV-sec
 - 1.5 second repetition rate
- ◆ Proton Coalescing in Main Injector
 - 6×10^{10} protons/bunch in 5-7 bunches, repeated 36 times with a 4 second period.
 - $\leq 15\pi$ mm-mrad transverse emittance
 - Longitudinal emittance in range ≤ 0.15 eV-sec
- ◆ Main Injector Fixed Target
 - 5×10^{12} protons per pulse
 - 20π mm-mr transverse emittance
 - Longitudinal emittance in range 0.2 eV-sec
 - 15 Hz operation with a duty cycle up to 6/28
- ◆ Tevatron Fixed Target
 - 5×10^{12} protons per pulse
 - 20π mm-mrad transverse emittance
 - Longitudinal emittance in range 0.2 eV-sec
 - 15 Hz operation with 6 consecutive Booster batches delivered to the Main Injector; two such ensembles, separated by 2.4 seconds, repeating about once per minute

1.3.2 Antiproton Source

- ◆ Antiproton Production
 - 2×10^{11} /hour stacking rate for stacks up to 10^{12} antiprotons
- ◆ Antiproton Extraction
 - Delivery of $1-6 \times 10^{11}$ antiprotons, in a bunch train 1.6 μ sec long to the antiproton Recycler ring.
 - Transverse emittance $\leq 10\pi$ mm-mrad
 - $\Delta p/p \leq 10^{-3}$ (full width)

1.3.3 Recycler

- ◆ Antiproton Accumulation
 - Accumulate/cool $1-6 \times 10^{11}$, 8.9 GeV antiprotons, every 0.5 to 3 hr, up to a total stack of 3×10^{12} antiprotons.

- Equilibrium transverse emittance of $\leq 10\pi$ mm-mrad
- Equilibrium longitudinal emittance of ≤ 60 eV-sec
- ◆ Antiproton Recovery
 - Cool dilute antiprotons at 8.9 GeV with cooling time < 2 hours.
 - Initial transverse emittance $\leq 30\pi$ mm-mrad
 - Initial longitudinal emittance ≤ 144 eV-sec for 36 bunches
- ◆ Antiproton Extraction (36x36 operation)
 - Deliver to the Main Injector four bunches containing 7×10^{10} antiprotons each, capable of being captured in 2.5 MHz buckets. Nine cycles are required.
 - Transverse emittance $\leq 10\pi$ mm-mrad
 - Longitudinal emittance ≤ 1.5 eV-sec/bunch

1.3.4 Main Injector

- ◆ Antiproton Production
 - 5×10^{12} , 120 GeV protons on target every 1.5 sec
 - 20π mm-mrad transverse emittance
 - Longitudinal emittance < 0.3 eV-sec
- ◆ Collider Protons
 - Coalesce and recapture into 53 MHz buckets, 5-11 bunches of 0.15 eV-sec each containing $3-6 \times 10^{10}$ protons/bunch delivered from the Booster. Accelerate to 150 GeV and deliver to the Tevatron. A total of 36 coalesced bunches is required. The number of cycles required depends on the number of Booster batches simultaneously coalesced.
 - Transverse emittance $\leq 15\pi$ mm-mrad
 - Longitudinal emittance ≤ 2 eV-sec per coalesced bunch
- ◆ Collider Antiprotons
 - Bunch rotate and capture into 53 MHz buckets, four bunches of 1.5 eV-sec each containing 7×10^{10} antiprotons provided from Recycler at 8.9 GeV. Accelerate to 150 GeV and deliver to the Tevatron. Nine cycles are required.
 - Transverse emittance $\leq 10\pi$ mm-mrad
 - Longitudinal emittance ≤ 1.5 eV-sec per coalesced bunch
- ◆ Antiproton Deceleration
 - Accept 4 antiproton bunches at 150 GeV from the Tevatron with transverse emittance of 35π mm-mrad and longitudinal emittance of 3.5 eV-sec/bunch, decelerate to 8.9 GeV, and transfer to the Recycler. Repeat nine times.
- ◆ Main Injector Fixed Target
 - Resonantly extract 3×10^{13} protons per pulse, at 120 GeV, with a 1.9 second repetition rate and a several millisecond extraction time.
 - Resonantly extract 3×10^{13} protons per pulse, at 120 GeV, with a 2.9 second repetition rate and a one second extraction time.
 - Resonantly extract 2.5×10^{13} protons per pulse, at 120 GeV, with a 1.9-2.9 second repetition rate, after delivering 5×10^{12} protons onto the antiproton production target in the same cycle.
 - $\leq 30\pi$ mm-mrad transverse emittance
- ◆ Tevatron Fixed Target

- 1.5×10^{13} protons per Main Injector cycle at 150 GeV
- $\leq 30\pi$ mm-mrad transverse emittance
- Longitudinal emittance in range 0.1-0.5 eV-sec

1.3.5 Tevatron/Switchyard

- ◆ Proton-Antiproton Collider Mode
 - Accelerate and bring into collision 36 proton and 36 antiproton bunches, at 1 TeV per beam, with the above listed beam parameters.
 - Reliably produce a luminosity of $2 \times 10^{32} \text{ cm}^{-2} \text{ sec}^{-1}$.
- ◆ Antiproton Deceleration
 - Remove protons at end of store, decelerate antiprotons to 150 GeV, and transfer 4 bunches at a time into the Main Injector. Repeat nine times.
 - $\leq 25\pi$ mm-mrad transverse emittance
 - Longitudinal emittance in range ≤ 3.5 eV-sec/bunch at 150 GeV
- ◆ Proton Fixed Target Mode
 - Accelerate and slow spill 3×10^{13} protons to the experimental areas at 800 GeV.
 - Tevatron beam delivered to Meson, Neutrino, and Proton Areas

1.4 Accelerator Improvement Plan

Upgrades to the existing accelerator complex required to meet the performance goals listed above have been and will be funded mostly as Accelerator Improvement Projects (AIPs). A summary of projects required is given in Table I.4-1. Further details may be found in subsequent chapters of this report.

Table 1.3. Accelerator Improvement Projects required to meet Run II performance goals.

AIP	Why	R&D	Start Project	Install/Commission
Antiproton Injection Kicker	Injection with 396 nsec spacing	Complete	1992	Summer 1995
Coalescing Cavity Upgrade	Improved coalescing efficiency	Complete	1994	Spring 1995
Antiproton BPM Upgrade	Reliability, simplification, dynamic range	Complete	1995	Summer 1998
MR/Tev TBT Upgrade	Turn-by-turn capability at all BPMs	Complete	1995	Summer 1995
Booster Extraction Upgrade	Improved aperture	Complete	1995	Fall 1997
Debuncher Cooling Upgrade	20E10/hour stacking rate	Underway	1996	Winter 1998
Accumulator Lattice Upgrade	Accommodate 2-4 GHz Stack-tail upgrade	Complete	1997	Summer 1998
Accumulator Stack-tail Upgrade	20E10/hour stacking rate	Underway	1998	Winter 1998
Antiproton Target Sweeping*	5E12 protons on target	Underway	1998	Fall 1999
Tevatron Dampers*	3E11/bunch 3E13 total beam	Complete	1995	1998-1999

*These projects will probably be funded as R&D projects.

2. BOOSTER PERFORMANCE AND PROJECTIONS*

The Booster accelerates protons from 400 MeV to 8 GeV (kinetic energy). Performance of the Booster has improved dramatically over the last few years following implementation of the Linac upgrade and new damping systems. The Booster recently delivered a total beam intensity of about 4.2×10^{12} protons. At that intensity the beam transverse emittance filled the Main Ring aperture. Figure 2.1 shows the total intensity delivered from the Booster as a function of the intensity injected from the Linac. There is little evidence of roll-off with intensity. As a result, we expect that only modest improvements to the Booster will be required to meet the total intensity performance goal of 5×10^{12} protons (6×10^{10} protons/bunch) in Run II. These improvements are described in Sections 2.3-2.7 below, after present performance is reviewed in Sections 2.1-2.2.

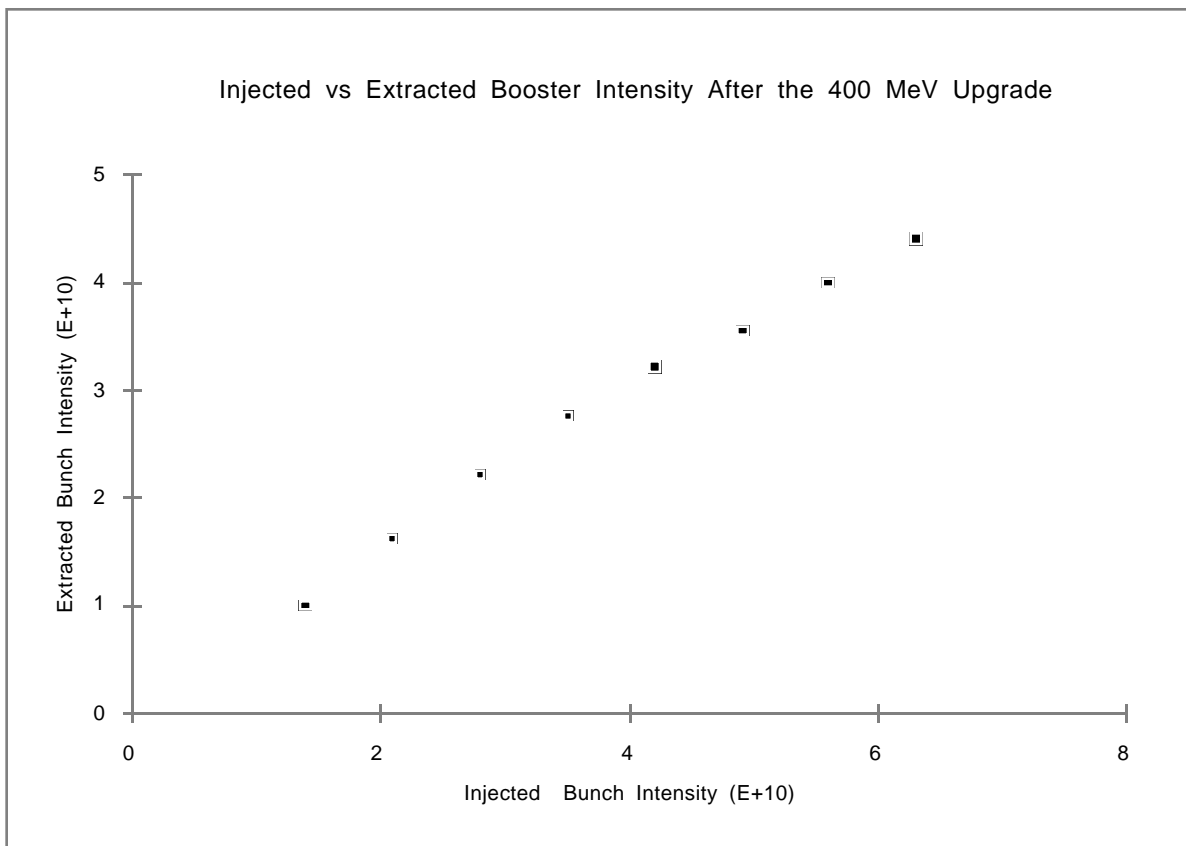


Figure 2.1. Proton bunch intensity delivered from the Booster as a function of injected bunch intensity for current operations.

2.1 Transverse Emittance vs. Intensity

The Booster has been known for some time to operate in a regime in which the transverse phase space density is strongly influenced by space-charge forces at low energy. In the past the transverse emittance rose in direct proportion to the beam intensity at high intensity. This behavior has been interpreted as reflecting a space-charge tune shift limit of about 0.4. Raising the beam

* *This chapter was last revised on March 11, 1998.

brightness limit motivated the Linac upgrade, which increased the injection energy from 200 to 400 MeV in 1993.

Current performance is displayed in Figure 2.2. Measured horizontal and vertical emittances at 8 GeV are displayed as a function of bunch intensity. The difference between horizontal and vertical emittances may be entirely due to systematic errors in the normalization of the data. The emittances are seen to display a small linear dependence on intensity at the higher intensity levels. Based on extrapolation of the data in Figure 2.2, the transverse emittance delivered from the Booster at the specified Run II intensity of 6×10^{10} protons/bunch is thus expected to lie in the range $18-20\pi$ mm-mrad.

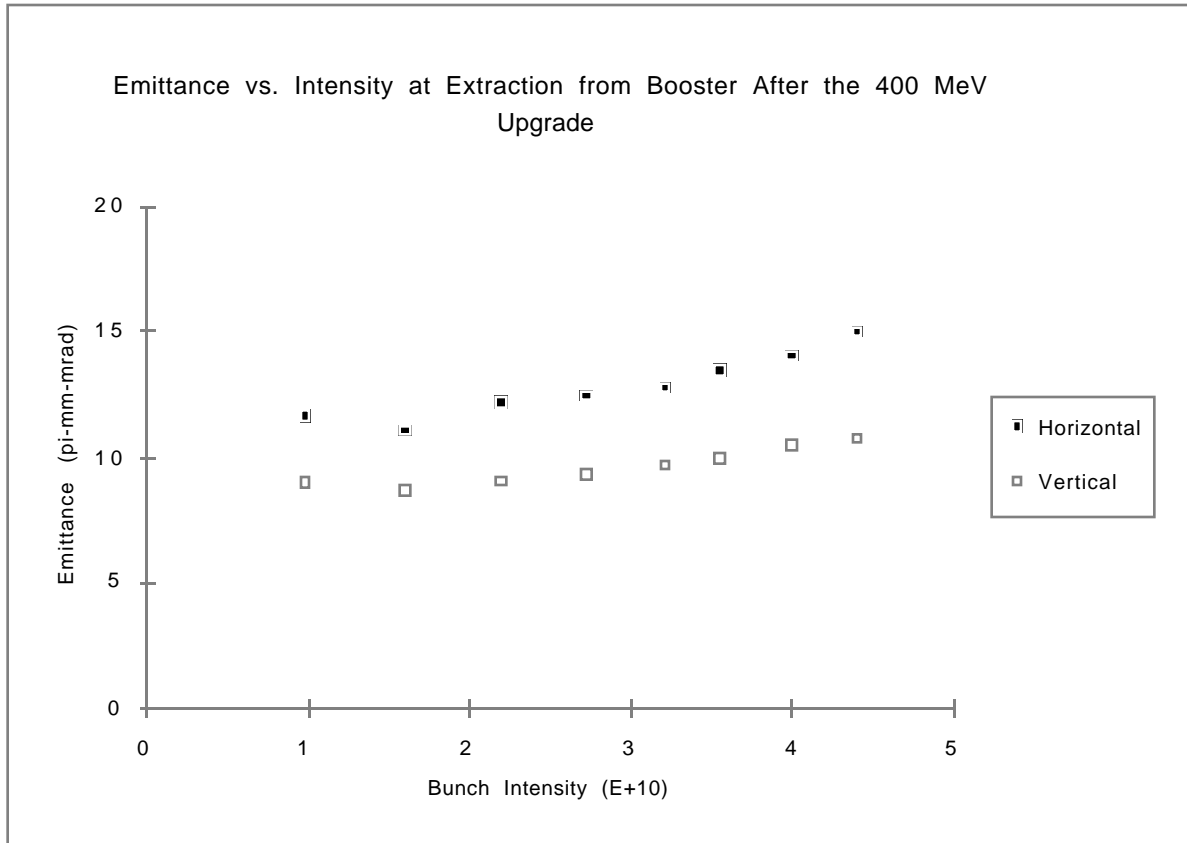


Figure 2.2. Measured 8 GeV transverse beam emittance delivered from the Booster as a function of beam intensity.

2.2 Longitudinal Emittance vs. Intensity

Beam delivered from the Linac to the Booster is allowed to debunch prior to adiabatic capture by the Booster rf system. The bunches thus formed have a longitudinal emittance of less than 0.05 eV-sec. Historically, the Booster has suffered from strong longitudinal coupled bunch instabilities driven by modes in the rf cavities above transition. Implementation of narrow-band longitudinal dampers tuned to the most offensive modes has been effective at controlling growth at present intensities. Current performance is summarized in Figure 2.3. The longitudinal emittance delivered from the Booster is seen to be 0.1 eV-sec/bunch, nearly independent of intensity up to 4.5×10^{10} protons/bunch. Improvements to the damper systems, summarized in Section 2.4, are expected to allow maintenance of this longitudinal emittance in Run II.

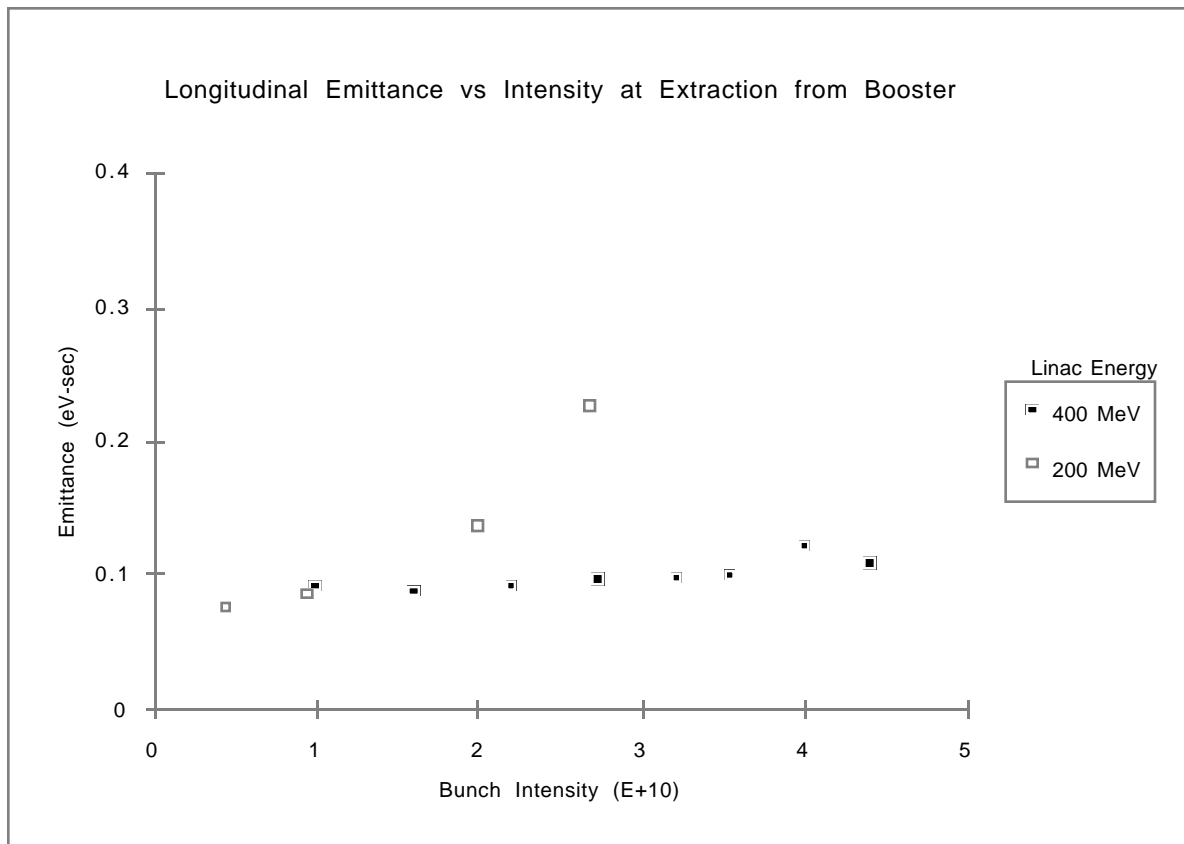


Figure 2.3 Longitudinal emittance of the 8 GeV beam extracted from the Booster as a function of bunch intensity. The points labeled "400 MeV" represent current performance.

2.3 Aperture

The Booster aperture was restricted in the vertical plane by the two extraction septa, one used to transfer the beam to the Main Ring (at long 13) and the other to the AP-4 dump (at long 3). These septa remain in place for operation with the Main Injector although their roles change. The septa were obstructing the top part of the aperture in the extraction regions. There was a set of four bending magnets in each of the two regions that displace the beam away from the septum in a double dogleg configuration. However, the displacement was small because the magnets are not strong enough. The septa had to be vertically positioned to strike a compromise between the aperture requirements of the circulating beam and the extracted beam. The vertical acceptance in the extraction regions at injection energy was approximately half of that available elsewhere in the Booster. The old dogleg magnets gave a normalized vertical aperture of $\sim 12\pi$ -mm-mrad for circulating beam at injection and a normalized vertical extraction channel acceptance of $< 20\pi$ -mm-mrad for the 8 GeV extracted beam.

A new set of dogleg magnets has been installed for Run II to remove the vertical restriction in the extraction regions. The new dogleg systems are designed for a normalized vertical aperture at the septa of 40π -mm-mrad throughout the acceleration cycle and a full normalized 40π -mm-mrad 8-GeV extraction aperture. Early measurements indicate that the doglegs are functioning as expected.

Aperture scans using 400 MeV circulating beam show that at both of the extraction straight sections the transverse apertures in both planes are as large effectively as any corresponding

straight section in the machine. The extraction septa have been effectively eliminated as aperture restrictions. The measured beam position at 400 MeV under the septa show the beam to be at the correct position to achieve a 40π mm-mrad (normalized) aperture.

Rather than ramping the dogleg magnets a set of ramped high field corrector magnets was installed that ramps the orbit at the extraction septa. The combination of the ramped orbit plus the deflection of the doglegs keeps the beam at the correct position (with respect to the septum) to achieve a 40π mm-mrad (normalized) aperture throughout the cycle. This position appears to be adequate, but no serious effort has yet been made to determine the optimum beam position.

Early measurements of vertical extraction apertures show that at Long 13 the extraction aperture is very large, much larger than the beam itself. At Long 3 the aperture is still limited. The reason for this is being investigated. It may simply be an alignment error of the septum or of the upstream Booster magnet. Whatever the cause, it should be possible to adjust the septum to compensate.

Outside the extraction regions, the Booster acceptance is determined by the apertures of the combined-function magnets and rf cavities and by their alignment. Misalignment of the magnets or rf cavities results in a reduction of the available aperture. The most serious vertical misalignments were removed in the last few years by moving some of the magnets and rf cavities. After the new dogleg magnets are in place in the extraction regions, the quality of the alignment of guide-field magnets and rf cavities will be critical in achieving the (normalized) design values of 27π mm-mrad in the vertical plane and 62π mm-mrad in the horizontal plane. It is anticipated that it may be particularly difficult to achieve the large horizontal aperture because of inadequate field quality in the gradient magnets and because of the difficulty in eliminating coupling between the horizontal and vertical betatron motion. Fortunately, a modest improvement in the vertical aperture will be sufficient to meet the Run II goals.

2.4 Damper Requirements

Achieving intensities of $\geq 6 \times 10^{10}$ protons/bunch will require both transverse and longitudinal dampers. The transverse dampers used during Run Ib can also be used for Run II with very little modification, but more significant upgrades will be required for the longitudinal dampers.

The Booster produces beam with a horizontal emittance of $< 17\pi$ mm-mrad and a vertical emittance of $< 12\pi$ mm-mrad. When the dampers are operating and the Booster is properly tuned, the emittances of the extracted beam show no effects of horizontal or vertical coherent instabilities at present intensities. This shows that the dampers currently have enough gain under these conditions to overcome the instability growth rates. The growth rate is proportional to the beam intensity and the proposed intensity is 1.2 dB higher than the current operating intensity. Provided that no new instabilities appear, the existing dampers will suppress coherent instabilities if the gain is increased proportionally. There are several simple options for increasing the gain of the system by another 1.2 dB; therefore there is no need for any major changes or additions to the transverse system.

The amplifiers for the longitudinal system are already saturated by longitudinal instabilities, so the gain cannot be increased as easily as the gain on the transverse system. Also, the longitudinal system only damps four specific coupled-bunch modes, and it is unclear how many additional modes would become unstable with the increase in intensity.

A wideband, high-level amplifier and longitudinal kicker should be designed and constructed in order to meet the longitudinal emittance specifications for the Booster. This will

make it possible to increase the gain of the current system and add other modes to the damper system if the new intensity requires it. The power amplifiers being used now are already saturated by the common mode signal, and although there is a strong effort to achieve better common mode rejection at the front end, it is doubtful that it can be improved to the level needed for the proposed intensities.

2.5 Booster Extraction to the Main Injector

Booster extraction in the Main Injector era will not be dramatically changed. Beam will continue to be extracted using a kicker/pulsed septum vertical extraction scheme from both areas. The functionality of the existing extraction regions will be interchanged: Long Straight Section 3 will become the extraction area for high energy physics, and beam to be dumped will be extracted at Long Straight Section 13. The dump will be used for studies, for short batch extraction, and for disposal of beam if an abort condition is detected prior to extraction at Long 3.

The extraction kickers in Long Straight Section 2 were modified for Run II so that both extraction areas could be operationally independent. The modification consisted of adding 1 additional kicker magnet at Long Straight Section 2 and 2 PFN (Pulse Forming Network) modulators. The modulators became available when the Main Ring was decommissioned. The Long 2 Kickers are now functionally identical to the Long 12 Kickers.

The present extraction kickers are essentially the same as those originally commissioned in the Booster. Their effective rise time is too slow, resulting in a 2% to 5% beam loss on the extraction septum each pulse. The measured kicker rise time is 50 to 60 nsec, far too slow for a full Booster ring with 19 nsec bunch spacing. The kicker dc high voltage power supplies will be replaced with resonant charging supplies of the Main Injector type. This change will allow the thyatron operating point to be changed so that a rise time of 30 nsec can be achieved. The resonant supplies should be installed and commissioned in summer 1998.

Further improvements in the rise time can be made by splitting the 20 nsec fill-time kicker modules in half to achieve a 10 nsec fill time, reducing the inductance in the thyatron cabinet, and possibly by using pulse sharpeners. The decision whether to proceed on these improvements will be made based on early commissioning experience with Run II.

2.6 Booster Losses

High intensity Booster operation results in beam loss of about 20%. The losses can be grouped into the following categories

1. Normal injection losses. These losses are probably caused by resonances driven by space charge forces and possibly by non-linearities in the magnet fields.
2. Normal extraction losses. These losses are probably due mostly to the inadequate rise time of the kicker (see section II.2.5) but the small aperture in the vicinity of the septum may also play a role (see section II.2.3).
3. Abnormal losses. These losses are typically caused by misadjustment of the Booster or the failure of some component.

During normal operation most of the beam loss occurs at injection with a few percent loss at extraction. The injection losses will be attacked by trying to increase the 400 MeV aperture by moving magnets and by possibly improving the compensation of the low order resonances. It is not clear how much progress can be made without major modifications, but the Run II goals do not require any performance improvement in the Booster at 400 MeV. The extraction losses should be

reduced by the improved aperture management that will be possible with the new dog leg magnets and particularly by the faster rise time kicker. In addition, we plan to operate the Booster with a missing bunch so that the kicker rise time requirement is reduced to about 30 nsec. The synchronization of the Booster gap with the Main Injector marker will be one of the challenges of operating the Booster with a gap in the beam.

Experiments on Booster losses were in progress when this was written (December 1997). Early measurements of extraction losses using the "notcher" (to create the gap in the beam) are encouraging. Long 13 losses at low intensities are nearly zero. At Long 3 the losses are reduced by over 90% with the beam gap. There are however known timing jitter problems the new Kickers at Long 2 and, as mentioned above, the extraction aperture still appears to be limited at Long 3. Nonetheless, losses at Long 3 should ultimately be as low as they are at Long 13.

2.7 Booster Shielding

The Booster Shielding is currently inadequate to fully contain the showers from loss of the 8 GeV proton beam, particularly in the vicinity of the Booster Tower Buildings. Fortunately, the shielding is adequate to contain the injection losses at 400 MeV. However, improvements to the shielding must be made to allow operation with the Main Injector and to support future projects like NUMI. A particular concern is that the extraction losses which formerly occurred on the septum at Long 13 when extracting to the Main Ring, will appear at Long 3 underneath the West Booster Towers. The plan to ameliorate the inadequate shielding has not been finalized but is likely to include the following:

1. Minimizing normal losses to the extent possible as outlined in section II.6
2. Adding steel shielding above the extraction septum at Long 3 inside the Booster Tunnel.
3. Adding steel shielding above the extraction septum at Long 3 outside the Booster Tunnel. This shielding requires a major excavation prior to installation.
4. Adding more interlocked detectors to protect against accident conditions
5. Modifying the aperture and/or orbit so that losses tend to occur at locations where the shielding is thickest (*i.e.*, not under the Booster Towers).

It appears that this combination of measures will be more than adequate for Run II (one Booster pulse every 1.5 sec) and may be adequate for continuous operation of the Booster at 15 Hz.

3. ANTIPROTON SOURCE PERFORMANCE AND PROJECTIONS*

3.1 Current Performance and Required Improvements

Figure 3.1 shows the general layout of the Antiproton Source. A brief review of antiproton production is given here in order to define terms. A 1.5- μ sec-long pulse train of 82 bunches of 120 GeV/c protons is focused to a small spot size on a nickel target. Antiprotons produced over a large spread of angles and energies centered about the forward direction and 8 GeV are collected and focused by a lithium lens into the AP2 beam line. At the end of the AP2 beam line, they are injected into the Debuncher ring, where the antiproton bunches are rotated and adiabatically debunched to form a dc beam. The dc beam is then stochastically cooled in all 3 dimensions by 2-4 GHz systems. The beam is then transferred via the D/A line to the injection orbit of the Accumulator ring. In the Accumulator, each pulse of beam is rf-stacked to the central orbit (the stack tail) and then stochastically stacked in momentum space to the core orbit of the Accumulator. There are 9 separate stochastic cooling systems in the Accumulator: 1-2 GHz stack tail momentum, vertical and horizontal, 2-4 GHz core horizontal, vertical, and momentum, and 4-8 GHz core horizontal, vertical, and momentum systems. (The stack tail horizontal system is currently used for longitudinal cooling.) When a sufficient number of antiprotons has been accumulated in the core (usually $80\text{-}200 \times 10^{10}$), stacking is stopped and the core is cooled to as high a density as possible.

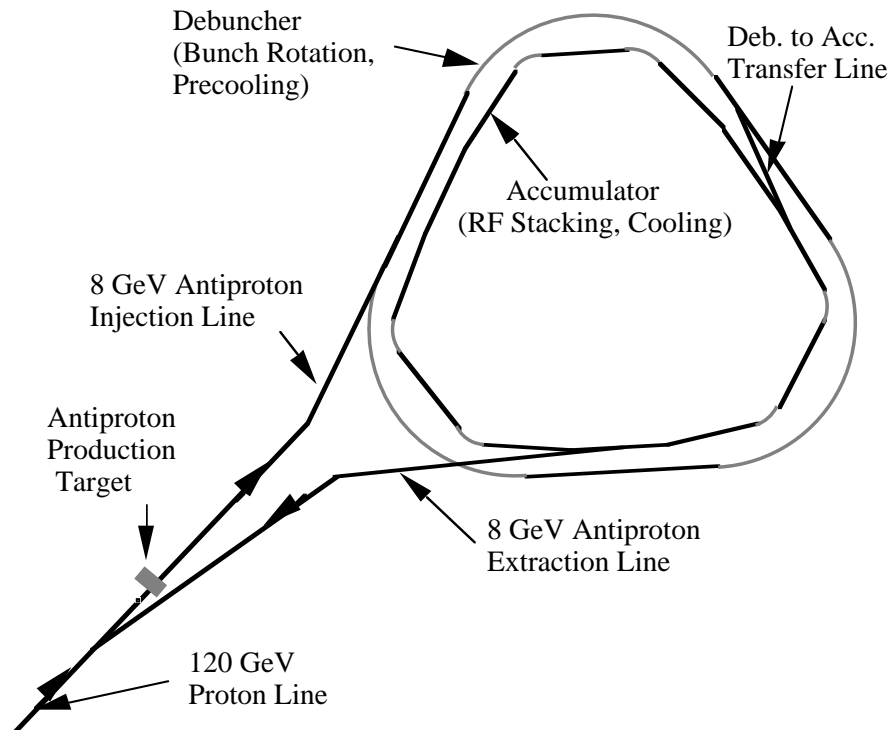


Figure 3.1. Antiproton Source Layout

Beam is then extracted from the Accumulator via the AP3 line and injected into the Main Ring for acceleration and injection into the Tevatron. Typically, 50% of the stack is extracted in six 1.5 eV-sec $h=2$ bunches. Table 3.1 lists some relevant machine parameters.

* Last revised on August 5, 1998.

Table 3.1. Debuncher and Accumulator parameters

	Accumulator	Debuncher
Central Momentum (MeV/c)	8815.	8883.
Revolution Frequency (MHz)	.628820	.590035
Circumference (meters)	474.4	505.2
Frequency slip factor η	-.023	-.006
Momentum Aperture	2%	4%
Transverse Aperture (π -mm-mrad)	7 - 12	24 - 28
Maximum Dispersion (meters)	10.0	2.1
Maximum β function (meters)	33.	20.
Stochastic Cooling Bands (GHz)	1-2, 2-4, 4-8	2-4

3.1.1 Antiproton Source Performance

During Collider Run 1b the Antiproton Source has been able to stack as much as 7.2×10^{10} antiprotons per hour at small stack sizes ($< 50 \times 10^{10}$) with 3.2×10^{12} protons/pulse incident on the production target every 2.4 seconds. The first column of Table 3.2 shows beam intensities and efficiencies at various stages of the antiproton collection and cooling process for Run 1b. In this table transverse emittances are the 95% real (unnormalized) emittances.

At large stack sizes, the stacking rate drops due to adverse effects of the stack tail cooling system in the Accumulator. Specifically, as the stack core grows the core cooling systems cannot overcome the transverse and longitudinal heating due to the stack tail momentum system. Beam is then lost longitudinally (by rf phase displacement of the stack tail beam back toward the injection orbit) and transversely. This effect is shown in Figure 3.2. The stacking rate does not drop noticeably until the core exceeds about 50×10^{10} . In practice, the stacking rate is optimized by decreasing the pulse repetition rate as the stack core grows. During Collider Run II, the maximum stack size is expected to be 100×10^{10} .

In preparation for extracting antiprotons, stacking is stopped and the Accumulator core beam is stochastically cooled in all 3 dimensions as much as possible. Figure 3.3 and Figure 3.4 show transverse emittance and σ_p as a function of stack size just prior to antiproton extraction. All 6 Accumulator core cooling systems are used in this process. For a stack size of 10×10^{10} antiprotons, extrapolated emittances are 0.4π to 0.6π mm-mrad (4π to 6π normalized) and $\sigma_p = 2$ to 3 MeV. The transverse emittance is well within the 10π mm-mrad (normalized) and more than 95% lies within the 10 eV-sec specified for transfers to the Recycler. However, the current core cooling systems performance will be degraded by a factor of about 2 with the Accumulator lattice change (the mixing factor is worse by a factor of 2) Furthermore, it should be noted that the emittances quoted are asymptotic emittances obtained an hour or more after stacking has ceased.

Table 3.2. Current and expected Antiproton Source performance under a variety of upgrades

	Run 1b	Run II no upgrades	+ cooling	+ cooling, beam sweep	+ cooling, beam sweep, Li lens upgrade	+ cooling, beam sweep, Li lens upgrade, 25 π aperture
upgrade designation			upgrade 1	upgrade 2	upgrade 3	upgrade 4
protons/pulse on target (10^{12})	3.2	5.0	5.0	5.0	5.0	5.0
cycle time (sec)	2.4	1.5	1.5	1.5	1.5	1.5
yield into Deb. ($\bar{p}/10^6$ proton)	21.0	17.8	17.8	21.0	22.5	28.1
\bar{p} /pulse into Deb. (10^7)	6.7	8.9	8.9	10.5	11.2	14.0
\bar{p} /hour into Deb. (10^{10})	10.1	21.4	21.4	25.2	27.7	33.7
initial Deb. emit. (π -mm-mrad)	20.0	20.0	20.0	20.0	20.0	25.0
final Deb. emit. (π -mm-mrad)	4.1	6.9	-	-	-	-
Deb. to Acc. transfer effc.	.80	.60	1.00	1.00	1.00	1.0
\bar{p} /pulse into Acc. (10^7)	5.4	5.3	8.9	10.5	11.2	14.0
\bar{p} /hour into Acc. (10^{10})	8.1	12.8	21.4	25.2	27.7	33.7
Accumulator stacktail+rf eff.	.90	.90	.90	.90	.90	.90
\bar{p} /hour stacked (10^{10})	7.2	11.5	19.3	22.7	25.0	30.3

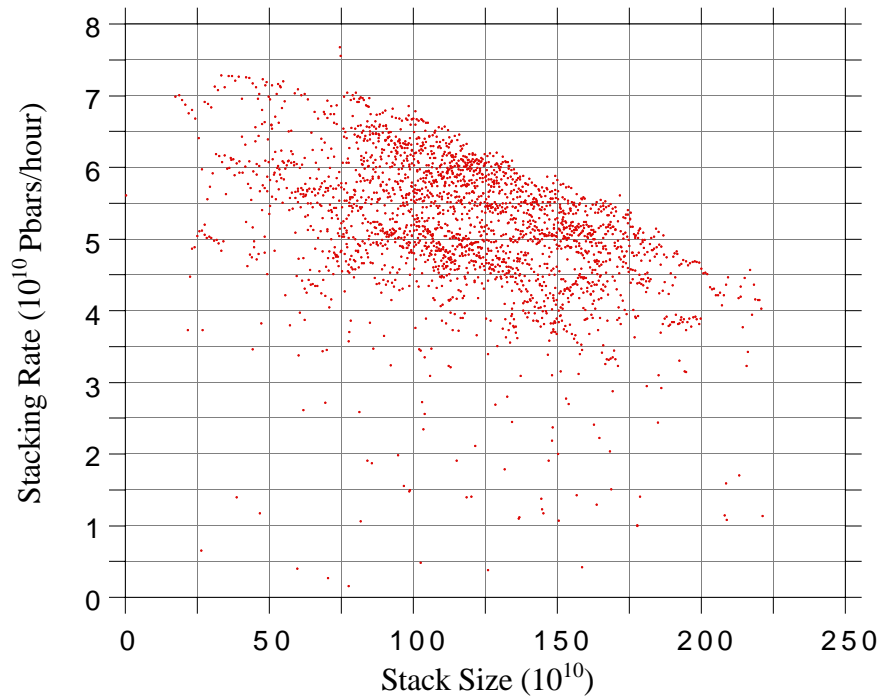


Figure 3.2. Antiproton stacking rate vs. stack size. The data are from April 1995.

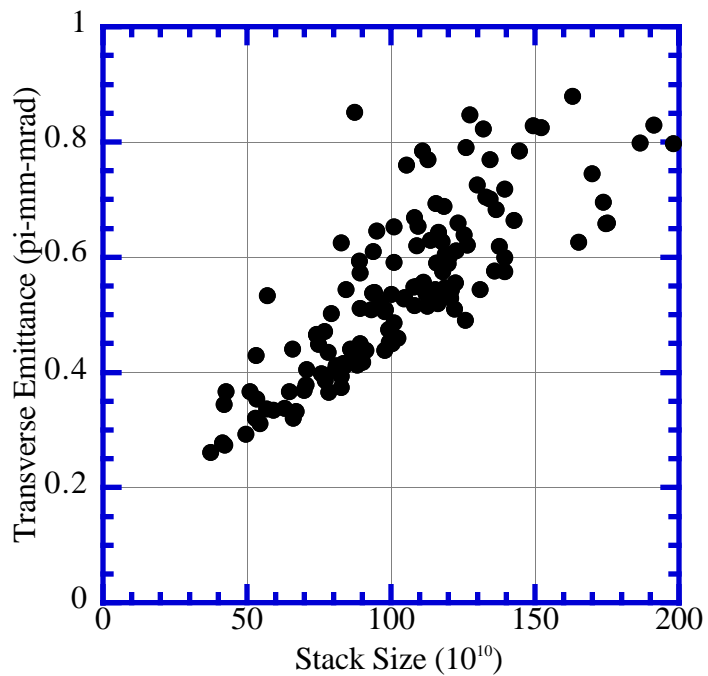


Figure 3.3. Transverse emittance (unnormalized) vs. stack size prior to antiproton extraction.

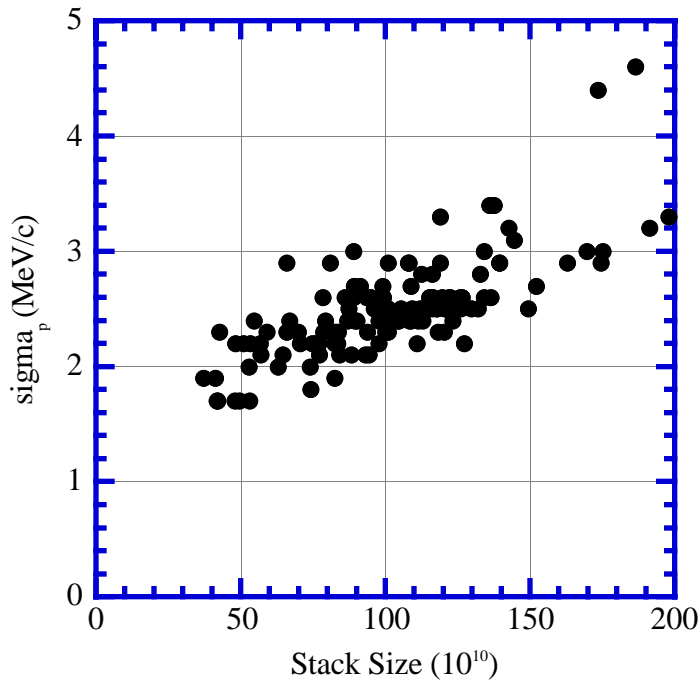


Figure 3.4. Core momentum width vs. stack size prior to antiproton extraction.

3.1.2 Antiproton Source Limitations and Required Improvements

For Run II it is required to stack 20×10^{10} /hour up to stack sizes of 100×10^{10} . At the end of each stacking period (1 to 4 hours) the emittances must be less than 10π -mm-mrad (normalized), and the amount of beam stacked must be contained in a 10 eV-sec longitudinal phase space (about 6 MeV full width). The time allotted for the extraction process 5% of the stacking time (about 5 to 10 min) so as not to compromise the average stacking rate. The major impediments to meeting these requirements are the following:

1) Target and lithium lens survivability: In order to maintain a small spot size on the target, which is necessary for keeping the antiproton yield high, a beam sweeping system will need to be built. This will increase the yield by approximately 18% over the no-beam-sweeping case. This increase is reflected as the second upgrade of Table 3.2. If the lithium lens can be operated reliably at a gradient of 900 T/m, the yield will increase another 17%. This is reflected as upgrade 3 of Table 3.2. These issues are discussed in detail in Section 3.2.

2) Debuncher stochastic cooling: The current system is gain-limited because the stochastic cooling kickers cannot handle the required power and the thermal noise power is large. The Debuncher-to-Accumulator transfer efficiency suffers as a result, and the Accumulator stack tail efficiency also suffers. In addition, the reduced cycle time in Run II will necessitate faster cooling. The proposed upgrades are discussed in Section 3.3. Table 3.2 indicates that the Debuncher cooling upgrade, coupled with other upgrades, should be capable of effectively cooling close to 30×10^{10} /hour.

3) Accumulator stack tail stochastic cooling: Simulations show that the current Accumulator cooling systems will stack 12×10^{10} /hour at small stack sizes. An experiment on proton stacking achieved at rate of 12×10^{10} /hour.¹ The flux of 8 GeV protons from the target was approximately 3 times the flux of antiprotons. By doubling the bandwidth of the stack tail cooling systems to 2-4

GHz and halving η to -0.012 , we will increase the stacking rate of the Accumulator to more than 20×10^{10} /hour. These issues are discussed in detail in Section 3.3.3.7.

4) Accumulator core cooling: The core cooling systems are marginal, particularly for frequent transfers to the Recycler. We plan to improve the performance of the 4-8 GHz core cooling systems utilizing R&D work that has been performed in the past few years. These issues are discussed in detail in Section 3.5.

Table 3.2 lists expected antiproton source performance following the various improvements discussed above for Run II. Note that in the absence of any upgrades, the estimated maximum stacking rate is about 11.5×10^{10} /hour.

3.2 Target Station Upgrades

The target station will be upgraded to handle the increased beam flux delivered by the Main Injector. Described below in summary are the status of two new systems (beam sweeping system and proton lens), upgrades to the target SEM and the collection lens, and beam dump/radiation shielding issues.

Figure 3.5 shows a layout of the future upgraded target station. The AP1 beam line transports and focuses the 120-GeV protons from the Main Ring onto the target. Antiprotons produced in the target are collected by a lithium lens and deflected by the pulsed magnet into the AP2 beam line for injection into the Debuncher. The upstream sweep magnets will be installed at the end of the AP1 beam line near the focal point of the proton lens. The downstream sweep magnet will be located between the collection lens and the pulsed magnet, near the focal point of the collection lens.

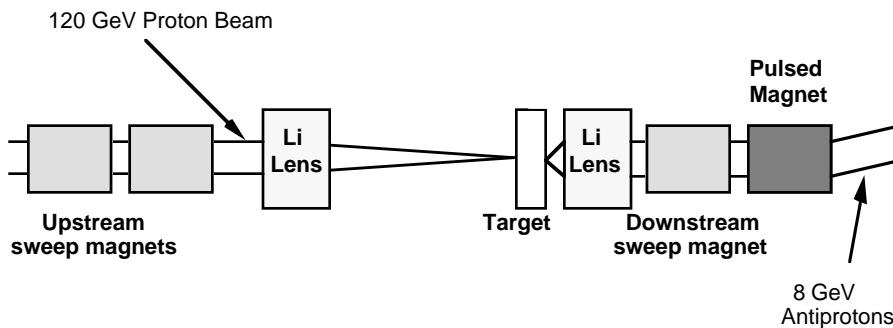


Figure 3.5. Components in the target vault of the upgraded target station. The pre-target SEM and the beam dump are not shown.

3.2.1 Beam Sweeping System.

The efficiency of collecting antiprotons from the target rises as the size of the proton beam spot on the target is reduced. However at the same time the peak energy deposition on target rises. To bring the density of energy deposition within a 0.1 mm (rms) spot size down to currently existing levels, a system to rapidly sweep the beam spot on the target is planned.² The calculated dependence of yield on spot size is plotted in Figure 3.6 for a circular beam spot. Also shown in this figure are MARS10 calculations of energy deposition for 5×10^{12} protons per pulse.³ Estimates of the peak density of energy deposition per pulse achieved to date are about 800 J/g. This is above the melting point of copper (about 600 J/g), and close to the melting point of nickel (about 1000 J/g). Local disintegration of a nickel target has been observed when the target rotation mechanism failed. Less severe damage was observed with a slowly-rotating target.⁴ In order to hold peak

energy deposition below damaging levels, the spot size was increased to 0.2 mm after the Linac upgrade, and under Main Injector conditions (5×10^{12} protons in a 1.6 μ s pulse), the spot size would have to be increased to at least 0.30 mm. The alternative is to sweep the beam on the target. Reducing the spot size to the smallest attainable size (0.10-0.15 mm) leads to a 15-20% increase in yield.

The beam sweeping system currently under development traces a 0.33-mm-radius circular pattern on the target over the 1.6- μ s proton beam pulse. The magnets have a 2-phase, 4-conductor stator excited by two power supplies that deliver 625 kHz sinusoidal current waveforms in quadrature to generate a 625-kHz rotating dipole field. Three identical magnets will be used. A pair of upstream magnets, placed at the downstream end of the AP1 beamline where the toroid M:TOR109 now resides, will sweep the 120-GeV proton beam. A single downstream magnet placed in a double module between the collection lens and the pulsed magnet will redirect the 8 GeV antiprotons exiting the collection lens parallel to the AP2 beamline. The sweeping radius is much smaller than the 2 cm diameter of the lithium collection lens and the aperture of the AP2 beam line. Each magnet is 56 cm long. The deflecting field is 900 G. An air gap is used since the beam is already transported through air from upstream of the target to downstream of the pulsed magnet. A water-cooled molybdenum pressed-powder magnetic core surrounding the current conductors provides a return path for the magnetic field. Approximately 6 kA will be required in the winding to provide the deflecting field, and the inductive voltage drop will be about 5 kV (peak voltage to ground 2.5 kV). Ionization of the air by the particle shower downstream of the target will increase the conductivity of the air between the conductor plates. Electrical losses through the ionized-air path across the gap reduce the Q of the circuit driving the magnet. Estimates based on CASIM calculations predict that the current drain will be less than 100 A, an acceptable amount. These estimates have been confirmed by measurements of leakage current between two conductors placed parallel to the beam path with a voltage drop of up to 16 kV.

Six power supplies will be required, 4 for the upstream magnet pair, and 2 for the downstream magnet. The prototype power supply is based on a 2-stage magnetic pulse compression circuit. Pulse compression is used because the requirements on a thyatron-based power supply driving a linear circuit are severe, and reliable operation under these conditions is questionable. The solid-state power supply is driven by a single thyristor, and pulse compression is provided by Metglas® cores.

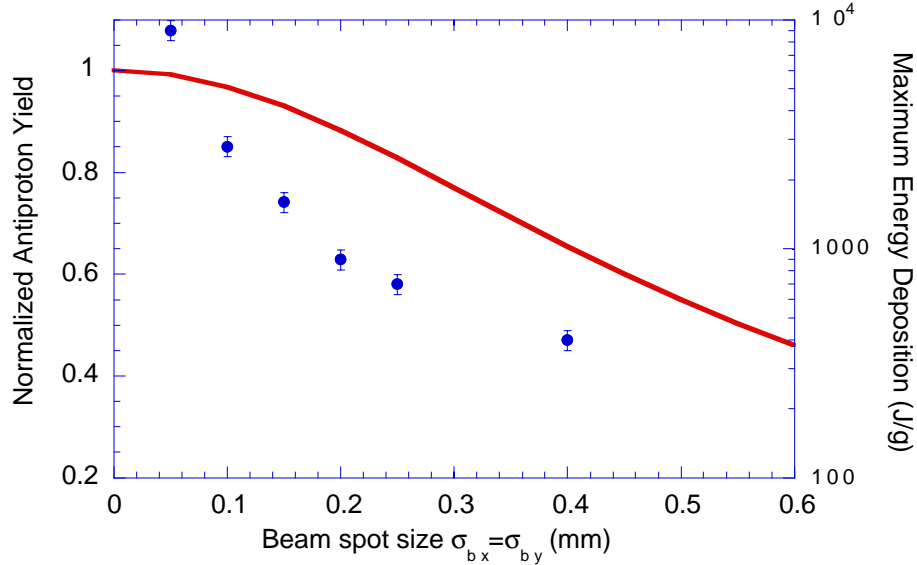


Figure 3.6. Scaling of yield (curve) and peak energy deposition (points) in the target as a function of beam spot size.

3.2.2 Lithium Lens for Proton Beam

A lithium lens has been built to focus the 120 GeV proton beam on the target to a spot size of 0.1 mm.⁵ Improved focusing increases antiproton yield and compensates for possible future emittance dilution of the proton beam in the Main Injector. Depending on details of the AP1 proton beam-line tune, we expect that the proton lens, combined with the sweeping system, will improve performance with a 15π mm-mrad (or larger) normalized emittance beam. The projected beam size of the Main Injector proton beam for stacking is about 20π mm-mrad. The lens, with a diameter of 6 mm and length of 8 cm, is expected to operate at a gradient of 2667 T/m and a current of 120 kA. The lens is similar in design to the collection lens. Its main disadvantage is that it absorbs 7.5% of the incident proton beam.

3.2.3 Pre-Target SEM

This SEM, located directly upstream of the target, measures the width and position of the incident proton beam. The titanium wires of the SEM break with less than 3 months of beam exposure at 2×10^{12} protons per cycle. Thus a new module which permits the SEM wires to be removed from the beam during operation has been constructed. When the SEM is placed into position in the path of the beam for measurements, the proton intensity will be temporarily reduced. The new SEM grid has a wire-to-wire spacing of 0.125 mm and will resolve a 0.1 mm beam spot. The SEM is crucial for the commissioning of the proton lens for Run II.

3.2.4 Lithium Collection Lens

The collection lens⁶ focuses the antiprotons produced at the target. The current-carrying lithium portion has a diameter of 2 cm and a length of 15 cm. The lithium is encased in a cylindrical water-cooled titanium alloy (type Ti-6Al-4V) pressure vessel. Fermilab lithium lenses of recent design have survived 8 million pulses at a lens gradient of about 740 T/m. Increasing the field gradient of the lens increases the yield. But even a small increase in repetitive stress in the titanium

pressure vessel leads to a much shorter fatigue life of the metal. Thus operation at even 5% greater field gradient has not proven possible beyond 1-2 million pulses. Several improvements in the design of the lens are expected to further improve reliability and field strength. Our goal is reliable operation at 900 T/m although we expect to operate at a lower gradient if we cannot achieve 900 T/m with the reliability of 10 million pulses. At the moment, we do not know how much improvement can be made with the modifications that have been made. Measurements of yield vs. gradient (Figure 3.7) show that 900 T/m will give an 18% increase in yield compared to 740 T/m with the existing AP2 beam-line at a fixed tune. Improvements to the AP2 beam line aperture may raise the antiproton yield at lower gradients while lessening the impact of gradient on yield.

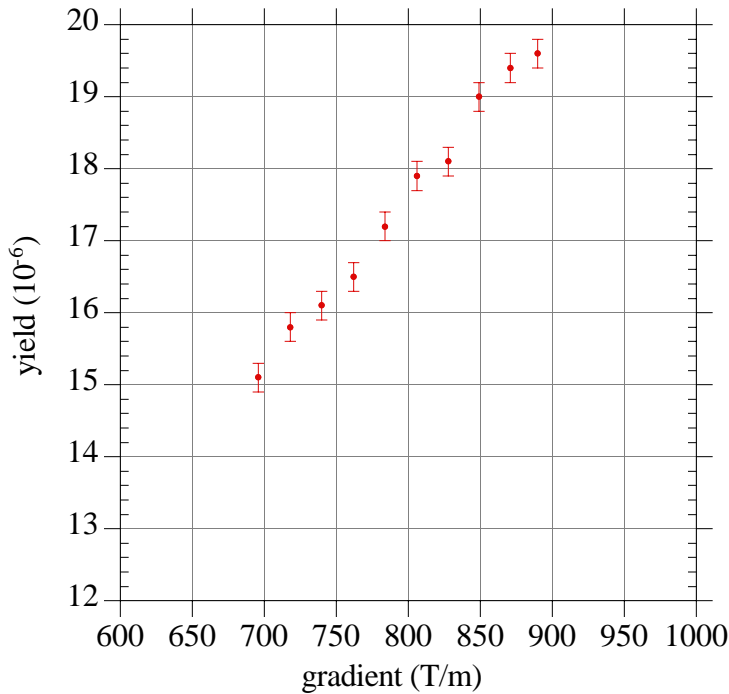


Figure 3.7. Measured yield vs. lithium lens gradient

A number of improvements to the mechanical design have been developed. These improvements include thicker endcaps for the cooling jacket, a stronger beryllium window, and improved handling and placement of welds during construction of the cooling jacket. These improvements have been incorporated into the latest lenses, but have not yet been operated extensively in the target vault. They are expected to enhance lens reliability.

During the filling process, lithium is pumped under pressure into the evacuated titanium vessel. The preload serves to insure that the lithium cylinder maintains its shape at mid-pulse, when significant magnetic pinch forces are present. Lower preload leads to lower operating stresses; a small stress decrease on the titanium cooling jacket should result in a great increase in the life of the lens for a given field gradient. A recent analysis using ANSYS⁷ shows that it is possible to lower the preload pressure in the lithium by at least 15%. The original lens design preload ensured that the lithium would maintain its shape on the first pulse when the lithium is at 20° C. At steady state, the lens is at 65° C and the additional thermal stress on the titanium is approximately the same as the stress due to preload. Thus, at steady state almost no preload is needed. If one could reduce the lithium preload from 2300 psi to 500 psi, then the lens would be able to operate at 1000 T/m

without deformation of the lithium cylinder. Lenses with preload as low as 1500 psi have been built for Run II.

Gaseous products from the ${}^6\text{Li}(n,\alpha){}^3\text{H}$ reaction between ${}^6\text{Li}$ in natural lithium and thermal neutrons are expected to build up over time, possibly affecting the operation of the lens.⁸ Swelling of the lens is expected, due to the pressure of the contained gas, potentially limiting the lifetime of the lens under an intense beam environment. To avoid this problem, we have identified a source of 99% isotopically pure ${}^7\text{Li}$. Collection lenses for Main Injector operation will be built using this material.

3.2.5 Single-Turn Pulsed Magnet

The single-turn pulsed magnet has survived more than 25 million pulses at proton intensities between 1.5 and 3.3×10^{12} protons per pulse. It is expected that no changes will be required for Main Injector operation.

3.2.6 Beam Dump

The Antiproton Source beam dump now absorbs 25 kW of beam power. A capacity of 56 kW is needed for Main Injector conditions. Since we are only using half of the available cooling channels, we can easily double the cooling capacity of the existing system. We plan to use all the channels for Run II. We can also increase the flow rate through the channels, but it should not be necessary.

3.2.7 Radiation Safety Issues

Since 1990, both the target vault shielding and the target air system have been upgraded. Under Main Injector conditions, the radiation level on the roof of the AP0 service building is expected to be less than 50 mR/hr. Posting a High Radiation Area sign on the fence around the ladder leading to the roof of the AP0 service building will be sufficient for Run II. No other shielding changes will be needed in or around the AP0 service building.

The existing air system keeps the portion of AP0 that can be occupied by personnel at a positive pressure with respect to the outside, the vault and both adjoining beam lines. A HEPA filter in the AP1 beamline removes dust from the air (some of which is radioactive). The flow is controlled in such a way that airborne radionuclides have two hours to decay in the tunnel enclosure before exiting. This is deemed to be sufficient for all radionuclides which could arise from proton-nickel interactions.

The 1991 Antiproton Source Radiation Shielding Assessment document presently limits the number of protons on target to $5.4\text{E}15$ protons per hour. This is only 2.25 protons per pulse for a 1.5 second duty cycle. This document must be updated to reflect the Main Injector goal of $5\text{E}12$ protons per pulse at a 1.5 second repetition rate.

3.2.8 Injection Line Transverse Aperture Increase

Using reverse protons, the transverse aperture of the Debuncher antiproton injection line (AP2) has been recently measured to be about $20\pi \times 20\pi$ mm-mrad for particles centered in the momentum aperture ($\delta p/p=0$). The aperture limitation is in the downstream end of the beam line, which involves a vertical bend downward by a dipole magnet, a vertical bend upward by the off-center traversal of a large Debuncher quadrupole, followed by vertical kicks by a septum magnet and fast kicker magnet. Detailed examination of the beam pipe in this area verifies that the maximum attainable transverse aperture is about $20\pi \times 20\pi$ mm-mrad. We have started a program to increase the AP2 aperture to nominally $40\pi \times 40\pi$ mm-mrad, with the eventual goal of attaining

a real aperture of $32\pi \times 32\pi$ mm-mrad for particles at $\delta p/p=0$. The transverse aperture of the Debuncher itself has physical apertures which are typically $40\pi \times 40\pi$ mm-mrad or larger, but the Debuncher acceptance is measured to be about $28\pi \times 24\pi$ mm-mrad at $\delta p/p=0$.

The following upgrades are underway or being planned for the downstream end of AP2:

1. Minor beam pipe modifications near D4Q4 to increase the vertical aperture for injected beam to 40π ;
2. Addition of a motorized stand to the Debuncher quadrupole D4Q8 to allow independent horizontal and vertical position and angle control of the closed orbit in the vicinity of the injection region;
3. Design of a new injection septum magnet, similar to the original one, but with a 10% larger horizontal aperture;
4. Modification to the Debuncher large quad used to bend the injected beam upward to allow for a 10% larger horizontal aperture beam pipe.

Upgrades 1 and 2 above will increase the downstream AP2 vertical aperture to 40π mm-mrad, while upgrades 3 and 4 will increase the horizontal aperture to 40π mm-mrad. The upstream end of AP2 is nominally $40\pi \times 40\pi$ mm-mrad, but beam studies will be required to understand optimum beam steering. In addition, beam studies will be required to understand the current limitations in the Debuncher transverse aperture if the full 32π mm-mrad aperture is to be realized. Table 3.3 shows projected antiproton yield increases under various upgrade scenarios. This table is based on Monte Carlo calculations and assumes a proton beam size of .15 mm RMS on the production target and a beam line tuned to optimize yield into the Debuncher.

Table 3.3. Antiproton yield into the Debuncher as a function of lithium lens gradient and downstream transverse aperture. Also listed are the beta function at the downstream lens focus, target thickness, and target-to-lens distance which optimize yield into the Debuncher. Yields are normalized to Run I operating conditions.

	yield ($/10^6$ protons on target)	β at ds lens focus (m)	target thickness (cm)	target center to lens face (cm)
$20\pi, 740$ T/m	21.0	4.5	6.5	21.2
$25\pi, 740$ T/m	25.6	4.3	6.5	21.2
$32\pi, 740$ T/m	30.0	3.9	6.5	21.2
$20\pi, 900$ T/m	22.5	4.3	6.0	17.0
$25\pi, 900$ T/m	28.1	3.9	6.0	17.0
$32\pi, 900$ T/m	34.1	3.7	6.0	17.0

3.3 Debuncher Stochastic Cooling

3.3.1 Performance of the existing 2-4 GHz system

Each pulse of beam is cooled in all 3 dimensions in the Debuncher during the entire production cycle. There are 128 LN₂ cooled pickup pairs and 128 kicker pairs for each transverse system. Momentum cooling is done by the "filter method" using the sum mode signals from the transverse electrodes, and notch filters are additionally used in the transverse systems to minimize thermal noise power. All 3 systems now operate in the 2-4 GHz frequency range.⁹ After bunch rotation, the momentum width (95% full width) is cooled from 0.30% to 0.17%. The transverse emittances are cooled from 16-17 π mm-mrad to 3-4 π mm-mrad (unnormalized 95% emittances). The

momentum width is inferred from the frequency width of the longitudinal Schottky spectrum. The transverse emittance at the beginning of the cycle is determined by measuring yield as a function of transverse scraper position, and the transverse emittance at the end of the cycle is determined by measuring the beam transverse dimensions with SEM's in the D/A line. In addition, the transverse emittance measurements are corroborated by measurements of the time evolution of the power in the transverse Schottky bands during the cooling cycle (Figure 3.8).

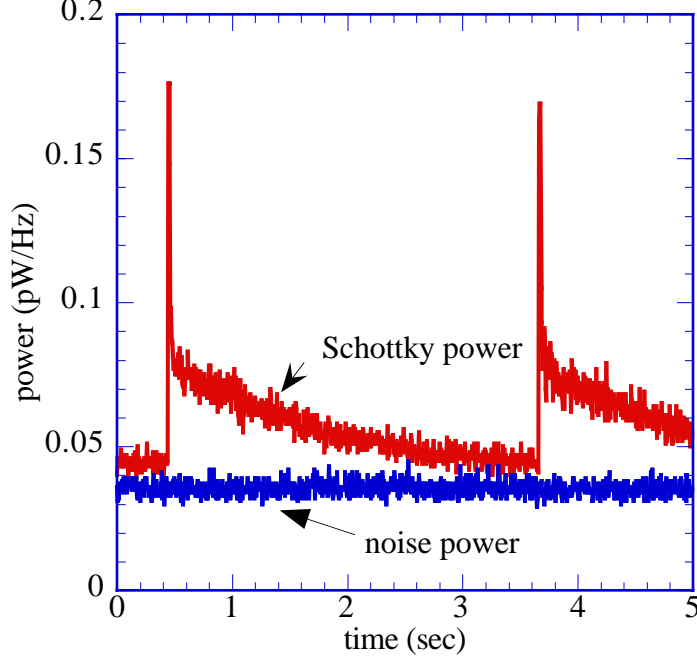


Figure 3.8. Power in a vertical Schottky band as a function of time during the cooling cycle. This power (minus noise power) is proportional to transverse emittance.

The transverse emittance cooling rate is given by¹⁰

$$-\frac{1}{\varepsilon_{\perp}} \frac{d\varepsilon_{\perp}}{dt} = F_0 \sum_l \left\{ g_l T_l - \frac{N}{2} |g_l T_l|^2 (M_l + U_l) \right\} \quad [3.1]$$

where for simplicity we have neglected imaginary parts due to "bad mixing", non-optimum pickup to kicker betatron phase advance, and microwave signal processing hardware. The summation is over Schottky bands and the quantities within the summation are averaged over beam frequencies in each Schottky band. In the above equation:

$$g_l = \frac{\sqrt{\beta_{PU} \beta_K}}{2} \cdot \frac{eF_0}{\beta^2 E} \cdot Z_{PU} \cdot g_{E,l} \cdot K_{\perp} \text{ is the gain function;}^{11}$$

$$M_l = \frac{1}{l \eta \sqrt{\pi} \frac{\Delta p_{95\%}}{p}} \text{ is the average mixing factor for a Gaussian beam distribution;}$$

$$T_l = \frac{1}{1 - S(\omega_l)} \text{ is the shielding factor, where } S(\omega_l) = \frac{-iF_0 N}{2} \int \frac{g_l(\omega) \Psi(\omega) d\omega}{\omega - \omega_l} \text{ and}$$

$$T_l \rightarrow \frac{1}{1 + \frac{N g_l M_l}{\sqrt{2}}} \text{ at the center of a Gaussian beam;}$$

$$U_l = (\text{thermal noise power density}) / (\text{average Schottky power density}).$$

where F_0 is the revolution frequency, β_{PU} and β_K are the beta functions at the pickup and kicker, and Z_{PU} is the pickup (and kicker) impedance. M_l is determined by measuring the longitudinal Schottky width during the cooling cycle, T_l is determined by measuring the signal suppression effect, g_l can be determined from M_l and T_l , and U_l can be directly measured by comparing the Schottky spectrum with and without beam. These quantities can then be inserted into the basic cooling equation above, and the time evolution of the emittances calculated and compared to the measured emittance cooling rate. The result is shown in Figure 3.9.

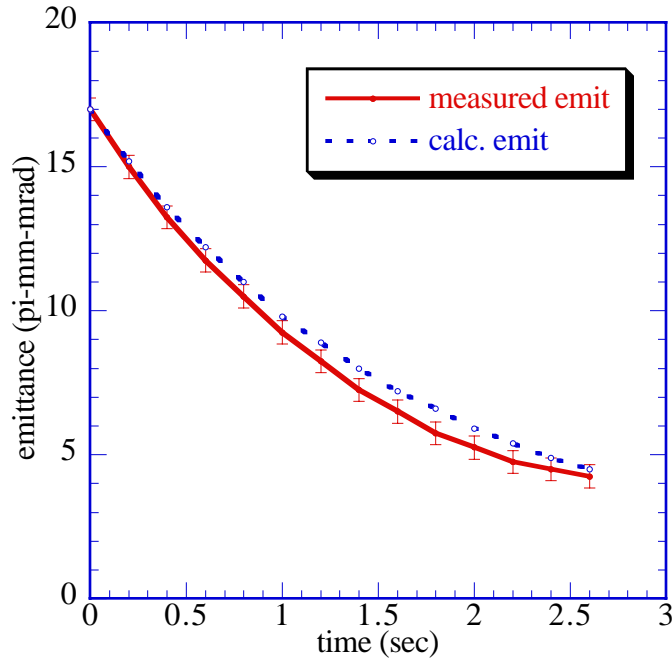


Figure 3.9. Comparison of the calculated and measured evolution of transverse emittance under Run 1b conditions. The observed cooling rate is slightly faster than the calculated rate.

At mid-band M_l is 6 at the beginning of the cycle, increasing to 11 at the end of the cycle; U_l is 10 at the beginning of the cycle, increasing to 40 at the end of the cycle. Optimum gain at the center of the beam distribution is given by

$$g_{opt,l} = \frac{1}{\frac{M_{peak,l}}{2} + U_l} \quad [3.2]$$

The system operates substantially below the optimum gain. In addition, the maximum cooling rate is limited by the thermal power (U_l). We are prevented from increasing the gain by the power limitation of the kicker tanks -- these tanks are limited to about 1200 W per system by the power handling capability of the terminating resistors, solder joints, vacuum feedthroughs, and microwave hybrids. (At 1200W 95% of the power at the kickers is thermal power.)

3.3.2 Overview of the new 4-8 GHz cooling systems

During Run II the cycle time will be $2.4/1.5 = 1.6$ times faster, and the intensity per pulse will be about $5.0/3.2 = 1.6$ times greater than in Run 1b. An improvement in the Debuncher cooling is required to meet the demands of Run II. It is possible to meet these demands with improvements to

the 2-4 GHz system. However, we have chosen to increase the bandwidth to 4-8 GHz so that we will be able to accommodate antiproton fluxes beyond those anticipated in the initial stages of Run II.

The most critical task is to develop 4-8 GHz pickup and kicker electrodes. The 4-8 GHz band will be spanned by 8 narrow band pickups and 4 narrow band kickers. The pickups and kickers are based on a new design¹² that was tested¹³ in 1997. This narrow-band approach is similar in concept to the one used at CERN.¹⁴

The pickups will be cooled to less than 10 °K by replacing the LN cryogenics (80 °K) with liquid helium. The pickup signals will be amplified by commercial cryogenically cooled amplifiers. The 8 pickup bands then be combined pair-wise into the 4 kicker bands and the signal will be transmitted across the ring using coaxial cable. It is unnecessary to use optical techniques (see section 3.4.4.4) because of the low bandwidths involved.

The four kicker bands will be implemented with 16 TWT's driving 16 kicker electrodes, namely 4 TWT/kicker pairs per band. The rated power of the system is 1600 W. A critical feature of the kicker design is the ability of the structure to dissipate 100 W at high vacuum. A schematic of the system is shown in Figure 3.10.

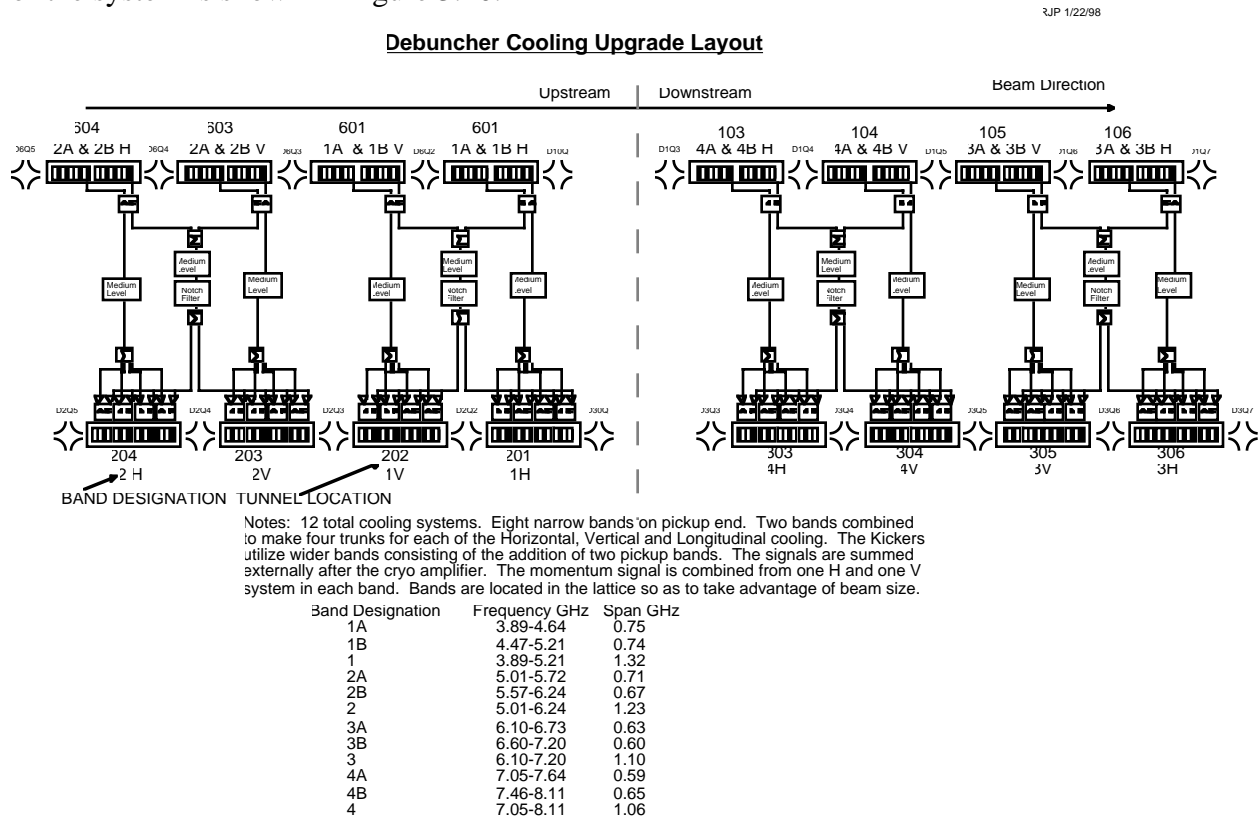


Figure 3.10. Layout of the 4-8 GHz Debuncher cooling systems. Momentum, horizontal, and vertical cooling systems are shown.

3.3.3 Simulations

3.3.3.1 Assumptions

The basic beam parameters are shown in Table 3.4. The beam size is assumed to be 25π mm-mrad (consistent with current estimates) although we hope to have 30π mm-mrad beams in Run II. The pickup apertures are assumed to be 40π mm-mrad—rather large for a 25π mm-mrad

beam. The momentum changes as momentum cooling proceeds. The calculations are done with a fixed momentum spread corresponding roughly to that obtained at the end of momentum cooling.

Table 3.4. Beam Parameters

Energy spread (full)	18	MeV
Beam Energy	8938	MeV
Initial Beam Emittance	25	π mm-mrad
Accumulator Acceptance	5	π mm-mrad
$\eta = 1/\gamma_t^2 - 1/\gamma^2$	0.006	
Number of particles (Run II)	1×10^8	
Number of particles (TeV33)	4×10^8	

We plan to use an entirely new 4-8 GHz system using 4 relatively narrow bands. This approach was used at the CERN AC. The parameters of the proposed 4-8 GHz Horizontal system are shown in Table 3.5. The Vertical system is identical except the pickup and kicker impedances are slightly different because of small differences in the lattice functions. The impedances were calculated by Dave McGinnis¹⁵ and are consistent with the recently measured sensitivity.¹⁶ The simulations include a more conservative 3 dB loss at the pickup and kicker, not the 1 dB loss specified in Table 3.5.

Table 3.5. 4-8 GHz Horizontal system parameters

PU/Kicker Impedance (peak)	3620	Ω
PU's/Kickers per band	8	
Number of Bands	4	
Combiner Loss	1	dB
Splitter Loss	1	dB
Amplifier Noise Temperature	25	$^{\circ}\text{K}$
Resistor Temperature	10	$^{\circ}\text{K}$
PU/Kicker Aperture	40	π mm-mrad
Gain (typical)	147	dB
Power	400	W/band

3.3.3.2 System Gain

The definition of the system gain G per Schottky band is

$$\frac{dA^2}{dt} = 2f_0GA^2 \quad [3.3]$$

where A is the betatron amplitude and $2G$ is the cooling rate for a particular Schottky band. A plot of system gain versus frequency is shown in Figure 3.11. The variations in gain are large and are entirely due to the variations in pickup and kicker sensitivity.

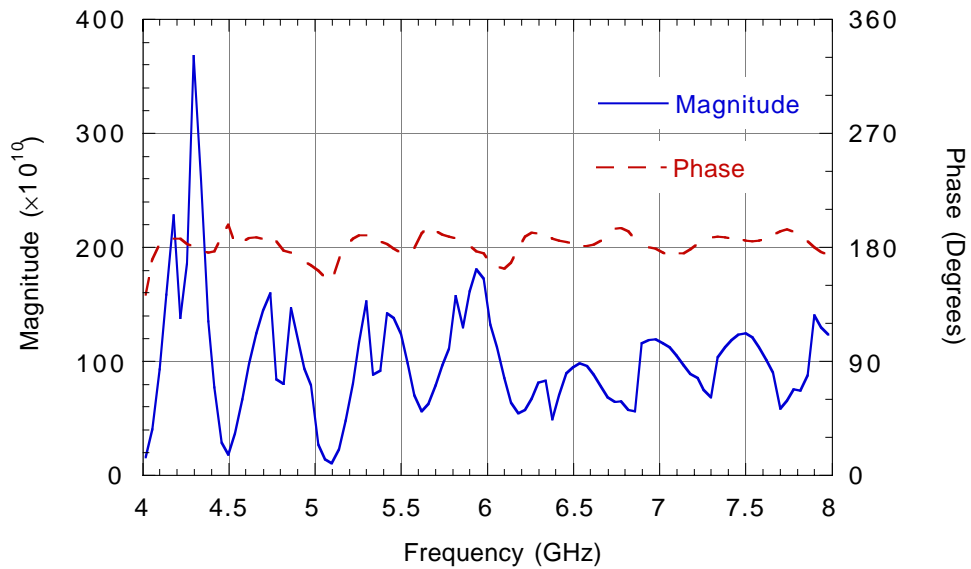


Figure 3.11. Cooling system gain. The gain response is dominated by the pickup and kicker response.

3.3.3.3 Mixing Factor

The mixing factor for the 4-8 GHz system is shown in Figure 3.12. The mixing factor depends only on the lattice parameters and the frequency.

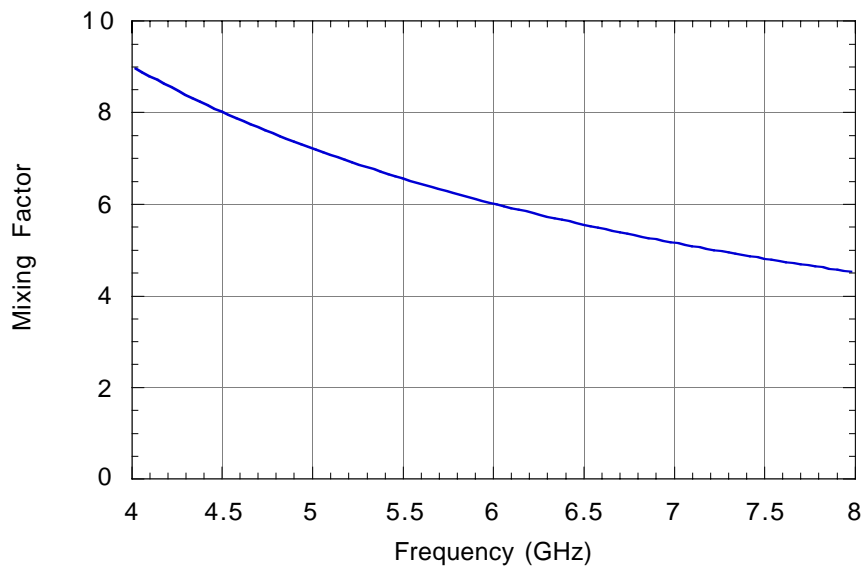


Figure 3.12. Mixing Factor.

3.3.3.4 Signal to Noise Ratio

The signal to noise ratio is shown in Figure 3.13. The large variations come from variations in the pickup sensitivity. It has been assumed that sharp transversal filters are to filter unwanted broad-band noise outside the pickup bandwidth.¹⁷

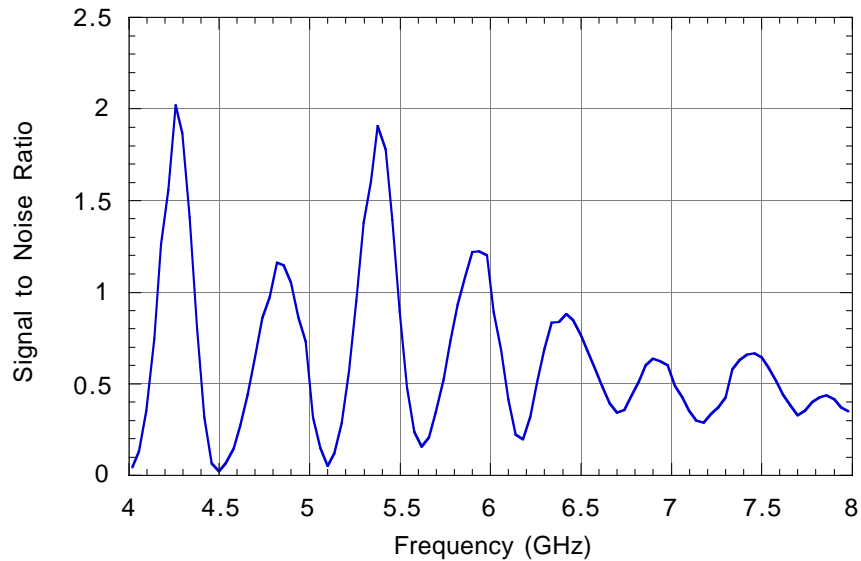


Figure 3.13. Signal to noise ratio.

3.3.3.5 Signal Suppression

Signal suppression is a measure of the strength of the feedback. The signal suppression factor is $(1-GF)$, and is equal to 2 at the optimum gain. The factor GF is plotted in Figure 3.14 for the 4-8 GHz Horizontal system.

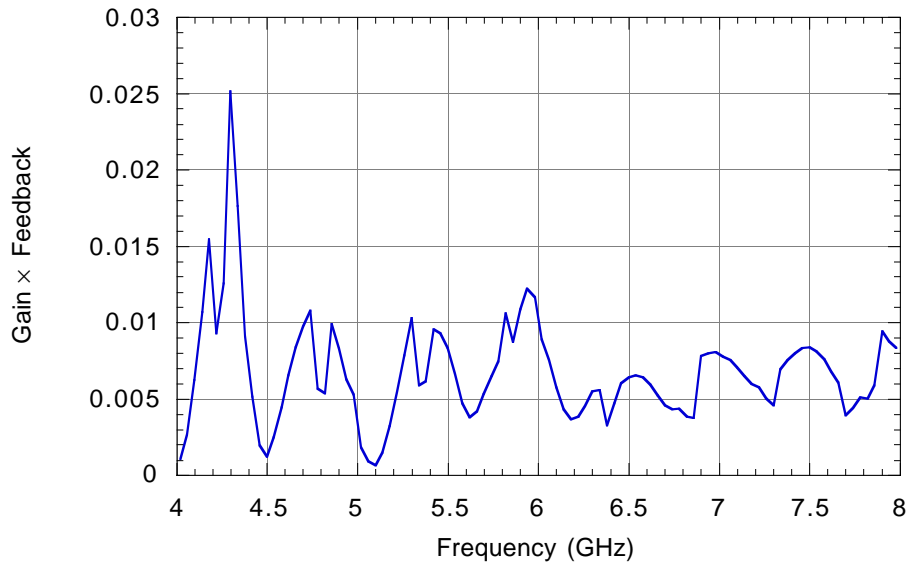


Figure 3.14. Signal suppression factor.

3.3.3.6 Performance in Run II

The performance predicted in Run II under the previously stated assumptions is shown in Figure 3.15, which shows the horizontal emittance versus time. Similarly, Figure 3.16 shows the vertical emittance versus time. The system bandwidths and sensitivities are not finalized, but at this point the vertical cooling system performs noticeably better.. The nominal cycle time is 1.5 sec. The four-band 4-8 GHz system outperforms the 2-4 GHz system. The 2-4 GHz system performs somewhere between 2 and 3 bands of the 4-8 GHz system.

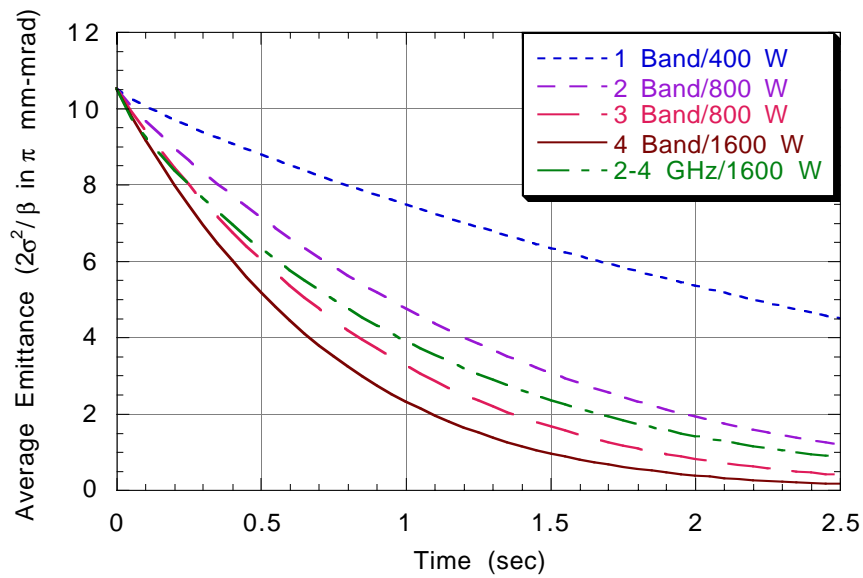


Figure 3.15. The horizontal emittance versus time for the various scenarios.

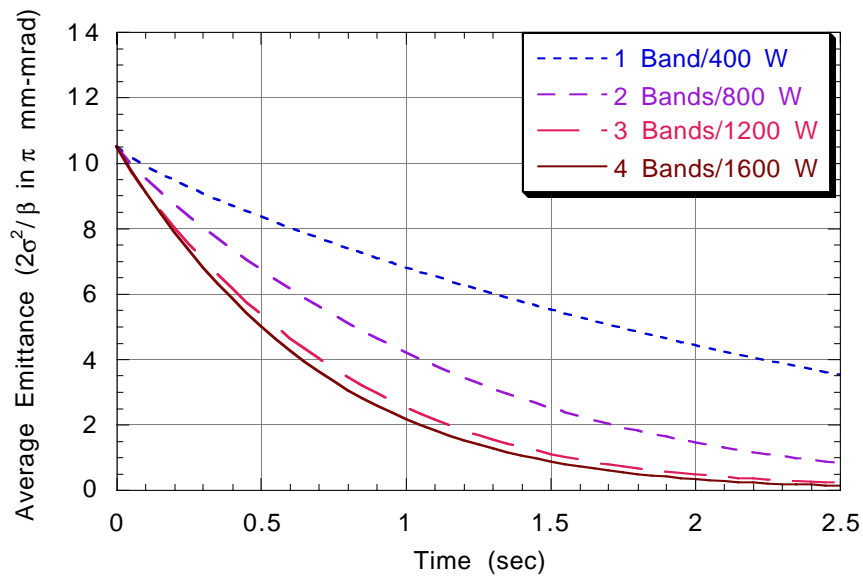


Figure 3.16. The vertical emittance versus time for the various scenarios.

The transfer efficiency is computed as the fraction of beam less than 5π mm-mrad horizontally times the fraction of beam less than 5π mm-mrad vertically. The combination of the data from Figure 3.15 and Figure 3.16 (assuming the 2-4 GHz cooling to be the same in each plane) is shown in Figure 3.17.

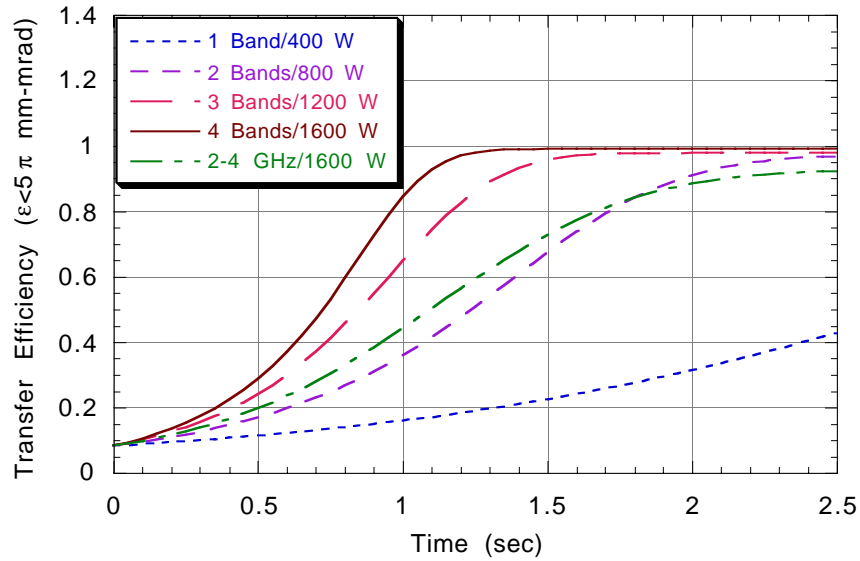


Figure 3.17. Transfer efficiency as a function of time for the various scenarios.

3.3.3.7 Performance with TeV33 parameters

We have also examined the system performance at higher intensity (TeV33 parameters). The results are shown in Figure 3.18 and Figure 3.19. The transfer efficiencies are obtained from the square of the fraction of the beam with a horizontal emittance less than 5π mm-mrad. Since the cooling is less effective in the horizontal plane, the transfer efficiency is probably underestimated. The 2-4 GHz system performance is limited primarily because of its lower bandwidth. The larger particle losses incurred with this system and shown in Figure 3.20 are indicative of the need for more bandwidth.

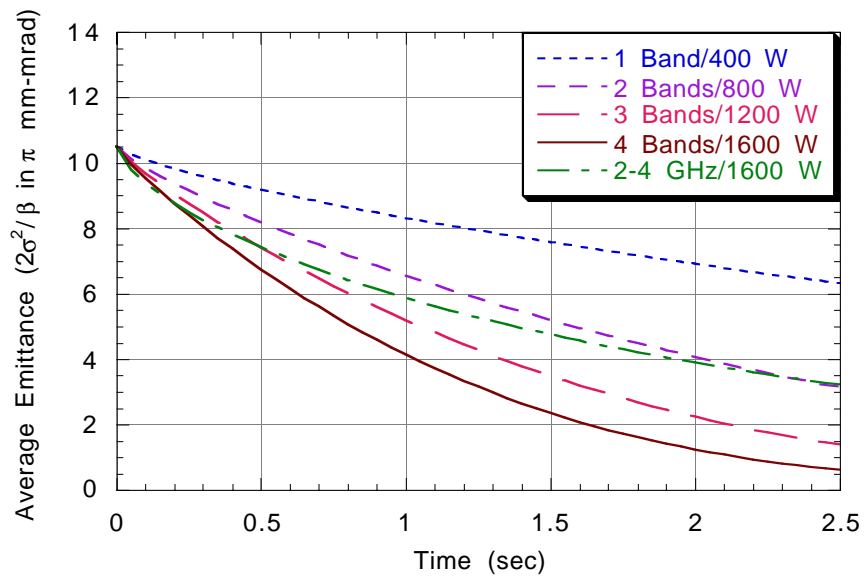


Figure 3.18. Horizontal emittance versus time for TeV33 intensities.

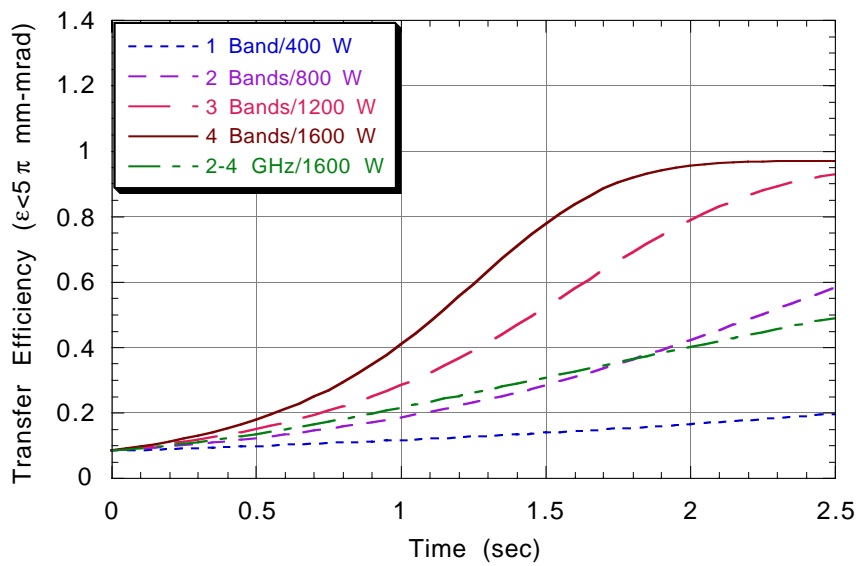


Figure 3.19. Transfer efficiency versus cooling time for TeV33 intensities. The transfer efficiencies are obtained from the square of the fraction of the beam with a horizontal emittance less than 5π mm-mrad.

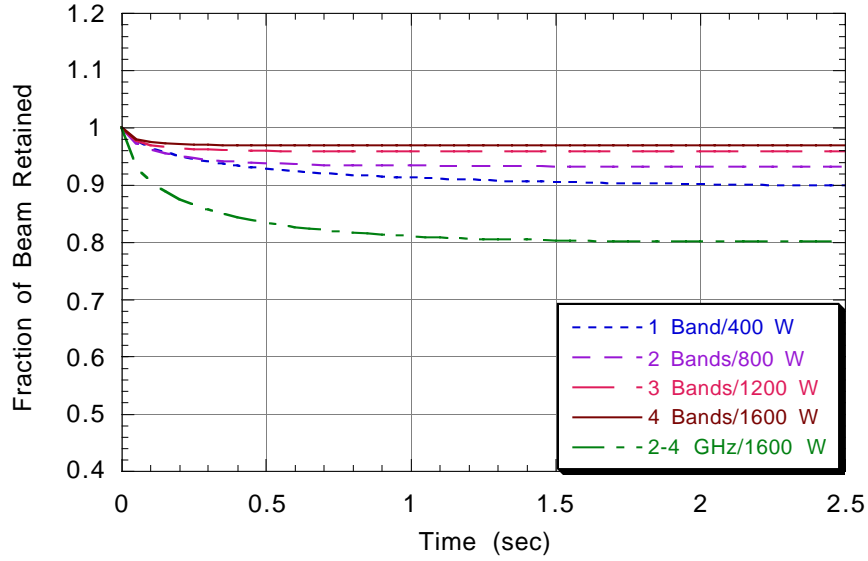


Figure 3.20. Fraction of beam retained as a function of cooling time. The limited bandwidth and relatively high gain of the 2-4 GHz system result in significant particle losses at the beginning of the cycle.

3.4 Stack-Tail System Upgrade

3.4.1 Overview

The beam parameters in the Accumulator will change in the following ways from Collider Run Ib to Run II:

- 1) The antiproton flux will increase from 2.0×10^7 (peak) to 5.6×10^7 (average) per second. These fluxes correspond to 7.2 mA/hour (peak) and 20 mA/hour (average) respectively;
- 2) Beam transfers from the Accumulator to the Recycler will take place every 1 to 4 hours.
- 3) The maximum antiproton stack size will be reduced from 200×10^{10} to 100×10^{10} ;

The current stack tail cooling system in the Accumulator is inadequate to cope with the increased flux. It is proposed to increase the bandwidth of the stack tail cooling system from 1-2 GHz to 2-4 GHz and to decrease η by a factor of two from $-.023$ to $-.012$. The bandwidth change will supply the necessary cooling force to handle the increased flux. The η change will avoid Schottky band overlap, which causes excessive beam heating, and will allow the use of conventional notch filters for gain shaping. In general aspects, the system will be similar to the current system.

The maximum attainable flux in a "perfect" stacking system having a bandwidth of a single octave is given by¹⁸

$$\phi_{\max} = \frac{1.4W^2 E_d |\eta|}{pF_0} \text{ sec}^{-1}, \quad [3.4]$$

where W is the bandwidth, $1/E_d$ is the slope of the exponential gain profile, p is the beam momentum, and F_0 is the revolution frequency. This equation neglects thermal noise, signal suppression, phase variations across the Schottky band, and the effects of periodic beam injection, but indicates that doubling the bandwidth and halving η will double the maximum attainable flux.

E_d is 10 MeV, so that we have for the current stack tail system $\phi_{\max} = 21 \times 10^{10}$ /hour. In addition to the factors mentioned above, other effects that will further reduce the stacking rate are intrabeam scattering, intermodulation distortion in TWT's, realistic gain and phase variations across the microwave band, and cross-talk from transverse cooling systems. We have attempted to include all of these effects (albeit crudely in some cases) so that the current performance of the Accumulator cooling systems is well predicted by the stochastic cooling simulation.

3.4.2 Lattice Modifications

<p>Using the Methodical Accelerator Design (MAD) simulation code, a strategy for raising γ_t in the Accumulator ring and hence lowering η has been developed. The Accumulator is divided into 6 sectors, each containing fourteen quadrupole magnets.¹⁹ The symmetry is three-fold, each of the six sectors being a reflection of the adjacent sector. Within each sector, nine of the quadrupoles are of the small TEV I variety and five are large TEV I quadrupoles.</p> <p>Changes to the quadrupole operation that will enable γ_t to be raised from 5.41 to 6.58, corresponding to an η</p>	<p>261.6</p>			<p>261.6</p>	
--	--------------	--	--	--------------	--

Q2	-QT	0.9900	264.2	261.6	
Q3	QT	0.9009	264.2	238.0	23.6
Q4	QF	0.9865	231.6	228.5	
Q5	QD	0.9908	234.3	232.0	
Q6	QF	1.1043	231.6	255.8	
Q7	QD	0.9908	234.3	232.0	
Q8	QF	0.9816	231.6	227.3	1.2
Q9	QD	0.9908	234.3	232.0	
Q10	.45724*LQ	0.9900	1294.3	1281.4	32.6
Q11	LQ	0.9900	1294.3	1281.4	32.6
Q12	-LQ	1.0152	1294.3	1314.0	
Q13	-LQ	1.0152	1294.3	1314.0	
Q14	LQ	1.0890	1294.3	1314.0	
Note that column 3 above includes the quad bus changes below.					
QT	10.3809T/m	.9900	264.3	261.6	
QF	9.66333T/m	.9816	231.6	228.5	3.5
QD	9.74126T/m	.9908	234.3	232.0	
LQ	8.93989T/m	.9900	1294.3	1314.0	

Since the current in Q6 will be significantly different from that of the other small quadrupoles, a separate power supply will be required for these 6 quadrupoles. Table 3.7 shows critical lattice parameters for the current lattice and the γ_t upgrade. The tunes remain at 6.609 (horizontal) and 8.607 (vertical), and the phase advance from pickup to kicker in the core and stack tail betatron systems remains close to $\pi/2$. The natural chromaticities in each plane ($\xi_x = -11.2$ and $\xi_y = -13.0$) are correctable by decreasing the current in one of the sextupoles in each sector. The dispersion is similar to that of the present Accumulator, with a slightly more negative dispersion in non-critical parts of the ring to accomplish the change in γ_t . The beta functions and dispersion function are shown in Figure 3.21 through Figure 3.23. The physical aperture and beam envelope functions are shown in Figure 3.24 through Figure 3.26.

Table 3.7. Lattice parameters for TEV I design and γ_t upgrade

Lattice Parameter	TeV I Design	γ_t Upgrade
Maximum β_x (m)	33.23	71.15
Minimum β_y (m)	30.87	31.49
β_x @ high D_x (m)	7.58	2.60
β_y @ high D_x (m)	7.51	6.76
β_x @ low D_x (m)	7.56	10.03
β_y @ low D_x (m)	7.27	4.97
γ_t	5.41	6.58
η	-.023	-.0119
$\Delta\phi_{PU-K}$ Core H	$9.16\pi/2$	$9.08\pi/2$
$\Delta\phi_{PU-K}$ Core V	$11.00\pi/2$	$10.82\pi/2$
$\Delta\phi_{PU-K}$ Stack tail H	$8.89\pi/2$	$8.95\pi/2$

$\Delta\phi_{PU-K}$ Stack tail V	$11.20\pi/2$	$11.16\pi/2$
----------------------------------	--------------	--------------

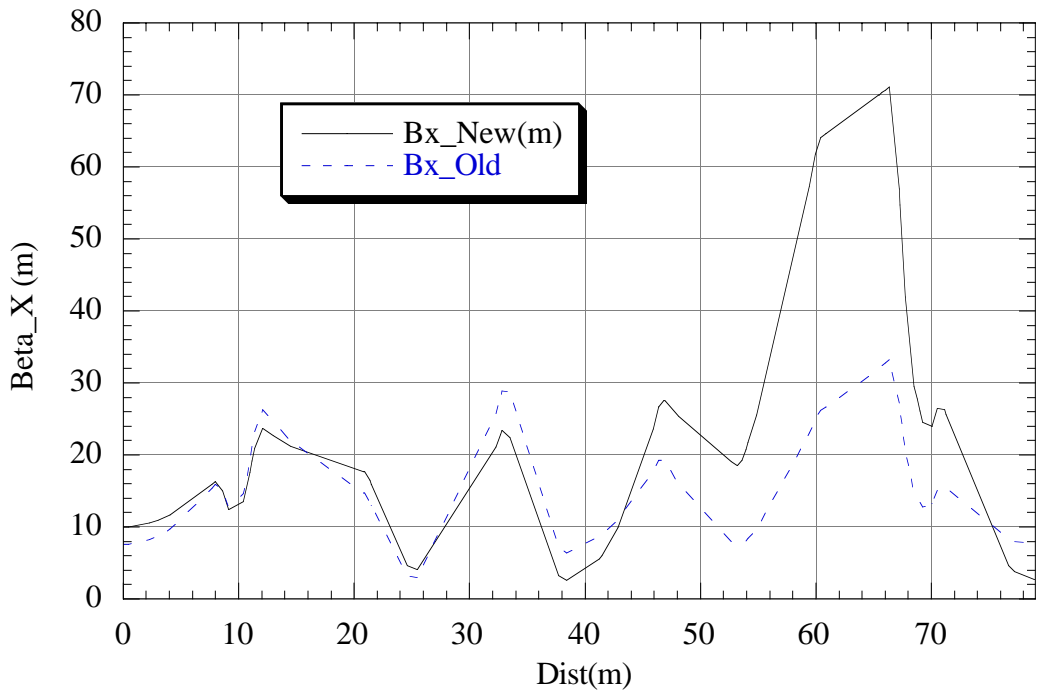


Figure 3.21. Horizontal beta function in one sector (1/6th) of Accumulator.

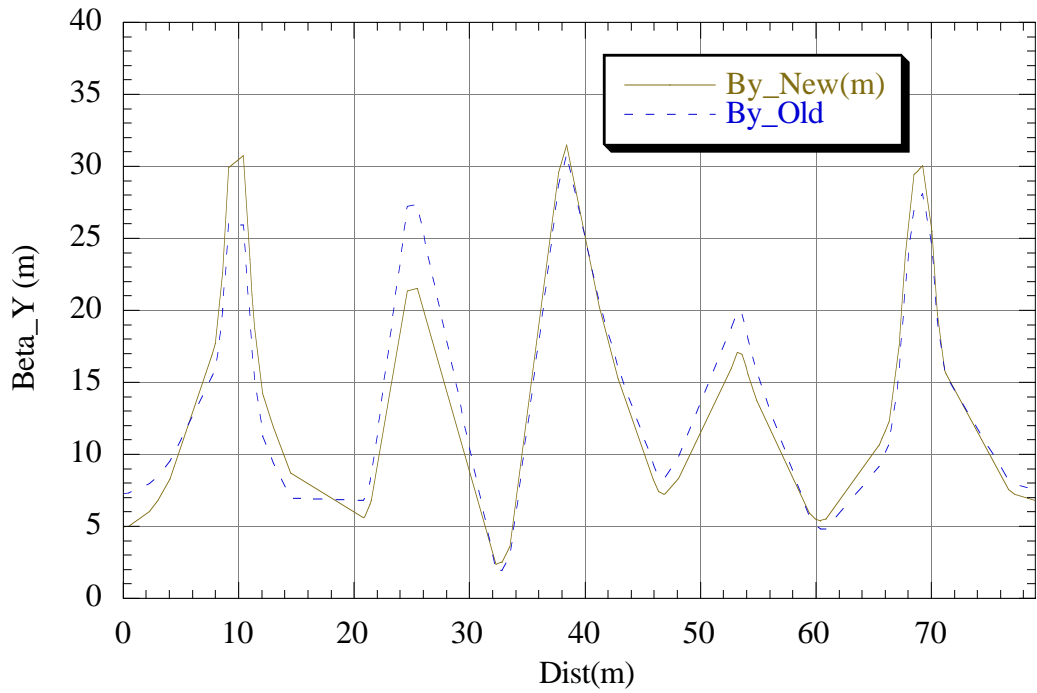


Figure 3.22. Vertical beta function in one sector (1/6th) of Accumulator.

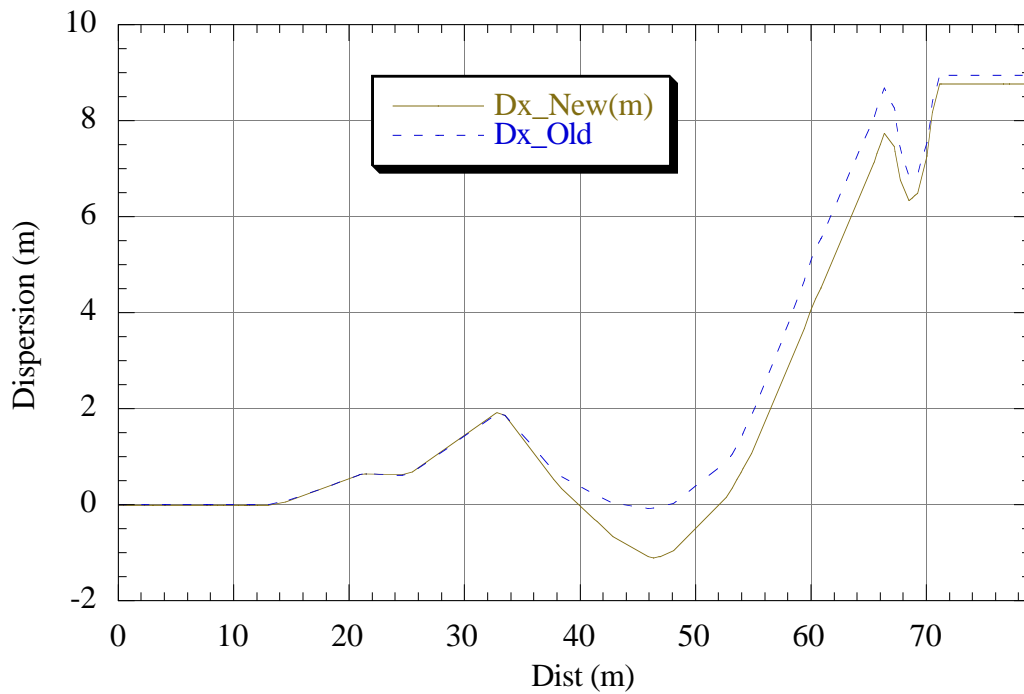


Figure 3.23. Horizontal dispersion function in one sector (1/6th) of Accumulator

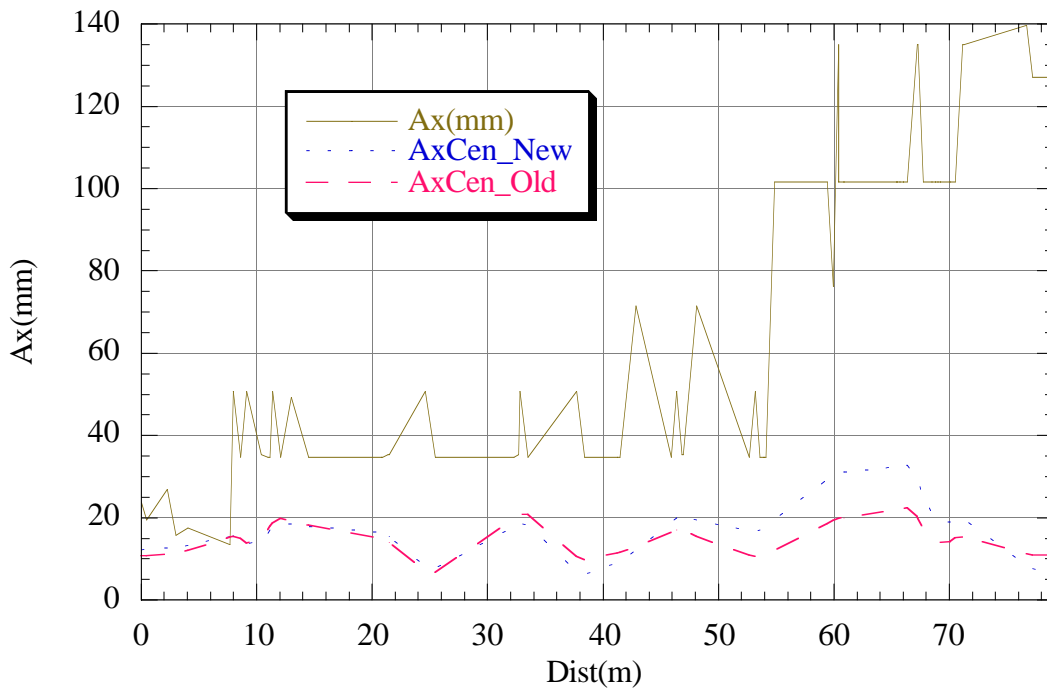


Figure 3.24. Horizontal aperture and beam envelope on the central orbit in one sector (1/6th) of Accumulator; the formula used for the beam envelope is $A_x = \sqrt{\varepsilon\beta/\pi}$ where $\varepsilon = 15\pi$ mm-mrad (unnormalized).

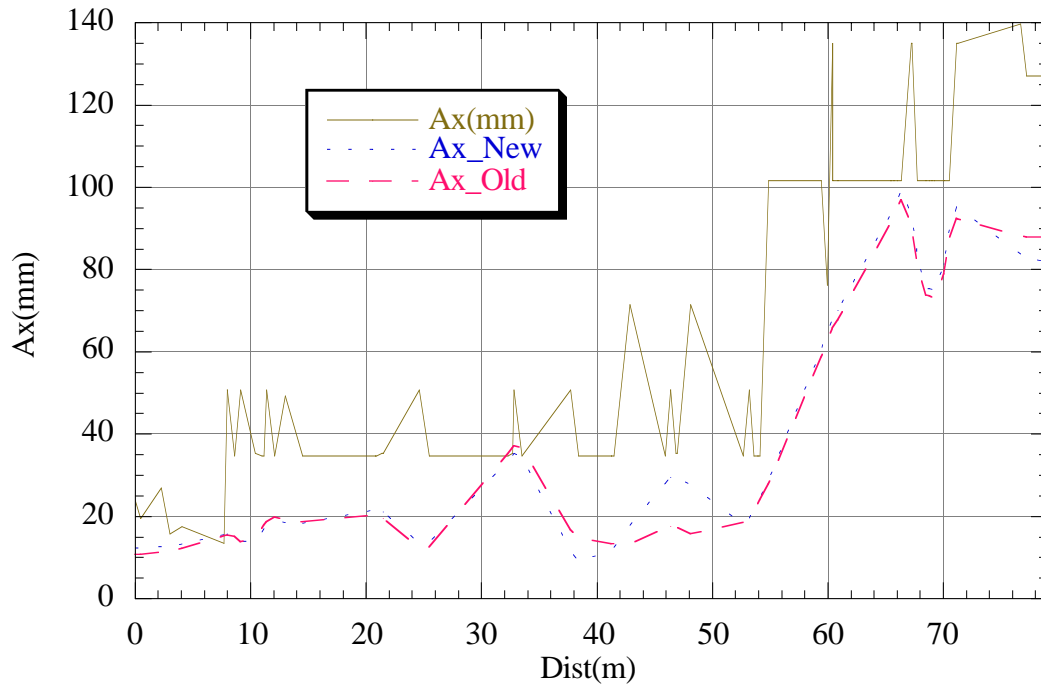


Figure 3.25. Horizontal aperture and beam envelope on the extraction orbit ($\Delta p/p = .0086$) in one sector (1/6th) of Accumulator; the formula used for the beam envelope is $A_x = \sqrt{\varepsilon\beta/\pi} + |D_x(\Delta p/p)|$ where $\varepsilon = 15\pi$ mm-mrad (unnormalized)

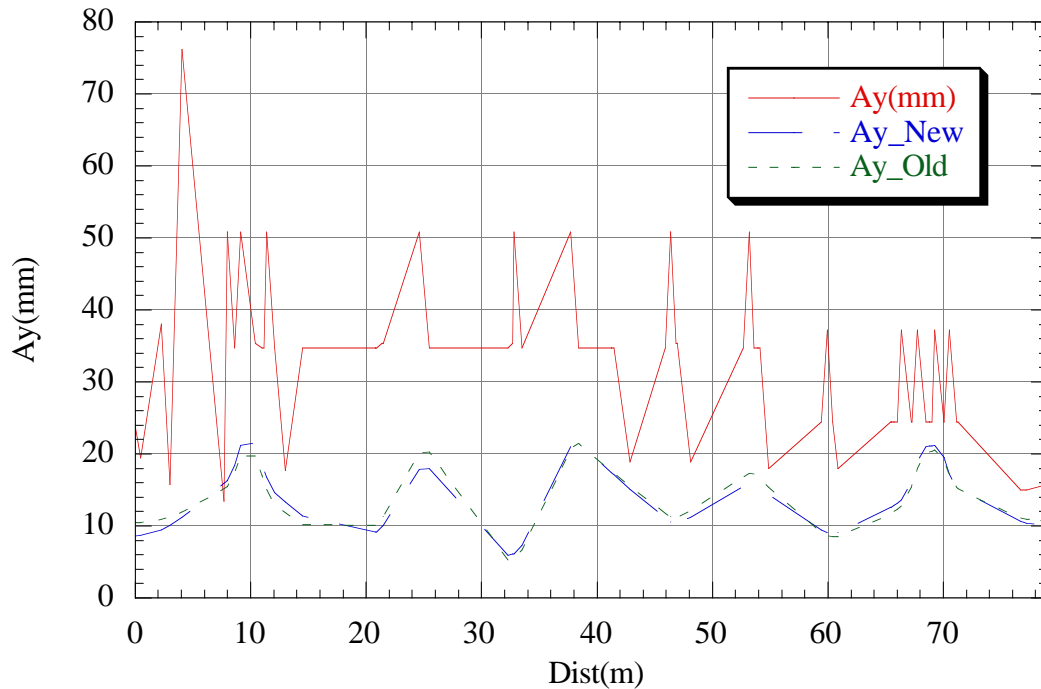


Figure 3.26. Vertical aperture and beam envelope on the central orbit in one sector (1/6th) of Accumulator; the formula used for the beam envelope is $A_y = \sqrt{\varepsilon\beta/\pi}$ where $\varepsilon = 15\pi$ mm-mrad (unnormalized)

The phase advances from injection septum to kicker and from extraction kicker to extraction Lambertson magnet remain $3\pi/2$. The horizontal beta functions at the injection and extraction kickers will be slightly higher than they are now, so that the present kickers will be adequate in strength. Table 3.8 lists the lattice parameters at the injection septum and extraction Lambertson magnets for beam on the injection or extraction orbit. Small adjustments to the beam line quadrupoles can be made so that the beam lines are matched to the new Accumulator lattice at least as well as they are now.

Table 3.8. Lattice parameters at the injection septum and extraction Lambertson magnets.

Quantity	$\beta_x(\text{m})$	$\beta_y(\text{m})$	α_x	α_y	$D_x(\text{m})$	D_x'	$\phi_x(2\pi)$
Septa and Lambertson ($\gamma_\tau=5.42$)	15.77	7.58	0.55	0.02	0.30	0.10	0.21
Injection/Extraction Kickers ($\gamma_\tau=5.42$)	11.44	13.46					1.01
Septa and Lambertson ($\gamma_\tau=6.58$)	20.46	7.22	0.21	0.24	0.41	0.07	0.20
Injection/Extraction Kickers ($\gamma_\tau=6.58$)	15.75	13.68					0.92

Nonlinear effects beyond those which can be corrected by families of sextupoles, octupoles, and skew quadrupoles are probably difficult to model with the magnetic field measurements that have been made to date. With the exception of the large β_x variation at Q10-Q11, the proposed lattice is very similar to that of the TEV I design, so that these effects will probably not change much. Figure 3.27 shows the measured tune variations across the momentum aperture with the extraction Lambertson magnet on. Turning the extraction Lambertson magnet off introduces a tune shift across the aperture, but does not change the basic shape of the tune vs. momentum plot. Introducing a local large orbit bump on the extraction orbit at any of the three high dispersion regions will produce a large tune shift. The Accumulator is operated with tunes decoupled on the core orbit, but the coupling is essentially 100% on the extraction orbit. A major portion of this coupling comes from the Lambertson magnet, and this coupling is a strong function of horizontal position in the Lambertson magnet. By design, the dispersion in the Lambertson magnet is 0.3 m, but the average measured dispersion is 0.8 m, and most of this arises between the extraction orbit and central orbit. In addition anomalous dispersion arises in all of the "zero dispersion" straight sections when the beam moves between the central orbit and the extraction orbit, making it impossible to optimize the aperture at all beam momenta. Figure 3.27 shows the measured orbit deviation between the core and extraction orbits, compared with the TEV I design. Beta function measurements at the core orbit and the central orbit agree well with each other and with the design; however beta function measurements at the extraction orbit deviate substantially from the design and have been difficult to interpret because of coupling.

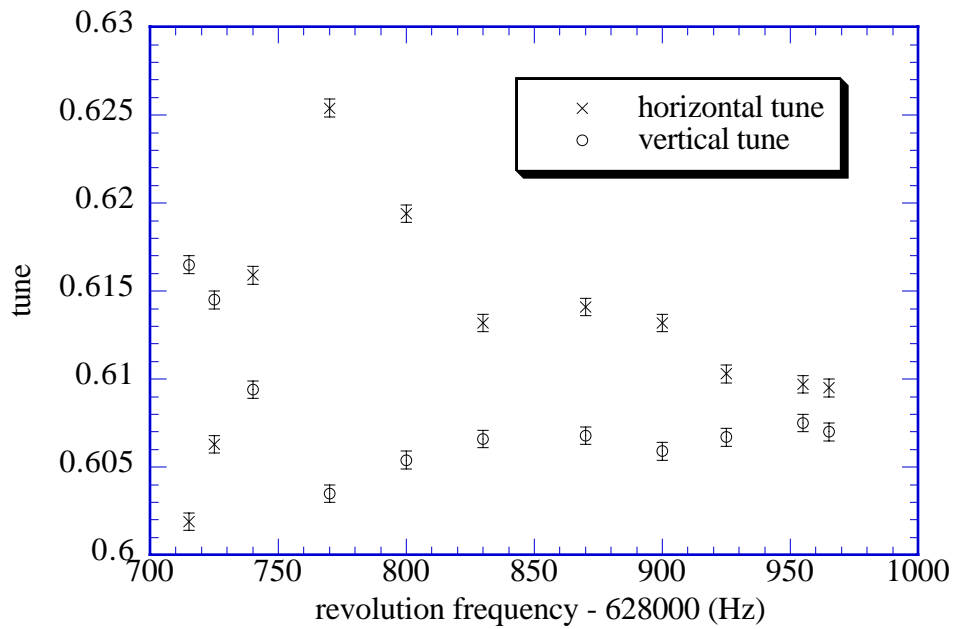


Figure 3.27. Measured Accumulator tune variations across the momentum aperture.

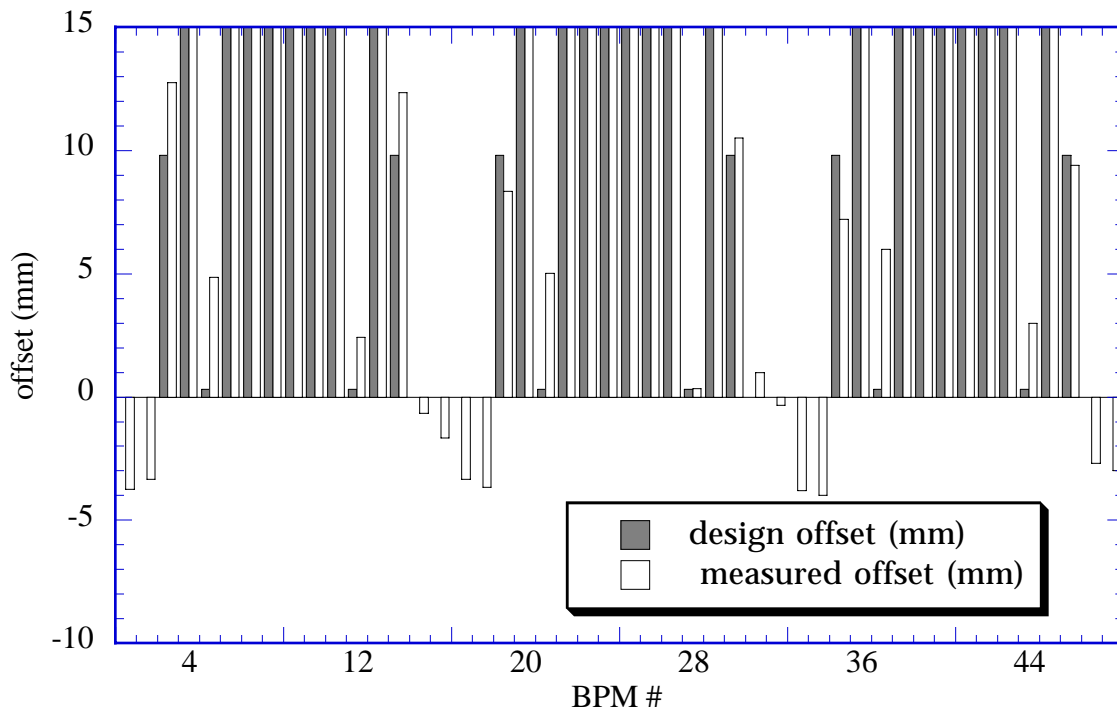


Figure 3.28. Measured and design Accumulator orbit difference between extraction orbit and core orbit on a scale showing dispersion error at the "zero dispersion" regions; high dispersion regions are off scale (about 140 mm).

It is known that some higher order resonances cause heating in the core – for example, the 8/13th (0.6154) and the 11/18th (0.6111). This is the motivation for choosing to run near the coupling resonance; it provides a large area in tune space free of higher order resonances. In addition, we currently operate with small negative chromaticities at the core, although there is no

strong evidence that operating at zero or slightly positive chromaticity at the core produces any instability.

3.4.3 Stack Tail Cooling System

The design of the 2-4 GHz stacktail system is based on scaling the TeV I 1-2 GHz stacktail design. The following quantities are scaled:

1. 1-2 GHz becomes 2-4 GHz
2. All beam energies stay the same
3. $\eta = 1/\gamma_t^2 - 1/\gamma^2$ becomes 0.012 (see section 3.4.2)
4. The gain functions stay the same

With this scaling, the maximum flux is doubled. The power requirement is the same if the signal to noise ratio remains constant -- it should actually improve somewhat. Thus, rebuilding the stacktail system is essentially replacing the entire system part-for-part with higher frequency components. Some issues do need further investigation:

1. Fewer pickups are required to achieve the same signal to noise ratio. One might be able to achieve some savings in pickups.
2. The dependence of pickup sensitivity on transverse displacement was not what was expected for the 1-2 GHz system.
3. The Accumulator is designed to operate with the Recycler and to accumulate antiprotons for 1 to 4 hours. The optimum design for this type of operation might differ from a scaled TeV I design.
4. The effect on the stacking process of continual transfers from the Accumulator to the Recycler needs to be considered.

However, it is not foreseen that a better optimized design would differ dramatically in either cost or performance from the design that is simply scaled from TeV I.

The ultimate upgrade of the stacktail system could be to 4-8 GHz in the TeV33 era. This upgrade is not foreseen as being possible on the 1999 time scale. The design of the 4-8 GHz stack tail system would be radically different from either the 1-2 or 2-4 GHz systems, requiring frequent transfers to the Recycler Ring to take advantage of stacking capabilities of the electron cooling system. The lattice modification ($\eta = 0.012$) implemented for the 2-4 GHz system would also be appropriate for the 4-8 GHz system.

3.4.3.1 Design Considerations

Stochastic stacking is described in terms of the Fokker-Planck equation, which relates the time rate of change of the particle density to the initial density and the derivative of the density with respect to energy:

$$\frac{\partial \Psi}{\partial t} = \frac{\partial}{\partial E} \left[-F\Psi + (D_0 + D_1 + D_2\Psi) \frac{\partial \Psi}{\partial E} \right]$$

where $\Psi = \partial N / \partial E$ is the particle number density, F is the coefficient of the cooling term, the three D terms represent heating due to intrabeam scattering, thermal noise, and mixing. A complete derivation has been given by Möhl, et al.²⁰ A simplified steady state solution (ignoring for the moment thermal noise, mixing, and intrabeam scattering) results in an exponential density distribution, developed by an exponential voltage distribution. Our goal is to create an exponential

voltage distribution using beam pickups, amplifiers, electronic filters and phase compensation networks, and kicker electrodes. More complete details can be found in the TeV I Design report.²¹

As mentioned previously, the Run II stacktail system design is a scaling of the TeV I design to the frequency range of 2-4 GHz. The predicted pickup behavior as a function of beam position is an exponential falloff²² as the particle moves far away from the center of the pickup. The pickup is placed in an area with large momentum dispersion (on the order of 8.5 m), correlating position with particle energy. With a symmetric lattice and non-zero value of η , there is a time difference in particle flight time between pickup and kicker as a function of energy. As the electronics time between pickup and kicker is fixed, the net phase of the voltage on the kicker changes with the particle energy. This phase slope leads to the use of multiple sets of pickups.

Three sets of pickups are used, two as the cooling inputs and two as compensation inputs (one set of pickups is used for both cooling and compensation). The compensation inputs are phased to null out the response in the region of the accumulated core. The first leg uses pickup set 1 as the cooling input and pickup set 2 as the compensation input. The peak response for leg 1 is centered in the vicinity where the input beam pulse is dropped off by the rf stacking. The second leg, which uses pickup set 2 as the cooling input and pickup set 3 as the compensation input, is positioned to best flatten the phase response. As the beam density is increasing as the beam energy decreases, there are fewer pickups required in sets 2 and 3 to attain a good signal to noise ratio.

3.4.3.2 Pickup Response Measurements

During the summer of 1997, a series of measurements was made using prototype 2-4 GHz pickups. These measurements were made in the Accumulator using antiprotons. Four different pickup designs were tested. A detailed account has been given by Derwent.²³ Figure 3.29 shows a comparison of the measured response and predicted response (with arbitrary normalization) as a function of the beam revolution frequency. The model response is normalized to the response of design #1. The measured response is in very good agreement with the predicted response.

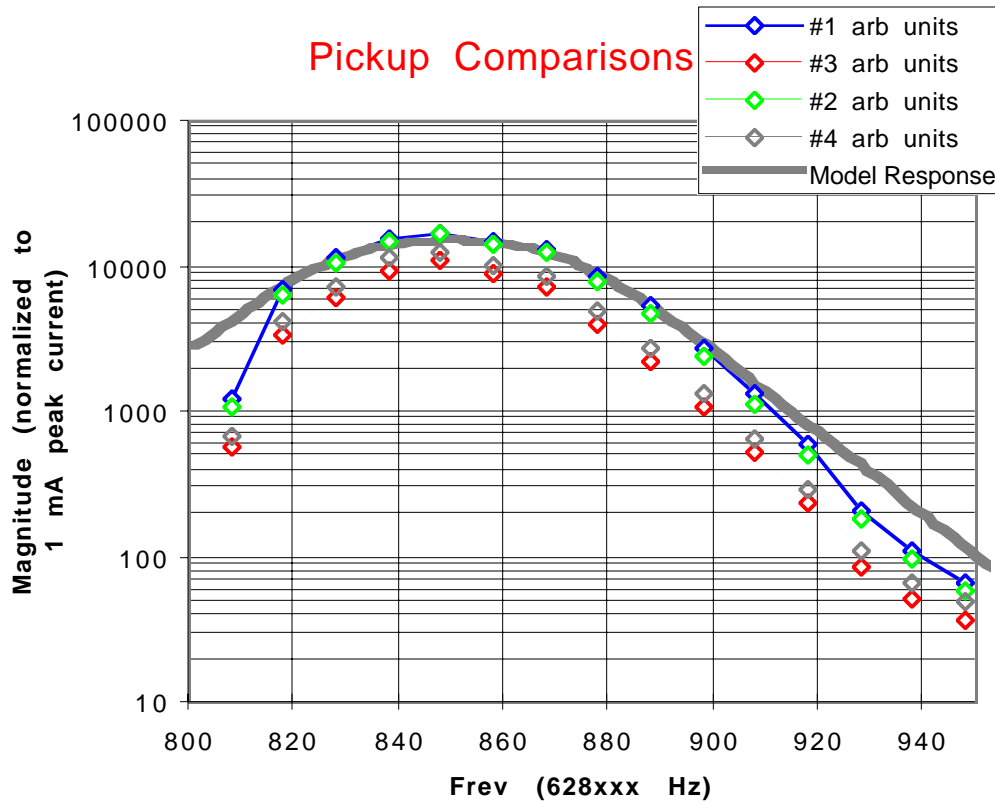


Figure 3.29. A comparison of measured and predicted pickup response

Of the four prototype pickup designs, two were similar to previous loop designs (#1 and #2) and two (#3 and #4) were designed to include phase compensation. By tilting the major axis of the pickup loop, thus changing the relative arrival time of the signal on the loop, it is possible to cancel some of the phase slope across the aperture. However, to keep the frequency response in the desired 2-4 GHz band, the pickup size became smaller. There is a tradeoff in the two designs -- better sensitivity (in #1 and #2) versus better phase behavior (#3 and #4). The impedance of the tilted loops is approximately 1/2 the impedance of the standard loops, requiring a factor of 2 in amplifier gain to get similar voltage response. This factor of two in amplifier gain results in a factor of four in noise power. As stacking simulations (discussed in the next section) achieve fairly uniform phase behavior using the standard loops, better pickup sensitivity has been chosen over better phase response.

3.4.3.3 Simulation Performance and Pickup Locations

The stacking simulation used in the system design is based on a simulation originally written by S. van der Meer for the CERN Antiproton Accumulator. The code does a numerical integration of the Fokker-Planck equation with a voltage gain function including the pickup response, amplification and electronic filtering, and kicker response. Beam feedback and thermal noise terms, which contribute to beam heating, are included. Further details can be found in reference.²⁴ The code has been modified to simulate the 2-4 GHz stacktail and the 4-8 GHz core cooling systems. At this time, it only simulates the longitudinal cooling and does not include any heating effects in the transverse plane.

The performance of the 1-2 GHz stacktail system, using the measured pickup response shapes as an input, has been simulated. With a minimum of optimization, the simulation predicts a stacking rate of 12 mA/hour, with an input flux of 18 mA/hour. Studies done with proton stacking

achieved a maximum rate of 12.2 mA/hour (see Ref. 1), well matched to the simulation results. This agreement gives confidence in the predictions of the simulation in extrapolating to the 2-4 GHz system.

The 2-4 GHz Accumulator stacktail system is assumed to have the following properties:

- $\eta = 1/\gamma_t^2 - 1/\gamma^2 = 0.012$
- Momentum Dispersion = 8.5 m at the pickup location
- Central Energy = 8.83 GeV
- Transverse aperture = 0.03 m at the pickup location
- Pickups and Amplifier are at 80 K physical temperature, with an amplifier noise temperature of 21 Kelvin (0.3 dB noise figure)
- Pulses are injected every 1.5 seconds
- RF stacking deposits $1e8$ particles per pulse at an energy of +14 MeV with respect to the central energy and with a half width of 7.8 MeV

These assumptions give a maximum stacking rate of 24 mA/hour.

In Figure 3.30 we show the calculated gain response for the choice of the pickup positions. Pickup set 1 is at an energy of 15.3 MeV (a position of 14.7 mm from the central orbit), pickup set 2 is at an energy of -3.8 MeV (-3.7 mm), and pickup set 3 is at an energy of -22.9 MeV (-22.0 mm). The phase of the system (desire 180° between 20 MeV and -60 MeV) is shown in Figure 3.31. The phase stays within 30° of the desired value, and the magnitude of the response varies only 15% from optimum.

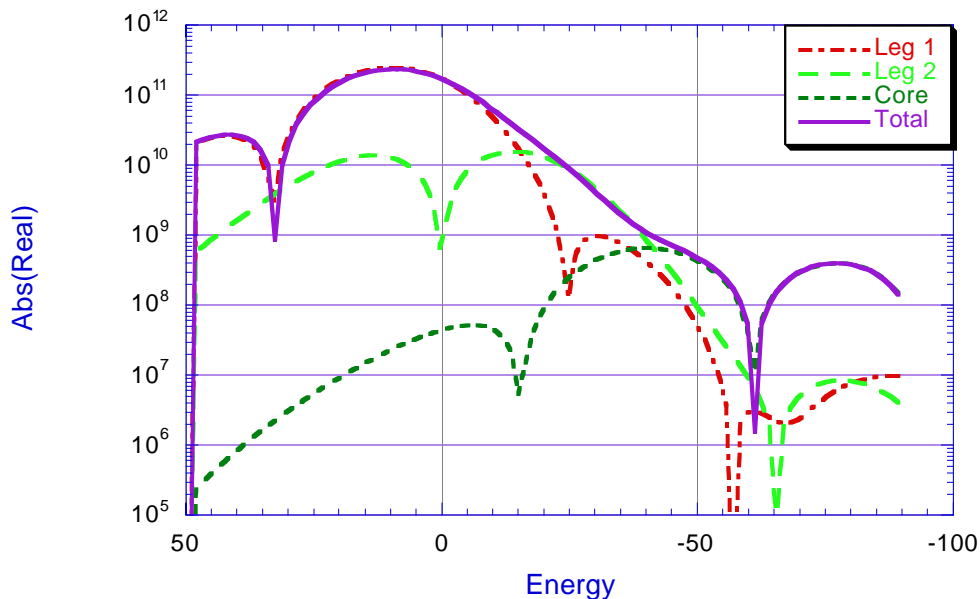


Figure 3.30. The absolute value of the real part of the system gain. The dips indicate where the gain changes sign (from cooling to heating).

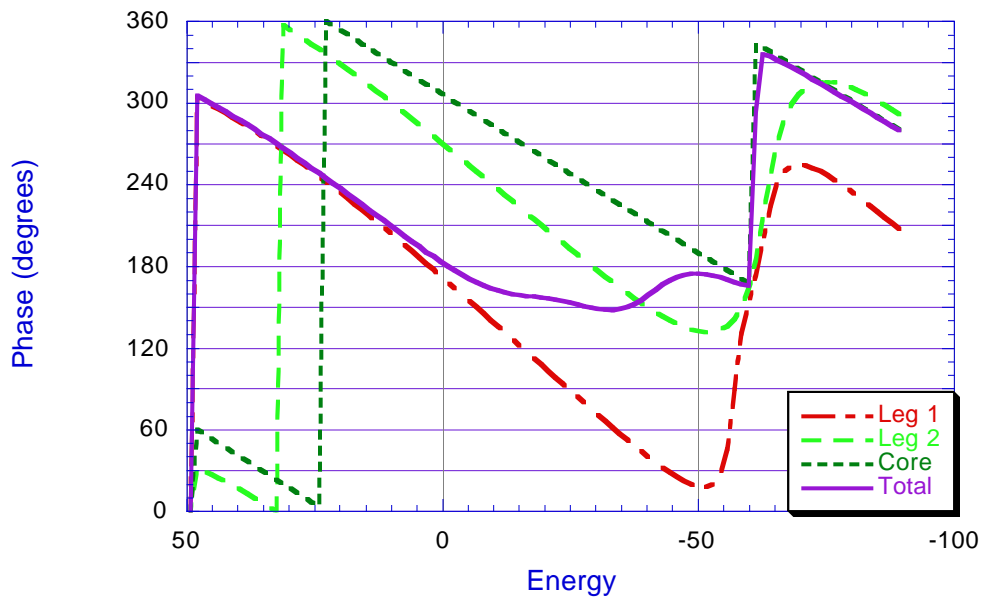


Figure 3.31 The Phase of the stacktail system. A phase of 180° is desired from 20 MeV to -60 MeV.

Simulations have been run for three hours of stacking with this system, putting in 1×10^8 antiprotons every 1.5 seconds. Figure 3.32 shows the energy density distribution, with one curve every 30 minutes of stacking. The core is evident after the first half hour. The effects of extraction to the Recycler have not been simulated.

Figure 3.33 shows the stack size (in mA) and stack rate (in mA/hour) over the three hour time period simulated. The stack rate is equivalent to the injected flux for approximately the first 90 minutes and then it begins to drop off slowly, going down to 22 mA/hour after 3 hours. Over the 3 hour time period, 70.5 mA are accumulated, an average of 23.5 mA/hour.

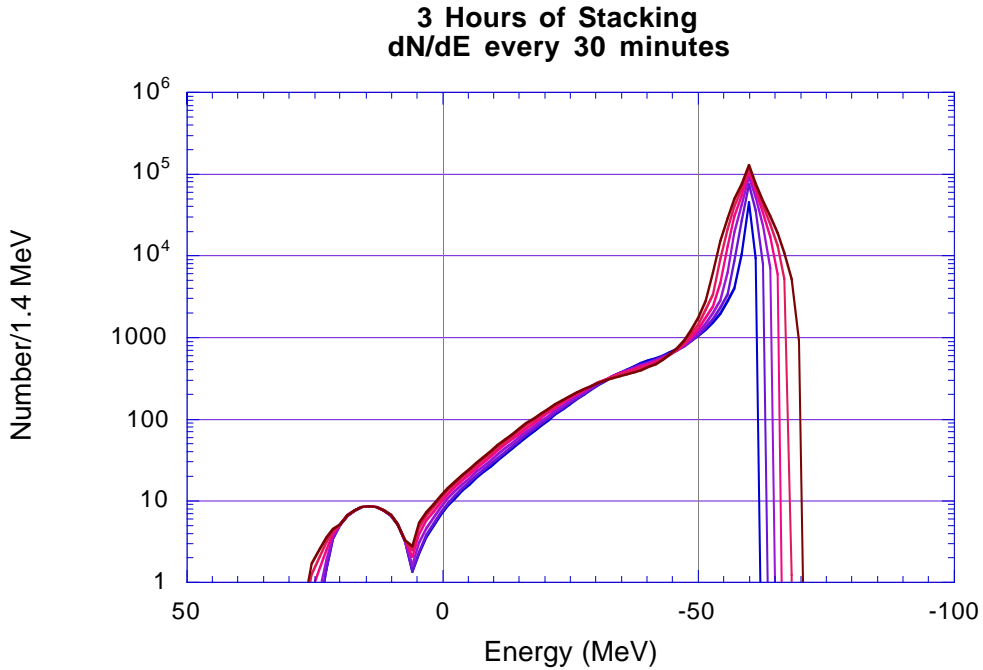


Figure 3.32. The stack density distribution for 3 hours of stacking, showing the distribution every 30 minutes. The bump on the left is the injected beam.

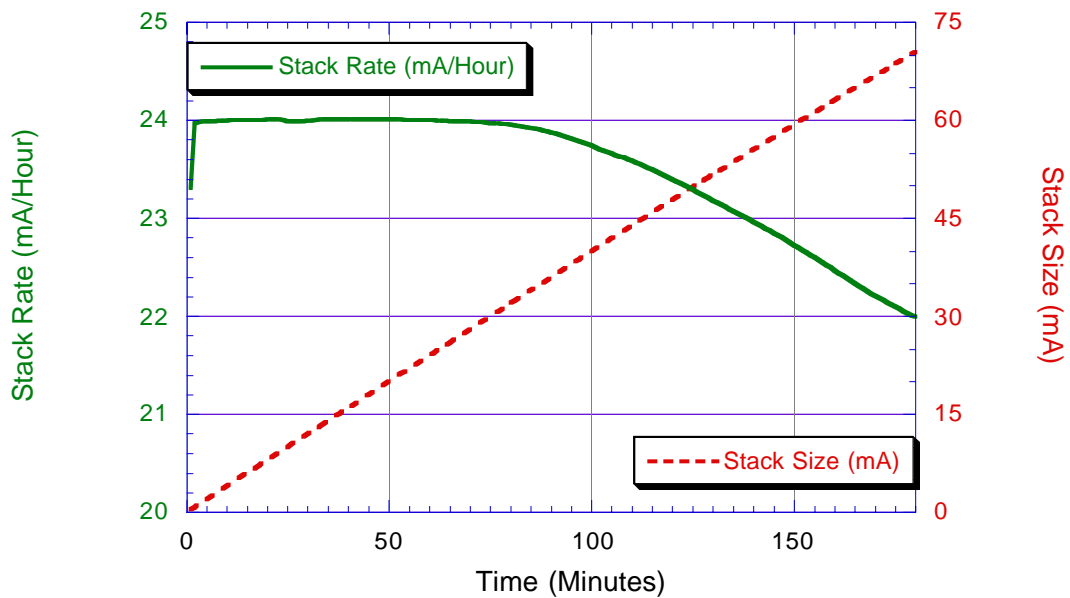


Figure 3.33. The stack rate (solid and left axis) and stack size (dashed and right axis) for the nominal configuration. 24 mA/hour are injected into the system. An average of 23.5 mA/hour over the three hours simulated is achieved.

3.4.3.4 Signal to Noise Ratio and Power

As the system uses high gain amplifiers, the dominant noise component for the signal to noise ratio calculation is the noise coming from the front-end amplifier. With 2 GHz of bandwidth and 80 °K temperature, the noise power is -86.3 dBm. The signal power is calculated using the measured impedance of the 16 loop combiner boards, multiplied by the number of combiner boards, and convoluted with the number density distribution from the stacking simulations. With 16 arrays at 15.3 MeV, the signal power is -80.8 dBm; 4 arrays at -3.8 MeV contribute -80.2 dBm. There is adequate signal to noise for the system in this configuration. The system design described in the previous section uses slightly more than 500 watts of power after two hours of stacking, with 90 watts of the total in noise power.

3.4.3.5 Design Sensitivity

The performance of the stacktail system is dependent upon the momentum dispersion (since the pickup sensitivity depends upon the position displacement) and pickup positions. Simulation runs have been done with variations in the dispersion and pickup position to quantify the sensitivity.

Two hour stacking simulations have been run with dispersion values of 8.1 m, 8.5 m, and 8.9 m. The pickups have been kept at the same physical location with respect to the central orbit (at 14.7, -3.7, and -22 mm respectively). The electronic phase and gain settings were not changed. Over the 2 hour time period, the stacking rate for the 3 scenarios varied by less than 1%. We conclude that small variations in the dispersion around the design goal of 8.5 m should not be a significant problem.

The phase hand-off between leg 1 and leg 2 depends upon the relative position, gain, and phase of the two legs. Displacement of the legs with respect to the beam can change the system performance. For example, assume that the central orbit is not centered through the pickup tanks. A coherent shift of the three pickup sets is used to simulate this possibility. Alignment errors can be simulated by moving the pickup sets independently. Both scenarios have been tested over a ± 10 mm range of displacement. Figure 3.35 shows the results of these simulations. Displacements within ± 5 mm of the nominal positions, in either leg or both legs, lead to small changes in the stacking rate. The stacking rate falls by factors of 1.1 to 3 when the displacements are extended to ± 10 mm.

15 Minutes of Stacking Time
No attempts to rephase system
Move leg position in mm
Independently (tank misalignments)
Coherently (beam off center through A60)

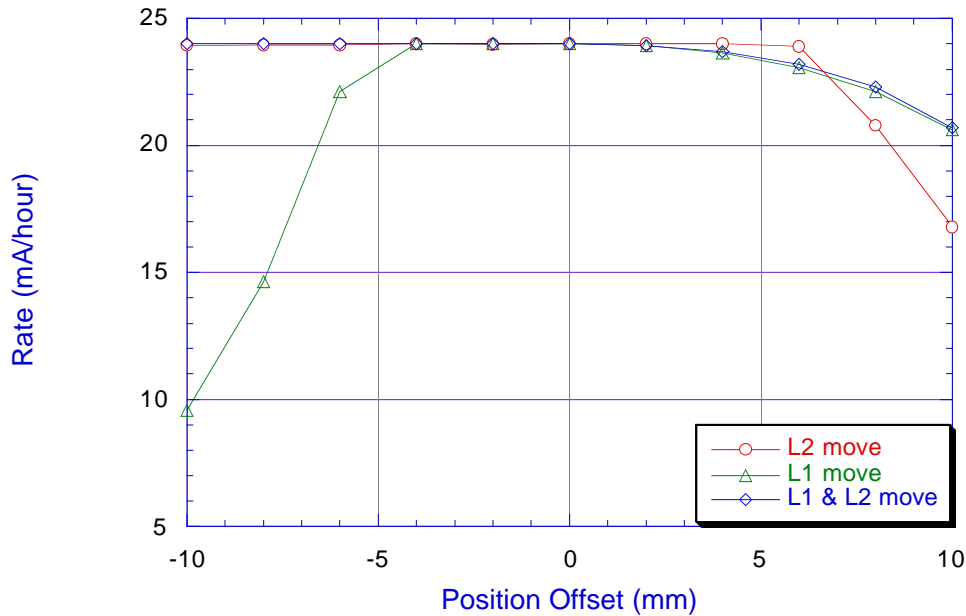


Figure 3.35. The stacking rate as the position of the pickup sets is moved relative to the nominal position. The open circles are moving Leg 2, keeping Leg 1 in the nominal position, the triangles are moving Leg 1, keeping Leg 2 in the nominal position, and the diamonds are moving Legs 1 and 2 together.

3.4.4 Core cooling systems

3.4.4.1 Core cooling requirements

The core cooling systems are required to provide a transverse beam size of 10π mm-mrad for transfer to the Recycler. The time allotted to achieve this emittance is 5% of the stacking time or about 5 to 10 minutes. Figure 3.36 shows the core transverse emittance during stacking as a function of stack size in Run Ib. At a stack size of 100×10^{10} the emittance is 0.6π to 1.0π mm-mrad (6π to 10π mm-mrad normalized), which meets the Recycler criterion immediately after stacking is turned off. However, the transverse cooling rate will decrease because of the factor of about 2 increase in the mixing parameter. This fact should result in a factor of two reduction in cooling rate, but it does not because the core cooling system operates well below the optimum gain. While Figure 3.36 provides a guide, there is no assurance that the transverse heating of the new stack tail system will be the same as the old system (it could be better or worse depending on construction details).

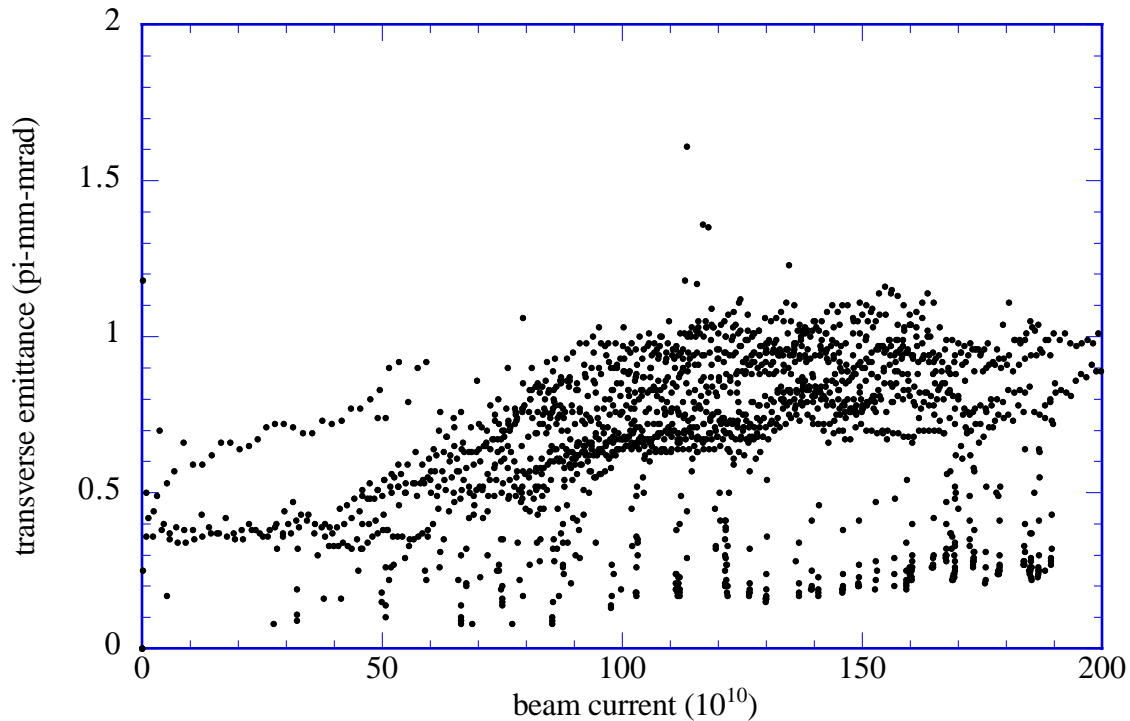


Figure 3.36. Transverse emittance vs. stack size during stacking

There is no specific requirement on the longitudinal density of the beam. We do not expect to be able to capture 100% of the beam longitudinally in a 10 eV-sec phase space. Our experience is that for a fixed longitudinal phase space, more beam can be extracted with a larger stack than a smaller one, but that the fraction of the stack that can be extracted decreases monotonically with stack size. If, for example, we start with a stack of 50×10^{10} antiprotons and we stack an additional 50×10^{10} antiprotons, then we must be able to capture 50% of the beam in order to return to the initial condition. The increase in the amount of beam captured with larger stacks, however, must be balanced against the larger transverse emittance and the frequency and duration of transfers required in order to maximize the efficiency of transfer to the Recycler.

During the course of Run 1b a variety of RF bucket areas were used for unstacking 6 antiproton bunches, but the total longitudinal phase space area was always 10 eV-sec or less.²⁵ The fraction of the antiproton stack extracted as a function of stack size for each size rf bucket is shown in Figure 3.37. Figure 3.37 shows that the fraction of the antiproton stack which is removed during the course of unstacking decreases with increasing stack size. At an intensity of 100×10^{10} antiprotons it is possible to remove 50 to 60% of the antiproton stack. However, these results were obtained long after the stack tail system had been turned off and we expect at least a modest decrease in cooling rate because of the increase in the mixing factor. The stack size, the longitudinal emittance, and the transfer frequency will all be optimized operationally in order to accumulate antiprotons at the maximum rate in the Recycler.

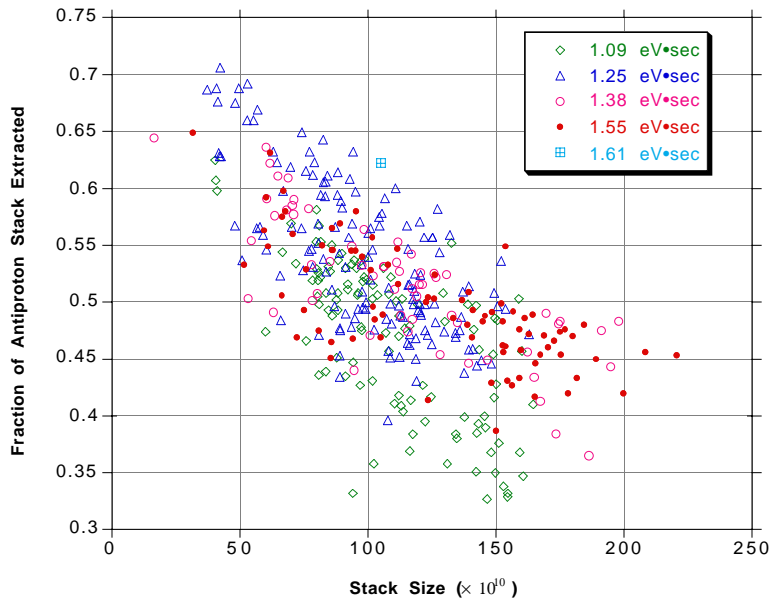


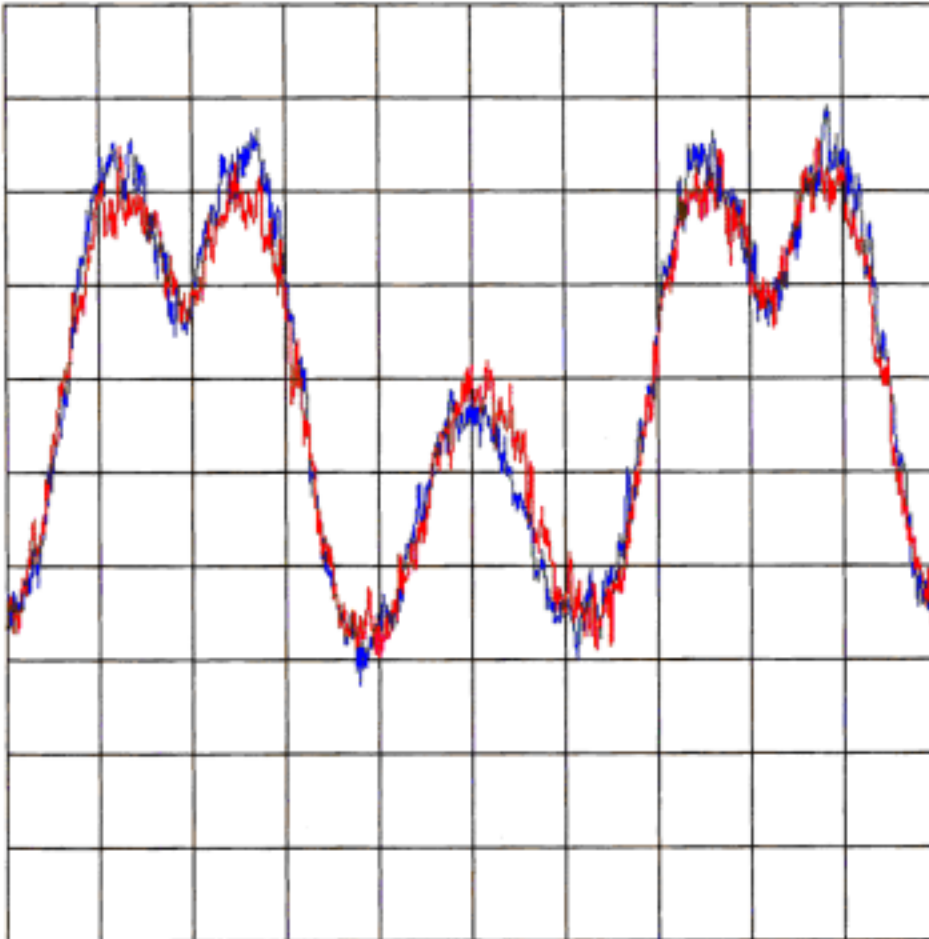
Figure 3.37. Fraction of Accumulator beam unstacked as a function of stack size for different RF buckets. Note the suppressed zero on the vertical axis.

3.4.4.2 Performance of the current 4-8 GHz systems

The currently installed core cooling systems are characterized by low gain (compared to the optimum gain) at the low end of the frequency band and even lower gain at the high frequency end. A measurement of signal suppression is shown in Figure 3.38. The measurement shows perhaps 1 dB of signal suppression (12% of the optimum gain) at 4.5 GHz. A measurement of the transfer function is shown in Figure 3.39. The system gain drops about 15 dB from 4 to 8 GHz. We believe that the gain can be substantially increased by improving the pickup response and improving the method of signal transmission across the ring.

SIGNAL SUPPRESSION 4-8 VERT

07/22/97 0936



Scale 2 dB/div

Atten 0 dB

Sup .999824 sec

Vid BU 100 Hz

Res BU 30 KHz

Ref Lvl -68 dB

Beam current - 46 mA

Power - 16 W

Start Freq 4.50282768 GHz

Stop Freq 4.503822688 GHz

Figure 3.38. Signal Suppression measurement on the 4-8 GHz Core Vertical Cooling system.

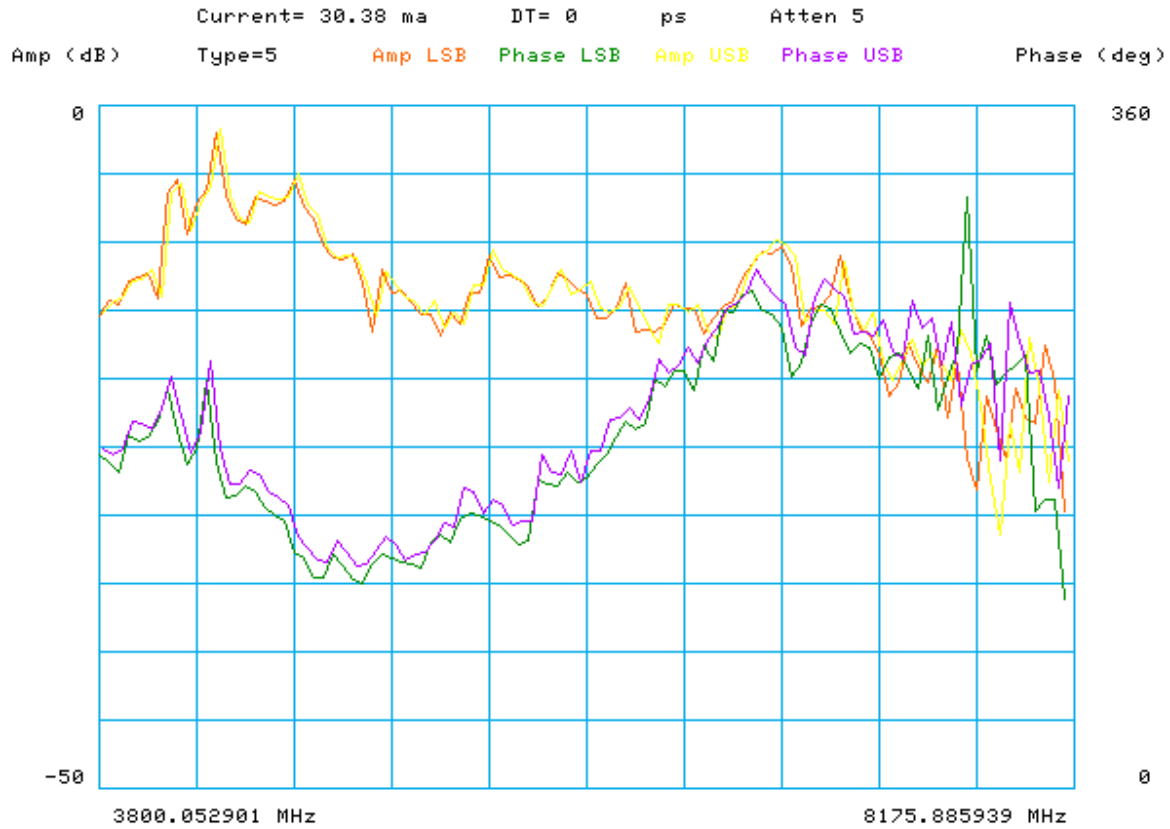


Figure 3.39. Transfer function measurement of the 4-8 GHz core cooling system.

3.4.4.3 Core cooling pickups and kickers

The core cooling pickups and kickers do not have a uniform response in the 4-8 GHz range. The measured signal to noise ratio of the sum mode from the core vertical PU is shown in Figure 3.40. The amplifier noise power is nearly independent of frequency, so the data indicate a decrease in sensitivity of about 10 dB over the frequency range. The non-uniform response makes it difficult to achieve the full cooling bandwidth of 4 GHz. The problem is particularly severe in the kickers which have an additional $1/f$ factor in the frequency response of the transverse kick applied to the beam.

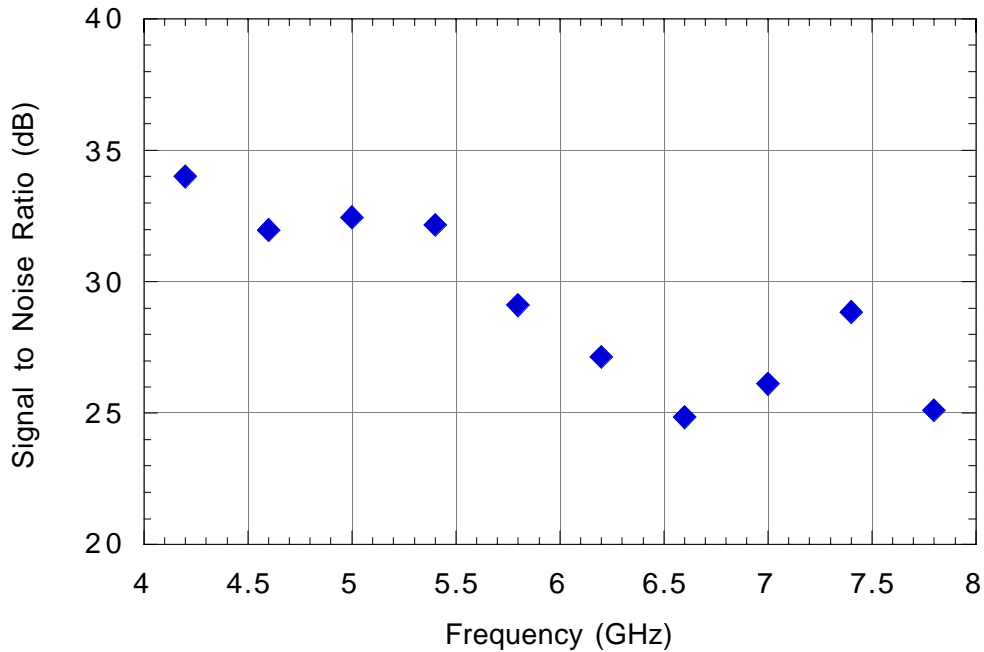


Figure 3.40. Signal to noise ratio measurement of the 4-8 GHz Vertical Core Cooling system.

We do not have a specific proposal for improving the frequency response of the 4-8 GHz pickups. However, our work with the Debuncher prototypes shows that high sensitivity can be achieved in this frequency range subject to the requirements of cost and space in the lattice. We intend to develop a practical plan when the design work of the stack tail cooling system is more advanced. The goal will be to increase the sensitivity at the low frequency end by 3 dB and to produce a pickup response that is flat to within 5 dB over the 4-8 GHz band.

3.4.4.4 *Transmission of the 4-8 GHz signals*

Aside from the pickup and kicker response, the most serious problem in shaping the gain of the 4-8 GHz cooling system is the transmission of the signal across the ring. The cable used for this purpose has a variation in attenuation across the 4-8 GHz band of about 10 dB. While it is possible to compensate this loss with equalizing filters, the equalization achieved is less than perfect. The measured gain of the electronics is shown in Figure 3.41 and shows a generally rising gain with frequency. However, it is clear from the sloping gain function (see Figure 3.39) that the equalization is far from perfect.

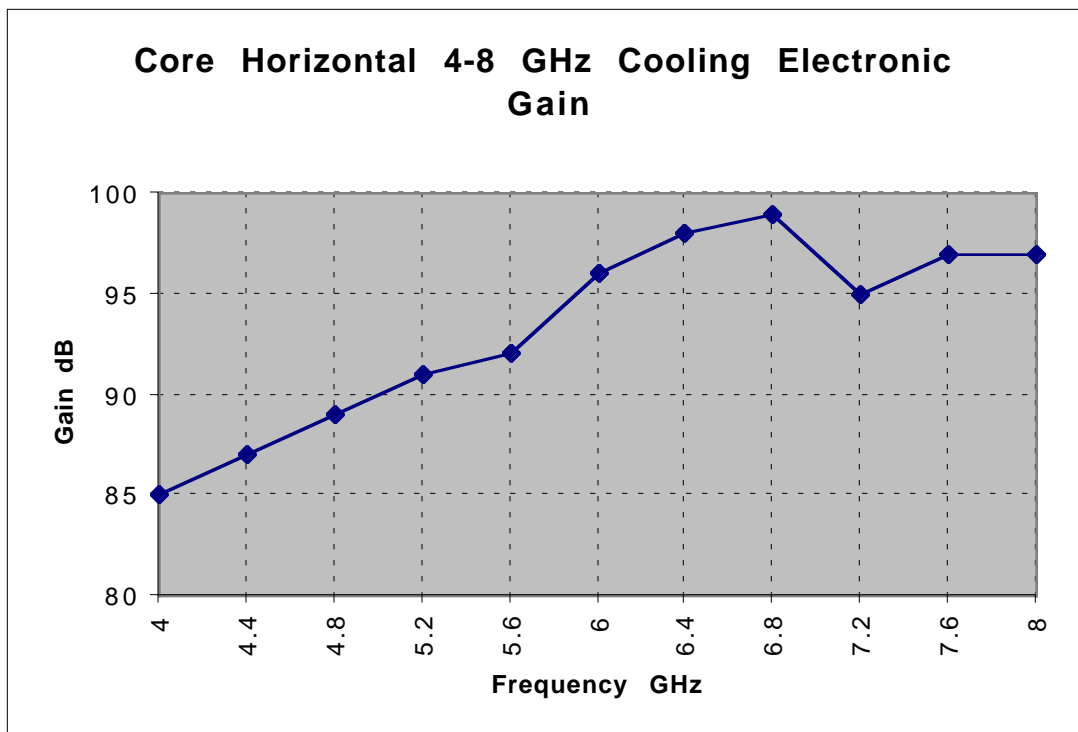


Figure 3.41. Electronic gain of the core vertical system from 4-8 GHz.

A R&D program was started in February 1996 to study the possibility of transmitting microwave signals using free space laser optical techniques. Initial calculations show that signal transmission is indeed possible over distances of hundreds to thousands of feet. This technique will reduce the severity of the equalization problem in the Accumulator and is essential for the Recycler stochastic cooling systems.

Wide band microwave optical transmission has been in use at Fermilab since the late 1980's. Signal bandwidths exceeding 12 GHz have been transmitted over 6 kilometers of single mode fiber with flat gain and phase response, plus minus 2 dB and 15 degrees of phase. The penalty of using fiber optic transmission links is a nominal 35-40 dB insertion loss due to matching networks between the microwave source/termination and the low impedance laser diode and pin photo diode. The insertion loss of the single mode fiber is on the order of 0.2 dB/kilometer and does not effect system performance for the delays associated with systems at Fermilab. Another consideration of optical transmission techniques is the dynamic range requirement. The development of Distributed Feedback Laser diodes, DFB, has increased the dynamic range of laser systems by providing a monochromatic laser source that also suffers less from the dispersion of the fiber optic waveguide. Dynamic range in excess of 40 dB is obtainable over moderate microwave bandwidths.

Unfortunately, the velocity of propagation on single mode fiber is approximately 67% that of light in free space. This slow propagation makes it impossible to send stochastic cooling signals across the ring in time synchrony with the beam. A solution utilizing free space propagation would solve this problem. Externally modulated lasers do not have octave microwave modulation bandwidths. Solid state lasers are the only available source of wideband analog optical transmission. Testing of free space optical transmission using fiber optic based optical transmission links was started in February of 1996. A test at the A0 test facility with the help of the University of Rochester graduate students showed that a series of beam expanding telescopes could be successfully employed to make the fiber to free space transition. The early test utilized components that were not properly coated for the 1310 nanometer wavelength of the optical system. Nonetheless successful transmission was made on a light table with acceptable results for

stochastic cooling systems. Based on this early success, procurement of catalog optical devices with the proper wavelength coating was initiated. The fiber to free space expanders and telescopes were received in the summer of 1996. The bench test of the new optics proved to have 10 times less insertion loss than the original bench test from February.

Mechanical stability proved to be the next obstacle. The core of the single mode fiber is 9 microns in diameter making alignment very sensitive to temperature variations and microphonics. The alignment stability of the system can be measured in minutes, so some type of feed back is required. Fortunately, our system is not the first to suffer from this problem and catalog hardware is available to remedy the alignment instability.

An additional requirement is that the free space propagation medium have an extremely stable index of refraction, on the order of ten parts per million. This specification is dictated by the 5-20 picosecond delay stability required for 4-8 GHz bandwidth cooling. The only conceivable means of providing such a stable medium is the use of an evacuated pipe with end windows that are transparent at 1310 nanometers. This requires some conventional construction for the placement of optically flat pipes buried at the tunnel ceiling level. (There is insufficient time of flight in the accumulator systems to come to the surface.)

A prototype system has been built, installed in the Accumulator 4-8 GHz cooling systems, and tested in the summer of 1997. The optical system was installed as a parallel path so that it could be tested concurrently with normal operations. The gain was measured to be flat within ± 2 dB. The optical system behaved as expected, but requires equalization before becoming operational. We plan to design the equalization when the new pickup and kicker assemblies are installed.

3.5 Unstacking Scenario

The scenario we propose for extracting antiprotons from the Accumulator to the Recycler uses only the 2.5 MHz H=4 rf system. The frequency of transfers will be determined based on experience, but in this section we assume transfers about every two hours. When the Accumulator stack reaches 60×10^{10} antiprotons into the core, the injection of new beam pulses will be interrupted and the core will be immediately adiabatically bunched with the H=4 RF system. The 2.5 MHz voltage will be raised adiabatically to about 250 Volts corresponding to a total bucket Area of 10 eV-sec in order to capture about 40×10^{10} antiprotons. The four bunches will be accelerated across the aperture with a synchronous phase angle of 5° while the voltage keeps increasing to 450 Volts. At the extraction orbit the bucket area will be about 3.7 eV-sec while the longitudinal emittance of each bunch will be around 2.5 eV-sec. The beam in each bunch will occupy about 240 nsec out of 400 nsec leaving about 160 nsec for the extraction kicker rise time.

At this point the antiprotons will be transferred bucket to bucket to the Recycler Ring. The Recycler low level rf RRRF has opened a beam gap and has clogged the Recycler aa marker (RRaa) to the gap.

The Accumulator synchronizes to the Recycler aa marker (RRaa) at the Recycler Revolution frequency F_{rr} and the MILLRF and MIBS will also synchronize to F_{rr} and RRaa. The required Recycler voltage for a synchronous bucket to bucket transfer is 2.3 kV.

Following transfer, the Accumulator will recommence stacking with an initial stack consisting of the remaining 20×10^{10} antiprotons. Assuming a stacking rate of 20×10^{10} antiprotons per hour transfers will occur every 2 hr.

¹ With a 5 sec main ring repetition rate. A stacking rate of 9.7×10^{10} /hour was achieved with a 2.4 sec repetition rate. See M. Church, Pbar Note 560 (unpublished) for more details.

²F. M. Bieniosek, K. Anderson and K. Fullett, Proc. 1995 US Particle Accelerator Conference. F. M. Bieniosek, Fermilab-TM-1857 (1993).

-
- ³C. M. Bhat and N. V. Mokhov, Fermilab-TM-1585 (1989).
- ⁴S. O'Day and F. M. Bieniosek, Proc. 1993 US Particle Accelerator Conference, p.3096.
- ⁵F. M. Bieniosek and K. Anderson, Proc. 1993 US Particle Accelerator Conference, p. 3163.
- ⁶G. Dugan et al., IEEE Trans. Nucl. Sci.30:3660-3662(1983).
- ⁷S. O'Day and K. Anderson, Proc. 1995 US Particle Accelerator Conference,
- ⁸F. M. Bieniosek, pbar Note #550 (1994).
- ⁹Fermilab. *Design Report for Tevatron I Project*. Batavia, Illinois: Fermi Natl. Accel. Lab (1984)
- ¹⁰Mohl D. *CERN Internal Rep. CERN 87-03 V2:453-533* (1987)
- ¹¹Bisognano J, Leeman C. AIP Conf. Proc. #87, Fermilab Summer School on Acc. Physics (1981)
- ¹²D. McGinnis, Pbar Note No. 564 (unpublished). See also the world wide web at http://131.225.123.174/DaveMc/debuncher_upgrade/debunch.htm.
- ¹³D. McGinnis, Pbar Notes No. 564 and 565 (unpublished) and the World-Wide-Web, *loc. cit.*
- ¹⁴ACOL reference
- ¹⁵PU calculation
- ¹⁶Dave McGinnis, pbar note xxx.
- ¹⁷Do we have a reference?
- ¹⁸Bisognano J, Leeman C. *AIP Conf. Proc. #87, Fermilab Summer School on Acc. Physics* (1981)
- ¹⁹Fermilab, *Design Report for Tevatron I Project* (1984).
- ²⁰D. Möhl, G. Petrucci, L. Thorndahl, and S. van der Meer, *Physics Reports C*, **58** (1980) 73-119.
- ²¹Design Report Tevatron I Project, Fermi National Accelerator Laboratory, September 1984.
- ²²A.G. Ruggiero, "Pickup Loop Analysis" Pbar Note 148 (1981), unpublished; A.G. Ruggiero, "More Analysis of Pickups (Strip Lines) Sum and Difference Modes Dependence on Vertical Displacement", Pbar Note 199 (1982), unpublished.
- ²³P.F. Derwent, "Stacktail Prototype Pickups", <http://www-bd.fnal.gov/ap/documents/upgrades/prototype.html> (1997), unpublished.
- ²⁴John Marriner and Vladimir Visnjic, "Fermilab Stochastic Cooling Code User's Guide", Pbar Note 498 (1991), unpublished.
- ²⁵The text of this paragraph and Figure 3.37 were adapted from V. Bharadwaj, et al., TM-1970.

5. MAIN INJECTOR PERFORMANCE GOALS*

5.1 Project Overview

This chapter contains a description of the design and construction schedule of the Fermilab Main Injector (FMI) Project. The technical, cost, and schedule baselines for the FMI Project have been established and may be found in the Fermilab Main Injector Title I Design Report, Revision 0, issued in August 1992. The FMI Technical Design Handbook (TDH) updates and expands upon the design and schedule for construction of all subsystem components and associated civil construction described in the Title I Design Report. The facilities described in the TDH have been designed in conformance with DOE 6430.1A, "United States Department of Energy General Design Criteria."

The purpose of the Fermilab Main Injector Project is to construct a new 150 GeV accelerator, and all required interconnections and interfaces to the existing accelerator complex, on the Fermilab site in support of the Fermilab High Energy Physics (HEP) research program. The construction of this accelerator will result simultaneously in significant enhancements to both the Fermilab collider and fixed target programs. The FMI is located south of the Antiproton Source and tangent to the Tevatron ring at the F0 straight section. The FMI will assume all duties formerly required of the Main Ring. Using the FMI reduces the background rates seen in the colliding beam detectors. The performance of the FMI, as measured in terms of protons per second delivered to the antiproton production target or total protons delivered to the Tevatron, is expected to substantially exceed that of the Main Ring. In addition the FMI will provide high duty factor 120 GeV beam to the experimental areas during collider operation, a capability which did not exist in the Main Ring.

The location, operating energy, and mode of construction of the FMI were chosen to minimize operational impacts on Fermilab's ongoing High Energy Physics program. The area in which the FMI was situated was devoid of any underground utilities which might be disturbed during construction, while the separation between the FMI and Tevatron was sufficient to allow construction concurrent with Tevatron operations. The energy capability of the FMI was chosen to match the antiproton production and Tevatron injection energies presently used in the Fermilab complex. The FMI is being built from newly constructed dipole magnets, thereby allowing a large portion of the installation process to proceed independently of Tevatron operations. The use of newly designed dipoles was also desirable from the standpoint of enhanced performance and reliability, and will result in a reduction of the operating costs by 33% relative to what would be obtained by recycling existing Main Ring magnets.

The Total Project Cost (TPC) of the FMI is estimated to be \$259,300,000, including a Total Estimated Construction Cost (TECC) of \$229,600,000 and \$29,700,000 in associated R&D, pre-operating, capital equipment, conceptual design, and spares costs. Included within the scope of the project are all technical and civil construction components associated with the ring itself, with beam lines needed to tie the ring into the existing accelerator complex, and with modifications to the Tevatron and switchyard required to accommodate the relocated injections. The project involves the construction of 15,000 ft of tunnel enclosures, 11 service buildings, and a new 345 kV substation. Construction on the FMI project was initiated in June, 1992. Construction will be largely completed late in 1998. Design of civil construction has been done by an outside

* Last revised on March 20, 1998.

Architectural Engineering firm, Fluor Daniel, with support from the Beams Division and from Fermilab Engineering Support Section. Design of technical components has been done by Beams and Technical Division personnel.

5.1.1 Role In The Fermilab III Program

The Fermilab Main Injector is the centerpiece of Fermilab's initiative for the 1990s, known as Fermilab III. Some of the more important goals of Fermilab III are to illuminate the properties of the top quark, the most recently discovered fundamental building block of matter, to provide a factor of two increase in the mass scales characterizing possible extensions to the Standard Model, and to support new initiatives in neutral kaon physics and neutrino oscillation investigations. In order to reach these goals Fermilab is planning to attain by the end of the year 2000 a luminosity in excess of $5 \times 10^{31} \text{ cm}^{-2} \text{ sec}^{-1}$ in the Tevatron proton-antiproton collider.

Several projects have been completed over the past four years that have resulted in a factor of 25 improvement over the initial $1.0 \times 10^{30} \text{ cm}^{-2} \text{ sec}^{-1}$ design luminosity of the Tevatron collider. These include upgrades to the Antiproton Source, development of new low- β systems which have allowed the implementation of a second high luminosity interaction region, development of separators to allow multi-bunch operation, an upgrade of the linac energy from 200 MeV to 400 MeV, and the installation of cold compressors to lower the temperature of the Tevatron. As a result of these enhancements, the Tevatron operated during Run Ib with initial luminosities in the range of $1.5\text{--}2.5 \times 10^{31} \text{ cm}^{-2} \text{ sec}^{-1}$.

Further improvements to performance require the construction of the FMI. The present bottleneck in the production of antiprotons and in the delivery of intense beams to the Tevatron is the Main Ring. The Main Ring is not capable of accelerating the quantity of protons which can be provided at injection by the 8 GeV Booster. This is for the simple reason that the aperture of the Main Ring (12π mm-mr) is about half the size of the Booster aperture (20π mm-mr). (These emittances are 95% normalized values.) As a result the Booster is typically run well below its full capability during normal operations. The restricted aperture in the Main Ring is due to perturbations to the ring which have been required for the integration of overpasses and new injection and extraction systems related to operations with antiprotons. With the 400 MeV Linac upgrade the Booster aperture at injection has increased to 30π mm-mr due to increased adiabatic damping within the new linac, and the ability to produce larger antiproton stacks has been increased. However, the mismatches between Booster/Antiproton Source and Main Ring capabilities have become even more acute. Only with the construction of the FMI will these mismatches be removed, and the full benefit to the collider and fixed target programs of the recently completed upgrade projects be realized.

The construction of the FMI will also provide beams of up to 3×10^{13} protons at 120 GeV to the experimental areas during collider runs. Such beams are envisioned as being used for detector development and for supporting fixed target experiments such as rare K decay and neutrino experiments which can benefit from the high average intensity deliverable from the FMI. The Main Ring as presently configured does not support a slow spill, nor is it felt that implementation of a high intensity slow spill in the existing ring would be feasible in light of the small machine aperture and the need to minimize backgrounds in the collider experiments.

Specifically, benefits expected from the construction of the FMI include:

1. An increase in the number of protons targeted for antiproton production from the current 4.8×10^{15} /hour to 1.2×10^{16} /hour.

2. An increase in the total number of protons which can be delivered to the Tevatron for fixed target to 6×10^{13} .
3. The ability to accelerate efficiently antiprotons originating in stacks containing more than 2×10^{12} antiprotons for injection into the Tevatron collider.
4. The ability to produce proton bunches containing as many as 3×10^{11} protons for injection into the Tevatron collider.
5. The reduction of backgrounds and dead time at the CDF and D0 detectors through removal of the Main Ring from the Tevatron enclosure.
6. Provision for slow extracted beams at 120 GeV year-round and potential development of very high intensity, high duty factor ($> 1 \times 10^{13}$ protons/sec at 120 GeV with 34% duty factor) beams for use in high sensitivity K decay and neutrino experiments.

It is expected that with the construction of the FMI and the completion of planned improvements to the Antiproton Source the antiproton production rate will be 2×10^{11} antiprotons/hour, and that a luminosity in the range $8-20 \times 10^{31} \text{cm}^{-2} \text{sec}^{-1}$ will be supportable in the Tevatron collider during Run II.

5.1.2 Performance

The FMI parameter list is given in Table 5.1. It is anticipated that the FMI will perform at a significantly higher level than the existing Main Ring as measured either in terms of protons delivered per cycle, protons delivered per second, and transmission efficiency. For the most part expected improvements in performance are directly related to the optics of the ring. The FMI ring lies in a plane with stronger focusing per unit length than the Main Ring. This means that the maximum β -functions are half as large and the maximum (horizontal) dispersion only a third of the Main Ring, while vertical dispersion is nonexistent. As a result physical beam sizes associated with given transverse and longitudinal emittances are significantly reduced compared to the Main Ring. The elimination of dispersion in the rf regions, raising the level of the injection field, elimination of sagitta, and improved field quality in the dipoles all have a beneficial impact on beam dynamics. The construction of new, mechanically simpler magnets is expected to yield a highly reliable machine.

The FMI is seven times the circumference of the Booster and slightly more than half the circumference of the existing Main Ring and Tevatron. Six Booster cycles will be required to fill the FMI and two FMI cycles to fill the Tevatron. The FMI is designed to have a transverse admittance of 40π mm-mr (both planes, normalized at 8.9 GeV/c). This is a factor of three larger than that of the existing Main Ring. It is expected that the Booster will be capable of delivering a beam intensity in the range $5-7 \times 10^{12}$ protons per batch with $20-30\pi$ mm-mr transverse and ~ 0.2 eV-sec longitudinal emittance in Run II. A single Booster batch needs to be accelerated for antiproton production while six such batches are required to fill the FMI. The FMI should be capable of accepting and accelerating these protons without significant beam loss or degradation of beam quality. Yields out of the FMI for a full ring are expected to lie in the range $3-4 \times 10^{13}$ protons ($6-8 \times 10^{13}$ delivered to the Tevatron for fixed target). By way of contrast, the existing Main Ring is capable of accelerating fewer than 3×10^{13} protons in 12 batches for delivery to the Tevatron.

Table 5.1. Main Injector Parameter List

Circumference	3319.419	m
Injection Momentum	8.9	GeV/c
Peak Momentum	150	GeV/c
Minimum Cycle Time (@120 GeV)	< 1.5	s
Minimum Cycle Time (@150 GeV)	2.4	s
Number of Protons	3×10^{13}	
Number of Bunches	498	
Protons/Bunch	6×10^{10}	
Max. Courant-Snyder Beta Function (β_{\max})	57	m
Maximum Dispersion Function	1.9	m
Phase Advance per Cell	90	degrees
Nominal Horizontal Tune	26.425	
Nominal Vertical Tune	25.415	
Natural Chromaticity (H)	-33.6	
Natural Chromaticity (V)	-33.9	
Transverse Admittance (@ 8.9 GeV)	$> 40\pi$	mm-mr
Longitudinal Admittance	> 0.5	eVs
Transverse Emittance (Normalized)	12π	mm-mr
Longitudinal Emittance	0.2	eVs
Harmonic Number (@53 MHz)	588	
RF Frequency (Injection)	52.8	MHz
RF Frequency (Extraction)	53.1	MHz
RF Voltage	4	MV
Transition Gamma	21.8	
Superperiodicity	2	
Number of Straight Sections	8	
Length of Standard Cell	34.5772	m
Length of Dispersion-Suppressor Cell	25.9330	m
Number of Dipoles	216/128	
Dipole Lengths	6.1/4.1	m
Dipole Field (@150 GeV)	17.2	kG
Dipole Field (@8.9 GeV)	1.0	kG
Number of Quadrupoles	128/32/48	
Quadrupole Lengths	2.13/2.54/2.95	m
Quadrupole Gradient at 150 GeV	200	kG/m
Number of Quadrupole Busses	2	

The power supply and magnet system is designed to allow a significant increase in the number of 120 GeV acceleration cycles that can be run each hour for antiproton production, as well as to allow a 120 GeV slow spill with a 35% duty factor. The cycle time at 120 GeV can be as low as 1.5 seconds. This is believed to represent the maximum rate at which the Antiproton Source could stack antiprotons, and is to be compared to the current Main Ring capability of 2.4 seconds. The FMI dipole magnets are designed with twice the total cross section of copper and half as many turns as existing Main Ring dipoles. This keeps the total power dissipated in the dipoles during

antiproton production at roughly the same level as in present operations while keeping the number of power supplies and service buildings low. The 344 dipole magnets are excited by 12 power supplies located in six service buildings.

With the major exception of the dipoles, existing components from the Main Ring are, for the most part, recycled. Such components specifically include quadrupoles and the radio frequency (rf) systems. The use of all 18 existing rf cavities in a ring roughly half the size of the Main Ring will support an acceleration rate of 240 GeV/sec compared to 120 GeV/sec in the present Main Ring.

5.1.3 Operational Modes

At least four distinct roles for the FMI have been identified along with four corresponding acceleration cycles for the configuration of the FMI in the absence of the Recycler. Operation of the Recycler for storing antiprotons or for cooling protons for the Collider does not require any additional cycles, but it does change some of the details of how the Collider filling operation is done. The one operation that is new with the Recycler is decelerating antiprotons which have been recovered from the Collider. The operating modes are listed in Table 5.2. More detailed descriptions of the acceleration cycles and power supply requirements are given below.

1) *Antiproton Production.* In the antiproton production mode a single Booster batch containing 5×10^{12} protons is injected into the FMI at 8.9 GeV. These protons are accelerated to 120 GeV and extracted in a single turn for delivery to the antiproton production target. As mentioned earlier, it is anticipated that with this flux of protons onto the target and expected improvements in the Antiproton Source the antiproton production rate will exceed 1.7×10^{11} /hour.

2) *Main Injector Fixed Target.* A much higher intensity, high duty factor (34%) beam can be delivered at 120 GeV with a 2.9 second cycle time. The average proton current delivered is about $2 \mu\text{A}$ (3×10^{13} protons/2.9 seconds). Running in this mode does not put any peak power demands on the power supply system beyond those imposed by the antiproton production cycle, but it does expend 67% more average power. This cycle can also be used to provide test beams to the experimental areas during collider running. In this instance it is likely that a much lower cycle rate, accompanied by a much lower average power, would satisfy experimenters' needs. Additionally, a high intensity, low duty factor beam can be delivered at 120 GeV with a 1.9 second cycle time for the production of high flux neutrino beams.

3) *Tevatron Fixed Target.* For Tevatron fixed target injection, the FMI is filled with six Booster batches, each containing 5×10^{12} protons at 8.9 GeV. Since the Booster cycles at 15 Hz, 0.4 seconds are required to fill the FMI. The beam is accelerated to 150 GeV, cogged, and extracted in a single turn for delivery to the Tevatron. The FMI is capable of cycling to 150 GeV every 2.4 seconds for short periods of time. Two FMI cycles are required to fill the Tevatron at 150 GeV at one minute intervals.

4) *Collider Operation.* The FMI operates on a 4 second, 150 GeV cycle for delivery of coalesced proton beams to the Tevatron for collider operations. A 1.45 second flattop is provided for bunch coalescing at flattop. Phase-locking to the Tevatron and synchronization of the transfer requires a few tens of milliseconds. Depending on the multi-bunch coalescing efficiency, 1, 2, 3, or 4 bunches will be accelerated per cycle. A total of 36, 18, 12, or 9 Main Injector cycles would be required, respectively, depending on the number of bunches per cycle.

The antiproton cycles are slower because of the unique rf manipulations described in section 5.5.2 and section 5.5.3. The ramps for acceleration and deceleration will be similar, and four bunches of antiprotons will be accelerated (or decelerated) per cycle.

Combinations of the above operational modes are also possible. One such example is simultaneous operation for antiproton production and high intensity slow spill. One could load the FMI with six Booster batches containing 3×10^{13} protons, accelerate to 120 GeV, extract one batch fast to the antiproton production target, and extract the remainder of the beam slowly over a second. This would produce slightly more than half the antiproton flux into the Source and 83% of the average MI fixed-target intensity of the dedicated scenarios listed in Table 5.2.

Table 5.2 Main Injector Cycle Parameters. “Booster Cycles” is the number of cycles required per Main Injector cycle. “MI Cycles” is the number of Main Injector cycles required to fill the Tevatron (blank if beam does not go to the Tevatron).

Purpose	Cycle Time	Flattop Time	Energy	Extraction Type	Booster Cycles	MI Cycles	MI Bunches	MI Intensity
1) Pbar Production	1.467	.04	8→120	1 Turn	1		84	5×10^{12}
2) MI Fixed Target		.						
• Fast (1 ms spill)	1.867	.04	8→120	Resonant	6		504	3×10^{13}
• Slow (1 s spill)	2.867	1	8→120	Resonant	6		504	3×10^{13}
3) Tev Fixed Target	2.4	0.25	8→150	1 Turn	6*	2	504	3×10^{13}
4) Tev Collider								
• Protons	4	1.4	8→150	1 Turn	1-4	36-9	1-4	2.7×10^{11} – 10.8×10^{11}
• Antiprotons	12	1.0	8→150	1 Turn		9	4	varies
• Pbar Recovery	12	1.0	150→8	1 Turn		9	4	varies

*The rise time of the existing Tevatron proton injection kicker is too slow to inject two groups of 6 batches into the Tevatron. The new short batch kicker will have a fast enough rise time provided that an appropriate pulse forming network is built.

The momentum program and the resulting total dipole bus voltage for each acceleration cycle have been calculated, using conservative extrapolations from Main Ring practice and not requiring the rf or power supplies to run close to design limits. The bus resistance is assumed to be 0.30Ω , and the inductance is 0.67 H. The lower resistance (relative to the value of 0.32Ω used in Title 1) allows increasing the ramp rate to 270 GeV/c/s while limiting the power supply voltage to ~11,500 V. The 2.8667 sec, 120 GeV cycle has been assumed to be run in rapid succession for calculations of rms power when designing the cooling systems and pond sizes, and for determining feeder currents and capacities. (The cycle times are required to be a multiple of the Booster 15-Hz repetition period, 0.0667 sec.)

A useful variant on the 120 GeV fixed target cycles is to fast extract one Booster batch for antiproton production before resonantly extracting to the switchyard. This approach, referred to as "mixed mode", is extremely attractive for fulfilling the demand for protons per hour. The sixth Booster batch is injected into the center of the $3.2 \mu\text{sec}$ gap that exists after the first five batches are injected. The beam is accelerated to 120 GeV, the sixth batch is extracted in a single turn to the antiproton production target, and then the remaining beam is extracted by resonant extraction to

Switchyard. For a loss of 17% in fixed target intensity the two types of operation are efficiently combined. The loss in stacking rate is about 50% when the long spill is needed but only about 20% when the short spill is used. The interleaving of single-purpose cycles is less efficient. For example, when a slow spill cycle is interleaved with an antiproton production cycle, the slow spill flux is reduced by a third, and the antiproton production is reduced by two thirds. The expected numbers of protons per hour that can be delivered in the various modes are given in Table 5.3.

The Tevatron is filled for fixed target physics by two FMI injection cycles. Average feeder power sets a limit on the frequency of the injection cycles; they can not be repeated more than a few times per Tevatron cycle. The operating limits for the magnet power supply and the rf systems are discussed in the TDH.

Table 5.3. Protons Per Hour Under Various Modes of Operation

Mode	Cycle Time (sec)	Protons/Hour		
		AP Target	Fast Spill	Slow Spill
Antiproton Production	1.466	1.2×10^{16}	–	–
Fast Spill	1.866	–	5.8×10^{16}	–
Slow Spill	2.866	–	–	3.8×10^{16}
Mixed - AP + Fast Spill	2.000	0.9×10^{16}	4.5×10^{16}	–
Mixed - AP + Slow Spill	3.000	0.6×10^{16}	–	3.0×10^{16}

This table assumes 6×10^{10} protons per bunch and additional time required for bunch manipulations and turning off magnetic switch at F17 in mixed modes.

There are two accelerator physics concerns which could lead to changes in the details of the magnet ramps, especially the initial parabola. The first relates to the Main Ring experience that bunches are seriously disturbed if the synchrotron frequency approaches 720 Hz for even a few milliseconds. Although the FMI has improvements on the Main Ring magnet power supply, there is some possibility that the initial parabola might need to be slowed down to provide adequate bucket area without approaching this critical value for the synchrotron frequency. It is not anticipated that this will be a dominant concern because it will be possible to pass through the 720 Hz region quite fast from a higher value. On the other hand, it may be highly advantageous to speed up the initial parabola as much as the rf and power supplies will allow to pass the transition energy quickly. There is further discussion of transition crossing later in this section, and in the TDH.

5.2 Lattice and Performance Simulations

The Fermilab Main Injector is situated in the southwest corner of the Fermilab site. The details of its location are determined by requirements for transfers of both protons and antiprotons into the Tevatron. The MI-60 straight section is parallel to the Tevatron F0 straight section, separated from it by 11.823 m (38' 9.5") horizontally and 2.3253 m (7' 7.5") vertically. The reference point defining the plane containing the Main Injector design orbit lies at the intersection of a line from the center of the Tevatron ring and passing near F0 normal to the F0 straight section, and a line parallel to the MI-60 straight section and equidistant from the MI-60 and MI-30 straight sections. Gravity at this point defines the normal to the plane. The plane containing the Main Injector orbit dips at an angle of 0.231 milliradians (47.65") toward the southwest corner (project coordinates) of the site.

The nominal elevation of the FMI was specified in earlier design reports to be 2.332 m below the Tevatron beam. To account for the relative tilt of the Tevatron and the FMI, it is now specified that MI-52 and MI-62 are placed at this elevation. The line from MI-52 to MI-62 is offset 28.789277 m from the MI-60 straight section and parallel to it. The tilt of the FMI then places the MI-60 straight section 2.3253 m below the Tevatron beam line.

The FMI contains eight straight sections; their numbering and their functions are as follows:

- MI-10 - 8 GeV proton injection
- MI-22 - (unused)
- MI-30 - (unused)
- MI-32 - (unused)
- MI-40 - proton abort
- MI-52 - 150/120 GeV proton extraction; 8 GeV antiproton injection
- MI-60 - FMI rf section
- MI-62 - 150 GeV antiproton extraction

The straight sections are capable of beam extraction at 150 GeV. Due to the fact the ring lies 11 meters from the Tevatron, two of these (MI-52, MI-62) are required to provide injection into the Tevatron, one each for protons and antiprotons. On the opposite side of the ring two straight sections (MI-22, MI-32) are added for symmetry. MI-10 is necessary for injection of protons from the Booster, and MI-40 is placed symmetrically for the proton abort.

The FMI is designed to accelerate beams of energy 8 GeV to 150 GeV from the Booster, the Recycler, and the antiproton source. The FMI lattice has two different types of cells, the normal 17.2886-meter FODO cells and the 12.9665-meter FODO dispersion-suppressor cells. The lattice has two different length dipoles: 6 m and 4 m. Also there are three different lengths of quadrupoles: 2.13 m for normal cells, 2.95 m for dispersion suppressor cells, and 2.54 m at the boundary between the two types of cells. The dispersion suppressor cells have shorter dipoles (4 m), and match the horizontal dispersion to zero in the straight sections. The FMI lattice has fewer magnets than the Main Ring. This requires higher field dipoles and larger bending angles. The resulting sagitta in a 6 m dipole is 16 mm. The new dipoles are being built with a curvature which eliminates loss of aperture due to sagitta. A 90° phase advance per cell is chosen, resulting in a maximum β in the cell of 58 m and a maximum η in the cell of 1.9 m. The vertical dispersion in FMI is very small. The Main Ring has maximum β and η of 110 m and 6.6 m respectively. In the lattice design, the beta function β and the dispersion η are kept small to have minimal effect on the beam size. The beam size due to transverse emittance is only 70% of what it is in Main Ring and the maximum beam size due to momentum spread is down by a factor of 3. The ring is designed to have twofold rotational symmetry. Figure 5.1 shows the lattice functions for one half the ring. The lattice function is generated by the program TEAPOT.

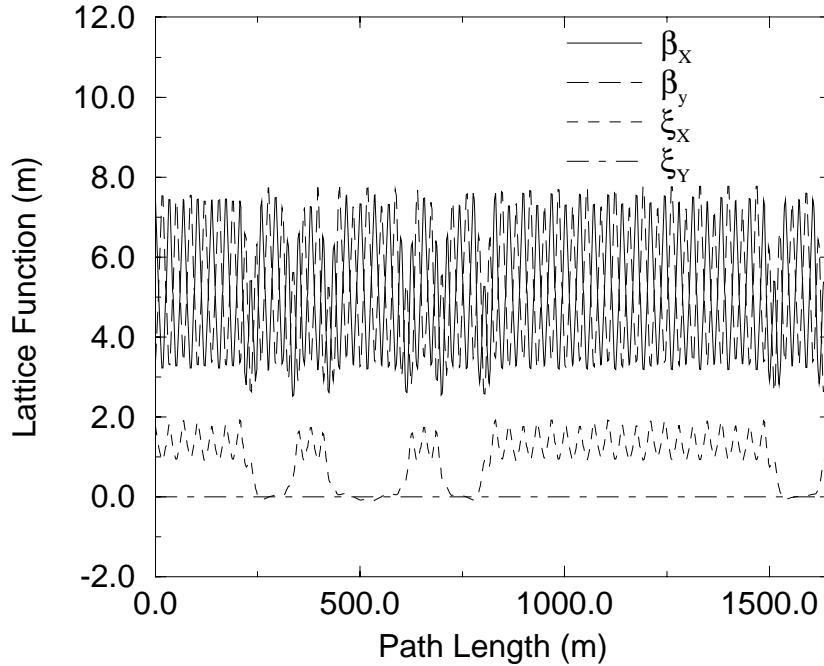


Figure 5.1. Main Injector lattice functions for one-half of the ring. The pattern shown repeats twice over the complete circumference. β_x, β_y label the square root of the horizontal/vertical beta functions and ξ_x, ξ_y ($=0$) the dispersion functions.

5.2.1 Sources of errors

Simulations have been made to investigate the performance of the Main Injector by using the code TEAPOT. Closed orbit errors and their corrections were analyzed. The extent to which field errors perturb beta functions and dispersion functions was explored. The variation of the betatron tunes, Q_x and Q_y , with respect to betatron amplitudes was recorded, and the expected dynamic aperture was predicted. All the results quoted here refer to simulations of the Main Injector at its most critical time, injection, when the beam is stored for approximately 35,000 turns at an energy of 8.9 GeV. All simulations were performed with the alignment errors of Table 5.4 and the magnetic field errors of Table 5.5.

Table 5.4. Random misalignment errors used in the Main Injector tracking simulations.

Magnet type	σ_h (mm)	σ_v (mm)	σ_{roll} (mrad)
Dipole	0.25	0.25	0.5
Quadrupole	0.25	0.25	—
Sextupole	0.25	0.25	—
Beam Position Monitor (Relative to reference orbit)	0.25	0.25	—

Although a complete explanation of all the errors listed in Table 5.4 and Table 5.5 is too lengthy to be included here, some comments are in order. Multipole field errors for dipoles are

quoted in units of 10^{-4} at a displacement of one inch. "Short" dipoles will be constructed to have 2/3 the magnetic length of the "long" dipoles, 6.096 meters, at the slow extraction energy of 120 GeV. Long dipoles nominally bend the beam through an angle of $6\pi/904$ radians. At 8.9 GeV injection, the magnetic lengths of long and short dipoles are 0.3 mm longer than their nominal values, 6.096 and 4.064 meters respectively, at 120 GeV. This is reflected in the non-zero dipole multipole in the dipole ends. The average effect of this magnetic lengthening is compensated by decreasing the dipole excitation, as reflected in the non-zero dipole component of the dipole body. The remaining relative error between long and short dipoles has a significant but easily correctable effect on uncorrected closed orbit errors. Figure 5.2 shows the field profile of the Main Injector dipole field at various energies.

Table 5.5. Magnetic errors used in the 8.9 GeV simulation.

Multipole Order	Normal		Skew	
	$\langle b_n \rangle$	σ_{b_n}	$\langle a_n \rangle$	σ_{a_n}
Dipoles				
dipole	1.10	15.30	–	–
quadrupole	0.06	0.80	–	–
sextupole	-0.40	0.60	0.00	0.20
8	0.04	0.15	0.03	0.40
10	0.33	0.30	0.00	0.15
12	-0.01	0.10	-0.03	0.50
14	-0.03	0.20	0.00	0.25
Recycled Main Ring Quads (New Style)				
quadrupole	–	24.00	–	–
sextupole	0.50	2.73	0.12	1.85
8	5.85	1.02	-1.16	2.38
10	-0.10	1.12	0.42	0.47
12	-1.82	0.63	0.40	0.70
14	0.21	0.64	-0.55	0.44
16	1.41	0.64	–	–
18	-0.03	0.12	0.14	0.16
20	-0.80	0.06	0.02	0.07
Newly Built MI Quadrupole				
quadrupole	–	24.00	–	–
sextupole	-0.51	2.73	1.08	1.85
8	3.41	1.02	-2.05	2.38
10	0.03	1.12	-0.75	0.47
12	-1.49	0.63	0.43	0.70
14	0.21	0.64	–	0.44
16	1.41	0.64	–	–
18	-0.19	0.12	-0.07	0.16
20	-0.77	0.06	-0.12	0.07

Field errors for quadrupoles are quoted as the multipole field divided by the design quadrupole field, again quoted in units of 10^{-4} , at a displacement of one inch. All skew quadrupole field errors are turned off, for the convenience of the simulation, under the reasonable assumption that the linear coupling effects that they cause are readily removed in practice, using a coupling compensation scheme. Random error distributions are truncated at three standard deviations inside the TEAPOT code.

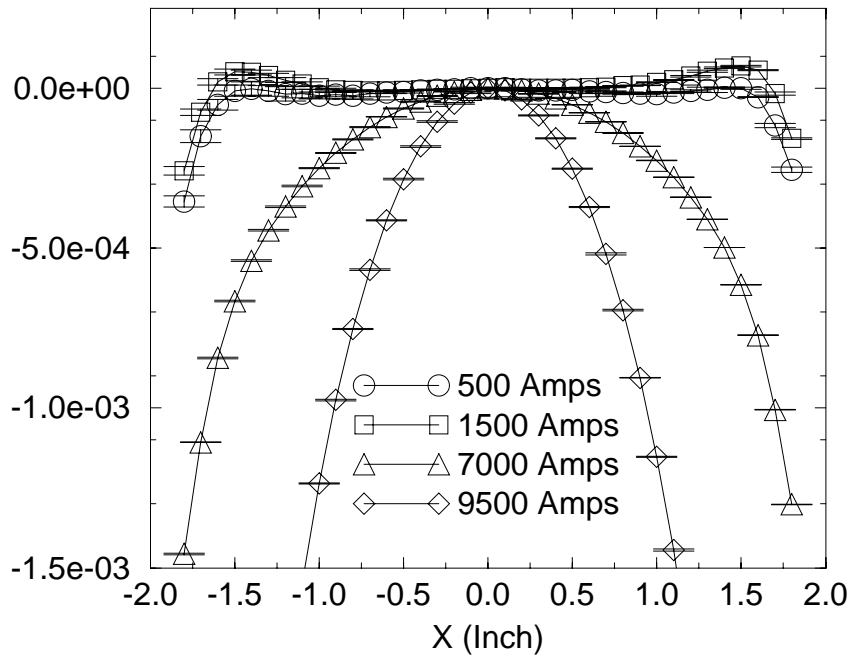


Figure 5.2. Field uniformity, $\Delta B/B$, measured in the Main Injector dipole. The four curves correspond to 8.9, 27, 120 and 150 GeV/c excitations.

5.2.2 Closed orbit and betatron function errors

Figure 5.3 shows two superimposed histograms, representing the distribution of uncorrected horizontal and vertical closed orbit errors that are found when 19 different seeds are used to construct independent sets of random errors. The average values over all the seeds of the root mean square orbit deviation for each particular seed is 5.0 mm in the horizontal, and 3.9 mm in the vertical. In order to correct these orbits for a typical seed, the maximum required corrector strength is less than 100 μr in both the horizontal and vertical planes. A typical uncorrected closed orbit is shown in Figure 5.4, where the two traces represent horizontal and vertical displacements. After three iterations of the orbit correction scheme, the average root mean square closed orbit deviation is reduced to 4.8×10^{-4} mm in the horizontal, and 1.0×10^{-8} mm in the vertical.

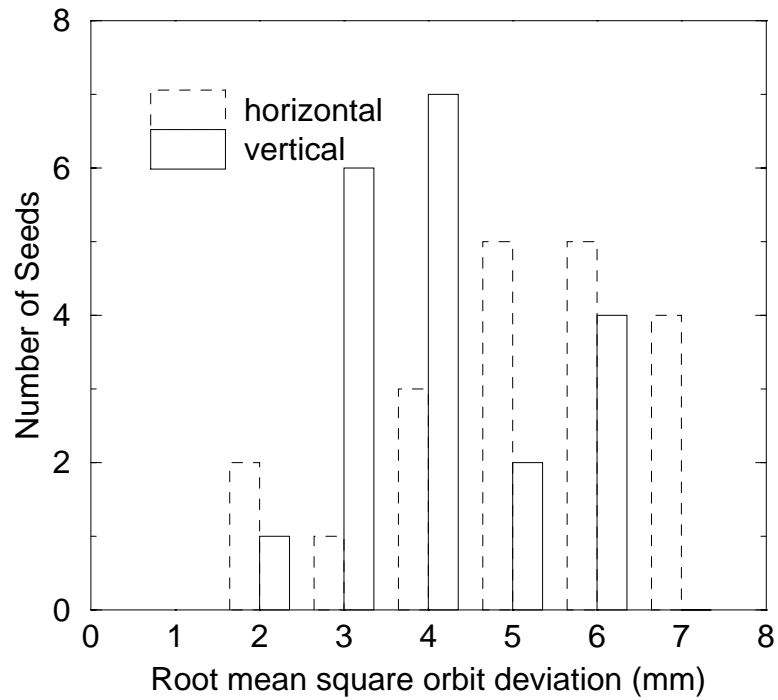


Figure 5.3. Distribution of uncorrected horizontal and vertical closed orbit errors for 19 different seeds.

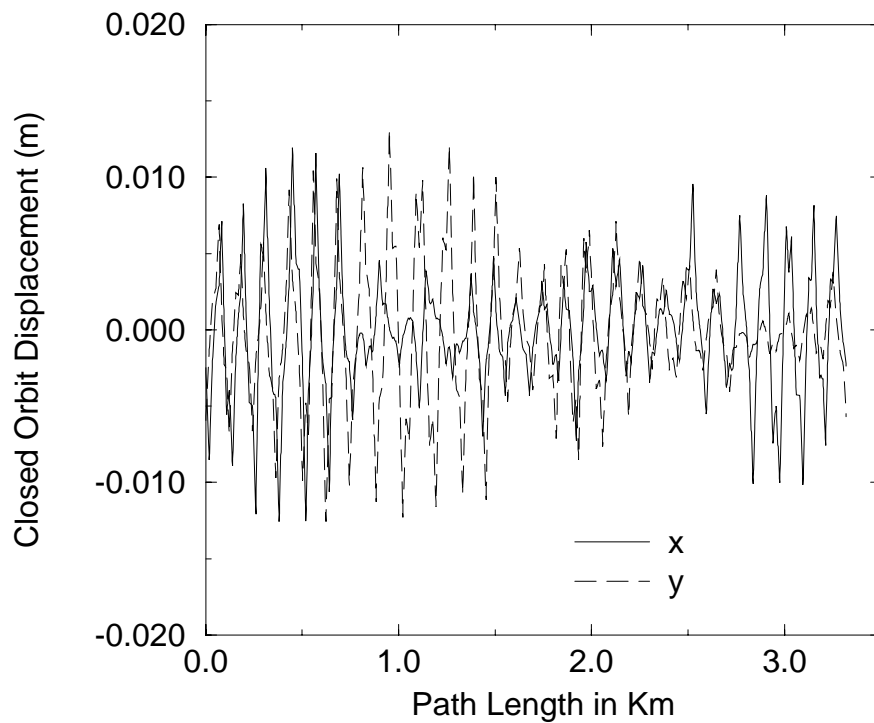


Figure 5.4. Typical uncorrected closed orbits resulting from misalignment and strength variations.

Figure 5.5 shows a plot of the typical variation of the horizontal and vertical beta functions in the Main Injector due to all sources of errors. These include dipole and quadrupole strength and misalignment errors. The main source of betatron function errors is the random quadrupole error of 2.4×10^{-3} measured in the Main Ring quadrupoles that are to be recycled, and that is conservatively assumed to be present in the newly built Main Injector quadrupoles.

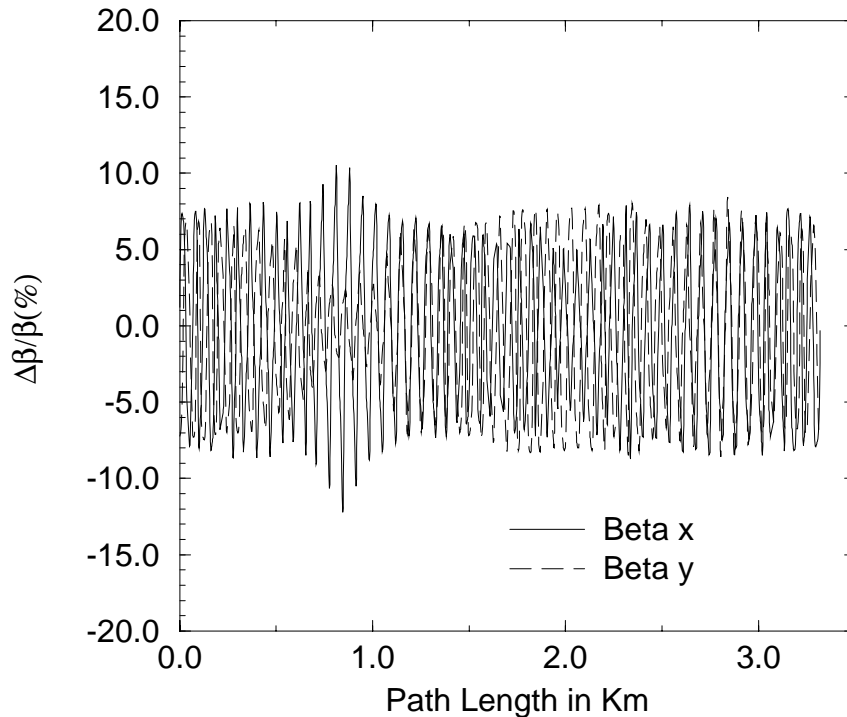


Figure 5.5. Typical beta function variation resulting from expected gradient strength and misalignment errors.

5.2.3 Tune versus amplitude and dynamic aperture results

The long-time behavior of the Main Injector at injection was tested by launching an array of particles at different amplitudes. In what follows, a test particle is labeled with an amplitude of A millimeters when, in the absence of nonlinear phase space distortions, it achieves a maximum horizontal displacement of A at a location where the horizontal beta function is 70 m. This value is chosen as a conservative maximum beta value—see Figure 5.1. The maximum vertical displacement of the same particle is $0.4 A$, also at a beta of 70 m. Synchrotron oscillations were included in the simulation by launching all test particles with an amplitude of $\delta_{\max} = (\Delta p/p)_{\max} = 0.002$, corresponding to twice the root mean square momentum width of the beam. Net chromaticities in both planes were set to $dQ/d\delta = -5$, a conservatively large value with the correct sign to combat the head-tail instability.

Base tunes of $(Q_x, Q_y) = (26.425, 25.415)$ were used in all the simulations, with unoptimized fractional tunes that were derived as follows. Slow extraction requires that the horizontal tune be moved onto the half integer without crossing a major resonance. It is conventional practice to operate near the tune diagonal, but with the tunes separated by, say, 0.01, with the horizontal tune larger to avoid crossing the coupling resonance during slow extraction. Finally, all test particles had a tune modulation amplitude in both planes of 0.01, due to non-zero

net chromaticity and finite amplitude synchrotron oscillations. It is necessary to be at least this far from major resonances. Assuming that the $2/5$ resonance is the resonance closest to the half integer that must be avoided, all of the above conditions are satisfied if

$$Q_y > 25.41, \quad Q_x = Q_y + 1 + 0.01$$

The base tunes were moved an extra 0.005 away from the $2/5$ resonance, without getting unduly close to the half integer.

Figure 5.6 shows the variation of horizontal and vertical tunes in the Main Injector as the amplitude of motion was increased, for a typical seed. The numbers on the tune plane plot correspond to the amplitude of a test particle, in millimeters. Points on the plot lie on a straight line up to an amplitude of about 20 mm, with the spacing between points increasing linearly. That is, both horizontal and vertical tunes depend quadratically on amplitude, for moderate amplitudes. This octupolar detuning is dominated by a combination of the systematic octupole error in the recycled Main Ring quadrupoles, and second order sextupolar effects. Points with an amplitude above 28 mm did not survive for the full 35,000 turns of the simulation, for this particular seed.

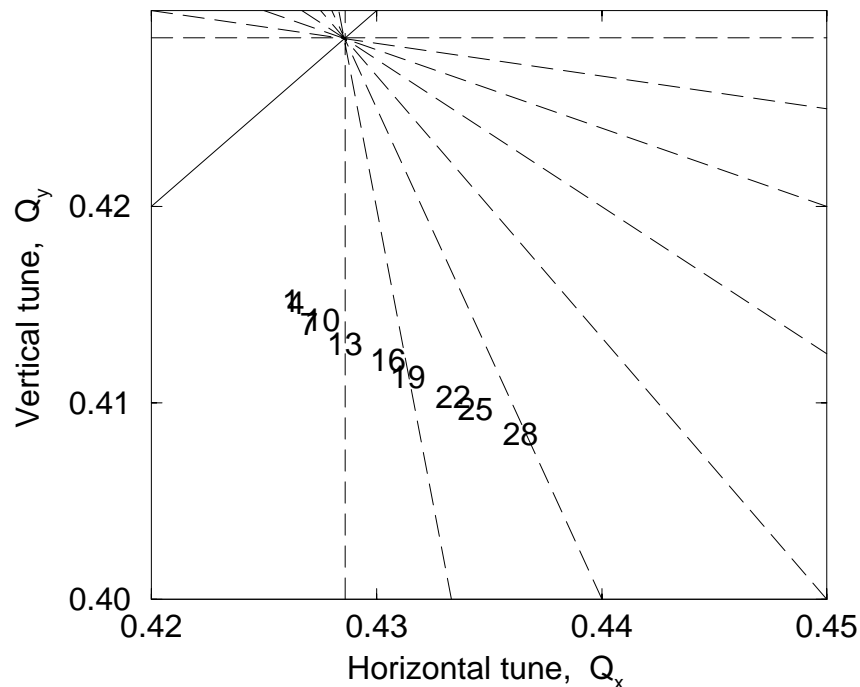


Figure 5.6. Tunes vs. amplitude in the Main Injector at 8.9 GeV/c, based on tracking for a typical seed. The numbers on the plot refer to the launch amplitude of a test particle in millimeters, and the position of the numbers indicates the tune. The lines represent resonances.

Figure 5.7 is a survival plot, displaying how many turns a particle survives in the Main Injector, as a function of its initial amplitude. Different symbols in the plot correspond to the 5 different seeds that were used. Particles that survived to the end of the simulation are plotted on a plateau at the 35,000 turn limit. If the dynamic aperture for a particular seed is defined as the amplitude of the smallest amplitude particle that does not survive for 35,000 turns, then the dynamic aperture for the Main Injector at the injection energy is predicted to be 30.6 ± 0.5 mm, corresponding to a normalized emittance of $127 \pi \pm 4 \pi$ mm-mr.

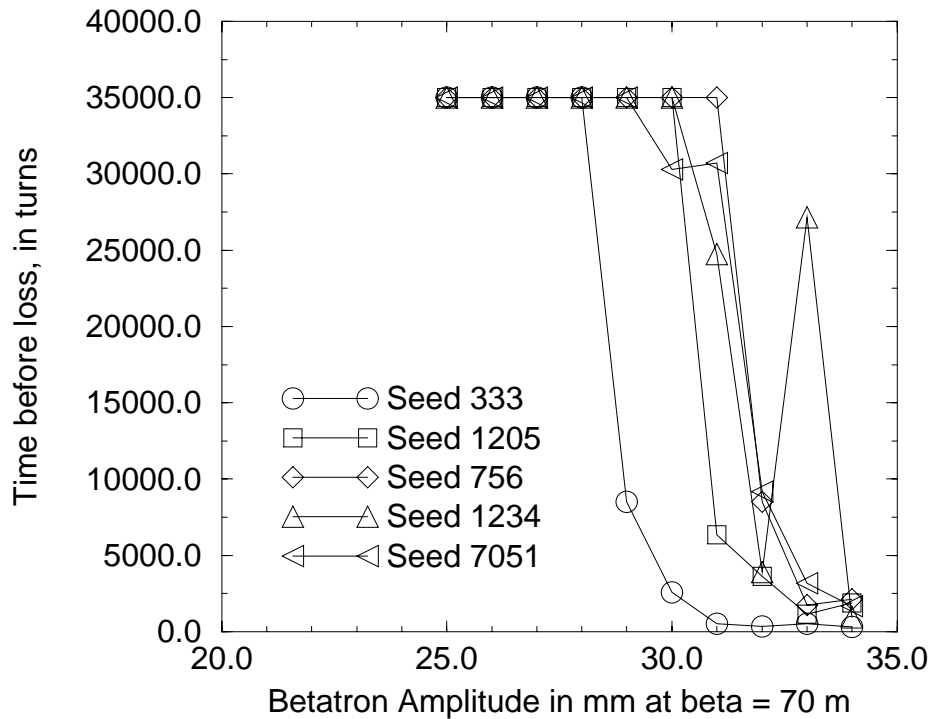


Figure 5.7. Survival plot for the Main Injector at 8.9 GeV/c. The number of turns survived, up to 35,000, is shown as a function of the launch amplitude.

5.3 Aperture

The Main Injector, as discussed above, has a dynamic aperture at injection of over 120π mm-mr, corresponding to ± 30.6 mm amplitude in the horizontal plane. The injection and extraction regions, as discussed in more detail in the TDH, unfortunately require physical restrictions near the center of the aperture. While these devices limit the available physical aperture, it is still substantially greater than 40π mm-mr. To preserve the large physical aperture, good closed orbit control is required, especially at injection. To ease demands on the dipole correction elements, it is intended to induce closed orbit distortions at the extraction-device locations by intentionally misaligning quadrupoles in a controlled manner.

In the vertical plane, the dipole beam tube has an inner dimension of $\sim \pm 24$ mm, corresponding to an admittance of over 80π mm-mr at injection and at a β of 60 m. The injection devices will likely limit the emittance of the injected beam (but not the circulating beam) to somewhat less than this, but still provide an aperture much larger than what is required.

5.4 Transverse Emittance

The Main Injector and associated transfer lines were designed originally to accept 40π mm-mr 8 GeV proton and antiproton beams. Continuing improvements in Booster operation, however, have since reduced transverse proton emittances below 20π mm-mr. In addition, pbar emittance is also anticipated to be less than 20π mm-mr. Emittance dilution will result primarily from position and optical mismatches in transferring the beams between machines.¹

An injection error in position and/or angle produces an oscillation which eventually decoheres and manifests itself as emittance growth in the beam. Simulations of beam transport in

the 8 GeV proton line including random field and alignment errors indicate that this effect will neither be excessive nor completely negligible. For 20 error sets the injection position mismatches were found to be $\Delta x(\text{rms}) = 0.39$ mm and $\Delta y(\text{rms}) = 0.14$ mm—comparable to the assumed random alignment errors.²

At mid Q101 ($\beta_x = 10\text{m}$ & $\beta_y = 60\text{m}$) this translates into $< 0.5 \pi$ growth horizontally and essentially zero growth vertically for a 20π mm-mr beam. A dispersion mismatch corresponds to a position error for off-momentum particles. However, since the transfer lines are matched to the zero dispersion of the Main Injector straight sections, emittance growth from this source is not expected to be a problem. At Q101, with a momentum spread $\Delta p/p = 10^{-3}$, dispersion would need to be mismatched by at least $\Delta\eta = 1.0$ m for emittance to grow by 0.5π . An optical mismatch in the amplitude β will also lead to emittance dilution, but the penalty is less severe in this case than for position errors. The transfer lines are capable of matching into $\pm 20\%$ variations of the amplitudes from their design values. Even for a beam line-machine β mismatch as large as $\Delta\beta/\beta = 0.25$, however, transverse emittance grows by only 0.5π for a 20π mm-mr beam.

5.5 Longitudinal Considerations and Emittance Projections

5.5.1 Proton Acceleration and Coalescing

Proton acceleration and coalescing will be similar to the process in the Main Ring in previous collider runs. Five to seven bunches containing 6×10^{10} protons in a 0.2 eV-sec emittance will be accelerated to flat top. A flat top the bunches will be coalesced into a single bunch of 27×10^{10} protons in a 1.5 to 2.0 eV-sec emittance.

5.5.2 Antiproton Acceleration

The cooled antiproton bunches will be synchronously transferred from the Recycler to Main Injector in 2.5 MHz buckets, four bunches at a time for a total of nine transfers. The cooled antiprotons bunches will have a longitudinal emittance of 1.5 eV-sec and a typical intensity of 60×10^9 particles per bunch.

Following transfer from the Recycler, the 2.5 MHz voltage will be adiabatically raised from 2 kV (matching voltage for the transfers from the Recycler) to 60 kV. Then the antiproton bunches will be accelerated through transition to a front porch at about 25 GeV. There the bunches will be transferred to the 53 MHz rf system as follows:

- a) The 2.5 MHz voltage will drop from 60-6 kV in 0.2 msec.
- b) The bunches will be rotated at 6 kV of 2.5 MHz for 1/4 of sync. period (about 100 msec).
- c) The 2.5 MHz voltage will be raised again to 60 kV in 0.2 msec.
- d) The bunches will be left to rotate for 1/4 of sync. period (about 30 msec).
- e) The 2.5 voltage will be turned off and the bunches will be captured with 800 kV of 53 MHz.

The whole process of acceleration through transition and transfer to the 53 MHz rf system has been simulated with ESME. A longitudinal emittance blowup of 25% is predicted with no particle loss.

5.5.3 Antiproton Deceleration

The antiproton bunches that have been decelerated from 1 TeV to 150 GeV in the Tevatron will be synchronously transferred to the Main Injector, four bunches at a time for a total of nine transfers. The antiproton bunches in the Tevatron will have a typical intensity of 50×10^9 and a longitudinal emittance less than 4 eV-sec.

The pbar bunches will be decelerated to an energy close but above transition (23-25 GeV), using the 53 MHz rf system. At this point the antiproton bunches will be transferred from the 53 MHz buckets to 2.5 MHz buckets. This transfer is necessary to reduce the momentum spread of the large longitudinal emittance antiproton bunches so that they don't exceed the momentum aperture of the machine during transition crossing.

The transfer from the 53 MHz to the 2.5 MHz buckets will be take place in four steps:

- a) Reduce first the 53 MHz voltage till the beam fills the bucket.
- b) Turn the 53 MHz voltage off and perform a 90 degree rotation with 60 kV of 2.5 MHz and 12 kV of 5.0 MHz.
- c) Go to a capture voltage of around 300 Volts of 2.5 MHz.
- d) Adiabatically raise the 2.5 MHz voltage to 60 kV.

After the transfer to the 2.5 MHz rf, the antiproton bunches will be decelerated through transition with a dp/dt of 4 GeV/sec. The transition crossing of the antiproton bunches with 2.5 MHz has been simulated with ESME. The simulations predict a 25% emittance growth but no particle loss. After transition the rate of deceleration will be reduced to about 1.7 GeV/sec so that the existing 2.5 MHz system can continue to provide the required bucket area.

At 8.9 GeV the Main Injector will transfer cog to the Recycler, and the 2.5 MHz voltage will be adiabatically reduced until the bucket area equals the beam emittance. At this point the antiproton bunches will be synchronously transferred to the Recycler. The deceleration cycle will be about 12 sec long.

5.5.4 Transition Crossing

A set of theoretical calculations has been performed to examine the transition crossing in the Main Injector with a proton bunch of longitudinal emittance of 0.5 eV-sec and intensity of 2.7×10^{11} particles—parameters applicable to preparation of collider protons with electron cooling in the Recycler ring. Electron cooling will not be available for the early part of Run II, but it is interesting to consider the demands of the potentially small emittance beams that could be produced by electron cooling. In the initial stages of Run II, the Tevatron collider proton bunches will be formed by coalescing 5 to 7 bunches each with 6×10^{10} protons in a 0.2 eV-sec emittance. Four different transition crossing effects were examined: Negative mass instability, space charge effects, microwave instability and non-linear effects.

5.5.4.1 Negative Mass Instability

The critical coefficient c defined by W. Hardt (W. Hardt, "Gamma-transition scheme of the CPS", Proc. 9th Int. Conf. on High Energy Accelerators, Stanford 1974; also: " Transition Crossing in the Fermilab Main Ring, Past and Present" I. Kourbanis, K.Y. Ng, Proc. of the 1993 Particle Accelerator Conference, Washington , D.C., May 17-20, 1993) to give the negative mass stability limit (unstable if $c \geq 1$) was calculated for the intensity above with different longitudinal emittances. The critical coefficient c is plotted as a function of longitudinal emittance in Figure 5.8. For emittances greater than 0.35 eV-sec it can be seen that $c < 1$ ($c \sim 0.3$ for 0.5 eV-sec) so the beam is expected to be stable.

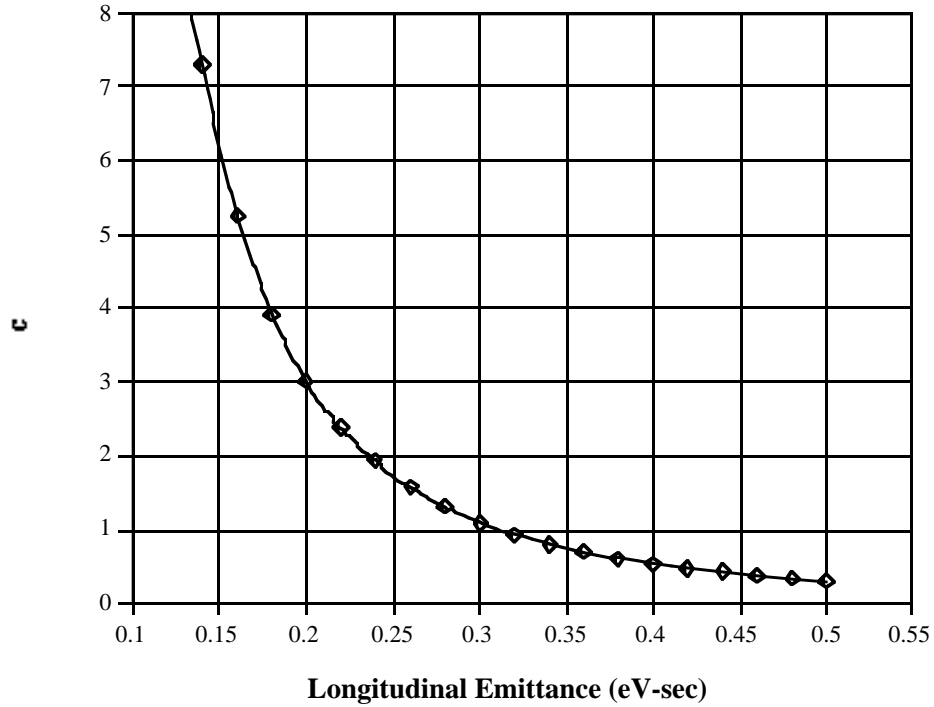


Figure 5.8. Critical coefficient c versus longitudinal emittance for 2.7×10^{11} ppb.

5.5.4.2 Space Charge Effects

The equations of motion near transition (with non-linearities neglected) have been solved numerically by Sorensen and others. To evaluate the importance of the longitudinal space charge effects on the transition crossing, the space charge parameter η_0 (ratio of the space charge-force to the rf force) is calculated. The space-charge mismatch at transition is defined as the ratio of the bunch length at transition with space charge to the bunch length without space charge (and the corresponding ratio of the $\delta p/p$ at transition) as a function of the space charge parameter. The space charge mismatch at transition is not so important provided the space charge parameter is smaller than one. The calculations for the Main Injector have been done with a bunch intensity of 2.7×10^{11} ppb and with different longitudinal emittances. The results of the calculation are shown in Figure 5.9, where the space charge parameter is plotted as a function of the longitudinal emittance. Figure 5.9 shows that for longitudinal emittances greater than 0.2 eV-sec, $\eta_0 < 0.5$, so space charge is not expected to be important during the transition crossing.

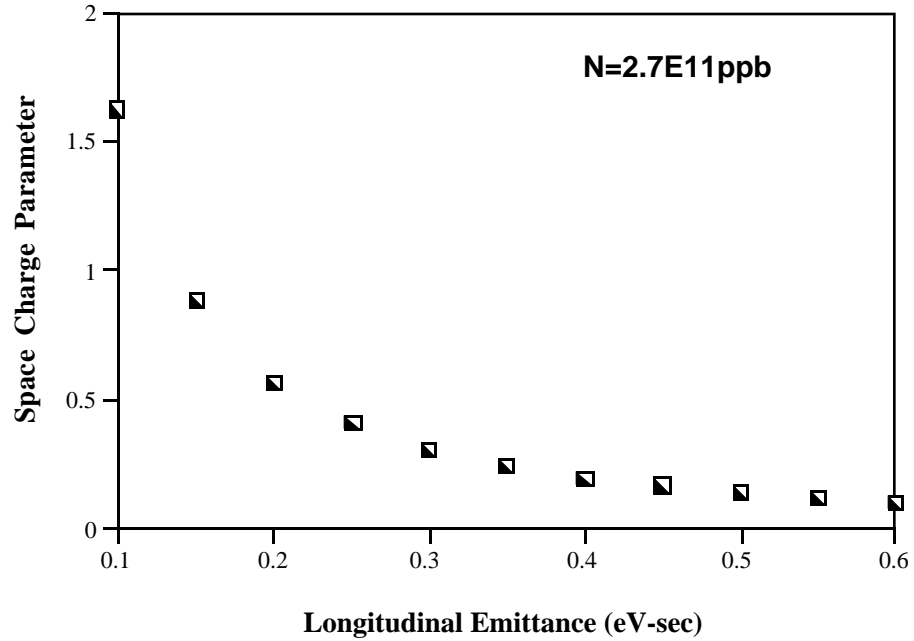


Figure 5.9. Space charge parameter η_0 versus longitudinal emittance.

5.5.4.3 Microwave Instability

The threshold for microwave instability to occur at transition for a parabolic bunch distribution is given by (J. Wei):

$$\frac{Z}{n} \leq \frac{3V|\cos\phi_s|\theta_0}{8hI} \quad [5.1]$$

where V is the rf voltage at transition, ϕ_s the synchronous angle, h the harmonic number, θ_0 the bunch length at transition (in radians) and I is the peak bunch current. Based on the formula above, the threshold Z/n for 2.7×10^{11} protons as a function of the bunch emittance is plotted in Figure 5.10. For emittances greater than 0.3 eV-sec the threshold Z/n for the microwave instability is greater than the estimated Z/n for the Main Injector (less than 3Ω), so no microwave instability is expected at transition.

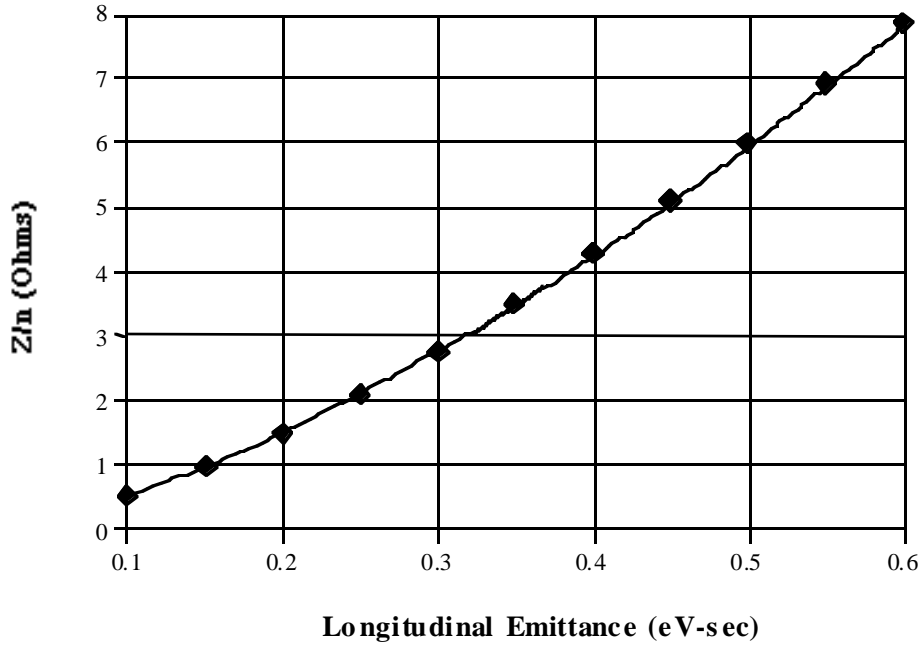


Figure 5.10. Threshold impedance Z/n versus longitudinal emittance for 2.7×10^{11} ppb.

5.5.4.4 Nonlinear Effects

Nonlinear effects are expected to dominate the transition crossing in the Main Injector under the conditions above. First the maximum $\Delta p/p$ at transition for a bunch without space charge is plotted as a function of longitudinal emittance in Figure 5.11. In these calculations a transition crossing rate dy/dt of 255 s^{-1} and a voltage at transition of 3.0 MV were assumed.

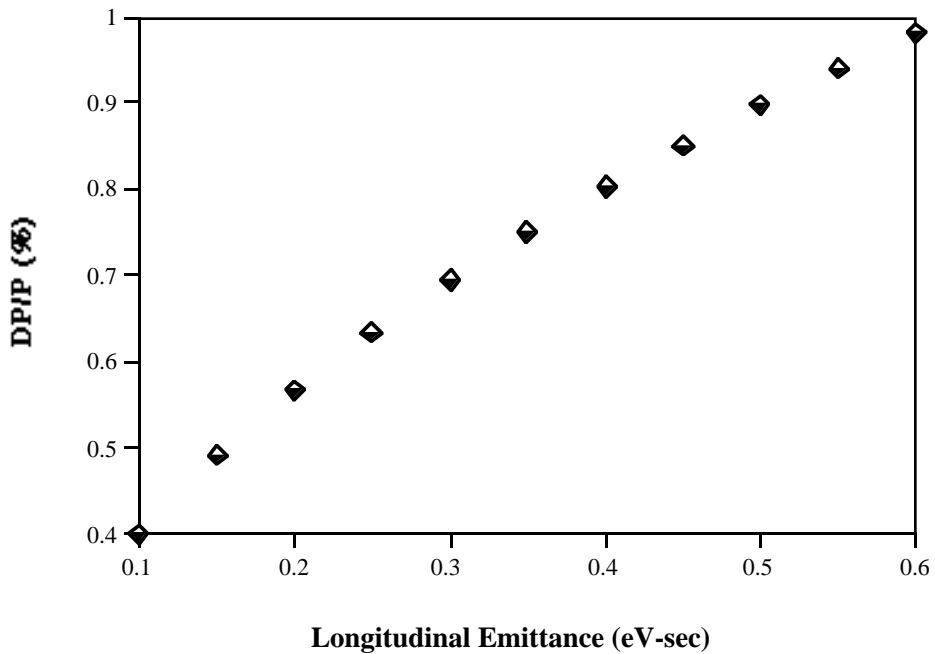


Figure 5.11. Maximum dp/p at transition as a function of longitudinal emittance.

As can be seen from Figure 5.11, for longitudinal emittances above 0.5 eV-sec, the peak excursion in $\Delta p/p$ at transition is approaching the momentum aperture and beam scraping might occur. Secondly the nonlinear time (the time ΔT that it takes the particle with the largest momentum spread $\Delta p/p$ to cross transition before the synchronous particle) was calculated according to the formula:

$$T_{NL} \approx \frac{(\alpha_1 + 3/2) \times \gamma_t}{\dot{\gamma}} \times \frac{dp}{p} \quad [5.2]$$

where α_1 is the Johnson nonlinear coefficient in the momentum compaction factor, taken to be equal to 0.65 in this case, and γ_t is the transition gamma. The results of the calculation are plotted in Figure 5.12.

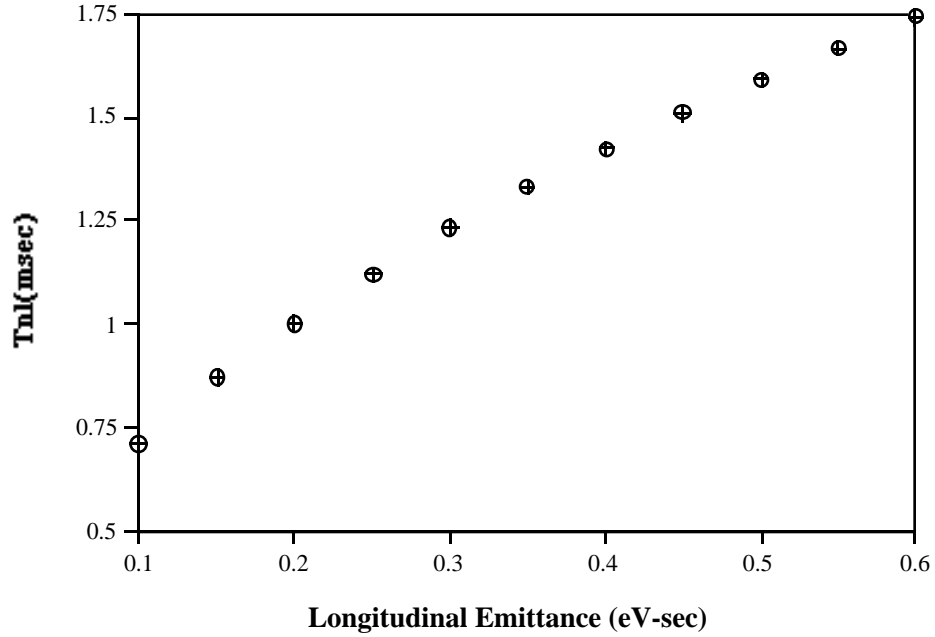


Figure 5.12. Nonlinear time as a function of the longitudinal emittance.

Figure 5.13 shows that for longitudinal emittances greater than 0.2 eV-sec the non-linear time is comparable with the characteristic time T_c (time around transition during which the particle motion is non-adiabatic), which in this case is calculated to be 2.04 msec. That will lead to the development of tails after transition, which will filament and increase the effective bunch area. The effective increase in the bunch area during the transition crossing depends on the ratio of T_{nl} to T_c (J. Wei Ph. D thesis) as follows:

$$\frac{\Delta S}{S} \approx \begin{cases} 0.76 \times \frac{T_{nl}}{T_c} & \text{for } T_{nl} \ll T_c \\ e^{\frac{4}{3} \times \frac{T_{nl}}{T_c}} - 1 & \text{for } T_{nl} \geq T_c \end{cases} \quad [5.3]$$

Beam loss occurs if the effective bunch area $S + \Delta S$ after transition is larger than the bucket area. The results of the formulas above for different longitudinal emittances are shown in Figure 5.13. Since T_{nl}/T_c is ranging from ~ 0.4 to ~ 0.9 , neither of the two regimes applies unambiguously, and

most likely, the emittance growth will fall somewhere in between the two curves. Simulations are needed to better understand the question of emittance growth in this case.

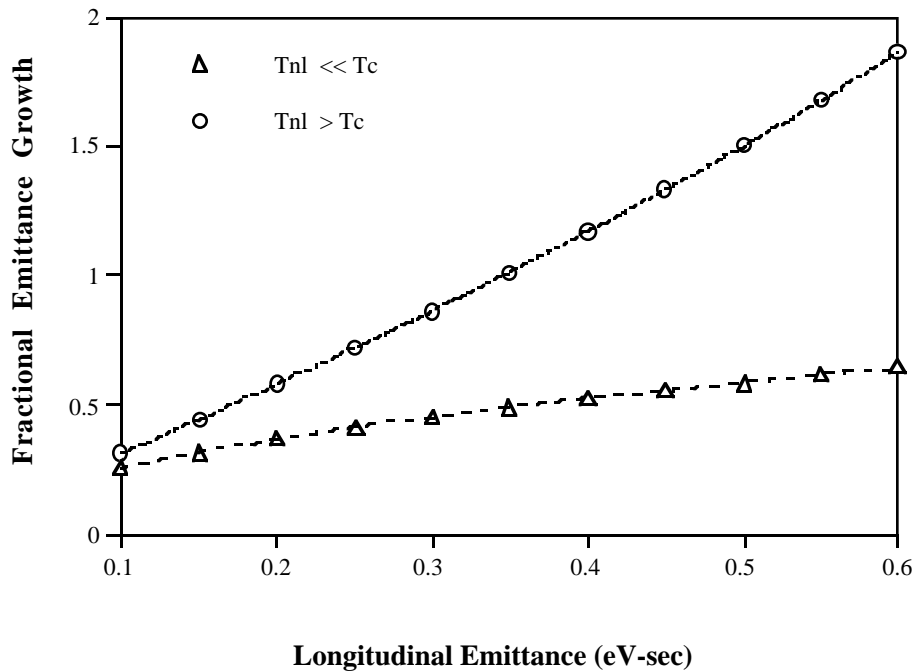


Figure 5.13. Fractional emittance growth due to nonlinear effects at transition.

A γ_t -jump of about 1.5 unit in 1 msec will decrease the nonlinear time by a factor of 6 while the characteristic time will be reduced only by a factor of 1.8, so for a given longitudinal emittance the ratio T_{nl}/T_c will become a factor of three smaller, minimizing the emittance growth and the particle loss. The gamma-t jump is a possible upgrade to the Main Injector project following initial operation for Run II.

5.5.4.5 Conclusions

The following conclusions are reached concerning transition crossing of bunches containing 2.7×10^{11} protons in a bunch of area $S_b = 0.5$ eV-s.

1. Stability against negative mass breakup requires $S_b > 0.32$ eV-s.
2. Space charge focusing mismatch at transition is not serious for $S_b > 0.2$ and is a very weak function of S_b for $S_b > 0.4$ eV-s.
3. The nominal momentum acceptance should support $S_b = 0.6$ eV-s, but potential loss at transition becomes a consideration for $S_b > 0.4$.
4. If $S_b > 0.32$ eV-s and $Z_{||}/n < 3$ Ohm there should be no microwave instability.
5. Emittance growth from the nonlinear bunch tilt becomes a serious consideration for larger

However, the coalescing process proposed for the initial portion of Run II should not suffer from these effects in a serious way.

5.6 Impedance and instabilities

5.6.1 Impedance budget and the microwave instability

The Main Injector is a high intensity proton synchrotron. In order to control beam instabilities, it needs to be a low impedance machine. Components in the vacuum, rf, diagnostic and injection/extraction systems have been carefully analyzed, and computer models have been built. The following guidelines have been adopted in the machine design:

- The bellows are to be shielded.
- The flange gaps are to be shielded.
- The gate valves are to be shielded.
- The pump ports are to be screened.
- The transitions are to be tapered.
- The weldment gaps are to be minimized.
- The dangerous higher order modes (HOM) of rf cavities are to be damped.
- The kicker beam tubes will be coated
- The Lambertson joints are being designed with care.

There are two characteristic frequencies associated with the beam instabilities. One is the cutoff frequency of the TM₀₁ mode of the elliptic beam tube (2"×5"), which is analytically calculable and is about 3.6 GHz. This gives an n (which is the ratio of the cutoff frequency to the revolution frequency) of 4×10^4 . Another is the rms frequency of the bunch spectrum (assumed Gaussian), which is below 300 MHz and is more than an order of magnitude smaller than the cutoff. This implies that the broad-band impedance model is applicable in the analysis.

The preliminary impedance budget is listed in Table 5.6, where Z_{\parallel}/n is the longitudinal impedance and Z_{\perp} the transverse one. The instability thresholds at injection and extraction are also listed. The ratio of the threshold to the budget, which is sometimes called the safety margin, must be greater than unity in order to avoid microwave instabilities.

Table 5.6. Impedance Budget

Component	Number	Impedance	
		Z_{\parallel}/n	Z_{\perp}
RF cavities (HMO)		0.09	0.023
Main cavities (53 MHz)	18		
Coalescing (2.5 MHz)	5		
Coalescing (5 MHz)	1		
2nd harmonic (106 MHz)	1		
Transitions (tapered)		0.012	0.01
RF section	10		
Injection section	2		
Bellows (shielded)	552	0.37	0.67
Flange gaps (shielded)	552	-	-
Weldments	2208	0.001	0.005
Gate valves (shielded)	34	0.04	0.05
Pump ports (screened)	577	0.1	0.07
Beam position monitors	208	0.18	0.3
Kickers		0.3	0.6
proton injection (2.27 m)	3		
pbar injection (2.24 m)	2		
pbar extraction (2.2 m)	2		
Abort (2.2 m)	2		
Lambertson laminations		0.1	0.3
Lambertson joints		0.3	0.1
Lambertson-quad	12		
Lambertson-Lambertson	6		
Lambertson-dipole tube	10		
Resistive wall		0.11	0.092
Total		1.6	2.2
Instability threshold:			
At 8.9 GeV/c		39	7.9
At 120 GeV/c		8.0	16

Specific attention is needed during the bunch coalescing at 150 GeV/c. In the process of adiabatic debunching, the minimum bunch height is constrained by the machine impedance. For a bunch full height of 12 MeV, the corresponding microwave instability threshold is $Z_{\parallel}/n = 1.0 \Omega$, which is already smaller than the budget.

Another critical stage during the cycle is the transition crossing at about 20 GeV/c, when the slip factor η tends to zero. Both analytical study and computer simulations have limited power in predicting the instability threshold. From the experiences at other high intensity proton machines (e.g., AGS at Brookhaven and PS at CERN), particle losses and emittance dilution have strong dependence on the beam intensity. However, based partly on our Main Ring experience, we do not expect the microwave instability at transition to seriously limit Main Injector performance in Run II.

5.6.2 Chromaticity and slow head-tail instability

The chromaticity in the Main Injector comes from four different sources: quadrupoles, sextupoles, eddy current in the beam tube and dipole saturation. The chromaticity model can be described as a summation of four terms:

$$\begin{pmatrix} \xi_H \\ \xi_V \end{pmatrix} = \begin{pmatrix} -33.65 \\ -32.87 \end{pmatrix} + \begin{pmatrix} 828 & 90.1 \\ -182 & -443 \end{pmatrix} \begin{pmatrix} S_F \\ S_D \end{pmatrix} + \begin{pmatrix} 0.0916 \\ -0.0859 \end{pmatrix} \frac{dp}{dt} (GeV/c/s) + \xi_{saturation} \quad [5.4]$$

It is seen that the eddy current term has a ramp rate dependence. In order to have enough room for manipulating the chromaticities in both positive and negative directions, it is necessary to have bipolar power supplies for the focusing sextupoles. (The defocusing sextupoles do not need to be bipolar.)

The head-tail growth time is inversely proportional to $Re Z_{\perp}(\omega\xi)$, the real part of the transverse impedance at the chromaticity frequency, which is equal to $\xi\omega_0/\eta$. Table 5.7 lists the growth time of the $m=\pm 1$ mode at injection for different chromaticities.

Table 5.7. Head-Tail Instability Growth Time

ξ	-33	-20	-10	-5
τ (ms)	26	27	22	17

It will be possible to adjust the chromaticity to be negative at injection and to avoid the instability. In addition, a damper will provide stabilization even if the chromaticity has the “wrong” sign.

5.6.3 Resistive wall instability

The beam tube is made of 316L stainless steel. Its resistivity ρ is $7.4 \times 10^{-7} \Omega\text{-m}$ and its thickness Δ is 1.5 mm. At low frequencies near $\omega_0\Delta v$, where Δv is the fractional tune, the skin depth δ is larger than the wall thickness. Therefore, the wall impedance is determined by the thickness.

Assuming $\Delta v = 0.4$, the wall impedance would then be $Z_{\perp} = (1 + j) 19 \text{ M}\Omega/\text{m}$. It would give a transverse coupled-bunch mode growth time $\tau = 1.2 \text{ ms}$, which is about 100 turns. The actual growth time could be longer due to other factors (chromaticity, octupoles, etc.) as observed in the Main Ring. The Main Injector damper system will suppress this instability.

5.6.4 Coupled bunch instabilities

Based on the preliminary higher-order mode (HOM) tables of the Main Injector rf cavities, the coupled bunch instability growth time is calculated and listed in Table 5.8.

Table 5.8. Coupled Bunch Instability Growth Time

Direction	Bunch Shape Mode	Growth Time (ms)	
		8.9 GeV/c	120 GeV/c
Longitudinal	$m = 1$	8.5	69
	$m = 2$	33	86
Transverse	$m = 0$	1900	L
	$m = 1$	L	L

Note: The entry "L" means Landau-damped.

The damper system should also be capable of damping these modes.

5.6.5 Transient beam loading

There are two transient beam loading effects that are of concern. One is the phase modulation due to the gap in a bunch train. For 18 cavities, each having $R/Q = 80 \Omega$ and $Q =$

4500, the phase modulation of several cases is listed in Table 5.9. While these phase errors are not too serious, the Main Injector will have a beam loading compensation system to reduce these effects.

Another effect is the instability driven by the fundamental mode (i.e., TM01) of rf cavities due to detuning. Feedback will be used to stabilize this potentially unstable mode.

Table 5.9. Phase Modulation from Transient Beam Loading

Case	Vrf (MV)	Io (mA)	Gap (μs)	Phase Modulation
A. 8.9 GeV/c 6 batches	0.38	430	1.7	5.3°
B. 120 GeV/c 6 batches	1	430	1.7	4.9°
C. 8.9 GeV/c 1 batch	0.38	72	9.5	20°
D. 8.9 GeV/c 5 batches	0.38	358	3.3	9.9°

5.7 Damper requirements

5.7.1 Transverse dampers

The damping process can be described as follows. Let us define a vector that represents the amplitude and phase of the collective beam oscillation:

$$\eta = \frac{x}{\sqrt{\beta}} + j \left(\frac{\alpha x}{\sqrt{\beta}} + \sqrt{\beta} x' \right) \quad [5.5]$$

where α and β are the lattice functions. When a feedback system with gain g is applied, the amplitude $|\eta|$ will be decreased. After N turns, we will have

$$|\eta(N)| = |\eta_o| \exp \left(-g \left(\frac{N}{2} + \frac{\sin(2\pi\nu(2N+1)) - \sin 2\phi_o}{4 \sin 2\pi\nu} \right) \right) \quad [5.6]$$

in which $|\eta|$ and ϕ_o are the initial amplitude and phase, respectively, and ν the betatron tune. Thus, the collective amplitude damps as an exponential with a characteristic period of $2/g$ turns, but the exponential also has some minor wiggles. The transverse feedback systems in the Main Injector serve three different purposes that are described below.

5.7.1.1 Correction of injection errors.

If there is a position error x_c at injection, the decoherence due to chromaticity is described by $A = (x_c - \bar{x})/x_c$, where x_c is the centroid of the particle distribution in a bunch. The decoherence factor can be calculated by

$$A(N) = 1 - \exp \left\{ -2 \left[\frac{\xi \cdot \left(\frac{\sigma_p}{p} \right)}{v_s} \sin(\pi v_s N) \right]^2 \right\} \quad [5.7]$$

in which ξ is the chromaticity, σ_p/p the rms relative momentum spread, v_s the synchrotron tune, and N the number of turns after injection. Table 5.10 lists the maximum value of A as a function of ξ , which occurs when $N = 1/2v_s$. It is seen that, for a large chromaticity, the damping time of the injection damper must be shorter than half of the synchrotron period in order to avoid any significant emittance dilution due to decoherence.

Table 5.10. The Decoherence Factor

ξ	33	20	10	5
A_{\max}	1	0.99	0.72	0.27

5.7.1.2 2. Damping of the resistive wall instability:

Because this is a fast beam blowup, a feedback system with a large gain is needed. The maximum bandwidth is determined by the batch separation.

5.7.1.3 3. Damping of the coupled-bunch instability:

In order to be able to damp the coherent oscillation of each individual bunch, this feedback system needs a wide bandwidth. It is planned to build two feedback systems in each transverse plane. System A has high power and medium bandwidth for correcting injection errors, while System B has low power and wide bandwidth for damping the resistive wall and coupled-bunch instabilities. The specifications are listed in Table 5.11.

Table 5.11. Specifications of Transverse Feedback Systems

Feedback system	A	B
Purpose(s)	Injection errors	Resistive wall instability Coupled bunch instability
Features	High power Medium gain Medium bandwidth	Low power Large gain Wide bandwidth
Gain	0.04	0.1
Damping time (turns)	50	20
Correction (mm)	± 3	± 0.3
Kick angle (μrad)	6	1.5
Kicker length (m)	1.4	1.4
Kicker voltage (V/mm)	160	400
Total voltage (V)	± 480	± 120
Kicker power (kW)	5	0.3
Bandwidth (MHz)	4	53

The simplest implementation of a feedback system consists of a pickup and a kicker, which are $(n+1/2)\pi$ apart in phase advance. But this simple scheme is sensitive to tune variations, closed orbit errors, and the initial phase of the bunch at the pickup/kicker.

An improved version is as follows:

1. Two pickups taken together determine both x and x' , thereby eliminating the sensitivity to initial phase and tune variations.
2. Two-turn (or multiple-turn) measurement will reject the closed orbit signal.
3. Two kickers, which can get rid of the initial phase dependence, will (in principle) provide almost exact orbit correction within one turn.

A new transverse feedback system, which has both high power (6 kW) and wide bandwidth (53 MHz), has been built for the Main Ring and will be used in the Main Injector.

Another important consideration for dampers is the noise level of the system. This may not be a problem for the Main Injector because of its short cycle time, but it is critical for any proton storage ring. The consequence of noise in the feedback system is the possible emittance dilution. The emittance growth due to the feedback noise can be described by

$$\frac{d\varepsilon}{dt} = \varepsilon_o \left\{ 0.64 f_o \left(\frac{x_N}{\sigma_x} \right)^2 \Delta\nu^2 \right\} \quad [5.8]$$

in which ε_o is the initial emittance, f_o the revolution frequency, x_N the equivalent noise level at the pickup, σ_x the rms beam size, and $\Delta\nu$ the total tune spread. It is interesting to note that the growth rate is independent of the gain and is proportional to the square of the tune spread (which is somewhat contrary to one's intuition). The theoretical limit of the pickup resolution due to thermal and electronic noise, Δx , is also calculable. In designing a feedback system, Δx must be smaller than x_N , which is determined by a specified allowable growth rate $d\varepsilon/dt$.

5.7.2 Longitudinal dampers

Passive mode dampers will be used on the Main Injector cavities (which are being reused from the Main Ring). In addition, phase feedback will be used as necessary to damp dipole oscillations. Quadrupole feedback will be used for the $m=0$ mode.

5.8 RF Systems and Beam Loading Compensation

The 18 existing 53 MHz Main Ring rf cavities will be installed in straight section MI-60 and operated at harmonic number 588. The operating levels below transition are determined by an interplay between cycle time, bucket area, and synchrotron frequency. Since the FMI must accelerate antiprotons as well as protons, a degree of simplicity and system flexibility will be achieved by placing the cavities at spacings that are multiples of one-half the rf wavelength. The 180° spacing of accelerating cavities will simplify the rf signal distribution (fan-out/fan-back) system as well as providing simpler choices for coalescing stations.

A bucket area of at least 0.2 eV sec is required to accept beam out of the Booster. Historically, it has been necessary to keep the synchrotron frequency in the Main Ring below 720 Hz to avoid resonance with power supply ripple at the twelfth harmonic of the line frequency. The rf system has the capability of generating enough voltage at injection to produce a 1.0 eV sec bucket area at injection, where the limit of 150 kV per cavity is set by the tendency of the tuners to spark because they are close to parallel resonance. In this mode the synchrotron frequency lies well above 720 Hz at injection and descends rapidly, crossing 720 Hz when the beam energy is about

15 GeV. At the frequency for transition energy the cavities are capable of producing 240 kV each, so that 4.0 MV are available even with one cavity inoperative. If the rf system has more than a 50% duty factor, it is not possible to maintain the 4 MV level all the way to top energy because of cavity heating. Operational experience will dictate the exact ramp scenario that is used.

One limitation of the existing Main Ring rf system is the power that it can deliver. The present requirements are 70 kW per cavity with the increased beam intensity provided by the Linac upgrade. The FMI will require 112 kW for accelerating the full intensity at 240 GeV/sec, which is excessive for rf amplifier reliability using the present Main Ring rf system. Provision in the original cavity design allowed for a second amplifier to be installed on the cavity. This choice, while possible, places additional amplifier components in the enclosure, thus increasing maintenance. To overcome this limitation, a new 200 kW power amplifier is placed in the tunnel with a 4 kW rf driver and 30 kV series tube modulator in the equipment gallery. R&D development of a 200 kW rf power amplifier and a 4 kW driver has been completed. Tevatron style 500 volt programmable grid and screen supplies are used for dc biasing. Rf drive is provided by a solid-state 4 kW rf driver coupled to the final tube cathode.

More than 200 kW of output power has been achieved with the new amplifiers. Reliability testing is being done in a test station and in an active accelerating station in the Main Ring rf System. Operation in a Main Ring Station since May 15, 1994 without failure, has given us encouragement that the design is sound.

The transient beam loading from 6×10^{10} protons per bunch will require about 1.25 amp delivered to the cavities, supplied by 15 A (12:1 cavity step-up ratio) of rf current generated by the power amplifier. A 200 kW rf power amplifier operated at a dc plate voltage of 20 kV will produce a peak rf current of approximately 21 A. The 40% surplus initial current capability will insure adequate operating lifetime as the power tube ages.

In the present Main Accelerator rf systems, two 30 kV anode power supplies provide dc power to 18 rf stations. Nine stations are powered by each anode supply. With 200 kW amplifiers, only six stations can be powered by a MR anode supply. One additional anode supply will be provided. The two existing MR anode supplies will be rebuilt at the MI-60 location when the Main Ring is decommissioned. Design improvements proven to increase reliability in a similar supply used in the Tevatron rf systems will be implemented. This will make the Main Injector anode supplies similar to the Tevatron supply. Uniformity of the systems will both ease maintenance and provide consistent safety requirements in the two systems.

The FMI will use the 2.5 and 5.0 MHz coalescing cavities from the Main Ring to prepare intense bunches for collider loading; no significant modifications are required. The system consists of five 2.5 MHz ferrite loaded cavities producing 12 kV per cavity and one 5.0 MHz cavity producing 15 kV. These cavities are driven with solid state amplifiers which will be located in the MI-60 Service Building. Because the harmonic number for 2.5 MHz is 28 in the FMI compared to its Main Ring value of 53, the system will provide 1.4 times the bucket height available in the Main Ring. For longitudinal emittance of 0.15 eVs, about 30 kV of 2.5 MHz rf is required, so there is substantial reserve in this system. The FMI will also use a 15 kV, 106 MHz cavity from the Main Ring. It is used to linearize the 53 MHz bunch rotation in the procedure called snap coalescing.

The four operating modes of the Main Injector are listed below.

Table 5.12. Operating Modes of the Main Injector.

Energy	Mode	Beam	Extraction
120 GeV	Antiproton Production	1 batch	1 turn
120 GeV	Slow Spill	6 batch	1 sec
150 GeV	Tevatron Fixed Target	6 batch	1 turn
150 GeV	Collider, 36 on 36	11 bunch	1 turn

For antiproton production and fixed target operation, the compensation is designed for an intensity of 6×10^{10} per bunch with a ramp rate of 240 GeV/sec. The maximum intensity that could be accelerated at this ramp rate without running into instabilities is not much larger, perhaps 7×10^{10} . The most critical beam loading compensation is necessary for snap coalescing twelve batches of protons at 150 GeV.

5.9 Intensity and Transmission Efficiency

The Fermilab Main Injector is designed to have a much larger aperture, greater than 40π mm-mr normalized at 8 GeV, compared to the Main Ring aperture of 12π mm-mr. The Main Ring aperture, both transverse and longitudinal, limits the performance of the Fermilab Tevatron complex. The Main Ring is not capable of efficiently accelerating the full intensity that will be available from the Booster, namely 6×10^{10} protons/bunch. The Main Ring is used in three different modes: 1) proton acceleration from 8 GeV to 120 GeV for antiproton production; 2) proton acceleration from 8 GeV to 150 GeV, coalescing and coggling for Tevatron injection; and 3) antiproton acceleration from 8 GeV to 150 GeV, coalescing and coggling for Tevatron injection. In the first two modes the Main Ring accepts beam from the Booster, and in the third mode from the Antiproton Source. In all of these modes the beam intensity is limited by the admittance of the Main Ring, and furthermore, the Main Ring has no transverse aperture left for any motion in orbit.

In the antiproton production mode the Booster runs with 84 bunches of about 4.5×10^{10} protons each. Main Ring delivers only about 3.5×10^{10} protons/bunch to the antiproton production target, with an efficiency of less than 80%. Figure 5.14 shows the efficiency of proton transfer through the Main Ring for different Main Ring cycles. In the Main Ring about 10% of particles get lost in the first few thousand turns. This loss is mainly caused by the small aperture of the Main Ring at injection. The small aperture is caused by a combination of poor magnetic field quality at low excitation and perturbations to the ring that have been required for the integration of overpasses and new injection and extraction systems. The second considerable loss of particles in the Main Ring, about 10%, is at transition energy. At transition the growing beam size also scrapes on the limited aperture of the Main Ring. Figure 5.14 also shows the transfer efficiencies for the other two cycles of the Main Ring operation, which are used to fill the Tevatron for collider operations. As in the antiproton production cycle, these two cycles have losses of particles from injection to transition energy. The total loss is about 20%. A few percent (<3%) of particles get lost between 20 GeV and 150 GeV. Due to the limited momentum aperture of the Main Ring, the proton loss during coggling and coalescing is about 25%. *The average transmission through the Main Ring during antiproton production cycles is at best 80%, whereas the average transmissions of coalesced proton and antiproton bunches are 50% and 70% respectively.* The antiproton transmission is larger due to the smaller emittance of the antiproton beam from the Accumulator.

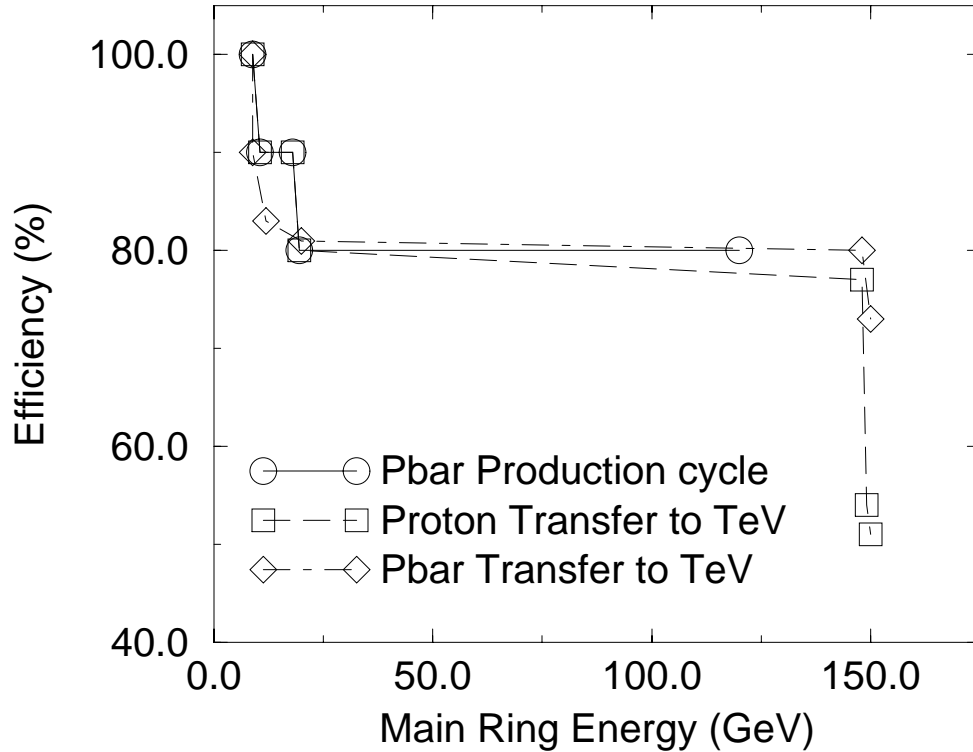


Figure 5.14. Main Ring transmission efficiencies for different particle transfer cycles.

In the Main Injector era, the Booster proton emittance is expected to be about 18π mm-mr for 6×10^{10} protons/bunch. The Main Injector, with an aperture more than three times larger than the Main Ring, will eliminate most of the losses currently caused by the aperture restrictions at injection. Any loss due to small injection oscillations will also be reduced. Figure 5.15 shows the expected particle transmission for different Main Injector cycles. Due to much larger transverse admittance of the Main Injector, the expected loss from injection to transition energy is less than 5%. The Main Injector is designed to have larger momentum aperture; hence loss of particles at cogging and coalescing is expected to be much smaller than in the Main Ring. A conservative estimate of these losses is less than 5%. The average transmission through Main Injector during antiproton production cycles is expected to be 95%. The average transmission efficiencies of coalesced proton and antiproton bunches are expected to be 85% and 90% respectively. The Main Injector is designed to exceed the Run II requirements of 2.7×10^{11} protons/bunch and 5.5×10^{10} antiproton/bunch delivered to the Tevatron.

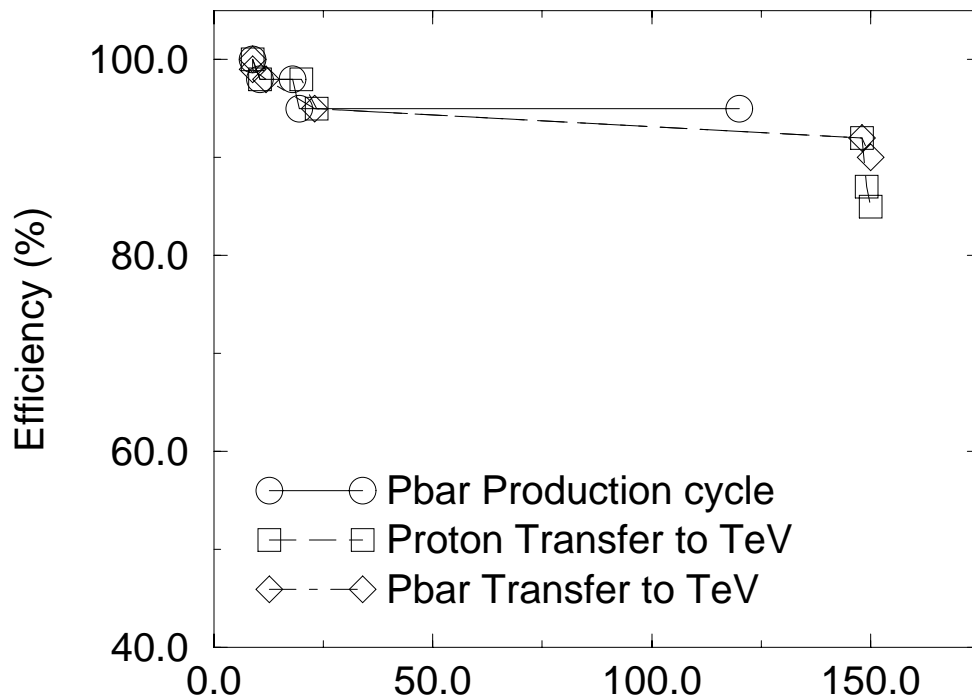


Figure 5.15. Expected Main Injector transmission efficiencies for different particle transfer cycles.

5.10 Resonant Extraction

The Main Injector slow extraction system is designed to be capable of providing year-round, uniform spills of 120 GeV beams, either with a 2.9 s cycle time and 1 s flattop, or with a 1.9 s cycle time and ~1 ms spill for neutrino experiments. The following sections outline the principle of slow spill through excitation of the half-integer resonance, and description of the hardware required. More detail is provided in the TDH on results from numerical simulation of the extraction process, and on spill modulation and duty factor considerations.

5.10.1 Half-Integer Resonant Extraction

The half-integer resonance is a linear resonance that can be induced solely by a quadrupole field. In that case, the beam is either entirely stable or entirely unstable, if tune spread resulting from chromaticity and momentum spread is ignored. With the addition of an octupole field, however, an amplitude-dependent tune spread is introduced into the beam ($\Delta\nu \sim x^2$). Particles with large betatron amplitudes have tunes closer to the half-integer than those of small amplitude. Consequently, the phase space splits into stable and unstable regions, thereby providing a means for manipulating the extraction rate through control of the stable area in phase space. Recycled Main Ring octupoles distributed around the ring on the 0th-harmonic provide the non-linear tune shift, while two orthogonal families of Main Ring trim quads distributed on the 53rd-harmonic provide the half-integer driving term. One quadrupole family alone produces the desired driving

term for extraction, while both families are available for correcting the intrinsic half-integer stop-band of the machine.

Slow extraction from the Main Injector proceeds basically as follows. The horizontal tune is raised towards the half-integer from $\nu_x = 26.425$ to 26.485 using the main quadrupole circuits. The desired orientation of the phase-space at the extraction septa is obtained by energizing the appropriate 53rd-harmonic quadrupole circuit plus the 0th-harmonic octupoles. The strengths of the harmonic elements are chosen such that the stable phase-space area equals the emittance of the circulating beam. The beam is just marginally stable, therefore, at the end of the initial ramp.

Extraction begins by further ramping the harmonic quadrupoles to increase the width of the half-integer stop-band and start the stop-band moving through the beam. Small amplitude particles (lower tune) remain stable, with their motion in phase-space oscillating between the 'fixed' points on successive turns. As the stable phase-space region shrinks, large amplitude particles enter the stop-band and become unstable, with their amplitude then growing exponentially from turn to turn. The unstable particles stream out along the separatrices until they ultimately jump across (or hit) the wires of the electrostatic septa and enter the extraction channel. The kick supplied by the electrostatic septa provides sufficient separation between extracted and circulating beams that magnetic septa are used for the final extraction from the machine.

5.10.2 Extraction Elements

There are five major components of the resonant extraction system:

1. magnetic and electrostatic extraction septa;
2. one family of 0th-harmonic octupoles;
3. two families (cosine and sine) of 53rd-harmonic quadrupoles;
4. low frequency extraction regulation quadrupoles (QXR), and;
5. high frequency spill modulation regulation quadrupoles (Buckers).

The extraction septa are located in straight section MI-52 for extraction to Switchyard and the present experimental areas beyond. This region must accommodate extraction of 120 GeV/c slow-spill protons and single-turn extraction of 120 and 150 GeV/c protons. The Lambertson magnetic septa and C-magnets are common to all beam transfers. There is sufficient phase advance in the straight section that both the extraction kicker magnets and electrostatic septa can be placed at the upstream end of the straight section. Separation between extracted and circulating beams is provided by three electrostatic septum modules located immediately downstream of the kickers, and 70.1° in betatron phase upstream of the entrance to the first Lambertson. Each septum has a wire plane length of 3.048 m. The high voltage gap is 10 mm, with the anode consisting of 0.1 mm tungsten-rhenium wires. The septa are designed to produce 200 μr of kick each at an applied voltage gradient of 79 kV/cm. Additional septa and Lambertsons are required in MI-60 for extracting to NUMI. Due to the presence of the rf cavities in the MI-60 straight section, the electrostatic septa will be located $\sim 3\pi/2$ in phase advance ahead of the first Lambertson magnet.

The 0th-harmonic octupole circuit is required to serve two functions. During resonant extraction it augments the (large) octupole component of the main quadrupoles to produce the appropriate stable and unstable phase-space regions. At injection, however, the octupole field generated by the main quads has a degrading effect on dynamic aperture. The harmonic octupoles in this case are used to cancel this detuning effect. The Main Injector has a single family of 54 octupoles - one at each focusing sextupole location. All octupoles are the same polarity, producing a 0th-harmonic contribution. The two-fold symmetry of the Injector ensures that half-integer driving terms cancel, and quarter-integer harmonics are found to be small.

The number of harmonic quadrupoles is determined by the strength required to raise the fractional horizontal tune from 0.485 to 0.500 at 120 GeV/c. With $\beta_x \sim 50$ m at the quadrupole locations, the total strength required is ~ 15 kG-m/m. For Main Ring trim quads this translates into 8 quadrupoles operating at ~ 7 A. In the Main Injector 16 quadrupoles are utilized. These are distributed around the ring, separated into two orthogonal families (cosine and sine) of eight quads each. Within each family 0th-harmonic contributions cancel because there are equal numbers of F and D quads. The 53rd-harmonic is retained by separating opposite polarity quads by odd multiples of 90° in betatron phase. The orthogonality of the families provides the capability both to cancel the intrinsic half-integer stop-band of the machine and to manipulate the orientation of the phase-space at the septa if necessary for extraction either at MI-52 or at MI-60.

Quadrupole errors in the ring propagate at twice the tune and contribute an additional (unwanted) half-integer driving term. The intrinsic half-integer stop-band is measured by ramping the two orthogonal families independently through positive and negative current values to attain resonance. In the absence of dynamic non-linearities the four resonant current values lie on the circumference of a circle. The circle center defines the stop-band width and phase and, therefore, the harmonic quad currents necessary to cancel it. The stop-band compensation is required to reduce the large variations in the Main Injector lattice functions. The maximum $\Delta\beta/\beta$ is reduced from 76% to 6%, and the rms deviation from 41% to just 3%. To a good approximation the design lattice is obtained.

5.10.3 Spill Regulation Elements

The spill regulation for extraction system can be divided functionally into two bandwidths.

1. A low bandwidth (dc to ~ 10 Hz) system, commonly called QXR, or quadrupole extraction regulation system, consists of two air-core quadrupoles, which may be configured either as a 0th-harmonic or as a 53rd-harmonic. Further analysis is being done to determine which mode is preferred. QXR is used to control the rate at which the beam is extracted. The system is regulated with feed-forward by monitoring the circulating beam intensity during slow extraction. On each machine cycle, the spill rate is sampled at 720 Hz, and compared to the desired spill rate. The error is saved, smoothed and time-shifted, and the current wave form for the next cycle is modified based on an average over many previous cycles.

2. A higher bandwidth (0.1 Hz to 3 kHz) system consists of two air-core, 0th-harmonic quadrupoles powered in series, mounted on ceramic beam pipe. These are commonly referred to as "buckers." By sampling the extracted beam intensity at 5760 Hz and through feed-forward to the buckers, higher-frequency repetitive spill modulation is removed. Real-time feedback is also applied, limited in bandwidth to a few hundred Hz due to the time delay between a change in quadrupole current and the beam response. Simulations have demonstrated that this system can compensate for 100 ppm ripple at 360 Hz in the main quadrupole bus, corresponding to tune modulation of $\Delta\nu \sim \pm 0.003$. Ripple in the main quadrupole bus could also be compensated by feeding back directly into the bucker system.

The 12-year-old Tevatron extraction regulation systems was recently redesigned using modern technology. Much of the Tevatron extraction system, especially in the area of software and controls, will be carried over directly to the Main Injector QXR system.

¹ M.J. Syphers, "Injection Mismatch and Phase Space Dilution", FN-458, 1987.

² *The Fermilab Main Injector Technical Design Handbook*, Section: 2.4, 1994.

6. Tevatron Performance and Projections*

This chapter presents the plan for the initial portion of Run II and plans to increase the number of bunches beyond the 36 planned for the initial phase of Run II. We have also included some speculative ideas that are not now included in the Run II plans. The following paragraphs summarize the important Run II issues and plans for the Tevatron. Details are given in the following sections.

Run II goals

The initial goal for Run II are to provide a luminosity of $5 \times 10^{31} \text{ cm}^{-2} \text{ sec}^{-1}$ with 36 proton \times 36 antiproton bunches at an energy of 2 TeV in center of mass system. The Run II goal for integrated luminosity is 2 fb^{-1} . Achieving this goal in a two year run will require a luminosity higher than the initial Run II goal. At the expected ultimate Run II luminosity of $2 \times 10^{32} \text{ cm}^{-2} \text{ sec}^{-1}$ there will be an average of 5.8 interactions per crossing. Since the performance of the detectors deteriorates rapidly as the number of interactions per crossing is increased, it is important to limit the luminosity per bunch crossing.

Luminosity leveling

One method for limiting the number of interactions per crossing is known as luminosity leveling. In the luminosity leveling the value of β^* is adjusted continuously during the course of the store to keep the luminosity at a constant value until the β^* reaches its minimum value, namely 35 cm. Implementing luminosity leveling is straight-forward in principle, but it may be difficult to achieve in practice since the Tevatron colliding beam lifetime and halo losses in the detectors are very sensitive to changes in tune and coupling.

132 nsec bunch spacing

Ultimately we plan to reduce the number of interactions per crossing while at high luminosity by distributing the antiprotons into more bunches. In the absence of other considerations, the luminosity would be proportional to the total number of antiprotons, *i.e.*, the number of bunches times the number of antiprotons per bunch. The number of interactions per crossing, however, depends only on the number of antiprotons per bunch. Since the experiments have been designed to accommodate a bunch spacing of 132 nsec, we ultimately plan to use this bunch spacing. Unfortunately, this mode of operation is complicated by the need to introduce a crossing angle at the interaction point, resulting in a loss of peak luminosity and introducing dynamical complications, such as the possibility of synchro-betatron resonances

Lattice modifications

For Run II we plan on adopting a lattice which has zero dispersion in the B0 and D0 interaction regions. Compared to the lattice used in Run Ia and Ib, the main advantage of the new lattice is a larger separation of the proton and antiproton orbits just outside of the triplet magnets. This helps reduce the beam-beam tune shifts from these parasitic crossings and reduces the tune spread of the antiproton bunches. The new lattice configuration can be achieved by a straight-forward reconfiguration of the existing hardware.

* Revised February 6, 1999.

For the 1999 fixed target run the tune trim quad magnets in the E and F sectors will be separated from the trim quad circuits. The E sector trim quadrupole magnets will be powered as an independent circuit, similarly for the F sector trim quadrupoles. This will allow us to change the horizontal phase of the beam at the F0 injection Lambertson magnets to reduce the horizontal beam width during resonant extraction. Without this modification the horizontal beam width during resonant extraction is too wide to fit comfortably through the Lambertson magnet aperture.

The polarity of the horizontal component of the helical orbit at injection during Run II will be the reverse of that in Run I. This change accommodates the injection of antiprotons at F0 onto the radially outward helical orbit. The polarity of the helical orbit between D0 and B0 when the beams are colliding will also be changed from Run I to move the antiproton orbit closer to the CDF Roman pots located at A48 and A49.

The possibility of moving the low beta triplet magnets closer to the interaction region at D0 and CDF has been investigated. A solution for the lattice was found which allows the triplet magnets to be moved 26 inches closer to the interaction region. This would provide space for adding roman pot detectors in the warm straight sections where the separators are located. Since there has been no official request for this lattice modification, it has not yet been studied in detail. In addition to verifying that the lattice does not adversely effect the beam-beam tune shifts (which we expect it does not), there is an engineering effort required to move the triplet magnets and mechanically support them adequately.

To create space at F17 for the proton injection kickers and beam halo scraping collimators, the F17 horizontal separator will be moved to the D48 warm straight section. Since the horizontal phase advance between F17 and D48 is nearly 360 degrees, and since the F17 separator provides a relatively weak kick, the helical orbit between F17 and D48 changes only a small amount (<0.5 mm) in this region. Since the F17 separator is not powered during injection this relocation does not affect the injection helical orbit.

It was observed during Run Ib that the present differential coupling feeddown circuit (dSq) was not capable of correcting the coupling of the proton and antiproton tunes independently. For Run II a second family of differential coupling feeddown circuits (dSq2) will be added to the Tevatron. Preliminary work suggests this will be possible by removing several of the trim sextupole magnets near D0 and B0 from the chromaticity circuit and powering them independently.

Injection kickers

For the 1999 Fixed Target run the proton injection kickers presently at E17 will be relocated to F17 as part of the new proton injection line from the Main Injector. Leaving gaps in the beam to accommodate the rise and fall times of the proton injection kicker means we will just barely be able to inject two groups of 5 Booster batches (one group per Main Injector cycle.) If the rise and fall times are problematic it may be necessary to load the Tevatron with fewer than 10 batches or to make some modifications to the kicker pulse forming networks to reduce the rise and fall times.

For the start of Run II a new short batch proton injection kicker is being designed and built which is capable of injecting successive proton bunches with a 396 nsec spacing. The Main Injector will coalesce 1 to 4 batches of protons simultaneously and with 9 to 36 Main Injector cycles the Tevatron will be loaded with 36 proton bunches. The proton injection kicker also serves as the antiproton extraction kicker used to eject the antiprotons in groups of four bunches into the Main Injector after deceleration. The kicker magnets are being designed to support 132 nsec bunch spacing after upgrades to the pulser system. The pulser upgrades required for 132 nsec are substantial and will require research and development before a design is specified.

For the start of Run II the antiproton injection kicker system presently at D48 will be relocated to E48. During testing of the kicker with 36×36 bunches it was found that the kicker fall time was too long. As a result the emittance of some proton bunches increased from the kick received from the ringing of the antiproton injection kicker. With the antiproton injection being moved from E0 to F0 only one antiproton injection magnet will be needed to inject antiprotons. The second magnet will be used as part of a kicker trim magnet (bumper magnet) system capable of delivering a small kick (~3% of main injection kicker strength) with the amplitude adjustable on a bunch by bunch basis. This will be used to correct for the ringing of the antiproton injection kicker and prevent the increase of the emittance of the previously injected beam.

The antiproton injection kickers cannot be installed in the Tevatron during Fixed Target operations since the kicker magnet aperture is too small to fit resonantly extracted beam. Therefore they will have to be installed during the Fixed Target to Collider switchover. The antiproton kicker magnets and pulsers achieve at 396 rise-time and support injecting antiproton bunches with a 396 nsec bunch spacing, but neither the magnet nor the pulser is compatible with a rise-time of 132 nsec.

TeV Program

The goal of the 1 TeV program is to achieve reliable Tevatron operation for colliding beam physics at 1 TeV per beam. Cold compressors and upgrades to the cryogenic controls have made it possible to increase operating beam energy of the Tevatron beyond the 900 GeV achieved in Run I. Ring-wide magnet tests suggest that reliable operation at 975 GeV is now possible. Further increases are expected by “shuffling” magnets. The shuffling procedure involves identifying the magnets with low quench currents and replacing them with high quench current magnets. Over the past several years 1 TeV testing has identified weak magnets and they have been replaced. An additional 7 magnets will be replaced in the Tevatron during the Main Injector shutdown. Part of the shuffling program involves placing weaker magnets into more cryogenically favorable (*i.e.*, colder) locations and grouping weak magnets together in houses than will be operated at colder temperatures than the average. It is likely that we will be able to operate the Tevatron at the specified 1000 GeV energy, but we do not intend to sacrifice reliability for a small increase in energy. Based on experience to date, we expect the actual operating energy will be between 980 and 1000 GeV.

Tevatron Dampers

For the 1999 Fixed Target run the longitudinal mode 1 damper system used during the 1996/97 Fixed Target run will be reinstalled. With this damper instabilities in Fixed Target should not be a problem for intensities as high as 3×10^{13} protons per batch.

With the increase from 6 to 36 bunches (and eventually 140 bunches with 132 nsec bunch spacing) it becomes more likely that coupled bunch instabilities will occur. Therefore a set of transverse and longitudinal beam dampers will be built for Run II. There will be two stripline pickups (one horizontal and one vertical each providing a proton and antiproton signal) located at D48 and two located at E11. There will be four striplines used as damper kickers (one vertical and one horizontal for each proton and antiproton) located in the E0 straight section. The electronics will reside in the E0 service building.

The longitudinal dampers in Run II will be similar to the damper system already used in the Fixed Target run. The damper will act on the beam by modulating the phase of the low-level RF.

Although this method is somewhat limited by the bandwidth of the RF cavities, we expect that there will be adequate feedback gain for any instabilities that occur.

Beam Halo Scraping

For Run II the beam halo scraping system will be redesigned. There will be a set of 5.0 mm thick tungsten targets and 1.5 meter long stainless steel collimators located at the D17 straight section, the F17 straight section, the E0/D49 straight sections, and the F48/F49/A0 straight sections. For each species of particle (proton and antiproton) there will be two tungsten targets, two secondary collimators located about 10 degrees phase advance downstream, and two secondary collimators located about 350 degrees phase advance downstream. To create space for the collimators at F17 (which will also have the proton injection kickers) the separator at F17 will get moved to the D48 straight section.

To reduce the time spent on beam halo scraping (typically it took 15 minutes in Run Ib) the collimator hardware and controls are being upgraded to allow faster operation and more automation. The goal is to automate the scraping procedure instead of having the operations group perform this task manually. However, we do not expect to be able to achieve this goal until we have obtained significant operating experience under Run II conditions.

Proton Removal

Before decelerating antiprotons it is desirable to remove the protons from the Tevatron. This will eliminate the beam-beam tune shift effects and provide more aperture for the antiprotons by allowing the helical orbit to be collapsed to an orbit centered in the beam pipe. The plan is to remove the 1×10^{13} protons in about 100 seconds by scraping them away with a collimator. Proton removal in Run Ib using a collimation system at D17 led to quenches at proton removal rates a factor of 20 slower than the Run II goal. Therefore a dogleg scheme will be used at E0 to shield the Tevatron superconducting magnets from the particle losses and prevent quenching. The dogleg will consist of 4 Main Ring B2-type magnets powered independently from the TeV bus with a 500 kW Transrex power supply. Calculations of the shielding provided by the conventional Main Ring magnets suggest it should be possible with the dogleg scheme to remove 1×10^{13} protons in 100 seconds without quenching the Tevatron magnets.

Deceleration

To increase the number of antiprotons available during stores the Tevatron will decelerate the antiprotons from 1 TeV to 150 GeV after a store and re-inject them into the Main Injector for further deceleration and eventually re-injection into the Recycler Ring. The Tevatron has already decelerated protons from 800 GeV to 150 GeV with nearly 100% efficiency. The major issue with deceleration will be the control of the chromaticity to correct for the changing sextupole component (b_2) in the dipole magnets created by eddy the currents in the dipole magnets and minimizing emittance growth.

Faster Shot Setup Time

In Run Ib a collider fill cycle (shot setup) took an average of 2.5 hours including time spent repairing accelerator components that failed during a shot setup and time spent tuning up the machines during shot setup. By reducing this time to 0.5 hours the integrated luminosity will increase by about 20%. Achieving this goal for Run II will require a lot of work to upgrade controls and require an effort to automate as much of the shot setup process as possible.

The projected shot setup time of 0.5 hours does not include “quiet time” for the CDF and D0 experiments. In Run I the Tevatron magnets were reset every store by ramping the Tevatron to 900 GeV six times. This provided a natural period for experimental quiet time with no beam in the Tevatron. During Run II the plan is to eliminate the six ramps and therefore it is expected that there will be beam present in the Tevatron during nearly the entire shot setup.

Instrumentation

Modifications to the instrumentation and beam diagnostics for Run II are needed to order to accommodate the increase in the number of bunches from 6 to 36 and to provide the faster data processing needed for the faster shot setup time. The upgrades are fairly simple. Much of the work will involve modifications to the applications programs to display data from 36 bunches in a convenient form.

Warm Straight Section Allocation

With Tevatron diagnostic equipment and instrumentation displaced from the F0 straight section to make room for the injection at F0, the insertion of proton removal at E0, a new damper system, and a new beam halo scraping system, careful attention needs to be paid to the allocation of warm straight sections in the Tevatron. We have made an accounting for all the devices needed for the start of Run II and for several future projects. This accounting does not yet include additional separators to provide the crossing angles needed for 132 nsec bunch spacing. Nor has there been any accounting for modifications to the lattice at C0 and the insertion of an experiment in the C0 straight section. However installation of devices in the C0 region was purposely avoided (with the exception of the already existing synchrotron light monitor) to leave room for a future detector at C0.

Tevatron Magnet Spares

A look at the inventory of spare Tevatron magnets suggests there are adequate Tevatron spares for the start of Run II. However, given the warmup and cooldown of the Tevatron during the Main Injector shutdown and the 1 TeV magnet shuffling a number of magnets are likely to fail. A significant effort will be required to fix these magnets and maintain the Tevatron spares inventory. Many of these may fail in a manner that requires relatively little effort to repair (a hole in the vacuum chamber near the end of the magnet for instance). Given that some magnet failures are impractical to repair and that high quench current magnets are needed for 1 TeV operations, it may eventually become necessary to build new Tevatron dipoles.

132 nsec Bunch Spacing

Investigations of 132 nsec bunch spacing has begun but more work is needed before a final plan is completed. As a starting point, the present plan is to implement 132 nsec bunch spacing by using 140 proton bunches and 121 antiproton bunches. Calculations with this bunch structure along with the introduction of crossing angles at B0 and D0 show that the tune footprint created by beam-beam tune shifts should be acceptable for 132 nsec bunch spacing. Other beam dynamics issues such as higher order effects and synchro-betatron resonances have not been considered fully. A complete understanding of these effects will require studies with colliding beams during Run II. Furthermore adding a crossing angle for 132 nsec bunch spacing requires stronger separators or the addition of more separators. Presently a configuration exists for such a scheme, but it may not be consistent with an experiment in the C0 interaction region.

C0 Interaction Region

The goal of the C0 Interaction Region project is to create a third proton-antiproton collision point where modest experiments and detector R&D may be undertaken. A FY98 project will provide an experimental hall to accommodate an experiment with maximum dimensions ± 40 feet along the beam and ± 8 feet transverse to the beams. A modest staging area, counting room facilities, and minimum utilities are also included. Future design and funding will be required to complete the outfitting of this facility for the installation of experiments and for the low-beta focusing elements and electrostatic separators necessary to bring beams into collision at moderate luminosities.

The only part of this project well defined at this point is the civil construction of the collision hall and the assembly hall. This construction will take place during the Main Injector Shutdown in 1997 and 1998. Presently the C0 straight section in the Tevatron is a normal straight section that contains the C0 proton abort. After the civil construction is complete the C0 abort and all of the Tevatron elements at C0 will be reinstalled. Eventually the C0 abort will be removed as experimenters begin to place detectors in the C0 straight sections and the A0 abort will be used to remove beam from the Tevatron during collider operations.

At this point there is only a preliminary design for lattice modifications to provide a low beta interaction region. Providing collisions at C0 would also involve a modification to the helix with the addition of separators. These and other issues need examining before it becomes clear how to incorporate a colliding beams experiment at C0 during Run II or with 132 nsec bunch spacing.

Superconducting RF

An introduction of a crossing angle at the interaction regions for 132 nsec bunch spacing will result in a lower luminosity for non-zero bunch lengths. The reduction in luminosity can be recovered by using higher frequency and higher voltage RF cavities to shorten the bunch length. Using superconducting RF cavities to produce 20 MV at 212 MHz can reduce the bunch length from 38 cm to 14 cm for a 2 eV-sec bunch. Superconducting cavities at this frequency require a substantial R&D effort and substantial fabrication costs. We have not yet started R&D on these cavities, but we would have to start soon to have them available for the latter part of Run II.

6.1 Performance During Run Ib and Run II Goals

6.1.1 Comparison of Parameters for Run I and Run II

In Collider Run II the Tevatron is expected to deliver a luminosity of up to 2.0×10^{32} $\text{cm}^{-2}\text{sec}^{-1}$ to each of the experiments D0 and CDF at a 2 TeV center of mass energy. During Collider Run II the Tevatron will operate much like in Run Ib with the higher luminosity coming from an increase in the number of bunches from 6 to 36 and slightly higher proton and antiproton bunch intensities. In Table 6.1 the expected beam parameters for Run II are compared to the beam parameters for a typical store in Run Ib. The beam parameters for Run Ib are derived from the data in Figure 6.1a-h. The data represent all the collider running from March 8, 1995 through April 21, 1995 except for a few stores where the data set was unavailable or internally inconsistent. All the parameters were obtained from the data which are periodically collected during the store during the interval from one to five hours after the beams achieved collisions at low beta.

Table 6.1. Summary of operating parameters for Run Ib (taken from the data shown in Figure 6.1) and the parameters required for Run II.

Parameter	Run Ib	Run II	
Protons per bunch	232×10^9	270×10^9	
Antiprotons per bunch	60×10^9	70×10^9	
Proton emittance	23π	20π	mm-mrad
Antiproton emittance	13π	15π	mm-mrad
Proton rms bunch length	63	37	cm
Antiproton rms bunch length	59	37	cm
Number of bunches	6	36	
Bunch spacing	~1500	396	nsec
Luminosity	1.6×10^{31}	2.0×10^{32}	$\text{cm}^{-2}\text{sec}^{-1}$
Head on Pbar tune shift	0.015	0.020	
Tevatron Energy	900	1000	GeV
Shot setup time	~2.5	<1	hours

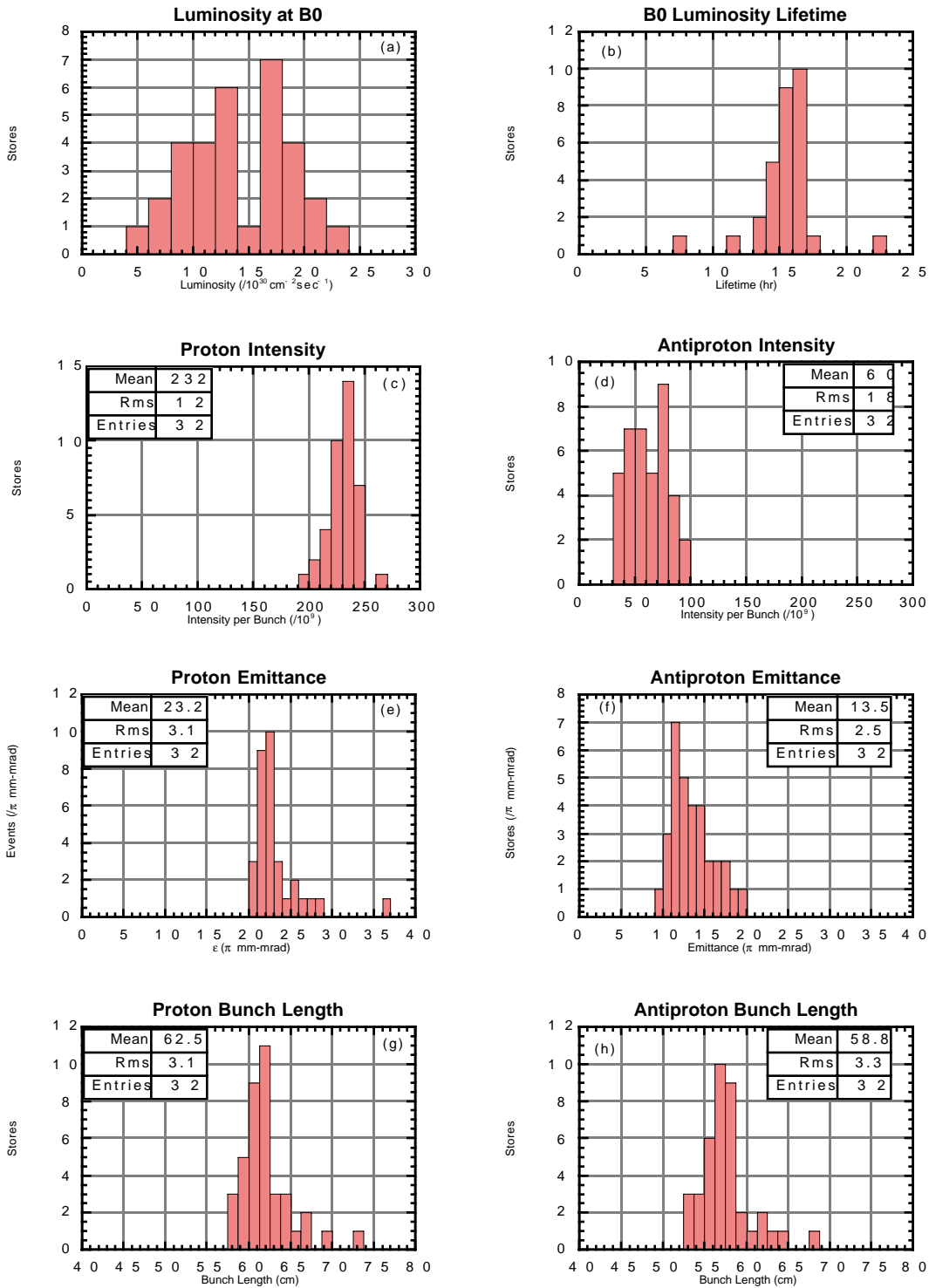


Figure 6.1. Summary of luminosity and beam parameters in recent collider operation.

6.1.2 Transverse emittance

The design proton transverse emittance in Run II is 20π mm-mrad—somewhat smaller than the typical Run IB emittance of 23π mm-mrad. The desired antiproton transverse emittance is 15π mm-mrad—somewhat larger than the typical Run Ib emittance of 13π mm-mrad. In Run Ib the smallest achievable emittances were used for both beams. The antiproton beam had a smaller emittance largely because it was delivered to the Tevatron with a smaller emittance.

There appeared to be about $5\text{-}10\pi$ mm-mrad emittance growth from the time the beam is at Main Ring flattop to collision optics in the Tevatron.¹ It is generally difficult to determine precisely the magnitude and source of the growth because the emittance measurements made in both the Main Ring and Tevatron have random and systematic errors at perhaps the level of 20%. The errors arise from uncertainties in the lattice, mechanical and electrical problems in the instrumentation, and uncertainties in the distribution function.

However, reliable measurements of emittance growth are made during the injection process. In Run Ib there were six injection cycles for protons and six more for antiprotons. After each injection, the emittance was measured. Significant emittance growth is observed in the stored beam, presumably because of non-ideal pulse shapes in the kickers (see reference 1 for more details). We expect this problem to persist and perhaps become more severe with the injection of 36 bunches.

6.1.2.1 Injection errors

Accurately matched injection is crucial to the preservation of emittance. The relation between the emittances of a beam being transferred from accelerator 1 to 2 is given by²

$$\begin{aligned} \varepsilon_2 = & \frac{1}{2} \left[\frac{\beta_1}{\beta_2} + \frac{\beta_2}{\beta_1} + \frac{(\alpha_2\beta_1 - \alpha_1\beta_2)^2}{\beta_1\beta_2} \right] \varepsilon_1 \\ & + 3\pi(p/m) \left[\beta_2 \Delta\theta_0^2 + 2\alpha_2 \Delta\theta_0 \Delta x_0 + \gamma_2 \Delta x_0^2 \right] \\ & + 3\pi(p/m) \left[\beta_2 (\eta'_2 - \eta'_1)^2 + 2\alpha_2 (\eta'_2 - \eta'_1) (\eta_2 - \eta_1) + \gamma_2 (\eta_2 - \eta_1)^2 \right] \left(\frac{\sigma_p^2 + \Delta p_0^2}{p^2} \right) \end{aligned}$$

Equation 6.1

where ε_1 and ε_2 are the normalized, 95% emittances (defined in terms of the rms beam size σ as $\varepsilon = 6\pi(p/m)\sigma^2/\beta$, where p is the particle momentum and m is its mass). The lattice functions of the two circular machines are β , α , η , and η' , where the subscript refers to the appropriate accelerator and η is the dispersion function. The lattice functions are compared at any convenient, common reference point. The injection position and angle errors are Δx_0 and $\Delta\theta_0$, and σ_p and Δp_0 are the beam momentum spread and the momentum injection error.

The errors from the mismatch in focusing (a beta mismatch) are proportional to the square of the error in the beta function for small errors. Thus a 10-20% mismatch in these functions is tolerable. The dispersion match between the Main Ring and the Tevatron is not very good in the vertical plane. The mismatch is calculated to result in a vertical emittance growth of about 0.5π mm-mrad for coalesced beams. In addition, windows in the Main Ring to Tevatron transfer line contribute about 0.5π mm-mrad emittance growth. The current transfer line has virtually no tuning

capability. The new Main Injector line is not only better matched, it will be possible to tune the line as well.

The steering errors, however, are critical. Injection oscillations of about 250 μm amplitude are achieved operationally, which corresponds to about 0.5π mm-mrad emittance growth. The steering becomes considerably more difficult when injecting more than one bunch at a time because the kicker may not give the same kick to each bunch. The antiproton kicker was specified to have a pulse uniformity of better than $\pm 0.5\%$. In order to avoid perturbing the bunches that have already been injected, the kicker must also quickly decay to a value less than about 0.5% of the peak field. These specifications are adequate to limit the emittance growth to 1π mm-mrad, but early beam tests with the kicker indicate that the specifications were not fully met, particularly for the kicker fall-time. As a consequence, we plan to use a kicker trim magnet to effectively improve the kicker pulse shape as described in section 6.6.5.

6.1.2.2 Emittance growth rate at 150 GeV

The emittance has been measured to grow by 1.5π mm-mrad/hour when the Tevatron is set at 150 GeV. This effect probably is responsible for about 0.5π mm-mrad emittance growth in a typical store. It is not known what mechanism causes the emittance growth, but the tune modulation from the large momentum spread and substantial chromaticity ($\xi \cong 10$) could be a major factor.

6.1.2.3 Emittance growth during acceleration and the low-beta squeeze.

During normal operation of the Tevatron, dramatic emittance growth can be observed when the tunes lie near resonances. Changing the tunes of the accelerator normally cures these problems. There may be some residual emittance growth from these effects during normal operation.

6.1.3 Longitudinal Emittance

The longitudinal emittance goal for Run II is 2.0 eV-sec compared to about 3.5 eV-sec in Run Ib. In order to maintain low intensity bunches with small emittance, it is necessary to inject the beam accurately and to avoid emittance dilution by rf noise. Synchrotron oscillations of about 0.5 mm amplitude are observed on the BPM's at the "17" locations (6 m dispersion) immediately after injection during routine operation of the Tevatron. These oscillations correspond to a fractional momentum error (or magnet field error) of about 8×10^{-5} . The resulting emittance dilution is about 0.1 eV-sec.

Injection is also complicated by beam loading considerations. The change in phase angle for the first bunch in a 12-bunch train is 13.5° and the change for the last bunch is 19.1° . An injection error of 8.2° results in an emittance growth of 0.1 eV-sec. It would appear that the emittance growth from beam loading will be negligible provided that we compensate for the average beam loading.

At low beta the bunch length grows by about 1 cm per hour. This corresponds to an emittance growth rate of about 0.1 eV/sec per hour. However, the observed growth rate is smaller than that expected from intrabeam scattering (see section 6.3.1). The intrabeam scattering experiment suggests that the noise contribution to the longitudinal emittance growth rate is closer to 0.01 eV-sec per hour.

6.2 Luminosity Leveling

With a fixed number of bunches, the number of interactions per beam crossing is proportional to the luminosity. For 36 bunches and a luminosity of $2 \times 10^{32} \text{ cm}^{-2} \text{ sec}^{-1}$ the number of interactions per crossing (assuming an effective inelastic cross-section of 45 mb) is 5.8. The performance of the detectors can deteriorate rapidly as the number of interactions per crossing is increased, and it may be desirable to limit the maximum luminosity through a technique known as “luminosity leveling.” Luminosity leveling is accomplished by manipulating the store parameters in the early part of the store to reduce the luminosity to the desired level but changing these parameters during the store to keep the luminosity as nearly constant as possible.

One technique to level the luminosity involves modulating β^* during the store. Figure 6.2 shows a calculation with Run II parameters that results in an initial luminosity of $2.17 \times 10^{32} \text{ cm}^{-2} \text{ sec}^{-1}$ and also shows stores with the same initial parameters except that the β^* has been adjusted to achieve luminosities of $0.5, 1.0,$ and $1.5 \times 10^{32} \text{ cm}^{-2} \text{ sec}^{-1}$. The luminosity of the leveled stores becomes greater than the unlevelled store after some period of time because the antiproton intensity is higher in a leveled store (fewer antiprotons are lost due to interactions). Figure 6.3 shows the integrated luminosity for these stores and Figure 6.4 shows the value of β^* that was required to achieve the luminosities shown in Figure 6.2.

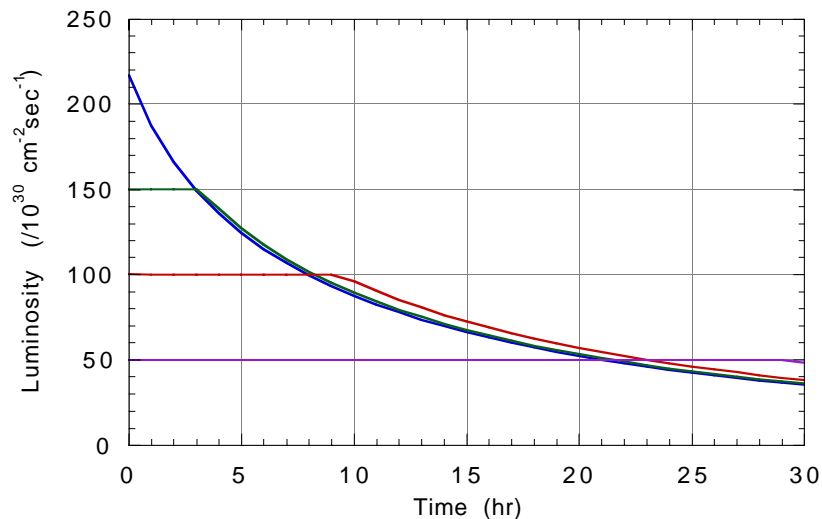


Figure 6.2. Comparison of the luminosity versus time of an unlevelled Run II store and stores that have been leveled to $0.5, 1.0,$ and $1.5 \times 10^{32} \text{ cm}^{-2} \text{ sec}^{-1}$.

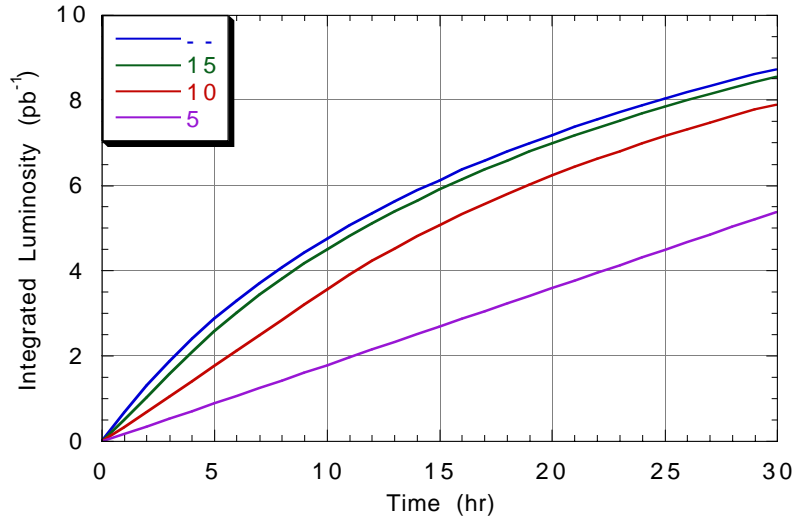


Figure 6.3. Comparison of the integrated luminosity versus time of an unleveled Run II store and stores that have been leveled to 0.5 , 1.0 , and $1.5 \times 10^{32} \text{ cm}^{-2} \text{ sec}^{-1}$.

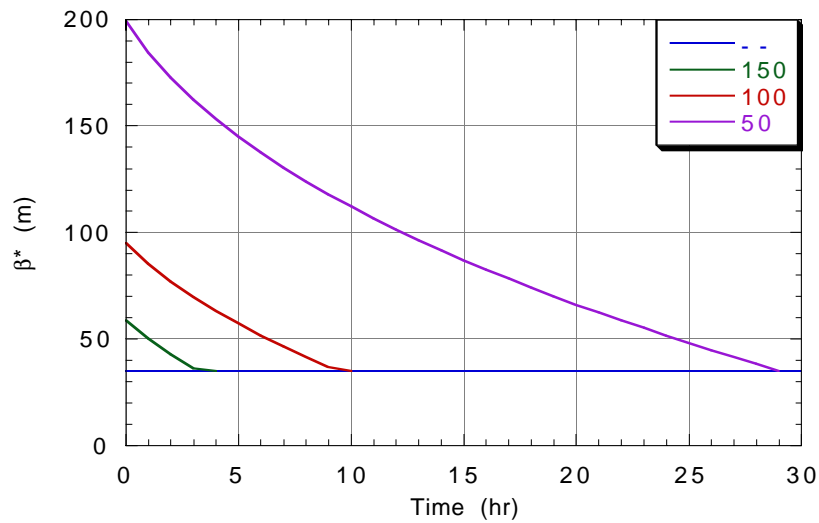


Figure 6.4. Comparison of the β^* versus time of an unleveled Run II store and stores that have been leveled to 0.5 , 1.0 , and $1.5 \times 10^{32} \text{ cm}^{-2} \text{ sec}^{-1}$.

Luminosity leveling is straightforward in principle, but it is not clear that it can be implemented without undesirable side effects. The Tevatron is sensitive to small changes in the operating point (particularly tunes and coupling), and it is not clear that the β^* can be changed over

the course of a store without introducing excessive background rates at the experiments. Two possible approaches are to make changes in a series of discrete steps or to make continuous changes. The method of discrete steps has the advantage that each step can be hand tuned for optimum performance. The continual change has the advantage that any increase in experimental background would be gradual allowing time for an operator (or appropriate software) to take corrective action before the problem became serious. We plan to study luminosity leveling techniques after the Run II luminosity reaches $5 \times 10^{31} \text{ cm}^{-2} \text{ sec}^{-1}$ so that an effective technique will be available when it is needed.

There are other techniques that could be used to modulate the luminosity. They include changing the rf voltage, colliding the beams with an offset or an angle, or changing the coggling. While we are not seriously considering any of these options (and some of them appear to be poor choices), we may choose to use one of these alternative techniques or a combination of these techniques in the future. Since luminosity leveling does not require any significant new hardware, the choices to be made are primarily operational in nature and can therefore be deferred until we have more experience with operation in Run II.

6.3 Integrated Luminosity and Store Lifetime

6.3.1 Experience in Run Ib

A model has been developed to describe the evolution of the luminosity of a store.³ The ingredients in the model include:

1. Particle loss from collisions. A total cross-section of 70 mb is assumed in the calculations described below.
1. Particle loss from the residual gas scattering.
1. Particle loss from other sources. The loss rate is assumed proportional to the number of particles present, but the rate is assumed to be zero in the calculations described below. Probably the most important contribution to particle loss is unstable particles extracted from the collider by resonant effects driven by the beam-beam interaction. There is no known calculational method that accurately predicts loss rates from these effects, but fortunately this effect is relatively small in the proton beam under normal operating conditions.
1. Emittance growth because of intrabeam scattering. It is assumed that the emittance growth rate is the same in the horizontal and vertical phase spaces because of coupling. The assumption is enforced in an ad-hoc way by calculating the growth rates in the absence of coupling and applying the average rate to each plane.
1. Emittance growth because of scattering from the residual gas.
1. Emittance growth from noise or other unknown sources. The calculations below assumed a constant emittance growth of 0.2π mm-mrad in transverse phase space and 0 eV-sec in longitudinal phase space.

Comparison of the model with the store data taken at the end of Run Ib is shown in Figure 6.5 through Figure 6.8. The initial beam intensities and emittances were taken from the measured values and then evolved according to the model. The luminosity measured by B0 is about 90% of the calculated value and the calculation is scaled by an ad-hoc factor of 0.9 to facilitate a better comparison of calculated and measured lifetimes. The lack of agreement between the B0 and D0 measurements could be the result of errors in the lattice parameters at the two IR's or in systematic errors in the luminosity measurement. The 10% initial discrepancy between the calculated numbers and the measurement at B0 could be explained by errors in the initial beam parameters as well as lattice and measurement errors.

The measured luminosity drops more quickly (see Figure 6.5) than the calculation. About half of this effect is caused by the shorter than calculated proton lifetime. The antiproton intensity is fairly well described (see Figure 6.6) by the model (the dominant effect is particle loss through beam-beam collisions), but the proton loss rate is much higher than predicted by the model. The longitudinal emittance growth of the proton beam is substantially less than predicted (see Figure 6.7) late in the store. This effect may be related to the proton lifetime: particles with large synchrotron oscillation amplitudes may be lost preferentially. The transverse emittance growth rate agrees reasonably well with the calculations although there is a suggestion of excess emittance growth of the antiprotons. The calculated transverse emittance growth comes primarily from intrabeam scattering, but the assumed ad-hoc emittance growth rate of 0.2π mm-mrad per hour also contributes to the growth.

Given this modest success in predicting performance in Run Ib, we will use this model to project performance in Run II. Since the single bunch intensities are similar to those in Run II, we should experience similar levels of intrabeam scattering. However, if beam-beam effects from the increased number of long-range interactions become more significant, the luminosity lifetime could be much shorter than predicted.

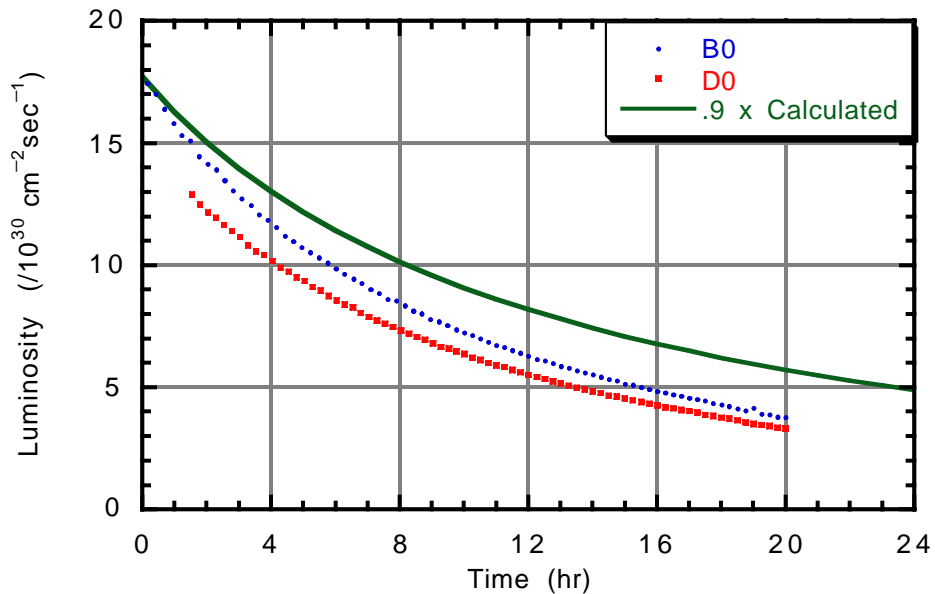


Figure 6.5. Luminosity as a function of time in Store 5903 in Run Ib. The calculated luminosity is based on measurements of the beam intensities and is multiplied by an ad-hoc factor of 0.9 so that the initial luminosity agrees with the measurement at B0.

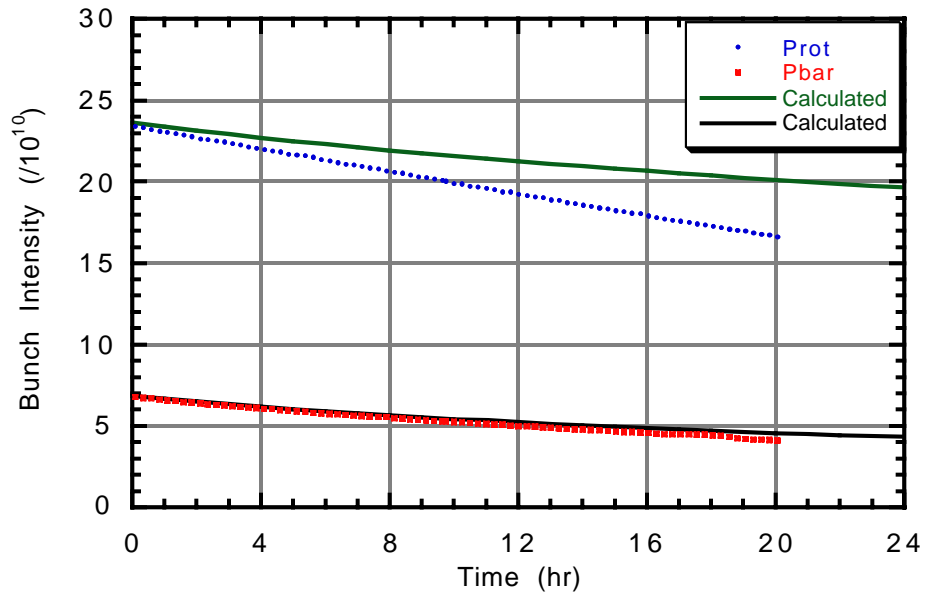


Figure 6.6. Beam intensity as a function of time in Store 5903 in Run Ib compared with the calculation.

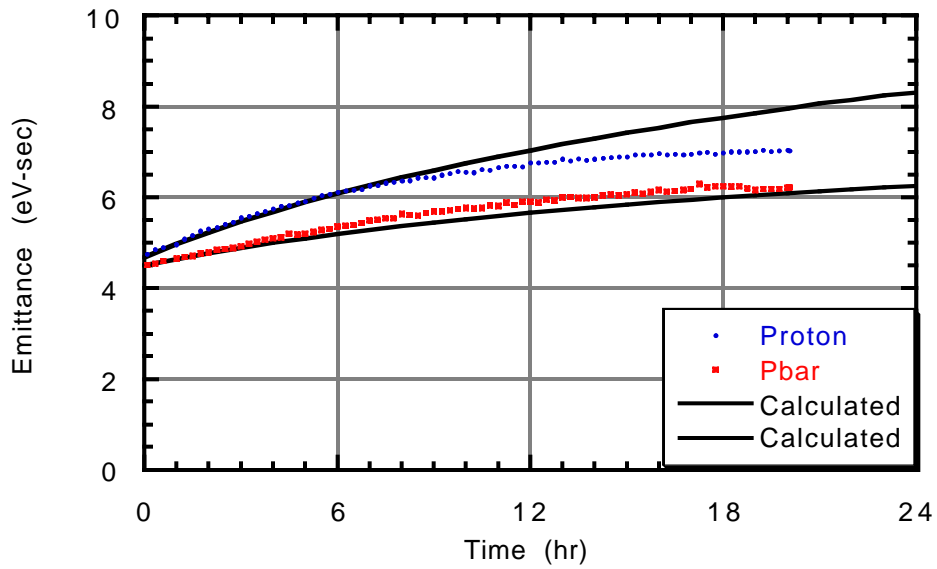


Figure 6.7. Longitudinal emittance as a function of time in Store 5903 in Run Ib compared with the calculation.

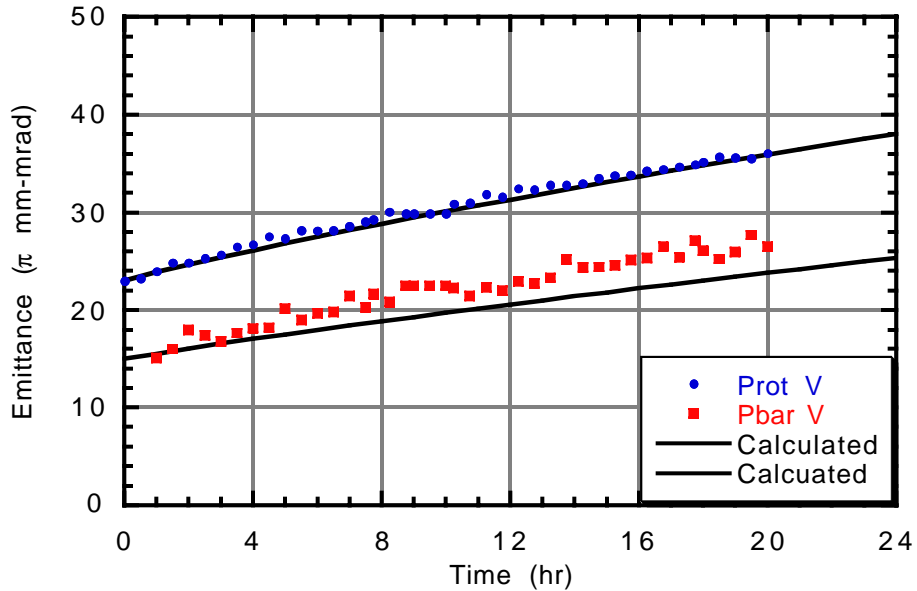


Figure 6.8. Vertical emittances as a function of time in Store 5903 in Run Ib compared with the calculation.

6.3.2 Predictions for Run II

The antiproton intensity is a critical parameter of the Tevatron antiproton-collider. With a fixed antiproton accumulation rate, the antiproton intensity can be increased by increasing the length of the accumulation period. However, the length of the store must also increase to match the accumulation period. Thus the length of the store is dependent on the initial antiproton intensity and can not be chosen arbitrarily. It is critical to include the constraint of limited antiproton production when comparing different scenarios.

In order to predict Run II performance the model for the evolution of a store has to be augmented with operational details including the recycling of antiprotons and antiproton acceleration efficiency. The following assumptions were made:

1. During a store antiprotons are accumulated in the Recycler at a rate of 18×10^{10} antiprotons per hour.
1. Shot setup (the time between stores) is exactly 1 hour and no stacking occurs during shot setup.
1. Ninety percent of the antiprotons are retained in the process of transferring beam from the Recycler, accelerating, and establishing collisions in the Tevatron.
1. Ninety percent of the antiprotons within an effective acceptance of 25π mm-mrad (horizontal and vertical) and 3 eV-sec (longitudinal) are recycled. No particles outside this acceptance are recycled. The “effective acceptance” is specified at low beta in the Tevatron, and allows for emittance dilution during the deceleration process. Note that a beam with 25π mm-mrad transverse emittance and 3 eV-sec longitudinal emittance (95% emittances) would have a calculated recycling efficiency of $0.90 \times 0.95 \times 0.95 \times 0.95 = 0.77$.

1. The Tevatron operation is characterized by random losses of stores with a mean time between failures of 72 hours. This loss rate is consistent the number of stores that ended abnormally⁴ in Run Ib but must certainly be a naive approximation to reality.
1. The length of the store is the optimum store length to compensate for the 1 hour shot setup time or the time to accumulate the required antiproton intensity, whichever is longer.

The initial antiproton emittance will probably depend on intensity because stochastic cooling, which is less effective at high intensity, will be used in the Recycler. In addition, the various antiproton transfer efficiencies will be poorer for high emittance (and high) antiproton beams. These considerations, which are not included in the model, bias the calculated optimum performance towards higher antiproton intensities and shorter store lengths than would be the case if these effects were included.

The proper response to the abnormal termination of a Tevatron store is a complicated issue. One can wait until the desired number of antiprotons has been accumulated or one can begin a new store sooner with lower antiproton intensity. In practice, the answer may depend on considerations such as whether there are other uses for the Tevatron, including the need to perform some measurements using proton beams. In the model, it is assumed that the same number of antiprotons is stacked for each store. While the model is at best a caricature of reality and the parameters are speculative, the model contains many features of actual machine operation.

As discussed in Chapter 1, we intend to operate initially with 36 proton and 36 antiproton bunches for Run II. As the luminosity increases it may be desirable to limit the maximum luminosity using luminosity leveling (modulating the β^* at the interaction point during the course of the store). In this section, we consider 36×36 stores leveled to a maximum luminosity of $1 \times 10^{32} \text{ cm}^{-2} \text{ sec}^{-1}$. We also consider 140×121 stores, where the 121 antiproton bunches are used to reduce the number of interactions per crossing compared to 36×36 operation. The beam parameters of these scenarios are given in Table 1.1 except for the initial antiproton intensity, which varies with the store length.

Figure 6.9 shows the initial store luminosity versus antiproton intensity. The unleveled luminosity is proportional to antiproton intensity (with the assumption that antiproton emittance does not depend on intensity), but the leveled store achieves a maximum luminosity of $1 \times 10^{32} \text{ cm}^{-2} \text{ sec}^{-1}$ because of the increased β^* . Figure 6.10 shows the store length versus initial antiproton intensity. For very short stores, the optimum store duration depends on the shot setup time, and there is excess antiproton production for that mode of operation. For higher antiproton intensities the store length is roughly proportional to the initial antiproton intensity. Compared to the 36×36 operation, the 140×121 stores require less stacking time for the same initial antiproton intensity. This effect occurs because the initial luminosity of the 140×121 stores is less because of the crossing angle (see Figure 6.9) and because the recycling efficiency is better (lower per bunch intensity reduces the intrabeam scattering).

Figure 6.11 shows the average luminosity per hour obtained with each of these modes of operation. It should perhaps be emphasized that the curves shown in Figure 6.11 represent different modes of operation with the same antiproton accumulation rate. The best integrated luminosity for each scenario is given by the maximum of its respective curve. The unleveled 36×36 operation achieves the greatest integrated luminosity (at any antiproton intensity largely

because of the luminosity penalty from leveling or from the crossing angle used in 140×121 operation. The relatively small effect of Tevatron failures on the integrated luminosity is seen most clearly in the leveled case where the small increase in integrated luminosity that comes from having long stores (reducing the effect of the 1 hour interruptions for shot setup) is offset by the possibility of the large loss in luminosity from the wait required to achieve the desired initial antiproton intensity*. The 140×121 operation is seen to be competitive with 36×36 operation (85% of the integrated luminosity of unlevelled 36×36 stores) under the stated assumptions (the recycling efficiency is critical).

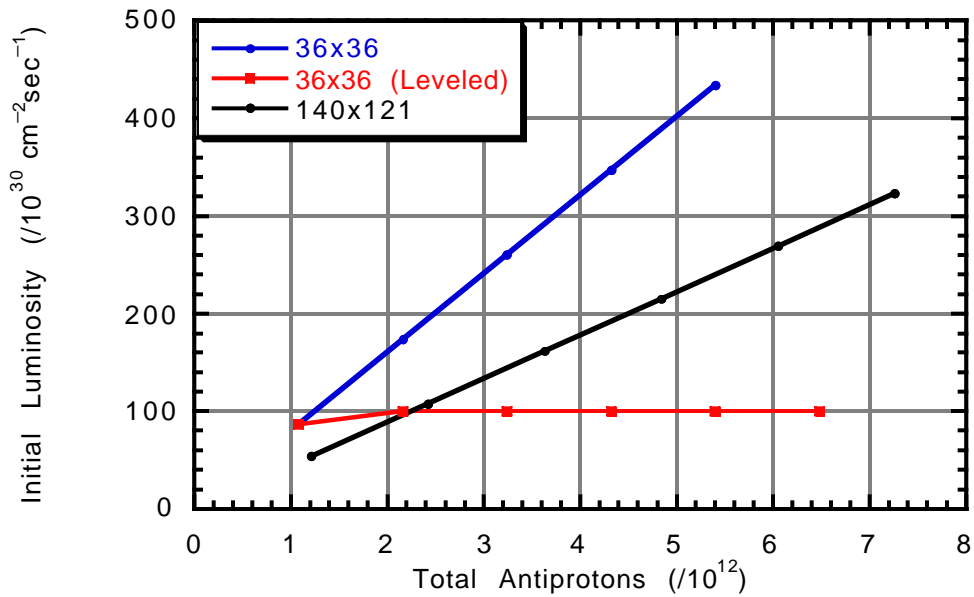


Figure 6.9. Initial store luminosity versus the initial antiproton intensity. The points are the results of the calculations described in the text; the curve joining the points serves to guide the eye.

* In the luminosity leveled case, however, the strategy of waiting to accumulate the desired antiproton intensity is probably not optimal.

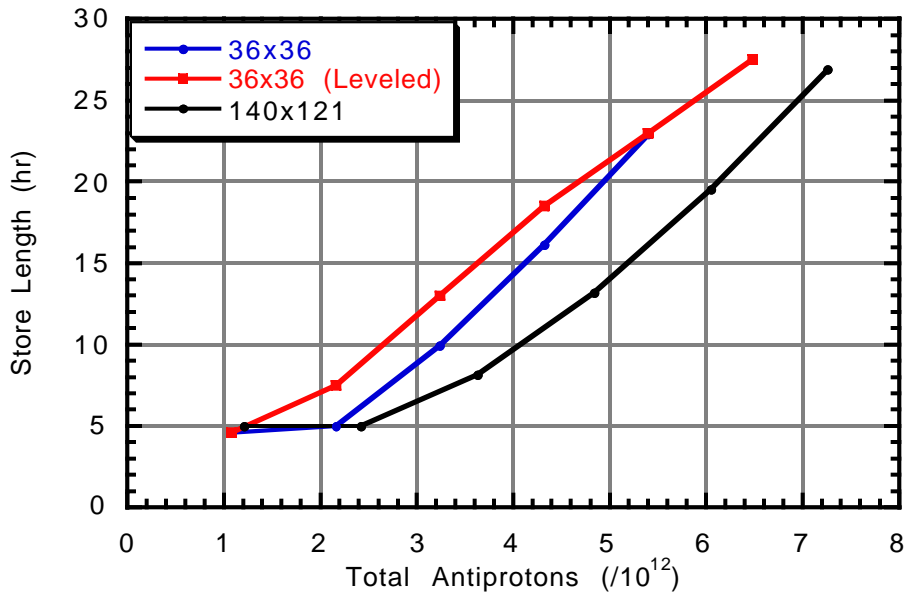


Figure 6.10. Store length versus the number of antiprotons for the 3 scenarios discussed in the text. The points are the results of the calculations described in the text; the curve joining the points serves to guide the eye.

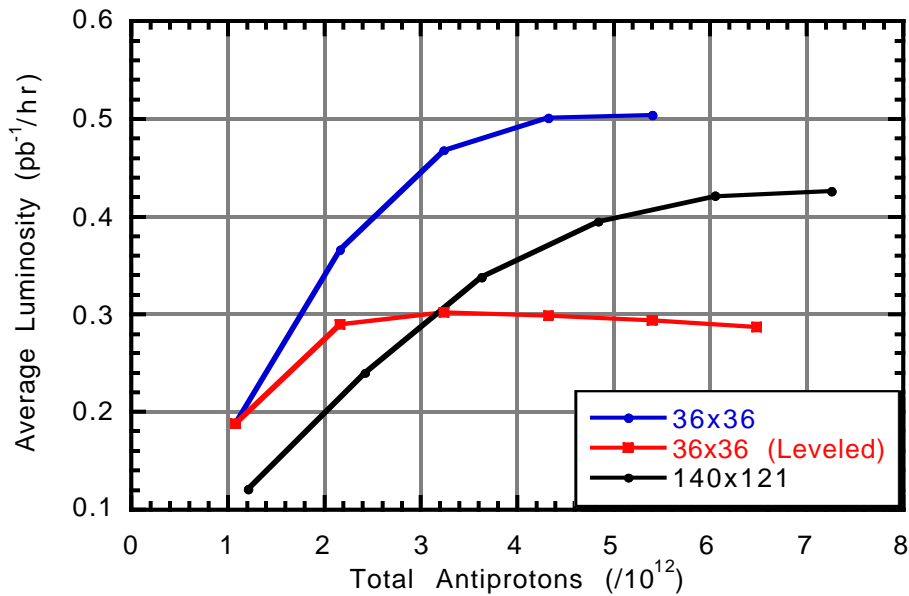


Figure 6.11. Average luminosity for the 3 scenarios discussed in the text. The points are the results of the calculations described in the text; the curve joining the points serves to guide the eye.

6.3.3 Intrabeam Scattering

Intrabeam scattering is a dominant growth mechanism for high intensity beams in the Tevatron and an important contributor to the luminosity lifetime. We have made a separate study of intrabeam scattering and made calculations using more detailed models than that described in Ref. 3.

6.3.3.1 Theoretical Estimates of Intrabeam Scattering

A number of authors have carried out analysis of intrabeam scattering.^{5,6,7,8,9,10} In this analysis we have compared the theoretical formalisms of Refs. 5-7 in detail. In particular, we consider a somewhat simplified case, which ignores the effect of coupling on the transverse emittance growth. In general, coupling is believed to lead to a reduction in the horizontal growth rate and a commensurate increase in the vertical growth rate. Since the product of the two emittances occurs in the expression for the luminosity, it can be assumed (with some error resulting from the different amount of dispersion in the two planes) that the effect on the luminosity is small. We have found that except for Ref. 6, a number of additional approximations have been assumed, based on the assumption of a regular lattice, which can lead to slight discrepancies in the results. However, these differences tend to be small and we have found overall good agreement among the various published results.

In the case of this analysis, we use the method of Ref. 6 applied on a point-by-point basis around the ring. The total scattering rate is then the ring-averaged value. Using the expected machine parameters from Table 6.1, we have evaluated the growth rates as a function of the longitudinal emittance, keeping other parameters fixed, and the results are shown in Figure 6.12.

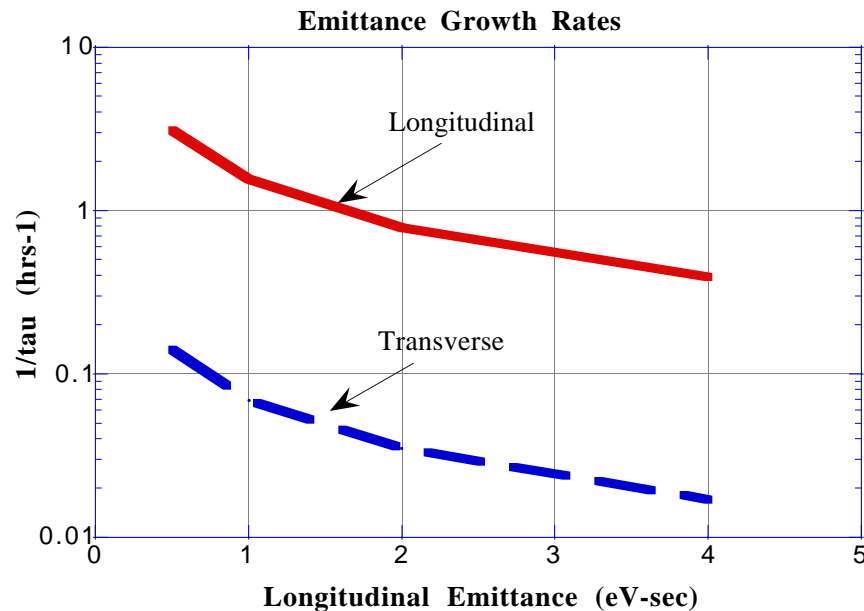


Figure 6.12. Emittance growth rates as a function of the longitudinal emittance in the Tevatron for Run II beam parameters.

In Collider Run Ib, we carried out a small number of measurements of intrabeam scattering, using proton-only stores with bunches of varying size. The growth rates are determined

empirically from the slope of the longitudinal and transverse emittances with time. The results of these studies are shown in Figure 6.13. Although the data are scant, there is reasonably good agreement with the model used in the above estimates at sufficiently high bunch intensity (shorter growth times). It is to be noted that a residual growth occurs at low intensity ($.008 \text{ hr}^{-1}$) which is presumably due to intrinsic machine noise. Based on these results, it is reasonable to assume that the intrabeam scattering models applied above are approximately correct.

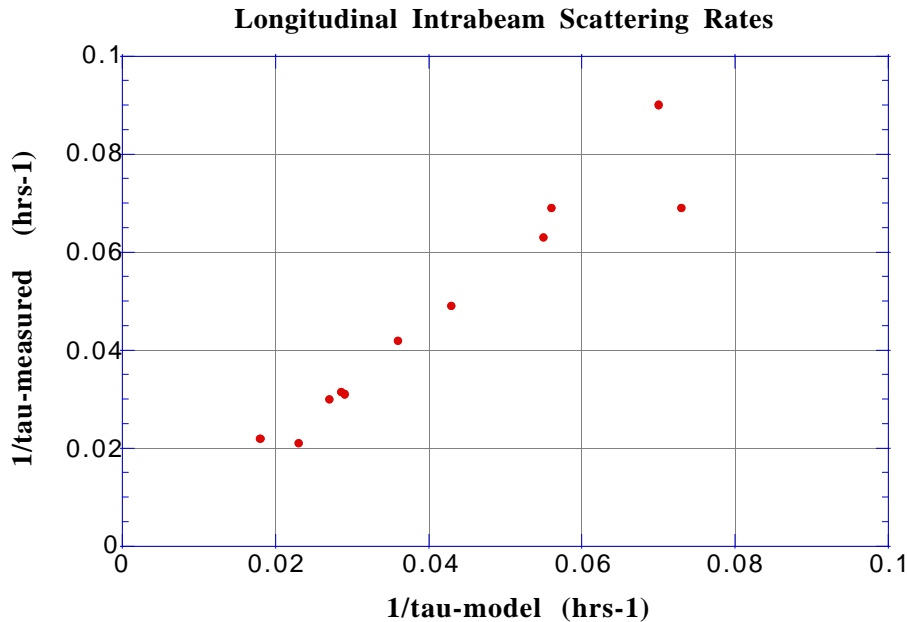


Figure 6.13. Comparison of measured longitudinal emittance growth rates with the Bjorken-Mtingwa model at low- β in the Tevatron.

6.4 Collider Fill Steps (Shot Setup)

This section lists the operational steps in the Tevatron during a collider fill. The major steps and the technical issues associated with each step are outlined.

6.4.1 Tevatron at 150 GeV and Proton Injection

Beginning with no beam in the Tevatron and the energy set at 150 GeV the first step is to inject 36 coalesced proton bunches into the Tevatron. In Run II the protons will be injected from the Main Injector into the Tevatron at the F0 straight section via the new 150 GeV proton injection transfer line. While there is nothing conceptually new or difficult with injecting beam at F0 (as compared to injecting from the Main Ring at E0) it will require the commissioning of a new injection line which will also be shared with antiproton stacking and Main Injector resonant extraction operations. Thus the hardware and software for maintaining efficient injection will require upgrading.

The proton bunches in the Tevatron will be in three groups of 12 with the bunches in each group spaced 21 rf buckets (396 nanoseconds) apart and the three groups of proton bunches spaced one third of the ring apart. Early attempts to coalesce 12 bunches of protons simultaneously in the Main Ring uncovered difficulties caused by beam loading in the MR cavities. These difficulties may be overcome and therefore it may be possible to inject protons in three groups of

12 bunches. However, we plan to build a new proton injection kicker with a rise time faster than 396 nsec. This will allow us to inject the protons in groups with less than twelve bunches. For instance we may inject 9 groups of protons each containing 4 coalesced proton bunches. If necessary the proton bunches could be injected with only one bunch per Main Injector cycle.

The kicker used to inject protons will also be used to extract antiprotons at 150 GeV after they have been decelerated. Thus, a new proton injection kicker with a rise time of 396 nsec is needed whether or not the Main Injector can coalesce 12 bunches simultaneously. The antiproton bunches will be ejected from the Tevatron in groups of four bunches as required by the Recycler Ring. The kicker design specifications for the Tevatron are presented in detail in another section of this report.

To inject the proton bunches into the correct Tevatron bucket the low level rf system is being redesigned to handle beam transfers between machines with different revolution frequencies. The system for generating the trigger for beam transfer will need modification in order to fire the Main Injector extraction kicker and Tevatron injection kicker on the correct Main Injector revolution.

Single bunch instabilities, believed to be the head-tail instability, have been observed in Run Ib while accelerating but these were usually eliminated by increasing the chromaticity. In Run II the higher proton intensity per bunch increases the likelihood of observing these instabilities. With 36 bunches instead of 6 the probability of observing coupled bunch instabilities is also increased. In Run Ib there was a longitudinal instability which was cured with the 6x6 longitudinal damper system. However in Run II this system will need modification to work for 36 bunches. Since it is difficult to measure or estimate the impedance of the Tevatron there is no good prediction for the intensity at which instabilities will appear. Therefore the preferred solution to the problem of instabilities is to build a set of 6 dampers (1 longitudinal and 2 transverse dampers for both protons and antiprotons) with enough gain to damp any expected instabilities. The design of the dampers is discussed in a later section of this report.

As in Run Ib the sextupole fields created by eddy currents in the dipole magnets must be compensated in order to keep the chromaticity at a constant and reasonable value while Tevatron is at 150 GeV. The compensation for these sextupole fields, the b_2 correction, worked well during Run Ib but there will be additional complications during Collider Run II. In Run Ib as part of every shot setup the Tevatron was ramped up to 900 GeV and back down again six times to reset the Tevatron magnets to the same state at the start of every shot setup. With each ramping of the Tevatron taking several minutes this resetting procedure takes 20 minutes which is inconsistent with the Run II goal of speeding up shot setup. Eliminating these ramps means that the b_2 correction algorithm will have to account for the history of Tevatron ramp such as the time at flattop and the time on the back porch while extracting antiprotons for recycling. This b_2 issue is also relevant for the chromaticity corrections while decelerating and extracting the antiprotons.

6.4.2 Antiproton Injection

The antiprotons are injected into the Tevatron after the protons have already been loaded. Before the antiprotons are injected a set of electrostatic separators are used to create a pair of non-intersecting helical closed orbits with the protons circulating on one strand of the helix and the antiprotons circulating on the other. This provides transverse separation of the proton and antiproton bunches as they pass each other longitudinally and eliminates the beam-beam tune shift from head on collisions. The antiprotons are injected onto the helical orbit after the separators have been turned on.

The antiproton bunches will be in 3 groups of 12 with the bunches in each group spaced 21 rf buckets (396 nanoseconds) apart and the 3 groups of antiproton bunches will be spaced one

third of the ring apart. This is the same bunch spacing as the protons. Because the antiprotons are extracted from the Recycler Ring in groups of 4 bunches there is no need to coalesce the antiprotons in the Main Injector. Injecting the antiprotons in groups of four with the 396 nanosecond spacing between bunches required the design and fabrication of a new set of antiproton injection kickers with a faster rise time. Since the antiprotons are injected in the gap between the groups of protons the kickers must also have a sufficiently fast fall time so that the kicker pulse does not disturb the protons already in the machine.

The antiproton injection kickers have already been built and tested in 36×36 studies conducted in the Fall of 1995. The tests showed that the field in the antiproton injection kickers did not fall rapidly enough after they were fired and therefore the emittance of some of the proton bunches were blown up from the kick of the antiproton kicker. The proposed solution to this problem is to design and build a bumper magnet and power supply which can give relatively small kicks on a bunch-by-bunch basis and compensate for the undesired kick from the antiproton injection kickers. The antiproton kickers and bumper magnets are discussed in another section of this report.

One of the big concerns with having 36 proton and 36 antiproton bunches in the Tevatron are the tune shifts of the antiprotons resulting from the long range beam-beam interactions. As an antiproton bunch travels past a proton bunch the electric and magnetic fields from the proton bunch affect the motion of the antiprotons and changes the tunes of the antiprotons slightly. In Run Ib there were 12 of these parasitic (or long range) crossings per revolution but in Run II this will increase to 72 parasitic crossing in 36×36 bunch mode. Furthermore the protons will have slightly higher intensities during Run II. Calculations of the tune shift for the small amplitude antiprotons have been done for 36×36 bunch mode with the proton intensities expected during Run II and do not indicate that there will be a problem. The validity of these calculations was tested during 36×36 bunch studies by measuring the tune shift of the antiprotons and the results showed good agreement between the calculations and the experiments¹¹.

Part of the tune shifts from the long range interactions can be compensated for by using the feed-down sextupole circuits to independently adjust the tunes of the protons and antiprotons. The feed-down sextupoles have enough strength at 150 GeV to adjust the tunes of the antiprotons and correct for the long range beam-beam tune shift on the average although of course the bunch to bunch variations can not be compensated with the feed-down sextupoles.

Even though the feed-down sextupoles are strong enough to adjust the tunes there is a problem with adjusting the coupling between the horizontal and vertical tunes for the protons and antiprotons independently. Adjusting the coupling requires two orthogonal families of skew quadrupoles. However the feed-down sextupoles presently provide only one family. In Run Ib it was discovered that the differential coupling due to the "missing family" of feed-down differential coupling sextupoles was too large and prevented the tunes from being adjusted properly. For Run II there are plans to add a second family of differential feed-down circuits to correct the coupling.

The largest uncertainty with the 36×36 operations is the effect that nonlinear beam-beam interactions will have on the antiproton emittance growth and beam lifetime. During Run Ib the antiproton lifetimes were often poor at 150 GeV (<1 hour) and constant tuning was required in order to keep the lifetimes reasonable. With 36 bunches and higher proton intensities the lifetime problem will certainly be worse in Run II. This issue was studied during the 36×36 studies period, however during the studies the proton intensities were 10^{11} or less per bunch which is much lower

than the 2.7×10^{11} expected during Run II. Until we gain experience with operations in Run II it is not known how much of a problem the antiproton lifetime and emittance blow up will be.

6.4.3 Acceleration

Once the protons and antiprotons have been loaded at 150 GeV both beams are accelerated to an energy of 1 TeV. In Run Ib the biggest problem with acceleration was controlling the tunes, coupling, and chromaticity in order to prevent beam loss and emittance blow up. In Run II, with more bunches and higher intensities, more effort will be required in maintaining the proper tunes while ramping the Tevatron.

6.4.4 Low Beta Squeeze

After the beam has been accelerated to 1 TeV, the Tevatron lattice is changed by ramping the currents in the low beta quadrupole magnets to reduce the minimum beta function in the CDF and D0 interaction regions from 1.7 meters to 35 cm. For Run II the basic plan for the low beta squeeze remains the same as in Run Ib although the option of luminosity leveling is also being considered. At luminosities of $2 \times 10^{32} \text{ cm}^{-2} \text{ sec}^{-1}$ the number of interactions per crossing will be 5.8 and it may be advantageous to the experiments to level the luminosity by changing the β^* as the store progresses. By starting with higher β^* at the start of a store and decreasing β^* as the store progresses, a constant luminosity can be maintained.

6.4.5 Beam Halo Scraping

Once the beams have been brought into collisions and the Tevatron begins to produce luminosity the halo of the proton and antiproton beams is scraped away to reduce losses in the experimental detectors at CDF and D0 resulting from the beam halo interactions with beam pipe. In Run Ib this process had been performed by the operations group manually at the start of each store and typically the procedure, which is somewhat of an art, took about 15 minutes. To reduce the shot setup time and make the most use of the luminosity it is important that this process of scraping be made significantly faster through automation of the scraping and improved collimator motor controls. The motor controllers for the collimators are being redesigned to allow for faster operations and independent control of the collimator motion. More thought is needed on halo scraping and much will be learned as we gain experience during Run II.

6.4.6 Proton Removal

Once a store has been completed and we are ready to begin the next collider fill it is necessary to first decelerate the antiprotons in order to recycle them. It is felt that a good deceleration efficiency will be difficult to achieve if the protons are also decelerated at the same time. This feeling is based on operational experience accelerating two beams at once. Decelerating with the presence long range beam-beam effects requires a more precise tuning of the Tevatron to maintain high efficiency. Also the decelerating protons at the same time requires that the separators remain on in order to separate the proton and antiproton orbits. Since the antiprotons will have a larger emittance at the end of a store, the aperture gained by turning off the helix will help improve the efficiency.

Since it is impractical to remove the protons but leave the antiprotons with a kicker at 1 TeV the plan is to remove the protons by scraping them away with a collimator. The challenge will be to remove the 10^{13} protons in 100 sec at 1 TeV without quenching the Tevatron magnets. The plan is to insert a set of four Main Ring dipoles into the E0 straight section, which form a dogleg with scraper in between the first and second magnets. The non-superconducting MR magnets will serve

to shield the Tevatron dipoles from particle losses during the scraping. Calculations have been done which suggest that the dogleg should provide sufficient protection of the superconducting magnets to prevent quenches.

6.4.7 Low Beta Unsqueeze

After the protons have been removed but before decelerating the antiprotons the low beta squeeze will be undone. This has been done successfully in the past during studies without significant beam loss and is not expected to be a problem.

6.4.8 Antiproton Deceleration

With the protons removed and the low beta unsqueezed, the antiprotons will be decelerated from 1 TeV to 150 GeV with the electrostatic separators turned off. During Tevatron studies protons have been successfully decelerated with nearly 100% efficiency so the deceleration procedure is not expected to be a problem. The main issue will be dealing with hysteresis effects on the orbits, tunes, and especially the chromaticity and the b_2 correction.

6.4.9 Antiproton Extraction

Antiprotons will be extracted from the Tevatron to the Main Injector using the proton injection kickers to remove the antiprotons in groups of 4 bunches. The only difficulty expected during this step will be the changing b_2 components in the TeV dipoles. These will need to be compensated for since the chromaticity changes fairly rapidly (~20 units in the order of one minute) after the Tevatron energy is stopped at 150 GeV. This completes the collider fill and store cycle.

6.5 Run II Tevatron Lattice Issues

The Run II Tevatron lattice will be similar to the Run I lattice with low beta insertions at B0 and D0. A new tune of the low beta insertion will attain a dispersion of zero throughout the interaction region. Separately powering the tune quads in E and F sectors will give a greater flexibility in perturbing the beta-functions to attain more favorable conditions for both fixed target and collider operations. Another possible modification is the relocation of the triplet low beta quads at D0. This provides additional warm space upstream and downstream of the separators for sets of roman pot detectors for the D0 experiment.

6.5.1 Dispersionless Interaction Region

The nominal Run I Tevatron lattice has zero dispersion at the B0 and D0 interaction points, $\eta = 0$, but the slope of the dispersion is not equal to zero, $\eta' = 0.3$. By running the low beta quads with gradient strengths different from Run I it is possible to produce a Tevatron lattice which has zero dispersion, $\eta = \eta' = 0$, in the B0 and D0 interaction regions. One advantage of this lattice is a slight decrease in the beam size at the interaction point and a corresponding increase in luminosity. Another, perhaps more significant advantage is that the beam-beam tune shift is reduced because the separation of the helix at the parasitic crossings near the interaction regions happens to be larger with the dispersionless interaction region (See the comments on 36¥36 bunch spacing in the 132 nsec section of this report.).

The gradients for the zero dispersion lattice are shown in Table 6.2. Figure 6.2 shows the resulting lattice functions in the IR with the zero dispersion solution with the low beta squeeze (also known as the JJ15C lattice) and without the low beta squeeze (also known as the JJ01 lattice). With $\beta^* = 3.50$ m, the maximum β is only 122m, which is essentially the same as the

regular long straight sections. Figure 6.3 shows the gradients required in the low beta magnets as a function of β^* for the zero dispersion solution.

Table 6.2. Gradients in low beta magnets at $\beta^* = 35$ cm for the dispersionless IR solution. The gradient strengths are in T/m at 900 GeV/c

Quad Name	$\beta^* = 0.35$ m	
	upstream	downstream
Q4	122.7384	-122.7384
Q3	-125.9696	125.9696
Q2	122.7384	-122.7384
Q1	-31.2656	31.2656
Q5	-120.7215	120.7215
Q6	-31.2656	31.2656
T6	-2.04752	
T7	33.6728	-33.1375
T9	-45.4510	47.4919
T0	9.43142	-10.7942

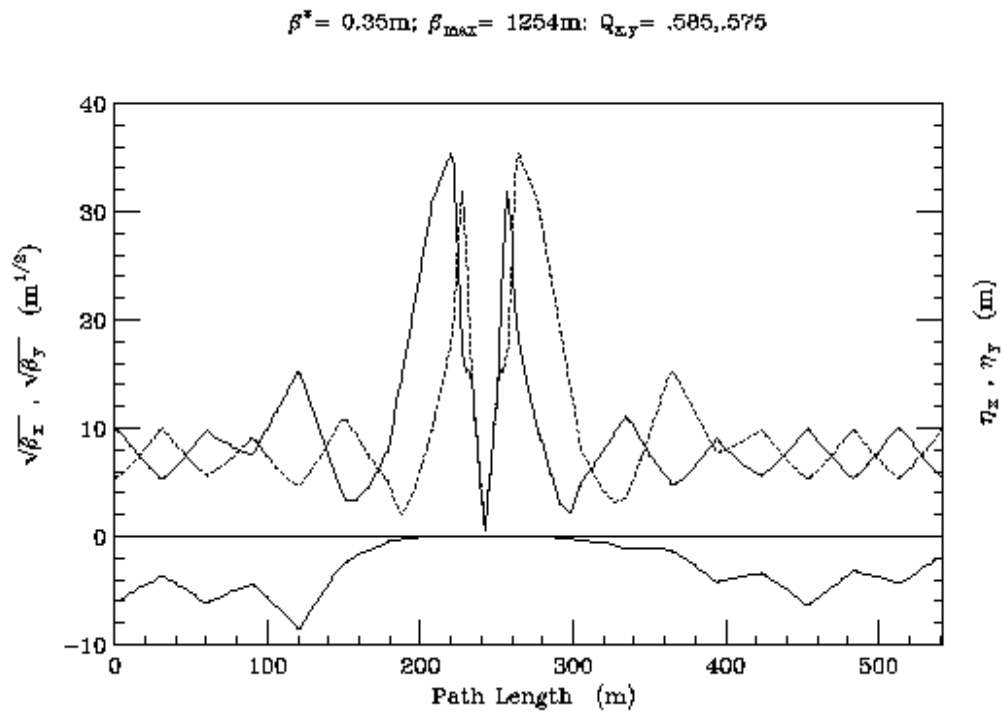
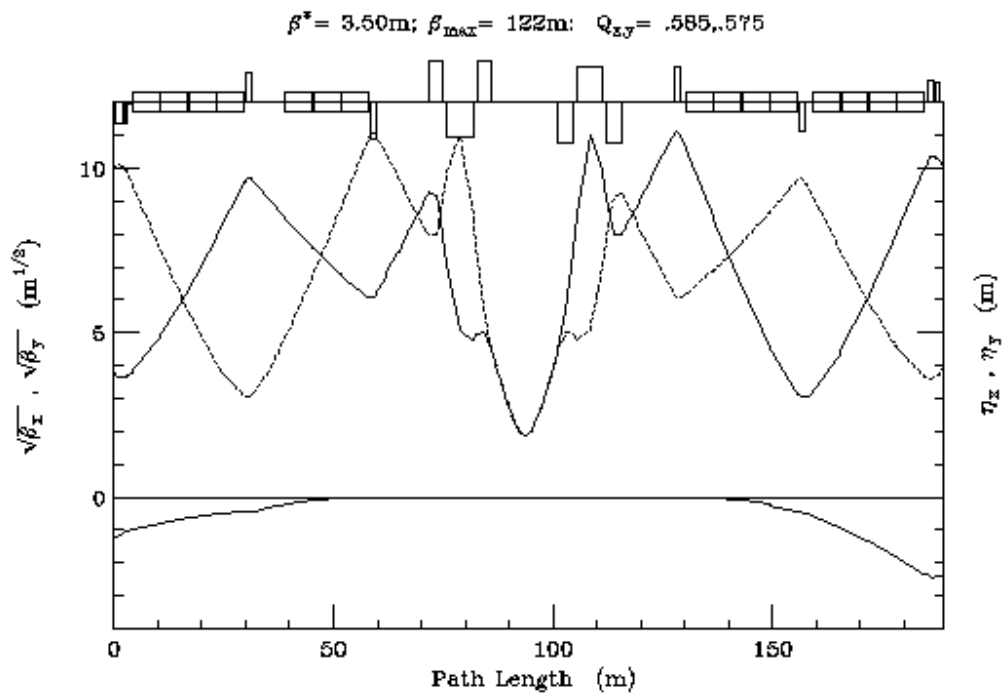


Figure 6.14. Lattice functions at B0 and D0 for the Dispersionless IR Solution a) with out the low beta squeeze (lattice JJ01) and b) with the low beta squeeze (lattice JJ15C.)

Gradients of the 25cm Low Beta Squeeze
(900 GeV/c)

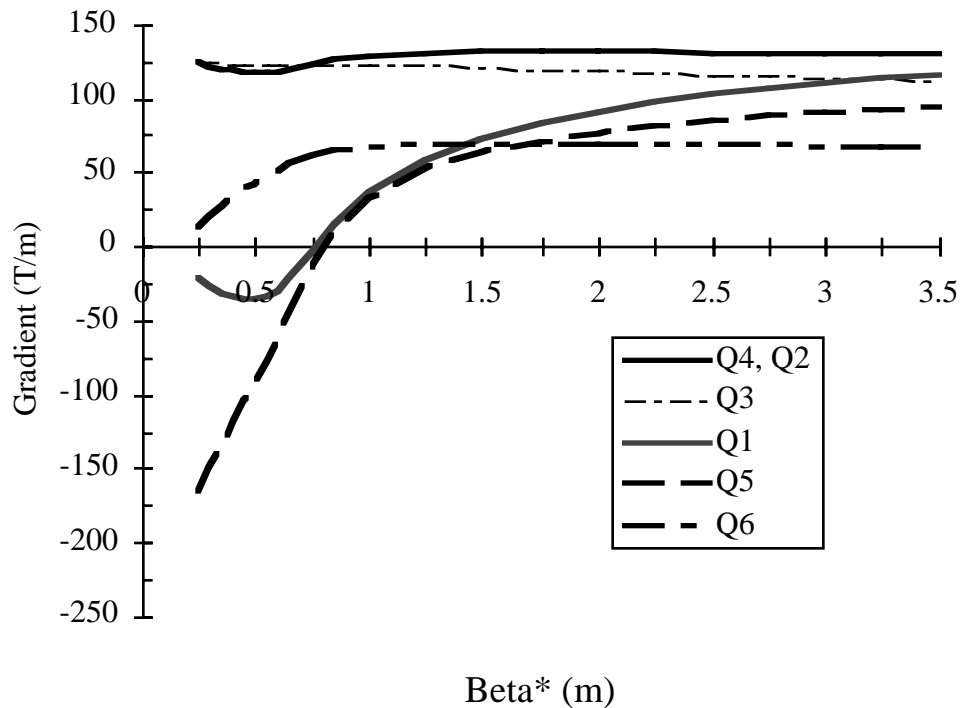


Figure 6.15. Gradients in low beta magnets as a function of β^* for the dispersionless IR solution.

The dispersionless solution will be implemented with the existing low beta quadrupoles at their present locations. Some modifications of the power supplies and reversing switches will be necessary, however. In the Run I lattice configuration the polarity of quadrupoles Q5 and T0 reverse during the low beta squeeze, whereas in the $\eta = \eta' = 0$ solution it is Q5 and Q1 that reverse polarity. Also, in the dispersionless lattice the maximum Q1 current is 4.3 kA, while the present Q1 power supply is rated at 2.5 kA. However, the Q6 magnet never exceeds 2.5 kA in the dispersionless lattice. Thus the existing switches and power supplies is adequate to implement the dispersionless lattice. The reversing switch will be moved from T0 to Q1 and the present Q1 supply will power the Q6 magnets and vice versa.

6.5.2 Individually Powering the Tune Quads in E and F sectors

Editor's note: This section is not yet available.

6.5.3 Roman Pots at D0

A possible lattice modification for Run II involves physically moving the low beta triplet quadrupoles closer to the D0 interaction region to provide additional warm space for forward proton detectors (roman pots) as part of a D0 experiment upgrade. The change in the lattice functions caused by the move are minimal. The gradients necessary in the magnets are shown in Figure 6.16. The limitation on the amount the low beta quads can be moved is the gradient on the

Q3 quadrupole. As shown in Figure 6.16, with a gradient limit of 140 T/m, the farthest the quads can be moved inward is about 26 inches. However, it should be pointed out that 140 T/m is a somewhat arbitrary limit: we do not know how the frequency of quenches will depend on gradient during Run II operations.

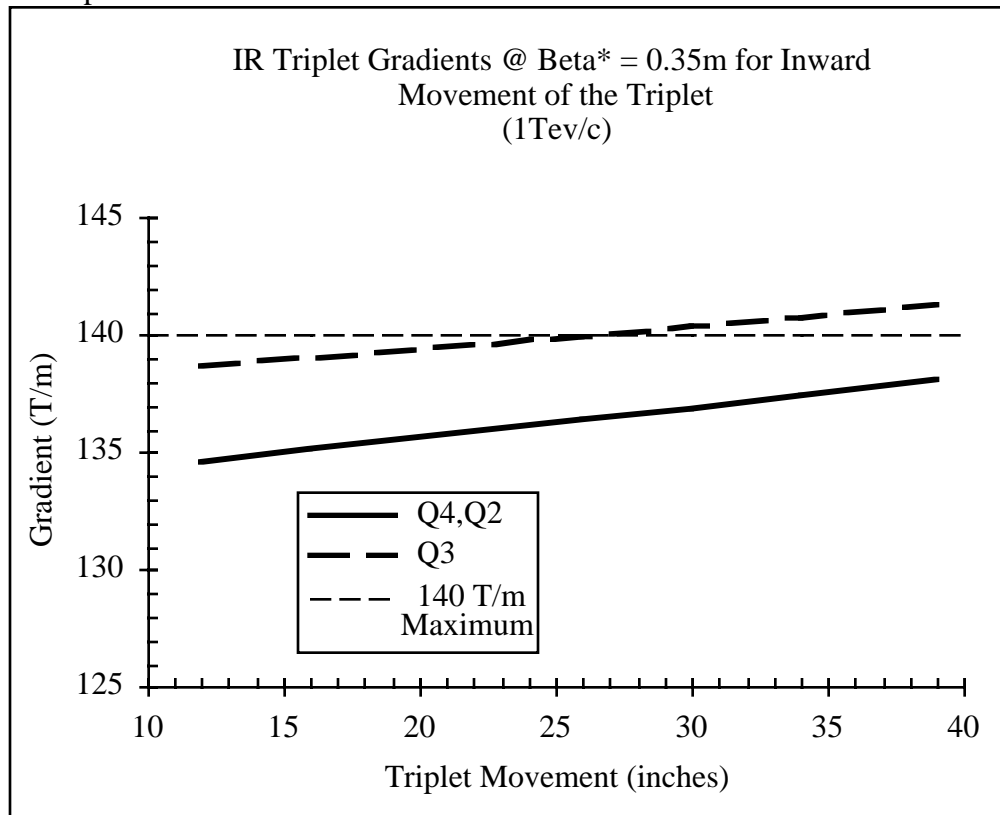


Figure 6.16. Gradient strength required at 1 TeV as a function of movement of the low beta quad triplet closer to the interaction region. 26" is the maximum inward movement of the triplet such that the 5000A (140 T/m) limit is not exceeded.

6.5.4 Interaction Point Orbit Control

The detector collaborations (CDF and D0) plan on utilizing impact parameter triggers to find events with B-meson decays. These systems use the r - ϕ information from the silicon tracking detectors to find events with vertices displaced from the primary interaction. Based on the CDF data taken during Run I, an impact parameter (distance of closest approach in the transverse plane) cut at 100 μm is efficient for physics signals (e.g., $B^0 \rightarrow \pi^+ \pi^-$) while rejecting enough background to keep the total trigger rate acceptable. The CDF studies assumed that the beam center position with respect to the silicon vertex detector was well known and stable and that the beam axis and the silicon detector axis were in alignment. Because of the 2D track reconstruction, an angle between the beam axis and detector axis causes a decrease in the accuracy of determining the impact parameter and therefore a decrease in trigger performance.

To keep the total trigger rate within the capability of the data acquisition system, it is necessary to keep the center position stable and the relative angle small. CDF has requested that the center position not wander by more than 30 μm during the course of a Tevatron store and that

the relative angle be kept less than 100 μrad . Changes larger than these amounts will significantly degrade the capabilities of the impact parameter trigger systems.

Corrections to the orbit will be made during a store in Run II using the dipole corrector magnets located on either side of B0 or D0. The orbit will be adjusted based on position information provided by the CDF and D0 experiments. The dipole correctors should have enough range to keep the orbits fixed to the specifications given above. The only potential problem would be if the corrector strength were at its maximum value due to alignment errors of the low beta quadrupoles for instance. This would require an adjustment to the alignment of the detector or the low beta quadrupoles.

6.5.5 Differential Coupling Feed-down Circuit

During Run Ib the differential feed-down circuits were used to adjust the tunes of the protons and antiprotons independently. There is also a feed-down sextupole circuit, called dSq, which can be used to adjust the coupling between the proton horizontal and vertical tunes independently from the coupling between the antiproton horizontal and vertical tunes. During Run Ib operations however it was found that the dSq circuit alone was unable to eliminate the differential coupling of the protons and antiprotons. This made it difficult to adjust the tunes and coupling at 150 GeV and may have contributed to the poor lifetimes observed at 150 GeV. The source of the differential coupling could be magnet errors in the triplet, which create a differential skew quadrupole error, and these could not be corrected because there are no feed-down sextupoles in the appropriate locations in the Tevatron. Essentially what is needed is a second differential feed-down coupling circuit which is orthogonal to the dSq circuit. This section looks into the possibility of installing a second differential feed-down circuit in the Tevatron

A beam traveling off center through a sextupole field experiences a quadrupole field. For a normal sextupole with the beam traveling through with a closed orbit offset (x_{co}, y_{co}) the linear transfer matrix is:

$$\begin{pmatrix} 1 & 0 & 0 & 0 \\ -\frac{B''L}{B\rho} x_{co} & 1 & \frac{B''L}{B\rho} y_{co} & 0 \\ 0 & 0 & 1 & 0 \\ \frac{B''L}{B\rho} y_{co} & 0 & \frac{B''L}{B\rho} x_{co} & 1 \end{pmatrix}$$

Relative to a beam with no closed orbit offset this will produce a change in the horizontal and vertical tune and the coupling ΔQ_s . Thus, for a normal sextupole a horizontal orbit offset produces a differential tune and a vertical orbit offset produces a differential coupling. For a skew sextupole a horizontal orbit produces a differential coupling and the vertical orbit offset produces a differential tune.

For Normal Sextupole

For Skew Sextupole

$$\begin{aligned} \Delta v_x &\approx \frac{1}{4\pi} \frac{B''L}{B_\rho} \bar{\beta}_x \sum P \cdot X_{co} & \Delta v_x &\approx \frac{1}{4\pi} \frac{B''L}{B_\rho} \bar{\beta}_x \sum P \cdot Y_{co} \\ \Delta v_y &\approx \frac{1}{4\pi} \frac{B''L}{B_\rho} \bar{\beta}_y \sum P \cdot X_{co} & \Delta v_y &\approx \frac{1}{4\pi} \frac{B''L}{B_\rho} \bar{\beta}_y \sum P \cdot Y_{co} \\ \Delta Q_s &= \frac{B''L}{B_\rho} \sum P \cdot Y_{co} & \Delta Q_s &= \frac{B''L}{B_\rho} \sum P \cdot X_{co} \end{aligned}$$

where:

$$B'' = 9.176 \cdot I(\text{amp}) \frac{\text{tesla}}{\text{m}^2}$$

$$L = 0.732 \text{ m}$$

$$B_\rho = 3.336 \cdot P\left(\frac{\text{GeV}}{c}\right) \text{ tesla} \cdot \text{m}$$

$$\bar{\beta} = 90 \text{ meters at focusing locations}$$

$$\bar{\beta} = 30 \text{ meters at defocusing locations}$$

The correction for differential coupling is ideally obtained by two families of sextupoles that differ in relative phase $\Delta\Psi = \Psi_H - \Psi_V$ by $\pm 90^\circ$. It is sufficient, however, that $\Delta\Psi$ be a significant fraction of 90° . Figure 6.17 through Figure 6.22 show the difference between the horizontal and vertical phase, $\Delta\Psi(s)$, at various locations (s) around the Tevatron for the BD1 injection lattice and the BD15 low beta lattice (the lattices used in Run Ib.). We see that $\Delta\Psi(s)$ in the arcs is much different than in the straight sections. Currently we have one family of feed-down sextupoles, dSq, located in the arcs, which compensates for errors in the arcs. In order to get a second family we need to use sextupoles in the straight sections where the $\Delta\Psi(s)$ is different from the arcs.

One possible solution is to use some of the chromaticity sextupole magnets already in the tunnel at B0 and D0 but disconnect them from the chromaticity circuit and run them with independent power supplies. The suggestion is to remove the chromaticity sextupoles at VA47, VC47, VB14, and VD14 from the chromaticity circuit and individually power them. Table 6.3 shows location, $\Delta\Psi(s)$, horizontal closed orbit, X_{co} , and vertical closed orbit, Y_{co} , for the four chromaticity sextupoles to be used as feed-down sextupoles. Two will be used at injection and two will be used at low beta. You need 4 power supplies and you have to run cable from each magnet to its power supply. The amount of differential coupling (*i.e.*, the minimum tune split) produced by these magnets at full strength still needs to be calculated. These conclusions need to be re-examined in the context of the new Run II lattice (JJ01 and JJ15C).

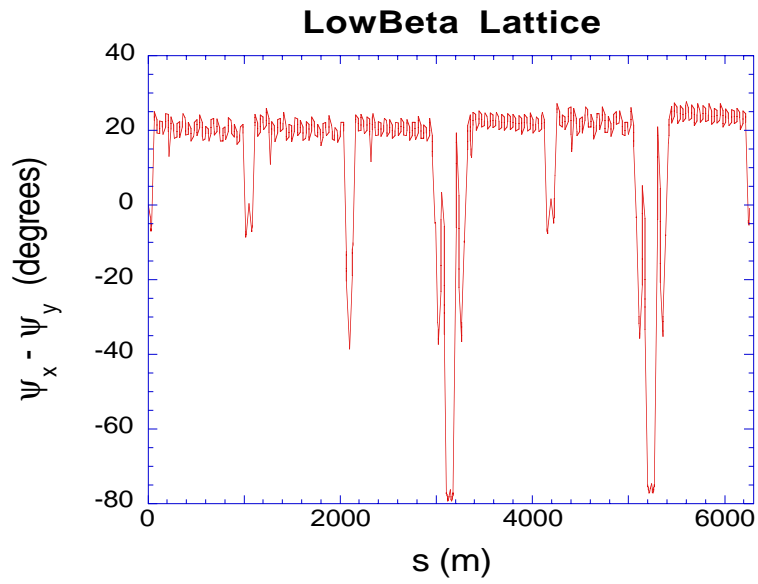


Figure 6.17. Difference between horizontal and vertical phase advance as function of position in the Tevatr

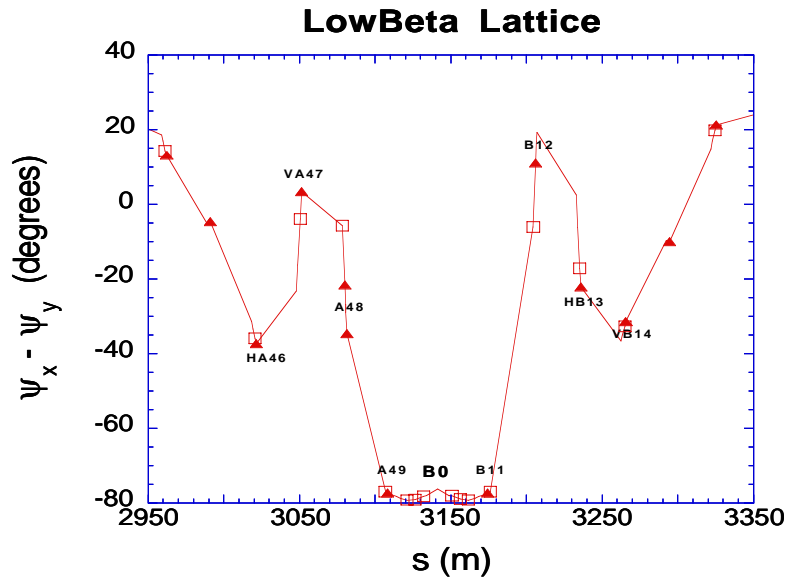


Figure 6.18. Difference between horizontal and vertical phase advance as function of position in the Tevatron at the low beta lattice for the region around the B0 straight section.

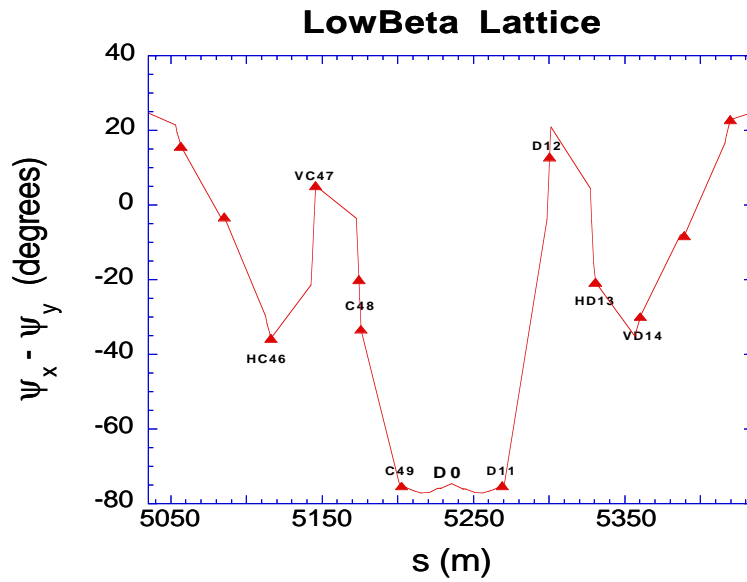


Figure 6.19. Difference between horizontal and vertical phase advance as function of position in the Tevatr

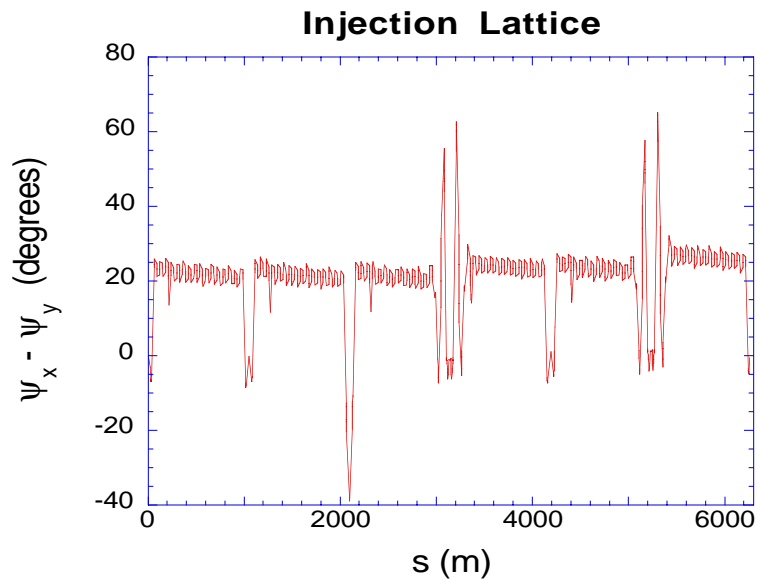


Figure 6.20. Difference between horizontal and vertical phase advance as function of position in the Tevatron at the injection lattice.

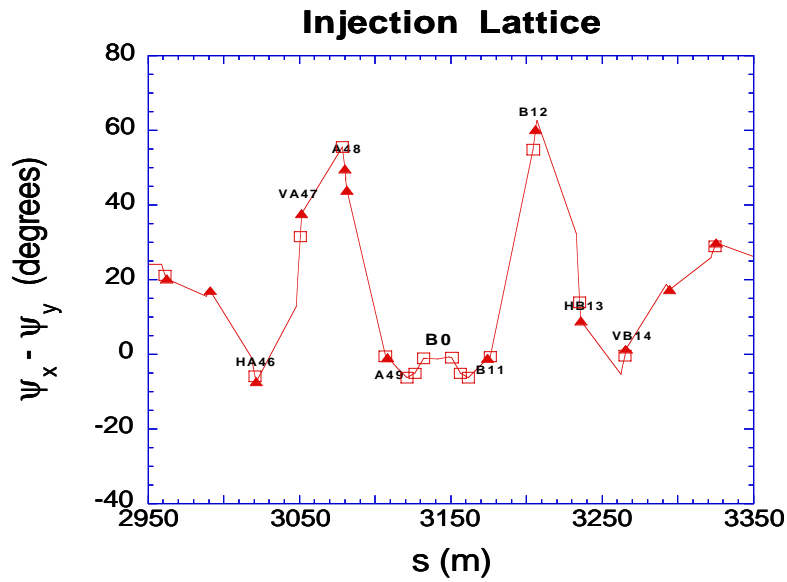


Figure 6.21. Difference between horizontal and vertical phase advance as function of position in the Tevatr

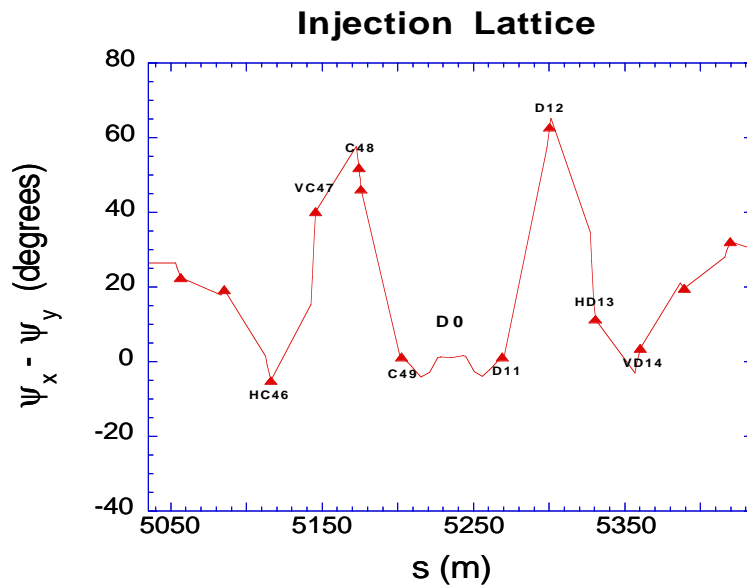


Figure 6.22. Difference between horizontal and vertical phase advance as function of position in the Tevatron at the injection lattice for the region around the D0 straight section.

Table 6.3_ Phase difference, closed orbits, and polarity at locations of the chromaticity sextupoles for the Run Ib lattice.

location (s)	$\Delta\Psi(s)$ degrees	Xco (mm)	Yco (mm)	polarity
Injection Lattice				
HA46	-7.4	5.0	-2.3	
HC46	-5.1	-5.0	2.1	
VA47	37.6	-0.8	-4.8	-1
VC47	40.2	0.7	4.6	+1
there are no chromaticity sextupoles in the 48 or 12 locations				
HA48	42.9	-6.5	-0.6	
HC48	46.2	6.6	0.6	
VB12	60.0	-0.5	-4.1	
VD12	60.0	0.1	4.1	
there are no chromaticity sextupoles in the 48 or 12 locations				
HB13	8.9	-5.0	-0.6	
HD13	11.3	4.4	0.8	
VB14	1.3	-3.0	1.7	
VD14	3.6	2.9	-1.1	
Low Beta Lattice				
HA46	-37.3	-2.1	0.2	
HC46	-35.7	1.7	0.2	
VA47	3.4	-0.6	-0.8	
VC47	5.1	0.5	-0.8	
there are no chromaticity sextupoles in the 48 or 12 locations				
HA48	-34.6	-0.1	-0.4	
HC48	-33.3	0.3	-0.6	
VB12	11.0	0.7	-0.4	
VD12	12.8	0.5	0.3	
there are no chromaticity sextupoles in the 48 or 12 locations				
HB13	-22.0	1.0	-0.9	
HD13	-20.7	0.7	0.7	
VB14	-31.0	-0.4	-2.4	-1
VD14	-30.0	-0.3	2.0	+1

6.6 Injection of 36 proton and antiproton bunches

The injection process will be described for the scenario where 36 proton bunches are injected followed by 36 antiproton bunches. Other schemes—particularly those involving more bunches—have been considered, but will not be presented in this section.

6.6.1 Injection at F0

Injection from the Main Injector into the Tevatron will be at F0. Injection is conceptually identical to the scheme currently used at E0 for beams from the Main Ring. The beam lines, including the Lambertson magnets in the Tevatron, are described in the Main Injector Project Technical Design Report.¹² This section will discuss the injected and circulating orbits in the Tevatron and the injection sequence. The antiproton kicker will be located at E48 (the current antiproton kicker is at D48) and the proton kicker will be located at F17 (the current one is at E17). The main difference with the injection system at F0 is that the Lambertson magnets are shared by the proton and antiproton injection lines and that the bend center of the Lambertson magnets is located towards the F11 end of the long straight section, 13.2 m downstream of F0. As a consequence, the required strength of the antiproton kicker is substantially reduced with the configuration at F0.

The antiproton and proton beam lines will match the respective beam parameters to the Tevatron orbits. The purpose of this section is to describe the kicker requirements and the modifications of the closed orbit in the vicinity of F0. Propagating the proton kick at F17 upstream to F0 gives an orbit distortion at the Lambertson magnet of

$$\begin{bmatrix} x \\ x' \end{bmatrix}_{\text{lambertson}} = \begin{bmatrix} -64 \text{ mm/mrad} \\ -0.06 \end{bmatrix} \theta_{F17\text{kick}}.$$

The angle in the F0 straight section is nearly zero, and the separation of the closed orbit and the injected beam is nearly independent of the position of the Lambertson. A separation of 26 mm is obtained with the current kick angle of 0.4 mrad (at E17). The positions of the injected beam and the circulating beam at the Lambertson magnet are shown in Figure 6.23. The beam size is drawn for a 20π mm-mrad beam that fills 2 eV-sec of the 4 eV-sec bucket (1 MV) at injection. The Lambertson magnet will have at least 0.5" of horizontal motion and the beam may be moved vertically to center the beam on the Lambertson magnet.

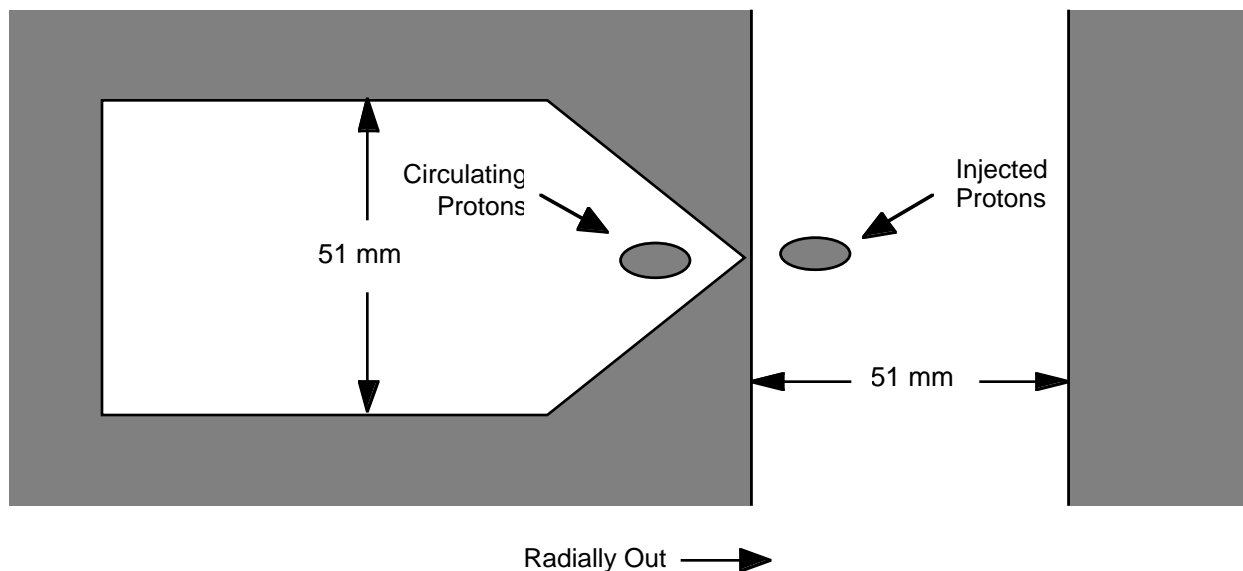


Figure 6.23. Tevatron beam positions and sizes at the injection Lambertson during proton injection.

The kicker at F17 is a bit less than 3/4 of a betatron wave from the Lambertson magnets. The maximum excursion of the injected beam relative to the center of the aperture may be reduced by distorting the closed orbit using the horizontal correction dipoles at F13, F15, and F17. Other bumps may be used to maximize the aperture by optimizing the position and angle of the closed orbit at the Lambertson magnet and the kicker. These bumps are currently implemented at E0 as pulsed orbit corrections (lasting a few seconds). The configurations of trim magnets at E0 and F0 are identical, so it is possible to implement the same type of orbit control by moving the ramped correction control. The upgrade of the correction dipole ramp generators to type 460 control cards (from the older 160 modules) provides the flexibility to perform this function (and more) at F0.

The injection of antiprotons is very similar to the proton injection. The kick at E48 corresponds to a beam displacement at the Lambertson magnet of

$$\begin{bmatrix} x \\ x' \end{bmatrix}_{\text{lambertson}} = \begin{bmatrix} 75 \text{ mm/mrad} \\ 1.2 \end{bmatrix} \theta_{E48\text{kick}}.$$

The antiproton beam has a substantial angle with respect to the closed orbit in the F0 straight section. For a given kick angle, the separation of the injected beam and the closed orbit at the Lambertson magnets (in the downstream portion of F0) is almost a factor of 2 greater than in the current system, where the Lambertson magnets are placed at the upstream end of E0. In order to avoid the deleterious effects of unwanted beam-beam collisions, the antiprotons are injected with the antiproton and proton orbits separated by the electrostatic separators. The circulating beam must be contained in the notch region of the Lambertson magnet (see Figure 6.). The antiproton beam must be injected fairly close to the point in the Lambertson magnet notch, so the proton beam must be separated radially inward by an amount that is at least as much as the vertical separation. For injection at E0, this requirement is met by using the horizontal separators at B11 and B17 and the vertical separator at C17. For injection at F0, an acceptable solution is obtained by using only

the separators at B17 and C17. The polarity of the B17 separator is reversed relative to the polarity used in Run I. The beam profiles at the injection Lambertson magnet at F0 are shown in Figure 6., where the antiproton kick angle is 0.4 mrad and the beam size is determined by a 15π mm-mrad transverse emittance and a 2 eV-sec longitudinal emittance with 1 MV of rf.

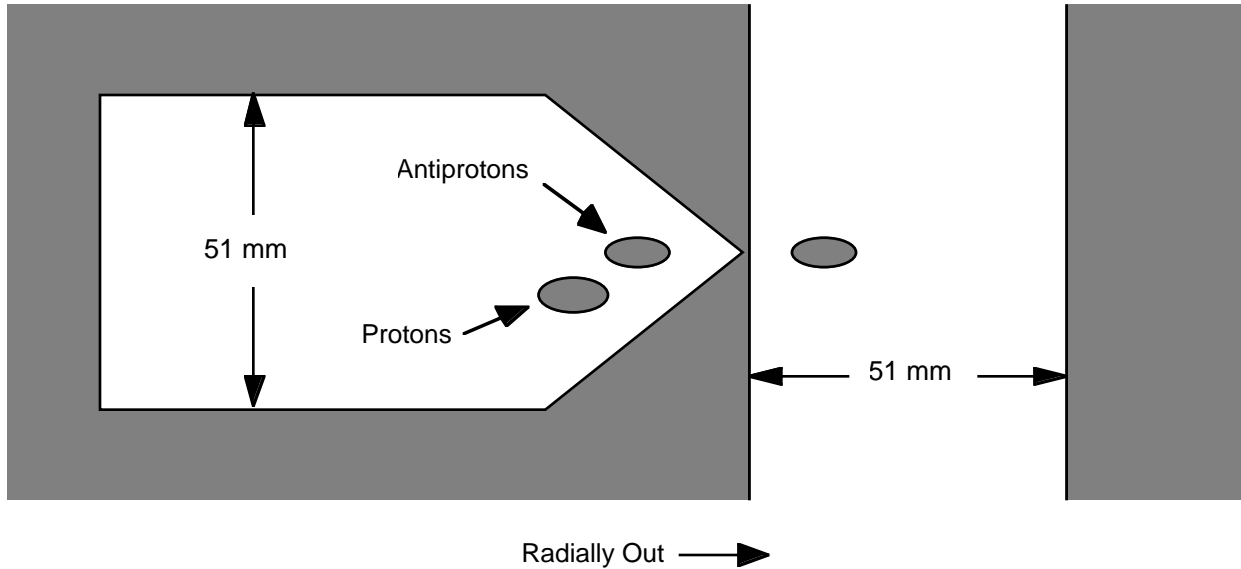


Figure 6.24. Tevatron beam positions and sizes at the injection Lambertson magnet during antiproton injection.

6.6.2 Injection Sequence

With the 6 bunch operation in Run I, a nearly uniform bunch spacing of about 3.5 μ sec is obtained. The requirements on the injection and abort kickers become significantly more stringent for 36 bunch operation. The beam configuration and injection scheme is illustrated in Figure 6.. The standard 36 \times 36 filling scheme consist of pattern of 12 bunches spaced by 21 rf buckets (395 nsec). Each bunch train is followed by a 139-bucket (2618 nsec) abort gap. The spacing of the antiproton bunch ensemble is the mirror image of the proton spacing.

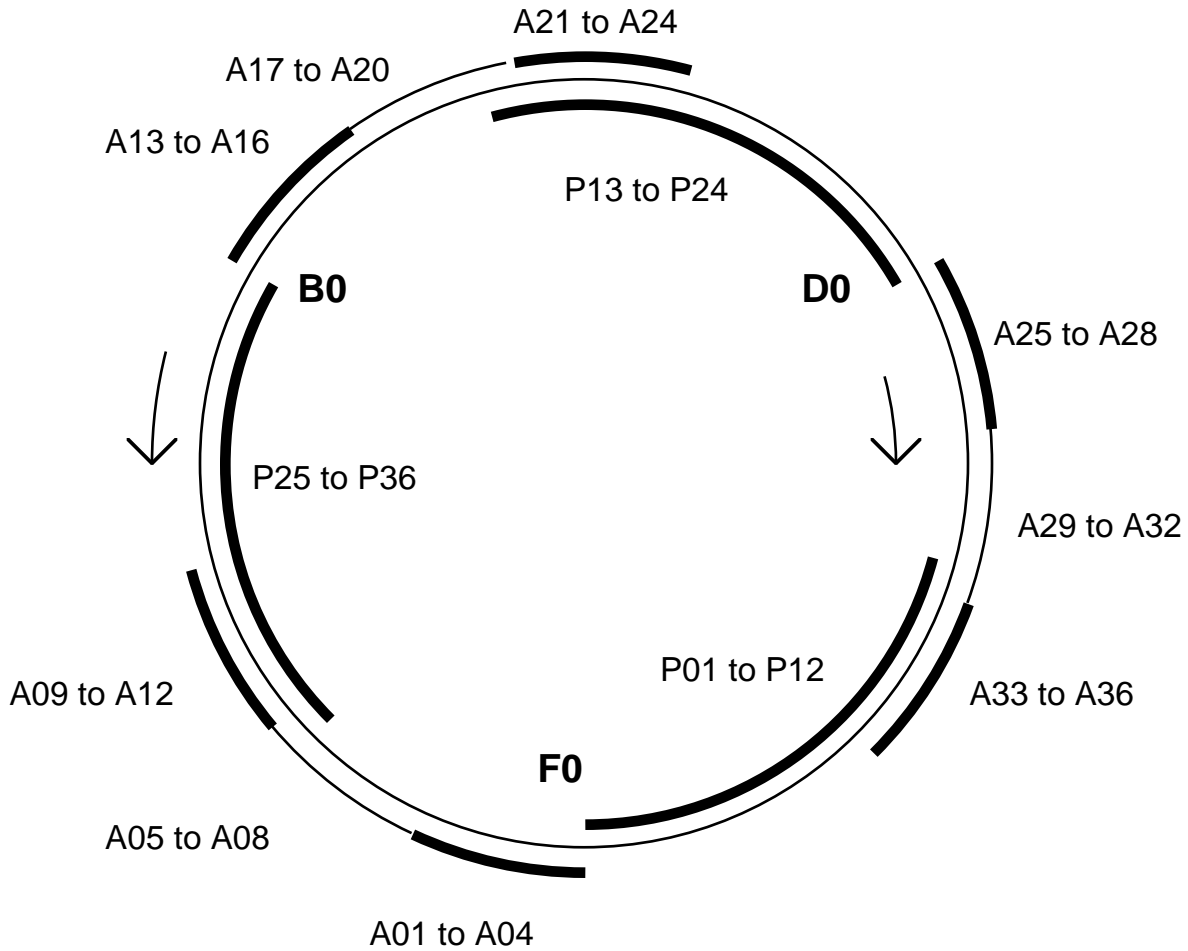


Figure 6.25. Beam spacing and injection configuration. The proton and antiproton bunches are labeled P01, P02, ... and A01, A02, ... starting from the upstream end of the bunch train so that A01 and P01 collide at F0.

The injection scheme is to inject in order P01, P02, *etc.* This scheme requires a fast (396 nsec) kicker rise time but tolerates a decay time of more than 2 μ sec. With the short batch kicker it will be possible to inject one to four bunches simultaneously. The number chosen will depend on the efficiency of multi-batch proton coalescing in the Main Injector.

The antiprotons must be injected during the time that the proton beam abort gap passes through the kicker. The only way this condition can be achieved is by rotating (or cogging) the antiproton distribution relative to the proton distribution for the injection of the various batches of antiprotons. Because there are 3 abort gaps in the proton beam, it is possible to inject 3 groups of antiprotons for each value of cogging. A likely sequence for the injection of the antiprotons would be A01-A04, A13-A16, A25-A28, A05-A08, A17-A20, A29-A32, A09-A12, A21-A24, and A33-A36. The antiprotons will be cogged by 84 buckets after the injection of A25-A28 and again after the injection of A29-A32. Prior to acceleration the antiprotons will probably be rotated to the nominal collision point cogging. The kicker rise and fall times are dictated by the need to inject bunches without disturbing those previously injected are discussed in section 6.6.3.

In order to abort both the proton and antiproton beams without losses, it is necessary for the abort gaps in both beams to be present simultaneously at A0. This condition occurs only for a

cogging offset of 0, so it will not be possible to abort the antiprotons cleanly during the injection process.

6.6.3 Tevatron Injection Kickers

This section describes the injection kickers in the Tevatron and their evolution as we prepare for the new injection lines at F0, the 1999 Fixed Target Run, Collider Run II operations with 36×36 operations (396 nsec bunch spacing), and eventually 132 nsec bunch spacing. The evolution of the kickers falls into three stages.

6.6.3.1 Stage 1- Main Injector shutdown and 1999 Fixed Target operations.

During the Main Injector Shutdown the present proton injection kickers will be moved to a new location to support injection from the Main Injector. The proton injection kicker magnets will be moved from E17 to F17 and the kicker pulsers and controls will be moved from the E17 kicker building to the F17 kicker building. For the 1999 Fixed Target run the protons will be injected using two Main Injector cycles with a group of 5 Booster batches on each cycle (84 bunches per Booster batch.) The pulse forming network (PFN) of the existing proton injection system will be modified to give a flat-top time 7.90 μ sec long, which is the length of 5 consecutive Booster batches. Since the proton injection kickers have a rise time of 2.07 μ sec and a fall time of 2.94 μ sec the kickers are just barely fast enough to inject the two groups of 5 Booster batches in the 20.94 μ sec revolution time. If the rise and fall times turn out to be longer than expected then some further modification of the kicker may be required. Another possibility would be to reduce the number of bunches that are injected leaving more time for the rise and fall of the kicker pulse.

The antiproton injection kickers are not used during the fixed target run and are not installed in the Tevatron since they are an aperture limitation during resonant extraction.

6.6.3.2 Stage 2 - Early Run II and 36×36 bunch operations.

Just before the start of Run II commissioning, during the fixed target to collider changeover, the proton injection kickers will be removed from F17 and replaced with a new set of short batch proton injection kickers capable of injecting protons with 396 nsec bunch spacing. The design of the short batch proton injection kicker is described in section 6.6.4. The kickers are being designed for 396 nsec bunch spacing with the option of going to 132 nsec bunch spacing with further upgrades to the kicker pulsers. These new proton injection kickers will also be used for the extraction of antiprotons from the Tevatron after deceleration.

The antiproton injection kicker magnets presently at D48 will be installed at E48 and the antiproton kicker pulsers and controls will be moved to the F0 south kicker room. The two antiproton injection magnets that are located at D48 were designed for 396 nsec bunch spacing and were tested during 36×36 studies in the Fall of 1995. The studies revealed that the fall time of the kickers was too long and as a result the protons already in the machine were kicked causing emittance blowup. The solution to this problem is to use one of the antiproton injection kickers as a bumper magnet. This is possible since a single magnet at E48 provides enough kick for injection from the Main Injector. The second magnet will be used for the bumper magnet, which will be capable of providing a small kick with adjustable magnitude on a bunch, by bunch basis. This can be used to compensate for the ringing of the antiproton kicker. This magnet is described in section 6.6.5.

The installation of the short batch injection kickers and the relocation of the antiproton injection kickers will take at least 6 weeks and could determine the length of the fixed target to collider changeover.

6.6.3.3 Stage 3 - Later Run II (132 nsec bunch spacing.)

When it becomes desirable to operate the Tevatron with 132 nsec bunch spacing the short batch proton injection kickers can be reconfigured from 396 nsec to 132 nsec mode by adding additional pulsers to the magnets. The short batch proton injection kickers consist of 5 magnets, which are connected, in series for 396 nsec operations. To shorten the rise time each of the 5 magnets will be powered individually thereby reducing the rise time.

To achieve 132 nsec bunch spacing for the antiprotons it will be necessary to rebuild the antiproton injection magnets since they are not capable of supporting 132 nsec bunch spacing without leaving gaps in the antiproton beam for the kicker rise time. Another possibility is to use the existing antiproton kickers and live with injection gaps in the antiproton bunch structure.

6.6.4 Short Batch Proton Injection Kicker

Several new kicker systems are required to achieve a 132 nsec bunch spacing in the Tevatron. As a first step, a new proton injection kicker is required for 36×36 injection. If new magnets are installed that also meet the 132 nsec bunch spacing, then it is possible to install the new magnet and initial pulse power supplies for 36×36 and then increase the number of pulse power supplies when 132 nsec bunch spacing is required. At that time, an entire new antiproton injection kicker system would also be required. For this analysis, the abort gap is assumed to remain at the present value of 2.6 μs.

The specifications for the new Tevatron proton injection kicker and antiproton injection kickers are shown in Table 6.4 and Table 6.5:

Table 6.4. Specifications for Tevatron Proton Injection Kicker

	Fixed Target	36×36	132 nsec
Nominal Kick Angle	.381 mrad	.381 mrad	.381 mrad
Nominal Charge Voltage	49 kV	49 kV	49 kV
Field Rise Time	1.26 μsec	.376 μsec	.113 μsec
Flattop	8.05 μsec	1.21 μsec	1.21 μsec
Field Fall Time	3.6 μsec	2.611 μsec	2.347 μsec
Field Flatness	±1%	±1%	±1%
Maximum Charge Voltage	66 kV	66 kV	66 kV

Table 6.5. Specifications for Tevatron Antiproton Injection Kicker

	Fixed Target	36×36	132 nsec
Nominal Kick Angle	.NA	.350 mrad	.350 mrad
Nominal Charge Voltage	NA	49 kV	49 kV
Field Rise Time	NA	.376 μsec	.113 μsec
Flattop	NA	1.21 μsec	1.21 μsec
Field Fall Time	NA	1.05 μsec	1.05 μsec

Field Flatness	NA	±1%	±1%
Maximum Charge Voltage	NA	66 kV	66 kV

Two important items not listed in the above tables are beam line space and aperture. There will be two locations where they will be installed: F17 (and F17 service building) for proton injection and E48 (and F0 south kicker room) for antiproton injection. At F17 there is a total of 458 inches. Everything presently at F17 can be removed (there is a collimator and three beam detectors) with the possible exception of the separator in which case we would have 330 inches. At E48 there are 226.5 inches available, vacuum flange to flange, including a 37 inch long resistive wall monitor used by the sampled bunch display. We will also need at least 16" of beam line space for two ion pumps.

The aperture should be as large as possible to avoid scraping beam yet be as small as possible to reduce the magnet field fill time. To calculate the aperture requirements we can assume the following for the horizontal plane:

$$\beta = 100 \text{ m at F17, } \beta = 100 \text{ m at E48}$$

$$\text{Dispersion} = 5.6 \text{ m at F17, Dispersion} = 1.8 \text{ m at E48}$$

$$\text{Momentum spread } \sigma_p/p = 0.4 \cdot 10^{-3} \text{ (corresponding to 2 eV-sec, 1.0 MV, 150 GeV beam)}$$

The momentum spread could be as much as two times larger if Tevatron superconducting rf is used. The beam width is given by $\sigma^2 = \epsilon\beta/6(\beta\gamma) + D^2 (\sigma_p/p)^2$. For a 95% normalized emittance of 40π mm-mrad we find $\sigma = 3.03$ mm at F17 and 2.17 mm at E48. The injection helix moves the protons to the outside by 1 mm and up by 3 mm at F17 and 8 mm outside and 3 mm up at E48. Assuming that the entire beam is contained within 6σ and that both protons and antiprotons have the same size, the contributions from each source to the aperture are shown in Table 6.6.

Table 6.6. Kicker Horizontal Aperture Requirements at Injection

Kicker Horizontal Aperture	F17 (mm)	E48 (mm)
$2 \times 6\sigma$ (σ =rms beam size)	36.4	26
Total Separation	3	16
Injection Oscillations	4	4
Beam Tube Straightness	2	2
Alignment Errors	2	2
Total Beam Aperture	50	50
Beam Tube Thickness	8	8
Inductance Tuning Range	8	8
HV Clearance	4	4
Total Magnetic Aperture	70	70

In the vertical plane $\beta \cong 70$ m, and, for a 40π mm-mrad beam, $\sigma = 1.7$ mm. The vertical aperture requirements are shown in Table 6.7. This proposed vertical aperture of 34 mm is substantially smaller than the current kicker vertical aperture of 50 mm.

Table 6.7. Kicker Vertical Aperture Requirements at Injection

Kicker Vertical Aperture	F17 (mm)	E48 (mm)
$2 \times 6\sigma$ (σ =rms beam size)	20	20
Total Separation	6	6
Injection Oscillations	4	4
Beam Tube Straightness	2	2
Alignment Errors	2	2
Total Beam Aperture	34	34
Beam Tube Thickness	8	8
HV Clearance	4	4
Total Magnetic Aperture	44	44

Our preliminary design is based on the apertures shown above, namely 70 mm (H) by 40 mm (V). Several other kicker parameters were studied: the number of magnets, the impedance and the type of magnet were all examined. The arrangement that comes closest to meeting the requirements is a system with 5 magnets. Each magnet is driven differentially by both a positive and negative pulsed power supplies. Each supply is 12.5 Ω and drives a 12.5 Ω magnet. This is the same type of magnet as used in the recent Tevatron antiproton injection kicker upgrade, but twice the impedance and less than half the length. The horizontal aperture was increased by 8 mm to allow for inductive tuning by movement of the high voltage buses. This is a different technique from D-48 where the capacitors had to be adjusted. Some of the design parameters are given in Table 6.8.

Table 6.8. Comparison of Apertures for D-48 and Short Batch Kickers

	D48 Kicker	New Kicker	Units
Bus Spacing	70	70	mm
Magnetic length	2.38	0.84	m
Ferrite gap	57	40	mm
Inductance/magnet	1.78	0.93	μ H
Number of sections	67	36	

To increase confidence in our analytic calculations, a SPICE model was used for both the existing D-48 antiproton injection kicker and the new short batch kicker. A SPICE simulation of the D48 kicker gives a field fill time of approximately 350 nsec in comparison to the actual beam measurements that yield approximately 370 nsec. This gives us some confidence in the model used.

If the magnet is divided into 36 sections, then each section will have a length of 23 mm, allowing for a ferrite length of 17 mm and a capacitor length of 6 mm. The inductance per section $960 \text{ nH}/36 = 26.5 \text{ nH}$ and the capacitance per section would be 170 pF. The PFL charge voltage would be 40 kV. The SPICE simulation of the magnet and pulser gives a field rise time of order 150 nsec. This is close to the requirements, but further work on the pulser and magnet must be done to get any definitive answers and to determine the best way to trim 40 nsec from the rise-time.

One challenge for the magnet is to purchase the proper capacitors. The required capacitance is sufficiently low that single lumped capacitors could provide enough capacitance, but probably

would have excessive parasitic inductance. One alternative is to build the capacitor into the potting of the magnet, but this entails high precision assembly (± 0.002 " tolerance) and hand tuning of the magnet before potting. One could also try again the printed circuit board capacitors that were developed for the Tevatron antiproton injection magnet. They were expensive and have lifetime problems to be solved, but have very low parasitic inductance. Finally, one could try another capacitor manufacturer for the lumped capacitors. Then one could make a custom value of 85 pF with the strontium titanate dielectric so that the inductance could be reduced by using two in parallel.

The pulser required initially could be modified from the new MI proton injection pulsers. They have a 25 nsec rise time to 95% of full current and 55 nsec to 98% of full current into a 25 ohm system. If we use them in a 12.5 ohm system, the rise time to 95% of full current will double to approximately 110 nsec. This will meet the requirements for 36x36. The pulser rise time will need to be substantially reduced to meet the 140x121 requirements. To reduce the rise time by 5 - 10 nsec we can perhaps use pulse sharpening techniques. Reducing the rise time further will require a substantial prototyping effort. Another possibility to reduce pulser constraints is to build on the bumper magnet idea (see section 6.6.5).

Since there are 3 possible modes of operation: fixed target, 36x36 and 140x121 there are 3 different configurations we can set up. In fixed target mode, the antiproton kickers are not needed and are removed from the beam line. The proton kickers can each be connected together as shown in Figure 6.26. The pulsers are PFNs with a thyatron switch much the same as the Main Injector antiproton injection/proton extraction kicker system. The system is 12.5 ohms per magnet half; each magnet has 8 RG-220 cables coming in and 8 cables going out.

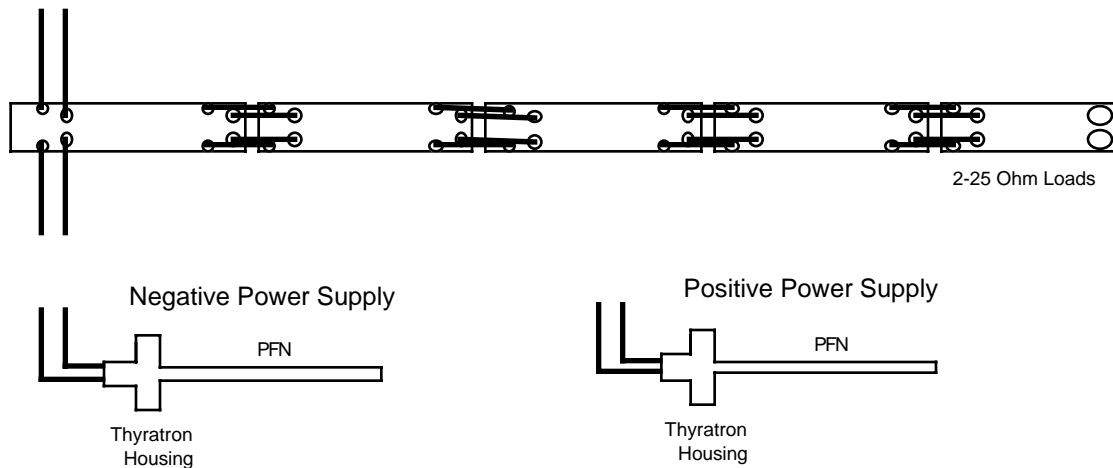


Figure 6.26. Pulser and Magnet Configuration for Fixed Target

For 36x36 operation, the system could be configured as shown in Figure 6.27. A field rise time of 376 nsec is required for 36x36 operation. Since each magnet has a voltage fill time of 80 nsec and a modified MI proton injection pulser has a voltage rise time of 110 nsec, up to 3 magnets can be connected in series and meet the requirements. There are 16 x 50 Ohm PFLs, 4 thyatron pulsers and 4 charging systems. In addition there are 16 cable runs to the tunnel. Using the MI pulser gives some time for pulser improvements to meet the 140x121 requirements.

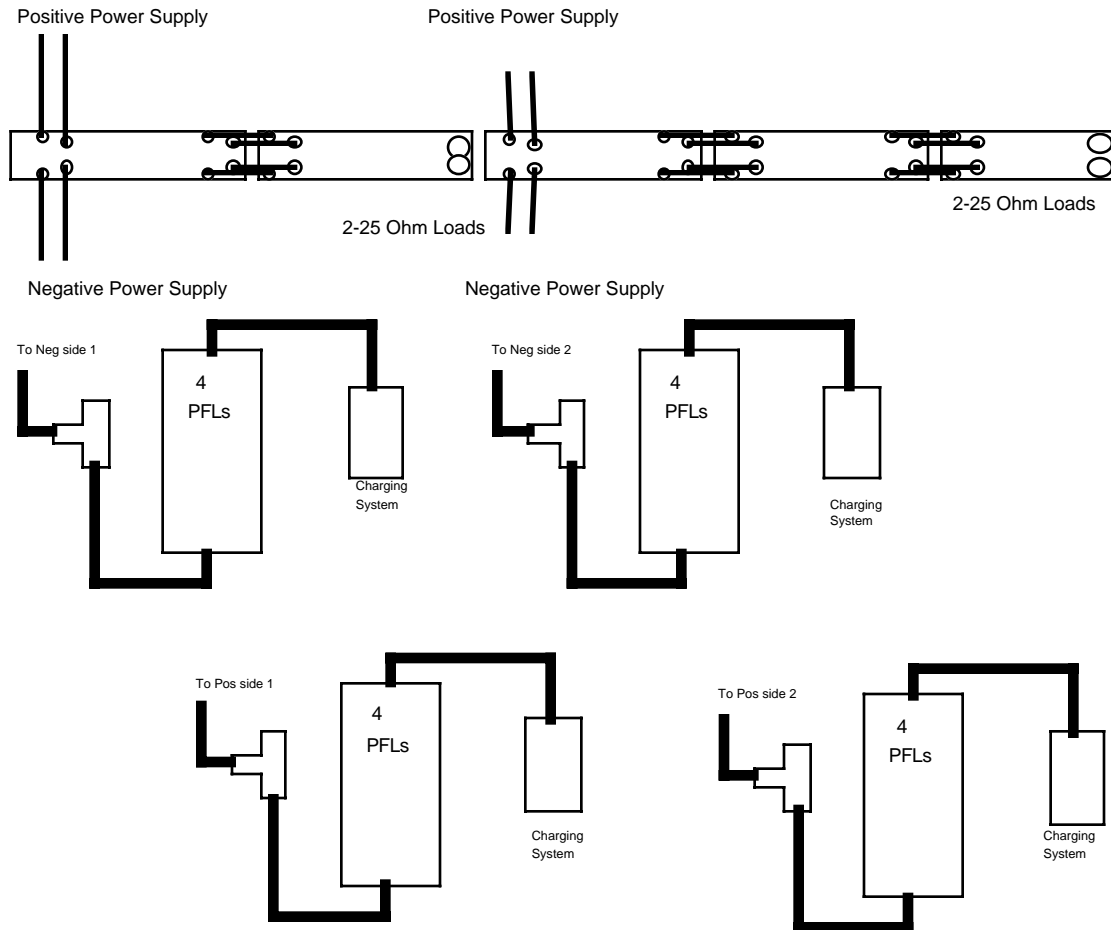


Figure 6.27. Pulser and Magnet Configuration for 36x36

The configuration for 140x121 has a 132 nsec bunch spacing so a rise time of 113 nsec is required. In this case each side of each magnet is powered by a separate pulser as shown in Figure 6.28. This case would require the new improved pulsers. In this configuration there are a total of 10 pulsers and 40 PFLs.

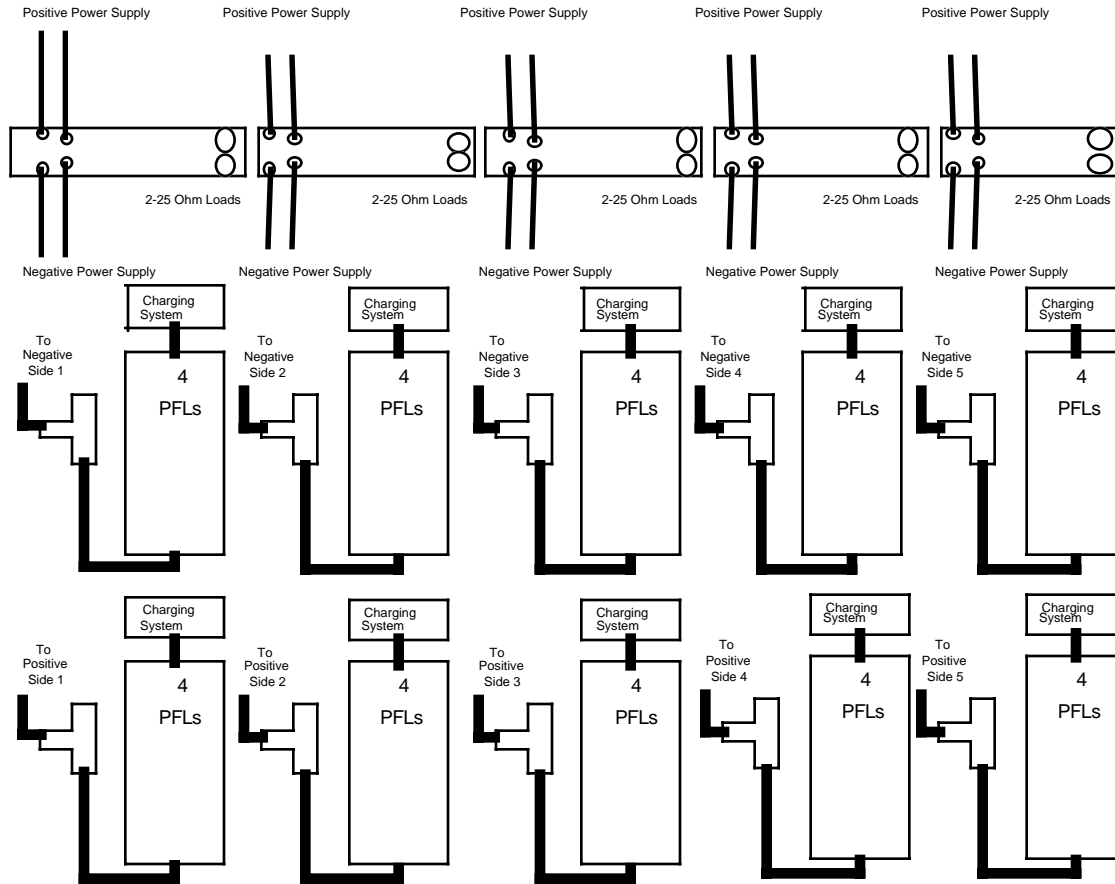


Figure 6.28. Pulser and Magnet Configuration for 140×121

6.6.5 Injection Bumper Magnet

The antiproton injection kicker to be used in Run II has been built, was installed in the Tevatron, and tested during the fall 1995 36×36 studies period. This kicker system was designed for the 396 nsec bunch spacing in Run II and will be moved from D48 to E48 for the start of Run II. In the fall studies while injecting the antiprotons it was noticed that the emittances of the protons were being blown up by the falling edge of the antiproton injection kicker. It was also noticed some of the bunches in the middle of the proton bunch train were also being blown up possibly due to the kicker ringing. Figure 6.29 below shows the difference in proton vertical emittance before and after the all the antiproton bunches had been injected. The blowup of the first two bunches in the proton batch is obvious and there is also evidence that the emittance of the sixth and seventh bunches in the proton batch is also being blown up by the antiproton kicker. A closer look at the emittances during the antiproton injection process confirms that it is the kicker that is causing the emittance blowup rather than some azimuthal position dependence on the emittance growth rate.

Emittance blowup during pbar injections for 36x36 store 5762.

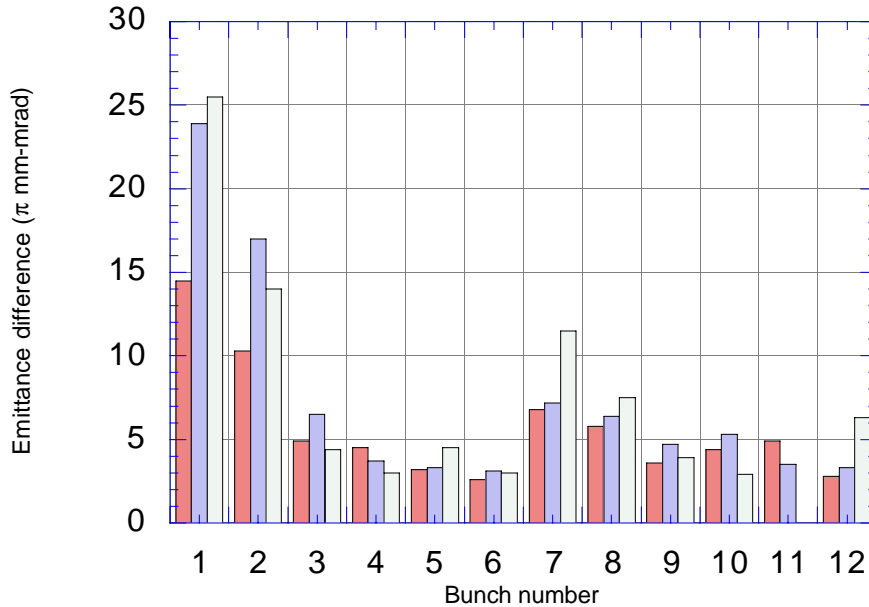


Figure 6.29. Emittance blowup of protons as a result of being kicked by the falling edge of the antiproton injection kicker. The plot shows difference between the emittance of the proton bunches (in groups of 12) before and after the antiproton injection sequence

It is difficult to reduce the fall time of the kicker system since it is limited by attenuation in the pulser cable. A solution to this problem in Run II is to build a bumper magnet system using one of the antiproton injection kicker magnets. When the kicker magnets are moved from D48 to E48 only one kicker magnet will be needed for injection into the Tevatron. This leaves the second magnet available as part of a bumper magnet system. This system will be able to provide a small kick with the amplitude programmable on a bunch by bunch basis. The magnitude of the kick will be about 3% of the main injection magnet and will be controlled by modulating the pulse width with high speed FET switches. Work is in progress on the design of such a system.

Energy of 1 TeV

6.7 Collective Effects and Damper Requirements

6.7.1 Coupling Impedances

6.7.1.1 Resistive Wall

The Tevatron beam pipe is square in cross section with sides $h=6.0$ cm and rounded corners. The longitudinal and transverse impedances of the Tevatron due to wall resistivity at frequency $\omega/(2\pi)$ are¹³

$$Z_{\parallel} = [1 + j \operatorname{sgn}(\omega)] \frac{\rho C}{\pi \delta h}$$

Equation 6.2

$$Z_{\perp} = [1 + j \operatorname{sgn}(\omega)] \frac{8c\rho C}{\pi\omega\delta h^3}$$

Equation 6.3

where $\rho=7.4\times 10^{-7} \Omega\text{-m}$ is the resistivity of the stainless steel wall and

$$\delta = \sqrt{\frac{2\rho}{|\omega|\mu_0\mu_r}} = \sqrt{\frac{2\rho c}{|\omega|Z_0}}$$

Equation 6.4

is the skin depth. In the above, μ_0 and $Z_0\approx 377 \Omega$ are, respectively, the magnetic permeability and impedance of free space, and the relative magnetic permeability of the beam-pipe wall has been taken as $\mu_r\approx 1$. Note that we have been writing the formulas for impedances in such a way that they are valid for both positive and negative frequencies. This is important, especially because it is the real parts of Z_{\parallel} and Z_{\perp} at negative frequencies that drive almost all the collective instabilities.

Putting in the ring circumference $C=2\pi R$ with $R=1$ km, we obtain

$$\frac{Z_{\parallel}}{n} = [\operatorname{sgn}(\omega) + j] 12.45 |n|^{-1/2} \Omega$$

Equation 6.5

$$Z_{\perp} = [\operatorname{sgn}(\omega) + j] 27.66 |n + \nu_{\beta}|^{-1/2} \text{ M}\Omega/\text{m}$$

Equation 6.6

where ν_{β} is the betatron tune.

For high frequencies, a more accurate expression for the resistive-wall impedances is¹⁴

$$Z_m^{\parallel} = \frac{\omega}{c} Z_m^{\perp} = \frac{Z_0 C c}{\pi} \left(\frac{2}{h}\right)^{2m} \left\{ [1 - \operatorname{sgn}(\omega)j] (1 + \delta_{m0}) \frac{hc}{2} \sqrt{\frac{Z_0 c}{2\rho|\omega|} - \frac{jh^2\omega}{4(m+1)} - \frac{jmc^2}{\omega}} \right\}^{-1}$$

Equation 6.7

What we have discussed so far are the lowest azimuthals m ; therefore the longitudinal impedance Z_{\parallel} corresponds to Z_0^{\parallel} in Equation 6.7 and Z_{\perp} corresponds to Z_1^{\perp} . We see that the resistive-wall impedances will follow Equation 6.5 and Equation 6.6 for all practical frequencies, because they will roll off only at very high frequencies when

$$f \gtrsim \frac{c}{2\pi} \left(\frac{2Z_0}{\rho h^2}\right)^{1/3} = 313 \text{ GHz}$$

Equation 6.8

6.7.1.2 Lambertson Magnets

The main concern of the Lambertson magnets is the low-frequency component created by the exposure of the beam to the bare laminations of the magnets. A rough estimation of the Lambertson magnets is made by approximating the magnet as a series of annular laminations of 0.953 mm thick separated by cracks of width Δ that are 3% of the lamination thickness. The inner radius is chosen to be $b = 3.0$ cm and the outer radius $d = 8.0$ cm. The low-frequency image current traveling through the magnet is assumed to flow in one lamination from the inner radius to the outer radius then cross over to the next lamination and flow from the outer radius to the inner radius. Even though we are concerned about the low-frequency impedance, due to the high relative magnetic permeability of the lamination, the skin depth for the frequencies we are considering is still less than the lamination thickness so that the current is constrained to one skin depth in the laminations. In this way the total resistance of the magnet is found by adding up the resistance along the entire current path.

For the current traveling from the inner radius to the outer radius the net impedance is found to be

$$Z_{\parallel} = [1 + j \operatorname{sgn}(\omega)] \frac{\rho_{\ell}}{\pi \delta_{\ell}} \ln \frac{d}{b}$$

Equation 6.9

where ρ_{ℓ} is the resistivity of the laminations and δ_{ℓ} is the skin depth. For the current traveling along the inner tip of the laminations the resistance per unit length is

$$Z_{\parallel} = [1 + j \operatorname{sgn}(\omega)] \frac{\rho_{\ell}}{2\pi b \delta_{\ell}}$$

Equation 6.10

There are four 110.25-inch Lambertson magnets, or 11.20 m in total. We use a resistivity of $\rho_{\ell} \approx 2 \times 10^{-7} \Omega\text{-m}$ and a relative permeability of $\mu_r \approx 100$ for the lamination material. The total low frequency resistive wall impedance around the laminations is calculated to be

$$\frac{Z_{\parallel}}{n} = [\operatorname{sgn}(\omega) + j] \frac{7.237}{\sqrt{n}} \Omega$$

Equation 6.11

To estimate the transverse impedance we use the approximate relation

$$Z_{\perp} = \frac{2c}{b^2} \frac{Z_{\parallel}}{\omega}$$

Equation 6.12

and arrive at

$$Z_{\perp} = [\operatorname{sgn}(\omega) + j] 16.08 |n + \nu_{\beta}|^{-1/2} \text{ M}\Omega/\text{m}$$

Equation 6.13

It should be noted that the Lambertson magnets were assumed to have a circular geometry with inner radius of $b=3.0$ cm. The actual shape of the Lambertson is much different so this estimate can only be approximate. Using a slightly larger inner radius can change the impedance by a significant amount; for example, if b is 10% larger the transverse impedance will drop by ~25%.

Therefore, at low frequencies, the *total* impedances due to the stainless steel beam pipe and the Lambertson magnets add up to

$$\frac{Z_{\parallel}}{n} = [\text{sgn}(\omega) + j] 19.680 |n|^{-1/2} \Omega$$

Equation 6.14

$$Z_{\perp} = [\text{sgn}(\omega) + j] 43.74 |n + \nu_{\beta}|^{-1/2} \text{ M}\Omega/\text{m}$$

Equation 6.15

At higher frequencies, the cracks between the laminations of the Lambertsons behave like radial transmission lines. We assume that the medium in the cracks of width $\Delta \approx 28.6 \mu\text{m}$ has a dielectric constant $\epsilon_c \approx 6$, a relative magnetic permeability of $\mu_c \approx 1$, and a high resistivity of $\rho_c \approx 100 \Omega\text{-m}$. At radius r inside the crack, the series impedance per unit radial length is

$$Z = \frac{j\omega Z_0 \mu_c}{c} \frac{\Delta}{2\pi r} + [1 + \text{sgn}(\omega)j] \frac{2\rho_c}{2\pi r \delta_c}$$

Equation 6.16

where the first term is the inductive contribution of the crack medium and the second term the resistivity of the lamination walls depicted in Equation 6.9. The shunt admittance per unit length is

$$Y = \left(\frac{j\omega\epsilon_c}{Z_0 c} + \frac{1}{\rho_m} \right) \frac{2\pi r}{\Delta}$$

Equation 6.17

which represents the capacitance and shunt resistance of the crack. The wave number of the transmission line is

$$\beta_c = \sqrt{-ZY}$$

Equation 6.18

which is r independent. The characteristic impedance is

$$Z_c = \sqrt{Z/Y}$$

Equation 6.19

which is a monotonically decreasing function of frequency. The longitudinal impedance seen by the beam is therefore

$$Z_{\parallel} = Z_c \tan(\beta_c d_c)$$

Equation 6.20

where $d_c = d - b = 5 \text{ cm}$ is the depth of the crack or transmission line. Note that Equation 6.20 reproduces the low-frequency impedance of Equation 6.9.

To study the resonances, first let us neglect the resistivity of the crack medium and also the lamination walls. Then the wave number in Equation 6.18 simplifies to $\beta_c = \sqrt{\epsilon_c \mu_c} \omega/c$. From Equation 6.20, the n th resonance occurs at the frequency

$$f_n = (2n - 1) \frac{c}{4d_c \sqrt{\epsilon_c \mu_c}}$$

Equation 6.21

or 0.612, 1.835, 3.060, ... GHz for the first few. From Equation 6.16, it is evident that the addition of the wall inductance is equivalent to replacing the permeability of the crack medium by

$$\mu_c \rightarrow \mu_c \left(1 + \frac{1}{\mu_c \Delta} \sqrt{\frac{\rho_l \mu_l c}{Z_0 |\omega|}} \right)$$

Equation 6.22

which is now frequency dependent. Substituting into Equation 6.21, we find that the wall inductance reduces the resonance frequencies to 0.250, 0.979, 1.813, ... GHz. When the real part of the wall resistivity is included, these resonances are highly damped and the resonant frequencies further reduced. The numerical computations of the longitudinal and transverse impedances for the Lambertson magnets are plotted in Figure 6.30 up to 1 GHz. The transverse impedance Z_{\perp} is estimated from the longitudinal Z_{\parallel}/n using the relation Equation 6.12. Therefore, they just differ by a constant and are plotted as the same curves but different scales in the figure. Notice that the resonances are so much damped that only the first one survives and has its frequency shifted to ~ 0.195 GHz. The small conductivity of the cracks plays a negligible role because it is very much less than the lamination conductivity. It is worthy to point out that the higher-order resonances do not show up because both Z_{\parallel}/n and the characteristic impedance Z_c decrease with frequency. We also see from Figure 6.30 that the impedances Z_{\parallel}/n and Z_{\perp} have the $n^{-1/2}$ low-frequency behavior of Equation 6.11 and Equation 6.13, which are also plotted in the figure as reference. They start to deviate from this behavior only near the first damped resonance. Actually, apart from this damped resonance, the impedances do not deviate too much from the $n^{-1/2}$ behavior even at higher frequencies.

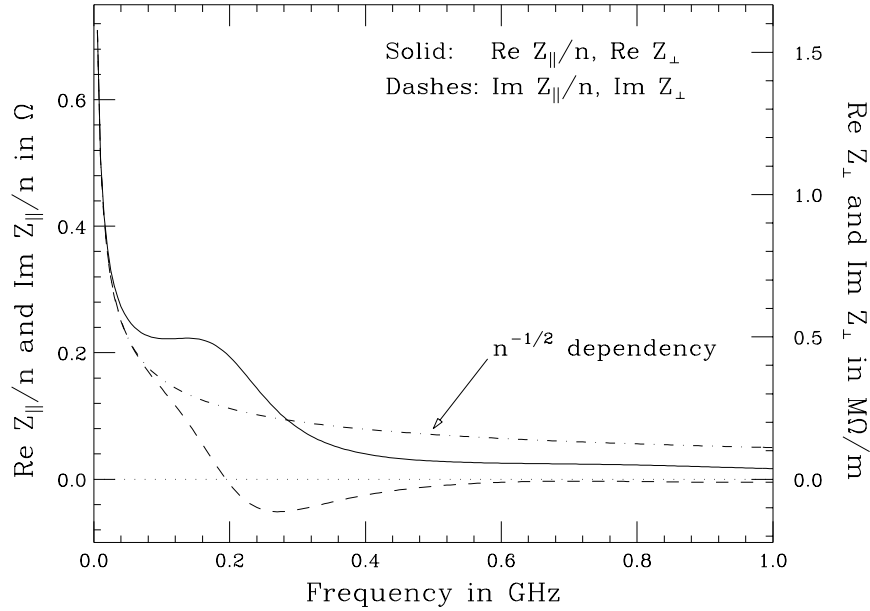


Figure 6.30. The real and imaginary parts of Z_{\parallel}/n and Z_{\perp} as functions of frequency for the Tevatron Lambertson magnets. Note that Z_{\parallel}/n and Z_{\perp} are drawn as the same curves but at different scales.

6.7.1.3 Beam-position Monitors

There are $M=216$ sets of beam position monitors (BPM's) in the Tevatron; half of them detect horizontally and half vertically. Each BPM consists of 2 cylindrical strip-lines of radius $b=3.5$ cm, each subtending an angle $\phi_0=110^\circ$ at the center of the beam pipe and is of length $\ell=18$ cm. Each strip-line is terminated at both ends and forms a transmission line of characteristic impedance $Z_c=50 \Omega$ with the beam pipe wall that bulges out. The longitudinal and transverse coupling impedances have been calculated to be¹⁵

$$Z_{\parallel} = 2MZ_c \left(\frac{\phi_0}{2\pi} \right)^2 \left(\sin^2 \frac{\omega\ell}{c} + j \sin \frac{\omega\ell}{c} \cos \frac{\omega\ell}{c} \right)$$

Equation 6.23

$$Z_{\perp} = \frac{c}{2b^2} \left(\frac{4}{\phi_0} \right)^2 \sin^2 \frac{\phi_0}{2} \frac{Z_{\parallel}}{\omega}$$

Equation 6.24

where the factor 1/2 is inserted in the expression for Z_{\perp} because one half of the BPM sets work for the horizontal and one half for the vertical. At low frequencies, the impedances are inductive,

$$\frac{Z_{\parallel}}{n} = j2MZ_c \left(\frac{\phi_0}{\pi} \right)^2 \frac{\ell}{R} = j0.363 \Omega$$

$$Z_{\perp} = j0.431 \text{ M}\Omega/\text{m}$$

Equation 6.25

At high frequencies, the reactive parts of the impedances oscillate between inductive and capacitive; for example, the first zero occurs when $f = c/(2\ell) = 0.833$ GHz. The real parts rise from zero quadratically with frequency and $\text{Re}Z_{||}$ has a peak value of $2.02 \text{ k}\Omega$ at 0.833 GHz, or $\text{Re}Z_{||}/n = 0.116 \Omega$.

6.7.1.4 Bellows

There are about 1000 bellows in the Tevatron, each of which consists of 24 convolutions of width 1.04 mm between inner and outer radii of 3.94 and 4.58 cm as shown in Figure 6.31. We run ABCI¹⁶ to obtain the wakes of azimuthal modes $m=0$ and $m=1$, from which the longitudinal and transverse impedances are computed and plotted in Figure 6.32 and Figure 6.33. We see that there is a broad band of peaks centered around 7.0 GHz with $Q \approx 2$ and shunt impedance $R_s \approx 100 \Omega$ (per bellows). This gives for 1000 bellows a broadband which peaks at $\text{Re}Z_{||}/n \approx 0.68 \Omega$ and an inductive part $\text{Im}Z_{||}/n \approx R_s/(Qn_r) \approx 0.34 \Omega$.

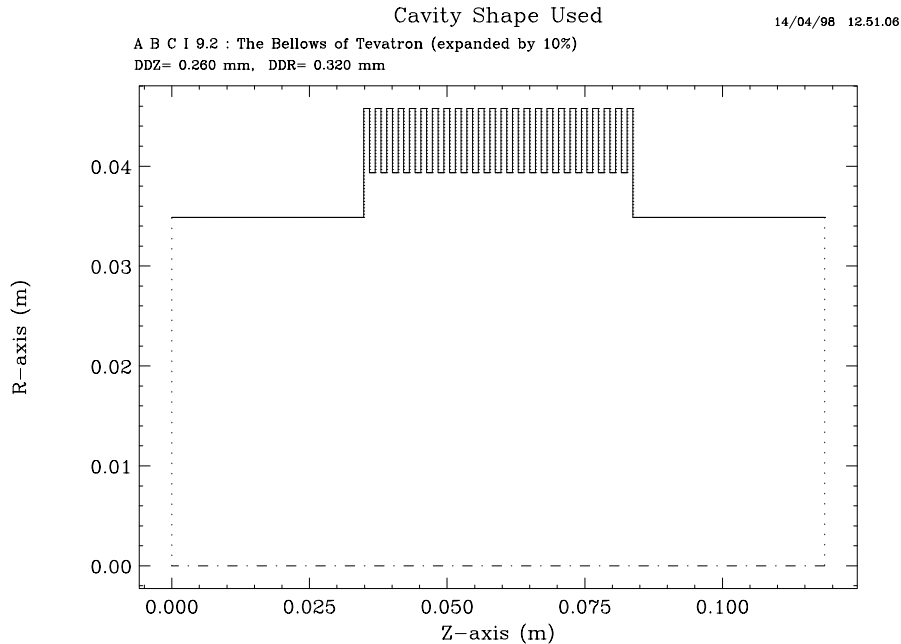


Figure 6.31. A model of one Tevatron bellows used in ABCI.

For the transverse impedance in Figure 6.33, there is also a broadband peak around 7.0 GHz with $Q \approx 0.73$ and shunt impedance $R_s \approx 1.5 \text{ k}\Omega/\text{m}$ (per bellows), or $\text{Re}Z_{\perp} \approx 1.1 \text{ M}\Omega/\text{m}$ for the whole ring. Below $\sim 2 \text{ GHz}$, the reactive part of the impedance is $\text{Im}Z_{\perp} \approx 0.40 \text{ M}\Omega/\text{m}$.

There are also sharp resonances. We believe, however, that they will be present at slightly different frequencies for different bellows. Therefore, it is reasonable to expect them to add up to broader resonances instead, but with much smaller areas under the impedance curves than the broad bands at 7.0 GHz for both the longitudinal and transverse impedances.

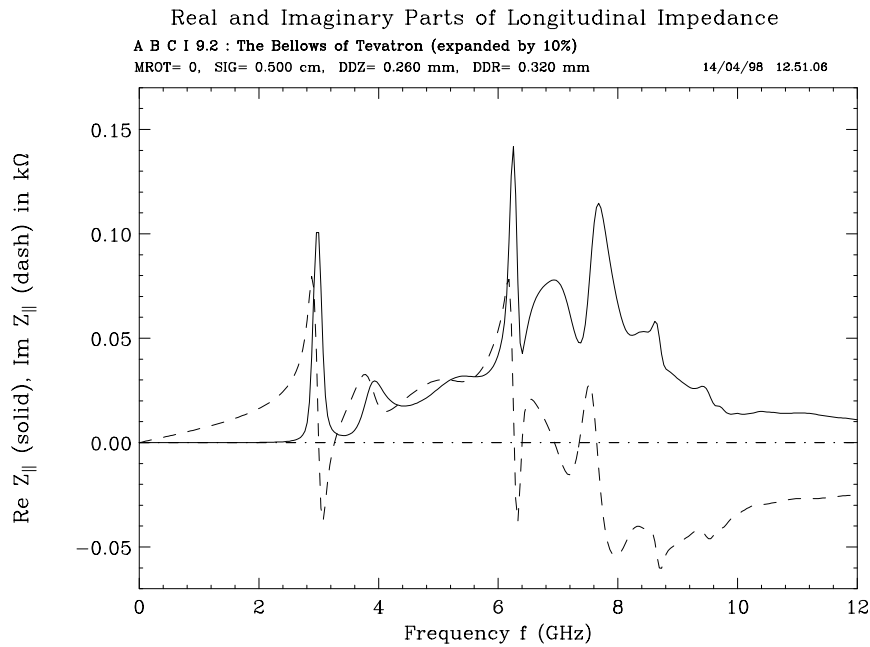


Figure 6.32. The real and imaginary parts of $Z_{||}$ in a Tevatron bellows as computed by ABCI.

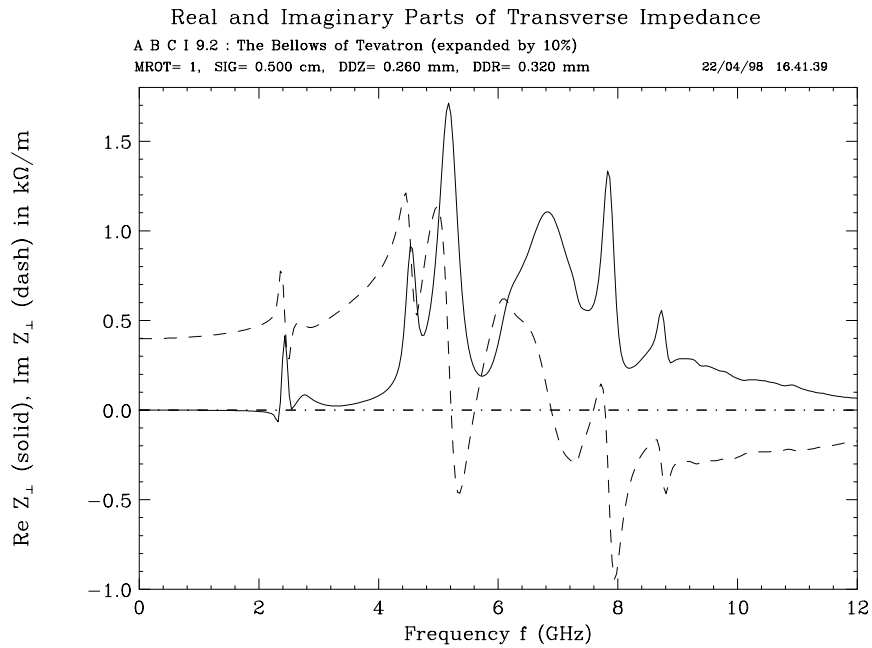


Figure 6.33. The real and imaginary parts of Z_{\perp} in a Tevatron bellows as computed by ABCI.

6.7.1.5 Separators

There are 11 electrostatic separators in the Tevatron vacuum chamber. Their function is to separate the proton and antiproton bunches so that they will not collide with each other except at

designated interaction points. We use the MAFIA code¹⁷ to compute the wake potentials left by a short bunch for both the monopole and dipole modes. Because of the limitation on number of grid points of the code, it is impossible to input the exact details of the separators. Instead, we model a separator system as two plates 20 cm wide and 2.57 m long inside a circular cavity chamber of length 2.75 m and radius 18 cm as illustrated in Figure 6.34. The beam pipe is circular in cross section with radius 4 cm. The grid size is 1 cm in the longitudinal and horizontal directions, but 1.125 cm in the vertical direction. The Fourier transforms are computed to arrive at the longitudinal monopole and impedance and transverse dipole impedance, which are plotted in Figure 6.35 and Figure 6.36 up to 3 GHz.¹⁸ We believe that this simplified model retains all the essential features of the impedances.

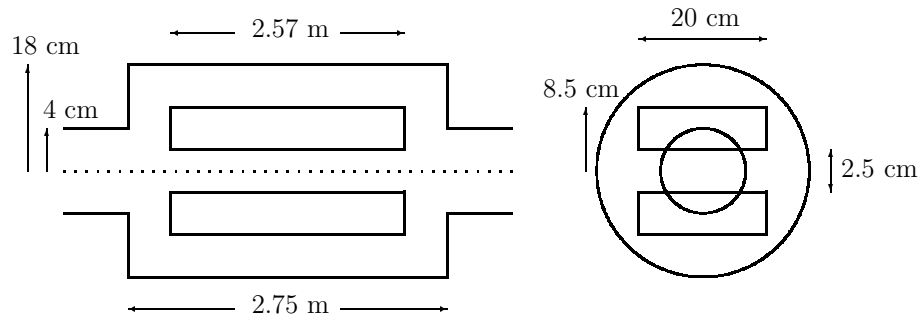


Figure 6.34. The simplified separator system used in MAFIA computation of monopole and dipole wake potentials.

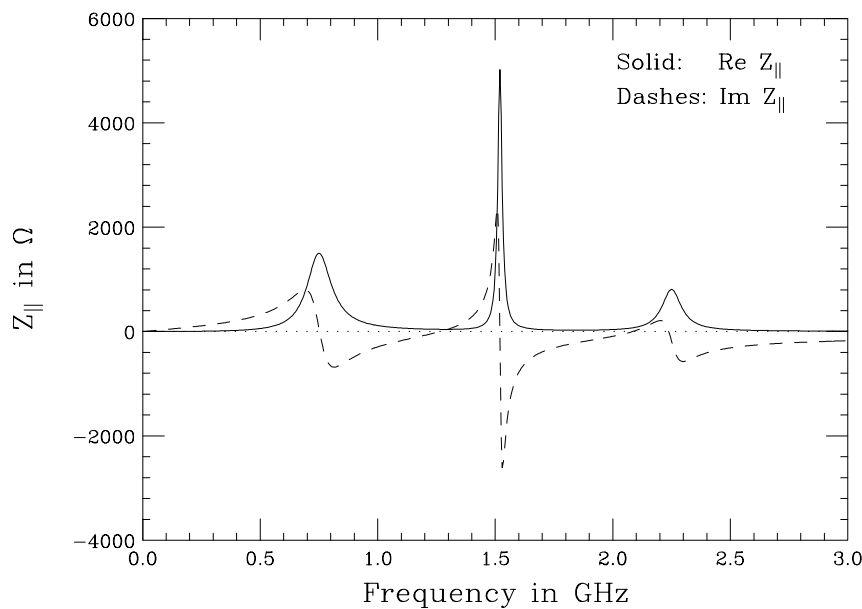


Figure 6.35. The real and imaginary parts of the longitudinal impedance $Z_{||}$ of one separator system.

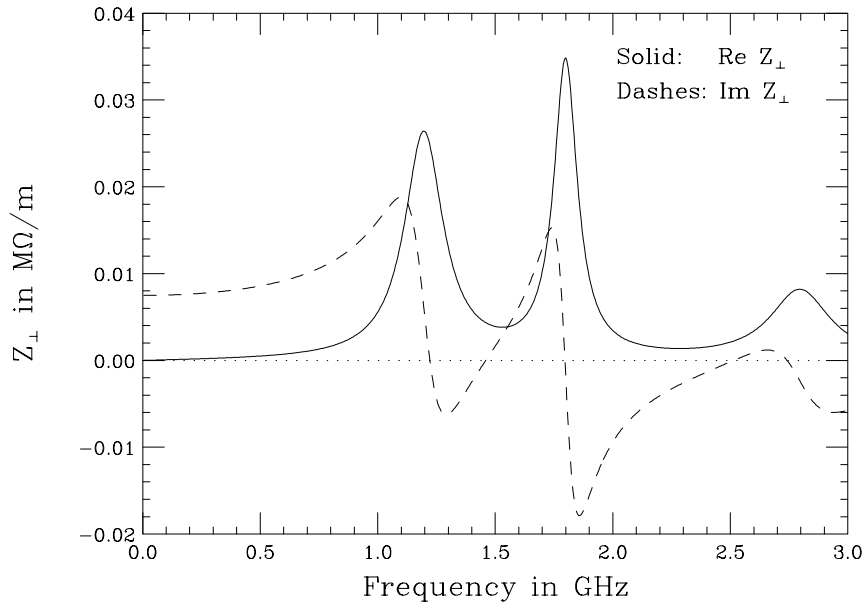


Figure 6.36. The real and imaginary parts of the vertical impedance Z_{\perp} of one separator system

The separator system can be viewed as two pillbox cavities joined by a transmission line. For a closed-end pillbox cavity of radius 18 cm the first few monopoles resonances are at $f_{010}=0.637$ GHz, $f_{020}=1.46$ GHz, $f_{030}=2.29$ GHz, ..., and the first few dipoles resonances are at $f_{110}=1.02$ GHz, $f_{120}=1.86$ GHz, $f_{130}=2.70$ GHz, Actually these resonances are seen at 0.75, 1.51, and 2.24 GHz in Figure 6.35 and 1.23, 1.80, and 2.74 GHz in Figure 6.36. The shifts are probably due to the fact that the cavities are not closed. These modes are below the cutoff frequency of 2.87 GHz for the 4 cm-radius beam pipe. However, some resonances are very much broadened. We believe that this is a result of the transmission effect between the two cavities. We see from Figure 6.35 and Figure 6.36 that the 11 separators will give below ~ 0.6 GHz the contributions $\text{Im} Z_{\parallel}/n = 0.21 \Omega$ and $\text{Im} Z_{\perp} = 0.82 \text{ M}\Omega/\text{m}$, which are not too small.

6.7.1.6 Rf Cavities

Some higher-order monopole modes of a Tevatron rf cavity have been measured by Sun and Colestock¹⁹ in 1995 using both the method of dielectric bead-pull and wire measurement. The resonances quoted in Table 6.9 are based on bead measurements only, as the modes with wire present were shifted in frequency so much that positive identification of the modes was precluded. A combination of dielectric beads, metallic beads and needles was used to perturb the cavity. The ultimate accuracy was determined most likely by temperature drifts in either the cavity or the network analyzer to about 0.5 degrees, corresponding to impedances (depending on their Q values) to a few $\text{k}\Omega$. We also use the URMEL code²⁰ to compute some lower modes and the results are listed also in Table 6.9 for comparison. We find that the URMEL resonant frequencies and R/Q for these modes agree rather well with Sun's measurement. On the other hand, the quality factors Q do not agree so well. This may be because URMEL computes the modes of the *bare* cavity, while some of these modes have actually been de- Q ed passively. Also there are a lot of

structures inside the cavity and these structures have not been included in the simplified model of the cavity used in URMEL computation.

Table 6.9. Longitudinal modes for one whole cavity.

Mode Type	URMEL Results			Sun's Measurements		
	Frequency (MHz)	R/Q Ω	Q	Frequency (MHz)	R/Q Ω	Q
TM0-EE-1	53.49	87.65	9537	53.11	109.60	6523
TM0-ME-1	84.10	22.61	12819	56.51	18.81	3620
TM0-EE-2	166.56	18.47	16250	158.23	11.68	6060
TM0-ME-2	188.94	10.83	18235			
TM0-EE-3	285.94	7.53	20524	310.68	7.97	15923
TM0-ME-3	308.46	4.07	22660			
TM0-EE-4	402.69	4.93	25486	439.77	5.23	13728
TM0-ME-4	431.34	1.72	26407	424.25	1.28	6394
TM0-EE-5	511.69	5.57	25486	559.48	6.73	13928
TM0-ME-5	549.57	1.36	29453			
				748.18	10.90	13356
				768.03	2.47	16191

There have not been any measurements of the dipole modes. Therefore, we need to rely on the URMEL results, which are listed in Table 6.10. Except for the fundamental, we believe that all these higher-order modes will have frequencies varied slightly from cavity to cavity. Therefore, we expect them to be broadened or the quality factors lowered when all the rf cavities of the Tevatron are considered.

Table 6.10. Transverse modes for one whole cavity.

Mode Type	Frequency (MHz)	R/Q (Ω/m)	Q
1-EE-1	486.488	229.80	31605
1-ME-2	486.864	148.95	31487
1-EE-2	513.370	117.38	33262
1-ME-3	518.317	117.93	34008
1-EE-3	561.727	81.62	33029
1-ME-4	575.298	3.84	35810
1-EE-4	625.123	61.00	32598
1-ME-5	650.853	35.21	37592
1-EE-5	699.723	54.76	33407

6.7.1.7 Summary

We try to add up the individual impedances studied in the previous sections and arrive at the total in Figure 6.37 and Figure 6.38. The impedances are plotted as functions of revolution harmonics and also frequencies. For the contributions of the resistive wall and Lambertson magnets to the transverse impedance, the residual betatron tune in Equation 6.6, Equation 6.13,

and

has been set to zero. Since logarithmic scales have been used, only the positive-frequency parts of the impedances are plotted and the capacitive parts of the impedances are not shown. The higher-order modes of the cavities have not been included, because they are too narrow to be visible in log-log plots. The impedances of the 11 separators are included, although they have not been plotted separately in order not to make the figures too crowded.

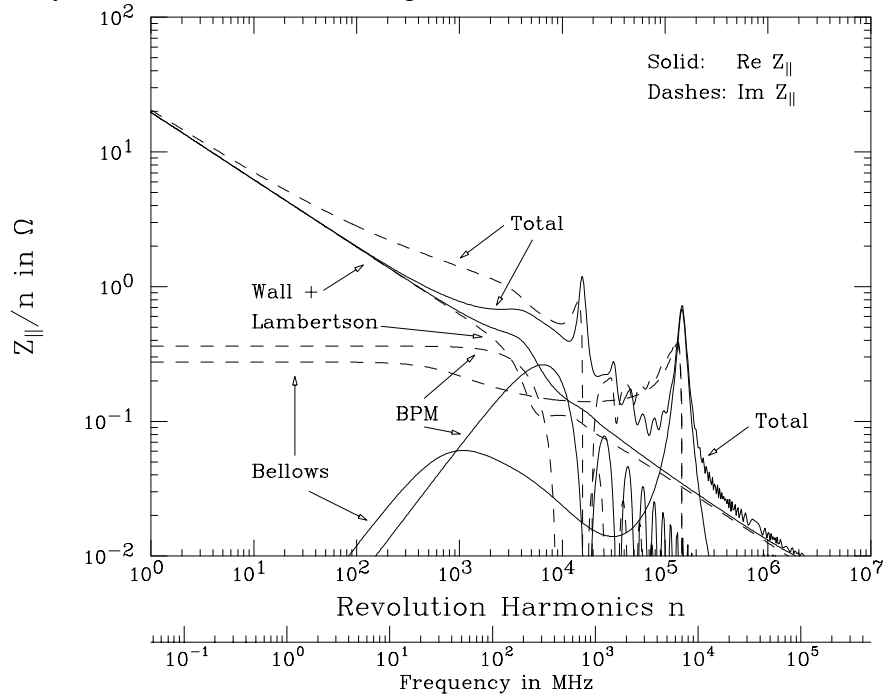


Figure 6.37. The real and imaginary parts of $Z_{||}/n$ contributions to the Tevatron vacuum chamber. The capacitive parts are not shown.

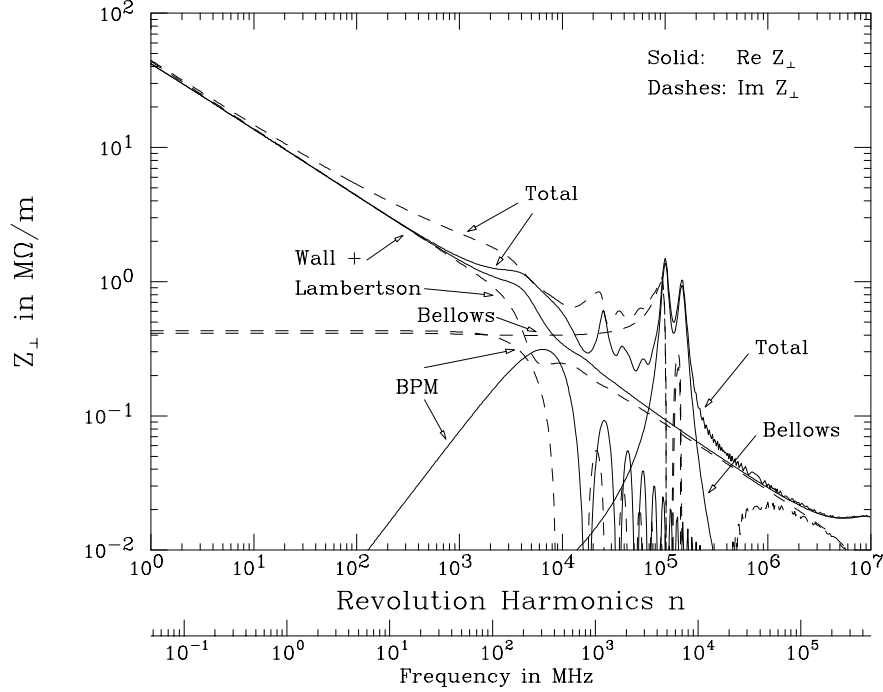


Figure 6.38. The real and imaginary parts of Z_{\perp} contributions to the Tevatron vacuum chamber. The capacitive parts are not shown.

We see that the resistive wall and the Lambertsons dominate mostly below ~ 10 MHz. Then the contributions of the bellows and BPM's are clearly seen in the region of 10 MHz to ~ 1 GHz. The peaks near 1 GHz are the resonances of the separators. Finally, there are the broad resonances of the bellows at ~ 7 GHz. Notice that the sharper resonances of the bellows around 2 to 3 GHz in Figure 6.32 and Figure 6.33 do not show up in these plots. This is because the increment in frequency in the logarithmic scale has not been fine enough. There are other contributions to the inductive impedances such as steps in the vacuum chamber, kickers, etc. Therefore, it will be reasonable if we add ~ 1 to 2Ω and ~ 1 to $2 \text{ M}\Omega/\text{m}$, respectively, to the longitudinal impedance per harmonic and transverse impedance around beam-pipe cutoff, which, for a square beam pipe of side $h=6$ cm, is roughly $f_{cutoff} \approx c/(2h)=2.5$ GHz. Thus, around f_{cutoff} the longitudinal impedance per harmonic and transverse impedance are roughly 1.8Ω and $2.0 \text{ M}\Omega/\text{m}$, respectively. The proton bunch has a rms bunch length of $\sigma_r=37$ cm which is very much larger than the radius of the beam pipe. The longest wavelength λ that can perturb the bunch is roughly two times the total bunch length, or $\lambda \approx 4\sqrt{6}\sigma_r = 3.63$ m. Thus we can define a bunch cutoff frequency as $f_c \approx c/\lambda = 82.8$ MHz. At this frequency, $\text{Re } Z_{\parallel}/n \approx \text{Im } Z_{\parallel}/n \approx 3.0 \Omega$ and $\text{Re } Z_{\perp}/n \approx \text{Im } Z_{\perp}/n \approx 3.0 \text{ M}\Omega$.

6.7.2 Potential-well Distortion

The proton or antiproton bunches will see an rf voltage of $V_{rf}=1$ MV per turn, implying a coherent synchrotron tune of $\nu_{s_0}=7.077 \times 10^{-4}$ at 1 TeV. For a bunch of rms length $\sigma_{\tau_0}=1.234$ nsec, the rms momentum spread is therefore

$$\sigma_{\delta_0} = \frac{\omega_0 \sigma_{\tau_0} V_{s_0}}{\eta} = 9.262 \times 10^{-5}$$

Equation 6.26

where $\omega_0 = 2\pi f_0$ is the angular revolution frequency. Assuming a parabolic bunch distribution, the half bunch length is $\hat{\tau}_0 = \sqrt{5}\sigma_{\tau_0} = 2.760$ nsec and the half momentum spread is $\hat{\delta}_0 = \sqrt{5}\sigma_{\delta_0} = 2.071 \times 10^{-4}$. Therefore the bunch area is $S = 5\pi\sigma_{\tau_0}\sigma_{\delta_0}E = 1.796$ eV-s. It is worthwhile to point out that the bunch area appears to be smaller than the actual Tevatron bunch area measured at injection. This is because once the rms is given, the bunch area depends very much on the bunch distribution one prefers. There are no tails in the parabolic distribution; the bunch area is therefore smaller. This can be thought of the area of the core part of an actual bunch. For the cosine-square distribution $\rho(\tau) = \cos^2 \pi\tau / (2\hat{\tau}) / \hat{\tau}$, we have $(\hat{\tau}/\sigma_{\tau})^2 = 3\pi^2 / (3\pi^2 - 6) = 7.65$ and the total bunch area will be much larger. On the other hand, the bunch area of a bi-Gaussian distribution encircling 95% of the bunch particles is $S_{95\%} = 6\pi\sigma_{\tau_0}\sigma_{\delta_0}E = 1.796$ eV-sec. In this section, we prefer the parabolic distribution because it makes the analysis much simpler.

In the presence of an inductive part of the longitudinal impedance, the bunch will be lengthened to $\hat{\tau} = k\hat{\tau}_0$ above transition, and the momentum spread diminished to $\hat{\delta} = \hat{\delta}_0/k$ so that the bunch area remains constant. The lengthening ratio k satisfies the quartic equation²¹

$$1 = k^4 - kD$$

Equation 6.27

where

$$D = \frac{3eN_p}{2\omega_0^2 h V_{rf} \cos \phi_s \hat{\tau}_0^3} \frac{Z_{\parallel}}{n} \Big|_{ind}$$

Equation 6.28

and ϕ_s is the synchronous angle, which we take as zero here. We find that the lengthening ratios are $k=1.015, 1.023, 1.030,$ and $1.038,$ respectively, when the inductive part of the impedance per harmonic $Z_{\parallel}/n|_{ind} = 2, 3, 4,$ and 5Ω . The Tevatron bunch spectrum has a rms frequency of $1/(2\pi\sigma_{\tau}) \approx 130$ MHz. From Figure 6.37, it is reasonable to assume $Z_{\parallel}/n|_{ind} \sim 2$ to 3Ω . Thus the amount of bunch lengthening will not be appreciable. The longitudinal impedance does have a real part that is of the same order of magnitude as the reactive part. The real part will lead to a left-right asymmetric distortion, which we think would be small also.

The potential-well distortion can have other consequences. Usually we measure the total bunch length $2\hat{\tau}$ and infer the half momentum spread $\hat{\delta}$ and bunch area S according to

$$\hat{\delta} = \frac{\omega_0 V_s \hat{\tau}}{\eta} \quad \text{and} \quad S = \frac{\pi E \omega_0 V_s \hat{\tau}^2}{\eta}$$

Equation 6.29

Because of the defocusing effect of the inductive impedance above transition, the incoherent synchrotron tune ν_s will be less than the coherent synchrotron tune ν_{s_0} . Comparing with Equation 6.26, they are related by

$$V_s = \frac{V_{s0}}{k^2}$$

Equation 6.30

Thus the effective rf voltage becomes

$$V_{rf\text{eff}} = \frac{V_{rf}}{k^4}$$

Equation 6.31

Usually the incoherent synchrotron tune is difficult to measure. If one substitutes the coherent synchrotron tune into Equation 6.29, one would have estimated the momentum spread and bunch area too big by the factor k^2 . This will give a wrong idea about the amount of Landau damping.

6.7.3 Longitudinal Microwave Instability

The beam current at a revolution harmonic n interacts with the longitudinal coupling impedance of the vacuum chamber at the same harmonic to create a bucket at that harmonic and the beam particles are bunched. This phenomenon of self-bunching is called longitudinal microwave instability. This bunching or growth will not take place if the spread in revolution frequency among the beam particles is large enough. Applying to a bunch, we have the Boussard-modified Keil-Schnell stability criterion on the coupling impedance^{22, 23}:

$$\left| \frac{Z_{\parallel}}{n} \right| < F \frac{\eta E}{e I_{peak}} \delta_{FWHM}^2$$

Equation 6.32

For a parabolic bunch, the form factor $F \approx 1$, $\delta_{FWHM} = \sqrt{2} \hat{\delta}$, and the peak current $I_{peak} = 3I_b / (4\hat{\tau}f_0)$ with I_b being the average bunch current. The above can also be written as

$$\left| \frac{Z_{\parallel}}{n} \right| < \frac{16\pi}{3I_b} (\omega_0 \hat{\tau})^3 h V_{rf\text{eff}}$$

Equation 6.33

or

$$\left| \frac{Z_{\parallel}}{n} \right| < \frac{8.2^{1/4}}{3\pi^{5/4} I_b} (f_0 S / e)^{3/2} \left(\frac{\eta}{E/e} \right)^{3/4} (h V_{rf\text{eff}})^{1/4}$$

Equation 6.34

Therefore if the bunch area S and momentum spread $\hat{\delta}$ are inferred from Equation 6.29 using the coherent synchrotron tune, and the effective rf voltage $V_{rf\text{eff}}$ is replaced by the unperturbed V_{rf} displayed in the oscilloscope, one needs to divide the right sides of Equation 6.32 through Equation 6.34 by the 4th power of the potential-well bunch lengthening factor k defined in Section 6.7.2. For a fixed unperturbed $V_{rf}=1$ MV, and half bunch length 37 cm, the stability limit is most stringent at the storage energy of $E=1$ TeV and is given in Table 6.11. Bunch lengthening ratio k and longitudinal microwave stability limits at $E=1$ TeV versus the inductive part $Z_{\parallel}/n|_{ind}$ for various values of the inductive part of the impedance per harmonic $Z_{\parallel}/n|_{ind}$.

Table 6.11. Bunch lengthening ratio k and longitudinal microwave stability limits at $E=1$ TeV versus the inductive part $Z_{\parallel}/n|_{ind}$.

$\frac{Z_{\parallel}}{n} _{ind}$	k	$\frac{Z_{\parallel}}{n} _{limit}$
0 Ω	1.000	20.63 Ω
1 Ω	1.008	20.01 Ω
2 Ω	1.015	19.41 Ω
3 Ω	1.023	18.84 Ω
4 Ω	1.030	18.30 Ω
5 Ω	1.039	17.78 Ω

Microwave instability is essentially a coasting beam effect and self-bunching must occur much faster than a synchrotron oscillation, otherwise the growth will decohere. Therefore the perturbation should have a half-wavelength less than the length of the bunch, or a frequency $f > 1/(4\hat{\tau}) = 90.6$ MHz. From Figure 6.37, together with a generous allowance for other contributions not included, $|Z_{\parallel}/n|$ of the Tevatron vacuum chamber will be at most a few ohms, which is very much below the Keil-Schnell limit listed in Table 6.11. Thus the longitudinal microwave instability should not pose any problem in Run II.

6.7.4 Longitudinal Coupled Bunch Instabilities

The long-range wake left by the higher-order resonant modes of the rf cavities may couple the longitudinal motions of the bunches in the Tevatron. Assuming M bunches of equal intensity equally spaced in the ring, there are $\mu=0, 1, \dots, M-1$ modes of oscillations in which the center-of-mass of a bunch lags behind its predecessor by the phase $2\pi\mu/M$. In addition, an individual bunch in the μ -th coupled-bunch mode can oscillate in the synchrotron phase space about its center-of-mass in such a way that there are $m=1, 2, \dots$ nodes along the bunch longitudinally (not including the ends). For example, $m=1$ is the rigid dipole mode, where the bunches move rigidly as they execute synchrotron oscillations, $m=2$ is the quadrupole mode where the bunch head and tail oscillate longitudinally 180° out of phase. Actually, this has been a simplified description of the modes of perturbation inside a bunch. The full description involves two eigen-numbers, for example, the azimuthal and the radial.

If the driving narrow resonance falls on a μ -th coupled bunch line, Sacherer's growth rate for the m th mode is²⁴

$$\frac{1}{\tau_{m\mu}} = \frac{e\eta MI_b R_s f_0}{2\pi E v_s B_0} DF_m(\Delta\phi),$$

Equation 6.35

where $B_0 = \tau_L f_0$ is the *single-bunch* bunching factor with $\tau_L = 2\hat{\tau}$ being the *total* bunch length, v_s is the perturbed synchrotron tune, R_s is the shunt impedance of the sharp driving resonance at frequency $f_r = \omega_r/(2\pi)$. The factor D is a function of the decay decrement $\alpha\tau_{sep}$ between successive bunches, where $\alpha = \omega_r/(2Q)$ is the HWHM of the resonance of quality factor Q and τ_{sep} is the bunch separation. It is defined as

$$D(\alpha\tau_{sep}) = -i2\alpha\tau_{sep} \sum_{k=0}^{\infty} e^{-2\pi i k \mu / M - k(\alpha - i\Omega)\tau_{sep}} \sin k\omega_r \tau_{sep},$$

Equation 6.36

The maximum magnitude of D is shown in Figure 6.39. The form factor for parabolic bunches is given by

$$F_m(\Delta\phi) = \frac{16m}{\Delta\phi} \left[J_m^2\left(\frac{1}{2}\Delta\phi\right) - J_{m+1}\left(\frac{1}{2}\Delta\phi\right)J_{m-1}\left(\frac{1}{2}\Delta\phi\right) \right],$$

Equation 6.37

where $\Delta\phi = 2\pi f_r \tau_L$ is the phase change of the resonator during the bunch passage from head to tail, and is plotted in Figure 6.40. Note that mode m peaks roughly at $\Delta\phi = m\pi$. This is reasonable because, as was mentioned above, mode m represents a longitudinal variation along the bunch with m nodes (not including the ends) and it will be most easily excited when the bunch sees a phase variation of $m\pi$ of the driving resonance as it passes through the cavity gap from head to tail. Note that F_m decreases as m increases, implying that the higher m modes will not be excited so easily.

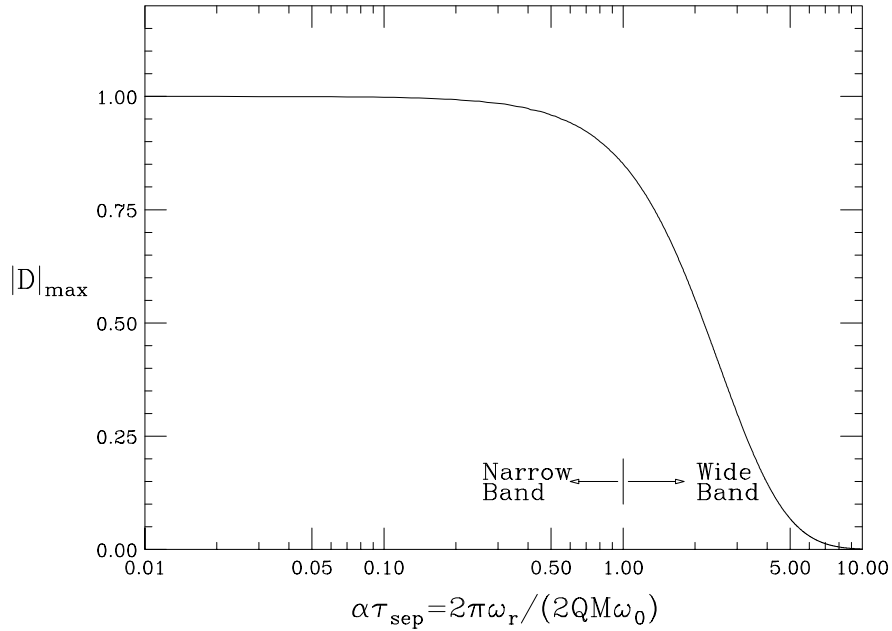


Figure 6.39. $|D_{\max}|$ as a function of bunch-to-bunch decay decrement $\alpha\tau_{sep}$. Note that $|D_{\max}| \approx 1$ for narrow resonances but drops very rapidly as the resonance becomes broader.

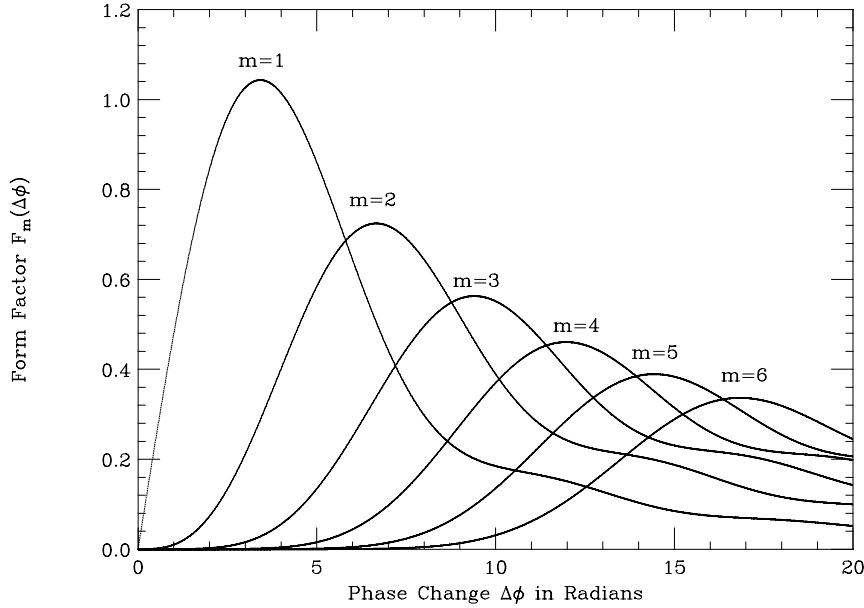


Figure 6.40. Form factor for longitudinal oscillation inside a bunch with $m=1, 2, 3, 4, 5$ and 6 nodes.

The rf voltage during the whole ramp is about 1 MV. Therefore the growth will be most severe at the injection energy of $E=150$ GeV. The growth rates for the first few modes are listed in Table 6.12 for the 36×36 scenario.

Table 6.12. Longitudinal coupled-bunch growth rates driven by the higher-order modes of the rf cavities at injection for the 36×36 scenario in Run II.

f_r MHz	R_s k Ω	Q	$\Delta\phi$ rad	Growth Rate in sec ⁻¹					
				m=1	m=2	m=3	m=4	m=5	m=6
56.5	68	3620	0.88	<u>0.606</u>	0.010	0.000	0.000	0.000	0.000
158.2	70	6060	2.45	<u>1.415</u>	0.189	0.009	0.000	0.000	0.000
310.7	124	15923	4.82	<u>2.329</u>	<u>1.443</u>	0.305	0.033	0.002	0.000
424.2	8	6394	6.58	<u>0.089</u>	0.124	0.056	0.012	0.001	0.000
439.8	71	13728	6.82	<u>0.714</u>	<u>1.089</u>	0.542	0.129	0.018	0.002
559.5	93	13928	8.68	<u>0.469</u>	<u>1.103</u>	<u>1.071</u>	0.478	0.120	0.019
748.2	145	13356	11.60	<u>0.484</u>	<u>0.789</u>	<u>1.333</u>	<u>1.397</u>	0.787	0.269
768.0	39	16191	11.91	<u>0.128</u>	0.206	0.342	0.386	0.236	0.087
Laudau Damping rate sec ⁻¹				0.000	0.555	0.679	0.784	0.877	0.961

These higher-order modes were measured by Sun (see reference 19) in 1995 using the method of dielectric bead pull. Here, we assume that the peak of each resonance is at exactly a synchrotron line on the left side of the revolution harmonic. Also, the higher-order resonances of each cavity will not be at exactly the same frequency. In other words, for all the 8 cavities, we

assume the resonances will be de-Qued 8 times. Therefore, for each mode, the shunt impedance of *one* cavity has been used in Equation 6.35 when the computation is performed.

The spread of the synchrotron frequency due to the nonlinear sinusoidal rf waveform can be written as

$$\frac{\Delta\omega_s}{\omega_s} = \frac{2}{3} \left(\frac{1+\Gamma^2}{1-\Gamma^2} \right) \left(\frac{h\tau_L f_0}{2} \right)^2 = 0.0143 \quad \text{or} \quad \Delta f_s = 1.25 \text{ Hz},$$

Equation 6.38

when the nominal synchrotron tune $\nu_s = 1.83 \times 10^{-3}$ is assumed at the injection energy of 150 GeV with an rf voltage of 1 MV, and the synchronous phase $\phi_s = \sin^{-1} \Gamma$ is taken to be zero. This supplies Landau damping. The mode will be stable if

$$\frac{1}{\tau} < \frac{\sqrt{m}}{4} \Delta\omega_s = 1.96 \sqrt{m} \text{ s}^{-1}$$

Equation 6.39

The Landau damping rates are listed in the last row of Table 6.12, and the modes that receive not enough Landau damping are underlined.

For the 140×121 scenario, the growth rates can be obtained by linearly scaling the number of bunches M . Of course, the growth of all modes will be faster.

We would like to point out that the inductive impedance gives rise to an incoherent synchrotron frequency shift of

$$\frac{\Delta\omega_s}{\omega_s} = -\frac{3I_b \text{Im}(Z_{||}/n)}{2\pi^2 h V_{rf} \cos \phi_s B_0^3} = -0.0463 \quad \text{or} \quad \Delta f_s = -4.05 \text{ Hz},$$

Equation 6.40

where $\text{Im}(Z_{||}/n) = 3 \Omega$ has been used. However, the coherent synchrotron frequency remains the same as the unperturbed synchrotron frequency f_{s0} . Thus the incoherent spread of the synchrotron frequency will not cover f_{s0} , and will not supply any damping to the $m=1$ mode. This is illustrated in Figure 6.41. The sizes of the incoherent frequency shift and spread depend rather sensitively on the bunch distribution. For example, for a cosine-square distribution and a Gaussian distribution with the same rms bunch length, the incoherent frequency shifts will be, respectively, ~ 1.74 or ~ 2.97 times larger than that of the parabolic distribution. Also due to the nonuniform distribution gradients in these two distributions, the incoherent frequency spreads will also be broader. Nevertheless, the conclusion is qualitatively the same. For all reasonable distributions, the incoherent frequency spread will not be able to overlap the coherent dipole synchrotron frequency, resulting in no Landau damping.

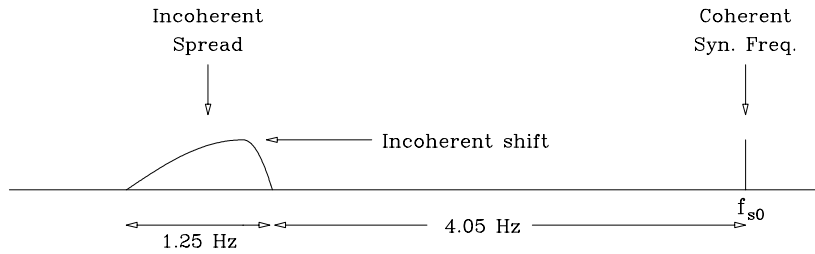


Figure 6.41. Schematic drawing showing the incoherent spread of $\Delta f_s \approx 1.25$ Hz is shifted by -4.05 Hz from the coherent synchrotron frequency f_{s0} , thus not being able to provide Landau damping to the dipole ($m=1$) modes.

We see from Table 6.12 that the azimuthal mode $m=1$ driven by the resonance at 310.7 MHz will grow at a rate of 2.33 per second. Although the growth rate is small, however, the growth is severe because the ramp rate of the Tevatron is slow; the energy reaches only ~ 220 GeV after ramping for 20 s. In computing the growth rates in Table 6.12, we have assumed that the resonant peaks of the 8 cavities do not fall on top of each other and the effective peak of the sum broadened. We took the shunt impedance to be the shunt impedance of the resonance of one cavity and increase the quality factor 8-fold. In this way, the FWHM is 3.27 revolution harmonics and the decay decrement of the resonant field is $\alpha\tau_{sep} = 0.194$. From Figure 6.39, it is clear that the function $D(\alpha\tau_{sep}) \approx 1$. However, if we assume the resonant peaks of the 8 cavities to fall on top of each other, the situation will be different. Although the decay decrement is 0.0242 and D is still equal to unity, the FWHM is only 0.409 revolution harmonic. This implies that resonant may not fall on top of an upper synchrotron side band of a harmonic line, and if this happens the growth rate will be very much reduced. Unfortunately, the resonant frequencies measured are not accurate enough for us to decide whether they are near a revolution harmonic or not.

If the growth turns out to be harmful, a fast 36×36 bunch by bunch damper may be necessary to damp the dipole mode ($m=1$). A damper for the quadrupole mode ($m=2$) may also be necessary. This consists essentially of a wall-gap pickup monitoring the changes in bunch length and the corresponding excitation of a modulation of the rf waveform with roughly twice the synchrotron frequency. The Tevatron bunches will be formed by coalescing 9 or more bunches in the Main Injector (formerly in the Main Ring). Usually there will be a 10% difference in the number of particles in the final bunches. This difference will break the symmetry of the coupled-bunch system and lead to some damping also.

We would like also to compute the longitudinal coupled bunch growth rates for Run I, where there were only 6 proton bunches with a rms length of 85.5 cm and the same number of protons per bunch as in Run II. A smaller number of bunches will certainly reduce the growth rates. The longer bunch length will make the driving force less effective because of the much larger change in phase of the resonator during the passage of the bunch. Also a bigger bunch in the longitudinal phase space will provide more Landau damping. The growth rates at 150 GeV are listed in Table 6.13.

Table 6.13. Longitudinal coupled-bunch growth rates driven by the higher-order modes of the rf cavities at injection for the 6×6 scenario in Run I.

f_r MHz	R_s k Ω	Q	$\Delta\phi$ rad	Growth Rate in sec ⁻¹					
				$m=1$	$m=2$	$m=3$	$m=4$	$m=5$	$m=6$
56.5	68	3620	1.91	<u>0.090</u>	0.007	0.000	0.000	0.000	0.000
158.2	70	6060	5.34	<u>0.090</u>	0.072	0.019	0.003	0.000	0.000
310.7	124	15923	10.48	<u>0.035</u>	0.067	0.105	0.081	0.034	0.009
424.2	8	6394	14.32	<u>0.001</u>	0.003	0.003	0.005	0.005	0.003
439.8	71	13728	14.84	<u>0.010</u>	0.022	0.027	0.037	0.045	0.032
559.5	93	13928	18.88	<u>0.009</u>	0.016	0.025	0.032	0.033	0.043
748.2	145	13356	25.25	0.008	0.014	0.022	0.028	0.033	0.042
768.0	39	16191	25.92	<u>0.002</u>	0.004	0.006	0.008	0.009	0.011
Landau Damping rate (s ⁻¹)				0.000	2.626	3.212	3.709	4.149	4.546

We see that Landau damping prevents all azimuthal coupled-bunch modes with $m>1$ from instabilities. The only unstable modes are the dipole modes, which have no Landau damping. However, the highest growth rate is only 0.090 s^{-1} . Such slow rate would be damped by the slight unequal number of particles in the bunches. This may explain why no longitudinal coupled-bunch instabilities had been observed during Run I.

6.7.5 Longitudinal Head-tail Instability

In general, the slippage factor η is not an even function of momentum offset and the particle trajectory will be asymmetric about the on-momentum axis. When the first-order coefficient $\alpha_0\alpha_1$ of momentum compaction factor is positive, the particle spends more time at positive momentum offset than at negative momentum offset. Thus the bunch becomes relatively longer at positive momentum offset than at negative momentum offset, as is illustrated in Figure 6.42. The bunch will therefore lose more energy in the lower trajectory than in the upper trajectory. The amplitude of synchrotron oscillation will therefore grow. This phenomenon is called longitudinal head-tail instability and was first observed at the CERN PS by Boussard and Linnekar.²⁵ The growth rate is given by

$$\frac{1}{\tau} = \frac{f_0}{2} \frac{dU}{d\sigma_\tau} \frac{\sigma_\tau}{E} \chi$$

Equation 6.41

where the energy loss per particle per turn is

$$U(\sigma_\tau) = e^2 N \int d\omega |\tilde{\rho}(\omega)|^2 \text{Re} Z_{||}(\omega)$$

Equation 6.42

and

$$\chi = \frac{\alpha_0 \left(\alpha_1 - \eta + \frac{3}{2} \right)}{\eta} \approx \alpha_1 + \frac{3}{2}$$

Equation 6.43

denotes the asymmetry, which has been measured to be $\chi \sim 1.17$ for the Tevatron. In the above,

$$\tilde{\rho}(\omega) = \frac{1}{2\pi} \int d\tau \rho(\tau) e^{-j\omega\tau}$$

Equation 6.44

is the spectrum of the bunch of rms length σ_τ with a distribution $\rho(\tau)$ normalized to unity.

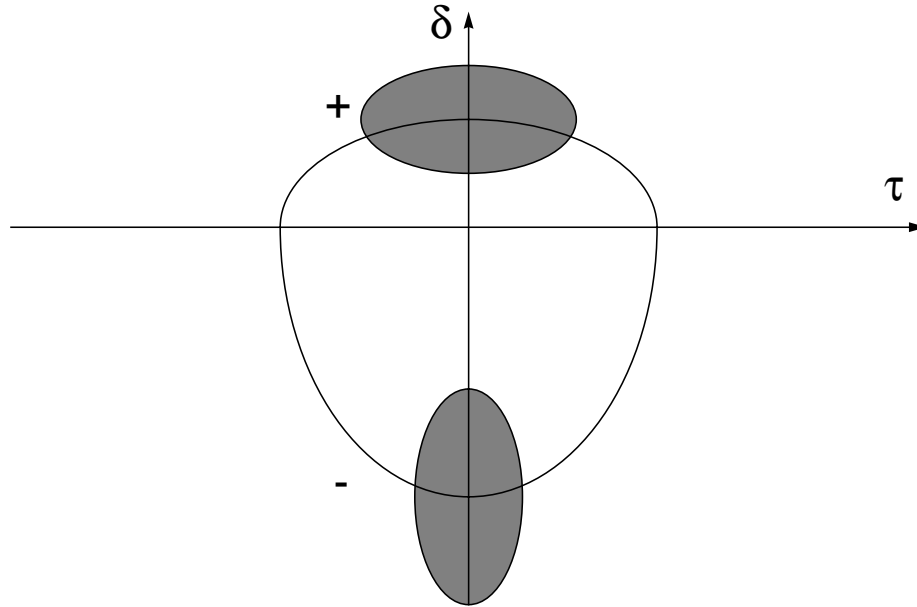


Figure 6.42. A particle trajectory is asymmetric about the on-momentum axis when the slippage factor is not an even function of momentum offset. The bunch will be longer at positive than negative momentum offset when the first-order momentum compaction $\alpha_0\alpha_1 > 0$ and above transition.

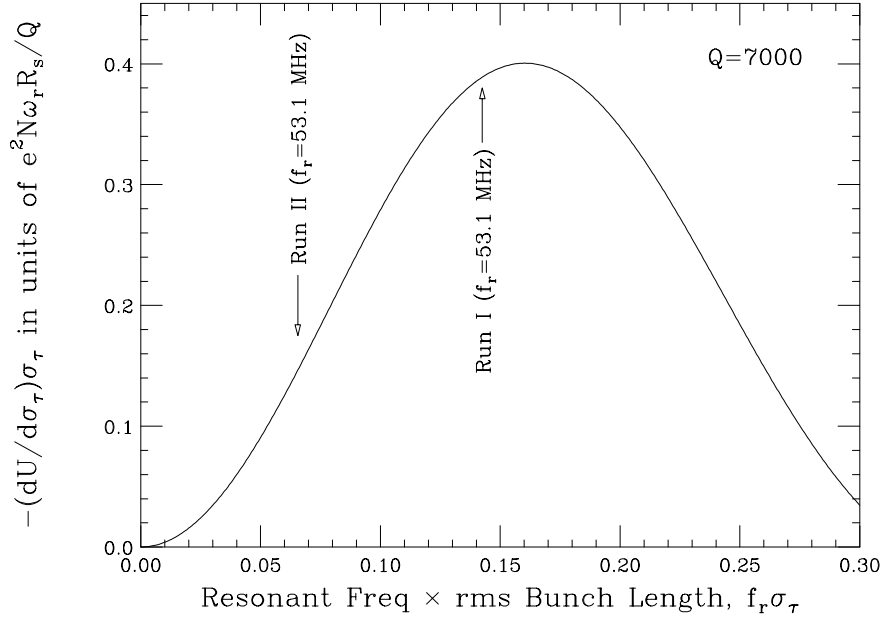


Figure 6.43. Plot of differential bunch energy loss $(dU/d\sigma_\tau)\sigma_\tau$ versus $f_r\sigma_\tau$ due to a sharp resonance. Note that the effect on the Run II bunch is much less than that on the Run I bunch because of the shorter Run II bunch length.

If the driving impedance $\text{Re}Z_{\parallel}$ comes from a narrow resonance with shunt impedance R_s at resonant frequency $\omega_r/(2\pi)$ and quality factors Q , we have for the energy loss per turn

$$U(\sigma_\tau) = \frac{\pi R_s \omega_r e^2 N}{Q} |\tilde{\rho}(\omega_r)|^2,$$

Equation 6.45

for a bunch containing N particles. For a broadband impedance, $U(\sigma_\tau)$ drops much faster with bunch length. For a general resonance, we have computed the asymmetric energy loss for a parabolic bunch distribution,

$$\begin{aligned} \frac{dU(\sigma_\tau)}{d\sigma_\tau} \sigma_\tau = \frac{9e^2 N \omega_r R_s}{4sQ} & \left\{ \frac{2}{z^3} [e^{-2cz} \sin(2sz + 2\theta) - \sin 2\theta] \right. \\ & + \frac{4}{z^4} [e^{-2cz} \sin(2sz + 3\theta) + \sin 3\theta] + \frac{12}{z^5} e^{-2cz} \sin(2sz + 4\theta) \\ & \left. + \frac{6}{z^6} [e^{-2cz} \sin(2sz + 5\theta) + \sin 5\theta] \right\} \end{aligned}$$

Equation 6.46

where $z = \sqrt{5}\omega_r\sigma_\tau$, $c = \cos\theta = 1/(2Q)$, and $s = \sin\theta$. This is plotted in Figure 6.43 for the case of a sharp resonance and in Figure 6.44 for the case of a broadband with $Q=1$. As is shown in Figure 6.43, the asymmetric energy loss vanishes when the bunch length goes to zero, because the change in bunch length from positive momentum offset to negative momentum offset also goes

to zero. On the other hand, when the bunch length is very long, the asymmetric energy loss will also be small, because the energy loss for a long bunch is small.

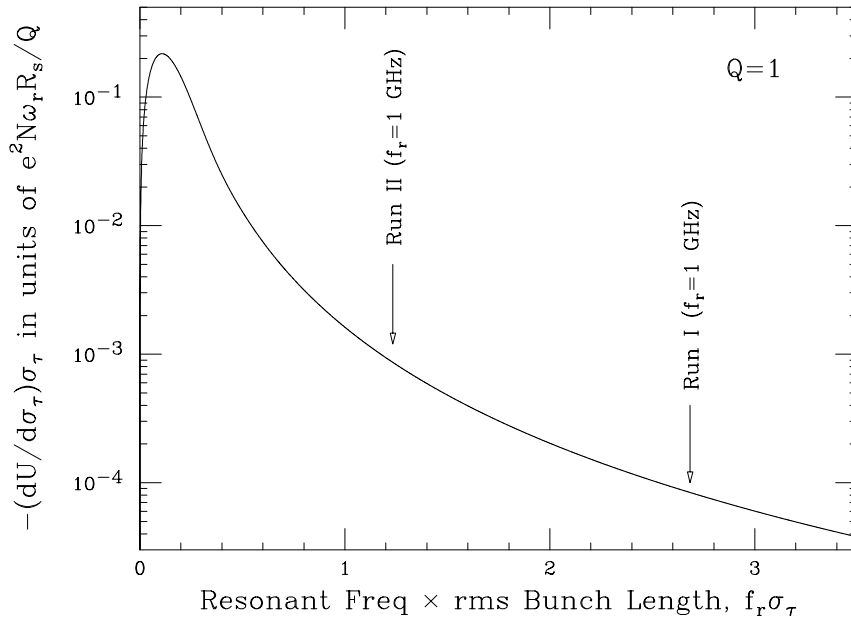


Figure 6.44. Plot of differential bunch energy loss $(dU/d\sigma_\tau)\sigma_\tau$ versus $f_r\sigma_\tau$ due to a broadband resonance with $Q=1$. Note that the effect on the Run II bunch is much more than that on the Run I bunch because of the shorter Run II bunch length.

The fundamental resonance of the 8 rf cavities serves as a good driving force for this instability. Each cavity has resonant frequency $f_r=53.1$ MHz, $R_s=1.2$ M Ω , and $Q=7000$. For Run I, where the rms bunch length was $\sigma_\tau \approx 2.684$ nsec or $f_r\sigma_\tau \approx 0.1425$, $(dU/d\sigma_\tau)\sigma_\tau \sim -0.3890e^2 N\omega_r R_s/Q$ is large and leads to a growth rate of $\tau^{-1}=1.433 \times 10^{-3} \text{ s}^{-1}$ at the injection energy of $E=150$ GeV for a bunch containing $N=2.70 \times 10^{11}$ particles. However, for Run II, the bunch will be much shorter. With $\sigma_\tau=1.234$ nsec or $f_r\sigma_\tau \approx 0.0655$, the asymmetric energy loss $(dU/d\sigma_\tau)\sigma_\tau \sim -0.1464e^2 N\omega_r R_s/Q$ is much smaller and the head-tail growth rate becomes $\tau^{-1}=0.539 \times 10^{-3} \text{ s}^{-1}$. As is shown in Figure 6.43, we are on the left side of the $(dU/d\sigma_\tau)\sigma_\tau$ peak; therefore a shorter bunch length leads to slower growth.

The broadband impedance can also have similar contributions since the resonance frequency is usually a few GHz and $\text{Re}Z_{||}$ is large although $Z_{||}/n$ is just a couple of ohms. Now $\omega_r\sigma_\tau$ falls on the right side of the $(dU/d\sigma_\tau)\sigma_\tau$ peak instead. We expect shorter bunch lengths to have faster growth rates, as is indicated in Figure 6.44. Table 6.13 shows the longitudinal head-tail growth rates for different resonant frequencies and quality factors; $Z_{||}/n=2 \text{ } \Omega$ has been assumed. The growth rates driven by the fundamental rf resonance are also listed in the last row for comparison. It is obvious that the longitudinal head-tail instability for Run I is dominated by the rf narrow resonance and that for Run II by the broadband impedance instead. We observed a growth time of ~ 250 s in Run I. From Table 6.13, it is very plausible that the growth of this head-tail instability will be at least as fast as that in Run I.

Table 6.14. Growth rates for a broadband resonance of $Z_{\parallel}/n=2 \Omega$ at various frequencies and quality factors.

f_r (GHz)	Q	Growth Rate (s ⁻¹)	
		Run I	Run II
1	1	0.178×10^{-3}	1.829×10^{-3}
1	3	0.022×10^{-3}	0.267×10^{-3}
2	1	0.089×10^{-3}	0.915×10^{-3}
2	2	0.023×10^{-3}	0.249×10^{-3}
1	5	0.009×10^{-3}	0.114×10^{-3}
2	3	0.011×10^{-3}	0.117×10^{-3}
2	4	0.006×10^{-3}	0.070×10^{-3}
Fundamental Rf Resonance		1.433×10^{-3}	0.539×10^{-3}

6.7.6 Transverse Microwave Instability

Similar to the longitudinal case, the beam current at a certain betatron spectral frequency $(n_r + \nu_\beta)f_0$ interacts with the transverse impedance to create a transverse deflecting force leading to an enhancement of the amplitude of the betatron oscillation. Here, n_r is a revolution harmonic and ν_β is the betatron tune. We need to consider only the slow wave that can cause instability and therefore $n_r < 0$. This growth can be damped by the incoherent spread of the betatron spectral line under consideration. As a result of momentum spread δ , this incoherent spread is

$$\Delta f_\beta = [-(n_r + \nu_{\beta 0})\eta + \xi]f_0\delta$$

Equation 6.47

where $\nu_{\beta 0}$ is the on-momentum betatron tune and ξ the chromaticity. Applying to a bunch, we can therefore write down a Keil-Schnell type of stability criterion:²⁶

$$\frac{1}{\tau_{\mu m}} = -\frac{1}{1+m} \frac{eMI_b c}{4\pi\nu_\beta E} \sum_k \text{Re } Z_\perp [(kM_s - \mu + \nu_\beta + m\nu_s)\omega_0] F'_m(\omega\tau_L - \chi)$$

Equation 6.48

where R is the mean radius of the accelerator ring. Similar to our discussion in section 6.7.3, if the momentum spread is inferred from Equation 6.29, it will be diminished by the square of the bunch lengthening factor k as a result of the inductive impedance.

Since the bunch length is much larger than the beam pipe radius, the half-wavelength of the driving impedance force will be less than the full length of the bunch. We therefore take the perturbing frequency as $f_r = 1/(4\hat{\tau}) = 90.6$ MHz or $n_r = 1/(4\hat{\tau}f_0) = 1899$, and obtain the stability limit $|Z_\perp| < 3.26$ M Ω /m at zero chromaticity and injection energy. Note the $|Z_\perp|$ near this frequency is 3 to 4 M Ω /m from Figure 6.38 together with other discontinuities of the vacuum chamber. Thus, transverse microwave instability will be plausible in Run II. However, a chromaticity of $\xi = +10$ implies raising $|n_r|$ effectively by $\xi/\eta = 3537$ and increasing the stability limit to

$|Z_{\perp}| < 9.41 \text{ M}\Omega/\text{m}$. On the other hand, a negative chromaticity will lower the stability limit and lead to instability.

6.7.7 Transverse Coupled-bunch Instabilities

6.7.7.1 Resistive Wall

A most serious transverse coupled-bunch instability in a storage ring may be driven by the resistive wall. If there are M_s identical equally spaced bunches in the ring, there are $\mu=0, \dots, M_s-1$ transverse coupled modes when the centers of mass of one bunch lags behind its predecessor by the betatron phase of $2\pi\mu M_s$. At the same time, each bunch can execute longitudinal motion with $m=0, 1, \dots$, nodes. The growth rate for the mode μm is²⁷

$$\frac{1}{\tau_{\mu m}} = -\frac{1}{1+m} \frac{eMI_b c}{4\pi v_{\beta} E} \sum_k \text{Re} Z_{\perp} \left[(kM_s - \mu + v_{\beta} + m v_s) \omega_0 \right] F'_m(\omega \tau_L - \chi)$$

Equation 6.49

where M is the number of bunches. Strictly speaking Equation 6.49 is correct only if $M = M_s$ or a completely filled ring. For example, in the 36×36 scenario, the bunch spacing is 21 buckets; therefore $M=36$ and $M_s=1113/21=53$, and in the 140×121 scenario, $M=140$ (for protons) and $M_s=159$. There are many unfilled buckets in both scenarios; thus Equation 6.49 will not be an accurate description of the beam dynamics.

As the frequency $\omega \rightarrow \pm 0$, the real part of the resistive-wall impedance approaches first $\pm \omega^{-1/2}$, then ω^{-1} when the skin depth exceeds the thickness of the pipe wall, and finally zero when the frequency is exactly zero. At the residual betatron tune of the Tevatron, $v_{\beta} \sim \pm 0.4$, we are in the regime of $\pm \omega^{-1/2}$ dependency. Therefore, there is always a mode μ that corresponds to a large negative $\text{Re} Z_{\perp}$ and drives the transverse coupled-bunch instability. For example, with the betatron tune $v_{\beta} = 20.57$, mode $\mu=21$ or frequency $-0.43 - 0.43\omega_0/2\pi$ with $k=0$ in the summation of Equation 6.49 contributes the largest negative $\text{Re} Z_{\perp}$, which is $-66.70 \text{ M}\Omega/\text{m}$ according to our former estimate made in Section 6.7.1.2. The next contribution with $k=1$ will give $\text{Re} Z_{\perp} = +6.03 \text{ M}\Omega/\text{m}$ in the 36×36 scenario and $+3.47 \text{ M}\Omega/\text{m}$ for protons in the 140×121 scenario. The average current per bunch is $I_b = 2.064 \text{ mA}$. The growth rate is therefore given mostly by the $k=0$ term in the summation and is very insensitive to the choice of M_s in Equation 6.49. For such a low driving frequency, only the lowest longitudinal mode $m=0$ will be excited. The growth rates after doing the actual summations are 31.0 and 120.6 s^{-1} , respectively, for the two scenarios. Modes $\mu=22, 23, 24, \dots$ are also unstable; the growth rates are, respectively, $16.9, 12.8, 10.6, \dots \text{ s}^{-1}$, and $66.1, 50.6, 42.5, \dots \text{ s}^{-1}$ for the two operating scenarios. The computation has been performed at zero chromaticity ($\xi=0$), so that the chromatic phase $\chi = \xi \omega_0 \tau_L / \eta = 0$. Also, we have used the form factor $F'_0(0) = 8/\pi^2 \approx 0.811$, where, for convenience, Sacherer's sinusoidal modes of excitation have been assumed. These growth rates are much larger than those in Run I because there are more bunches. If one operates at chromaticity $\xi = +10$, $\chi = 5.85$, $F'_0(5.85) \approx 0.155$ from Figure 6.45. The growth rates for $\mu=21$ drop to 5.9 and 9.7 s^{-1} , respectively, which can be damped easily by a tune spread. For example, a tune spread of $\Delta v_{\beta} = 0.0001$ will lead to a spread of betatron angular frequency of $\Delta v_{\beta} \omega_0 = 30 \text{ s}^{-1}$,

and will damp a growth rate up to $\sim 17.0 \text{ s}^{-1}$ (FWHM for a Gaussian spread) (see reference 27). For further discussion, we need to study the sinusoidal modes of excitation in the next subsection.

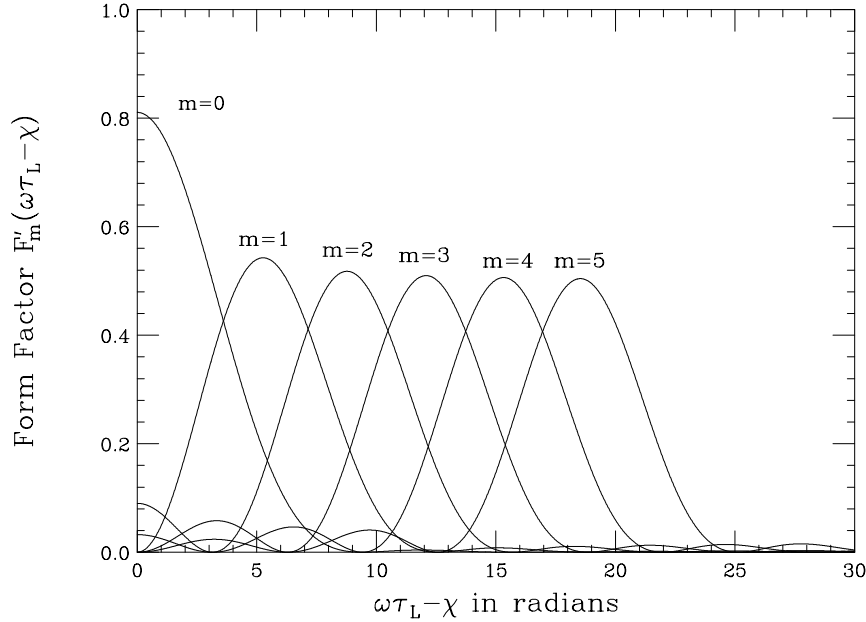


Figure 6.45. Plot of form factor $F'_m(\omega\tau_L - \chi)$ for modes $m=0$ to 5. With the normalization in Equation 6.51, these are exactly the power spectra h_m .

6.7.7.2 Sinusoidal Modes

The Sacherer's sinusoidal modes of excitation consist of the orthonormal set

$$p_m(\tau) = \begin{cases} \cos(m+1)\pi \frac{\tau}{\tau_L} & m = 0, 2, \dots \\ \sin(m+1)\pi \frac{\tau}{\tau_L} & m = 1, 3, \dots \end{cases}$$

Equation 6.50

such that $p_m(\tau)$ has m nodes along the bunch not including the ends. The power spectrum is proportional to

$$h_m(\omega) = \frac{4(m+1)^2}{\pi^2} \frac{1 + (-1)^m \cos \pi y}{[y^2 - (m+1)^2]^2}$$

Equation 6.51

where $y = \omega\tau_L/\pi$ and $\omega = kM - \mu + v_\beta + mv_s - \chi/\tau_L$. They are plotted in Figure 6.46. The normalization of $h_m(\omega)$ in Equation 6.51 has been chosen in such a way that, when the smooth approximation is applied to the summation over k , we have

$$B \sum_{k=-\infty}^{\infty} h_m(\omega) \approx \frac{B}{M\omega_0} \int_{-\infty}^{\infty} h_m(\omega) d\omega = 1$$

Here $B = M\omega_0\tau_L/(2\pi)$ is the bunching factor, or the ratio of full bunch length to bunch separation. Then the form factor $F'_m(\omega)$ in Equation 6.49 just equals $h_m(\omega)$.

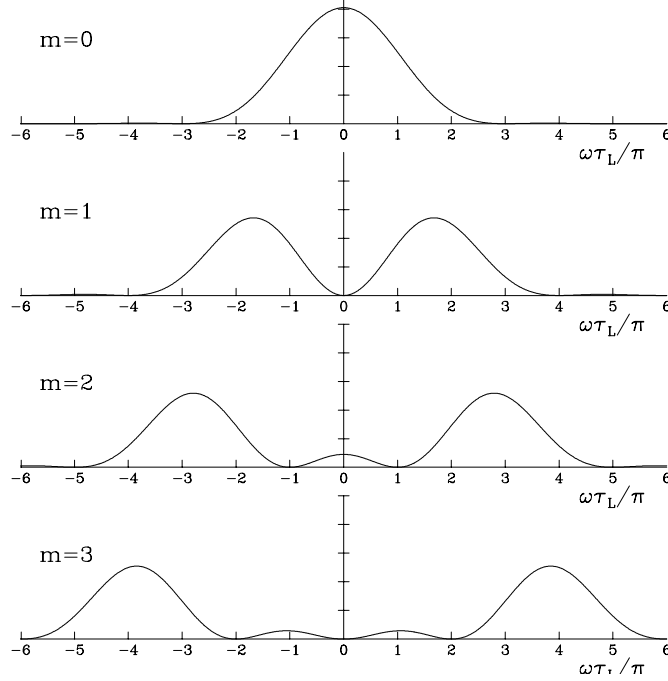


Figure 6.46. Power spectra $h_m(\omega)$ for modes $m=0$ to 3 with zero chromaticity.

The Sacherer integral equation for transverse instability is an eigen-value-eigen-function problem when the unperturbed longitudinal distribution $g_0(r)$ in the longitudinal phase space is given. Physically, the modes of excitation $p_m(\tau)$ are the projection of the eigen-functions in the longitudinal phase space onto the time axis. The sinusoidal modes corresponds to the water-bag distribution* in phase space, so that the linear distribution is

$$\rho(\tau) \propto \sqrt{\hat{\tau}^2 - \tau^2}$$

For the distribution $g_0(r) \propto (\hat{\tau}^2 - r^2)^{1/2}$ in the longitudinal phase space, $p_m(\tau)$ are the Legendre polynomials and the Fourier transforms the spherical Bessel functions j_m . When $g_0(r)$ is bi-Gaussian, $p_m(\tau)$ are Hermite polynomials. Sometimes the growth rates computed are rather sensitive to the longitudinal bunch distribution assumed. Therefore, results in this section are estimates only.

*In the Sacherer integral equation for transverse instability, the weight function is $W(r)=g_0(r)$. However, in the integral equation for longitudinal instability, the weight function is $W(r)=-r^{-1}g'_0(r)$. As a result, for that equation, the sinusoidal modes correspond roughly to $g_0(r) \propto (\hat{\tau}^2 - r^2)$, the Legendre modes correspond to

$g_0(r) \propto (\hat{\tau}^2 - r^2)^{1/2}$. But the Hermite modes correspond to the same bi-Gaussian distribution in phase space.

We now learn that a chromaticity of $\chi = \eta/(f_0\tau_L) = +10.73$ will push the power spectra in Figure 6.46 to the right (or positive frequency side) by two $\omega\tau_L/\pi$ units. The $m=0$ will then only see the positive-frequency impedance and no instability will result. However, the $m=1$ mode will now peak at zero frequency and the resistive wall impedance will drive the $m=1$ mode unstable and a quadrupole transverse damper will be required.

6.7.7.3 Transverse Coupled-bunch Instability Driven by Resonances

The narrow transverse resonant modes of the rf cavities will also drive transverse coupled-bunch instability. The growth rate is described by the general growth formula of Equation 6.49. When the resonance is narrow enough, only one frequency $\omega_r/2\pi$ contributes in the summation. Thus the growth rate becomes

$$\frac{1}{\tau_{\mu m}} = -\frac{1}{1+m} \frac{eMI_b c}{4\pi v_\beta E} \text{Re} Z_\perp(\omega_r) F'_m(\omega_r \tau_L - \chi)$$

Equation 6.54

where ω_r is negative. We calculated the growth rates of modes driven by the nine higher-order dipole modes computed by URMEL in Table 6.15. The results are listed in Table 6.15.

Table 6.15. Growth rates for transverse coupled-bunch modes driven by higher-order dipole modes of the rf cavities.

f_r MHz	R_s Ω/m	Q	m_{pk}	Growth	Growth Rate (s^{-1})					
					$m=0$	$m=1$	$m=2$	$m=3$	$m=4$	$m=5$
Chromaticity $\xi=0$										
486.5	7262	31605	4.4	4.173	0.001	0.008	0.008	0.057	0.346	0.276
486.9	4689	31487	4.4	2.694	0.001	0.005	0.005	0.036	0.223	0.179
513.4	3904	33262	4.7	2.243	0.001	0.001	0.008	0.007	0.135	0.180
518.3	4010	34008	4.7	2.304	0.002	0.001	0.008	0.005	0.128	0.189
561.7	2695	33029	5.2	1.549	0.001	0.000	0.004	0.001	0.031	0.121
575.3	137	35810	5.4	0.079	0.000	0.000	0.000	0.000	0.001	0.006
625.1	1988	32598	5.9	1.142	0.000	0.001	0.000	0.004	0.000	0.040
650.9	1323	37592	6.2	0.760	0.000	0.000	0.000	0.002	0.000	0.014
699.7	1829	33407	6.7	1.051	0.000	0.000	0.001	0.000	0.003	0.002
Chromaticity $\xi=+10$										
486.5	7262	3165	6.2	4.173	0.000	0.003	0.001	0.009	0.003	0.066
486.9	4689	31487	6.2	2.694	0.000	0.002	0.000	0.006	0.002	0.042
513.4	3904	33262	6.5	2.243	0.000	0.001	0.001	0.002	0.005	0.012
518.3	4010	34008	6.6	2.304	0.000	0.000	0.002	0.002	0.006	0.009
561.7	2695	33029	7.1	1.549	0.000	0.000	0.001	0.000	0.004	0.000
575.3	137	3580	7.2	0.079	0.000	0.000	0.000	0.000	0.000	0.000
625.1	1988	3258	7.8	1.142	0.000	0.000	0.000	0.001	0.000	0.003
650.9	1323	3752	8.0	0.760	0.000	0.000	0.000	0.001	0.000	0.002
699.7	1829	3347	8.6	1.051	0.000	0.000	0.000	0.000	0.001	0.001
Chromaticity $\xi=-10$										
486.5	7262	31605	2.5	4.173	0.014	0.048	0.476	0.483	0.054	0.018
486.9	4689	31487	2.5	2.694	0.009	0.030	0.306	0.313	0.035	0.011
513.4	3904	33262	2.8	2.243	0.009	0.003	0.166	0.285	0.074	0.002
518.3	4010	34008	2.9	2.304	0.009	0.002	0.154	0.294	0.087	0.001
561.7	2695	33029	3.3	1.549	0.003	0.003	0.029	0.162	0.122	0.007
575.3	137	35810	3.5	0.079	0.000	0.000	0.001	0.007	0.007	0.001
625.1	1988	32598	4.0	1.142	0.000	0.004	0.000	0.042	0.113	0.049
650.9	1323	37592	4.3	0.760	0.000	0.002	0.001	0.012	0.066	0.048
699.7	1829	33407	4.9	1.051	0.001	0.000	0.004	0.000	0.046	0.088

Some comments are in order. Here, we assume that the higher-order modes of the 8 rf cavities do not fall on top of each other at exactly the same frequency. In other words, we assume the resonances summed over 8 cavities will be de-Qued 8 times and the shunt impedance corresponding to a certain mode will be the same as that for a single cavity. From Table 6.15, we see that the frequencies of the lowest 9 higher-order modes range from 486.5 to 699.7 MHz. Therefore $\omega_r \tau_L / \pi - \chi / \pi$ (ω_r is negative) ranges from 5.4 to 7.4 for zero chromaticity. From the power spectra in Figure 6.46, this implies negative resonant frequencies ω_r are exciting the modes that peak in the region, or modes roughly from $m=4$ to 7. These are listed in column 4 of the table. We can see, for example, that the growth rate driven by the first resonance at zero chromaticity actually peaks at $m=4$. Since the growth rates are affected so much by the mode of excitation, we

also give the *bare* growth rate for each resonance in column 5 when the form factor F'_m and the factor $(1+m)^{-1}$ are not included. We see that increasing the chromaticity to $\xi=+10$ shifts the mode spectra to the right (positive frequency side); so only modes of much higher m will be excited. On the other hand, decreasing the chromaticity to $\xi=-10$ shifts the mode spectra to the right and lower m modes will be excited. As a whole, the growth rates are slow. Since a tune spread of $\Delta\nu_\beta=0.0001$, for example, will damp a growth rate up to $\sim 7 \text{ s}^{-1}$. Therefore, transverse coupled-bunch instabilities driven by the higher-order modes of the rf cavities should not be a problem at all.

6.7.8 Transverse Head-Tail Instability

Let us now consider the short-range field of the transverse impedance; *i.e.*, $Z_\perp(\omega)$ when Ω is large. This is equivalent to replacing the discrete line spectrum by a continuous spectrum. Since $\text{Re} Z_\perp(\omega)$ is antisymmetric, the summation in Equation 6.54 when transformed into an integration will vanish identically at zero chromaticity. There can only be instability when the chromaticity is nonzero.

Since the transverse impedance appears to be dominated by the resistive wall, the growth rate can be computed exactly if we substitute the impedance in Equation 6.54 by the resistive wall formula. The result of integration is (see reference 27)

$$\frac{1}{\tau_m} = \frac{1}{1+m} \frac{eMI_b c}{4\pi\nu_\beta E} \left(\frac{\pi}{MB} \right)^{1/2} |Z_\perp(\omega_0)| F_m(\chi)$$

Equation 6.55

where $|Z_\perp(\omega_0)|$ is the magnitude of the resistive wall impedance at the revolution frequency. Note that the bunching factor contains a factor of M , so that the growth rate is actually independent of the number of bunches. This is to be expected because the growth mechanism is driven by the short-range wake field and the instability is therefore a single-bunch effect. This explains why the growth rate τ_m^{-1} does not contain the subscript μ describing phase relationship of consecutive bunches.

The form factor is given by

$$F_m(\chi) = \sqrt{\frac{2}{\pi}} \int_0^\infty \frac{dy}{y} \left[h_m(y - y_\xi) - h_m(y + y_\xi) \right]$$

Equation 6.56

where h_m are the power spectra of mode m in Equation 6.51 written as functions of $y = \omega\tau_L/\pi$ and $y_\xi = \chi/\pi = \chi\omega_0\tau_L/(\pi\eta)$. The first term in the integrand comes from contributions by positive frequencies while the second term by negative frequencies. The form factors for $m=0$ to 5 are plotted in Figure 6.47.

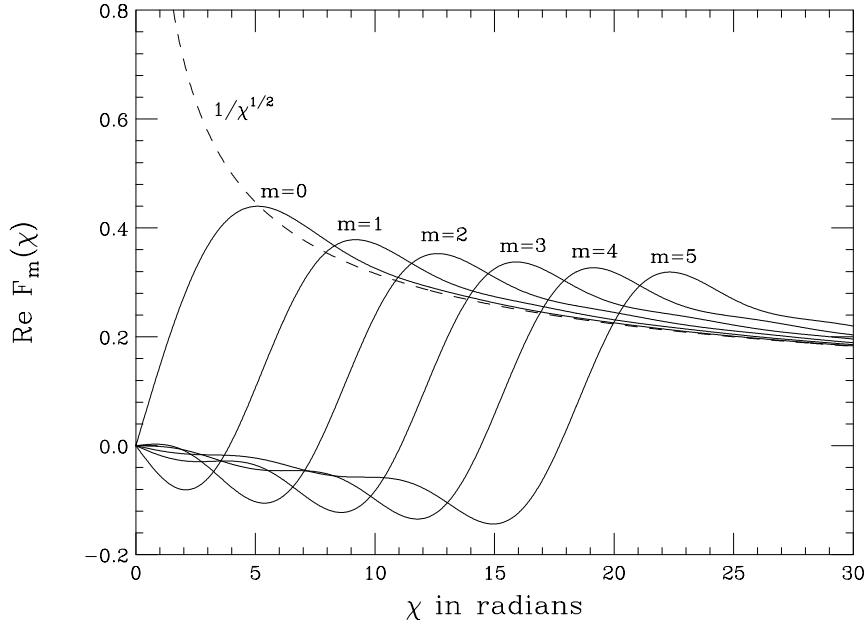


Figure 6.47. Form factor $F_m(\chi)$ for head-tail instability for modes $m=0$ to 5.

For small chromaticity $\xi \lesssim 4$, $\chi \lesssim 2.3$ the integrand in Equation 6.56 can be expanded and the growth rate becomes proportional to chromaticity. From the transverse resistive wall impedance in Equation 6.13, we obtain $|Z_{\perp}(\omega_0)| = 61.85 \text{ M}\Omega/\text{m}$. The growth rates for various modes have been computed and listed in Table 6.16, where negative growth rate implies damping rate. We see from Table 6.16 that mode $m=0$ is stable for positive chromaticity. This is expected because the excitation spectrum for this mode has been pushed towards the positive-frequency side. All other modes $m>0$ should be unstable because their spectra see relatively more negative $\text{Re} Z_{\perp}$. However, the growth rate for $m=4$ is tiny and mode $m=2$ is even stable. This can be clarified by looking closely into the excitation spectra in Figure 6.47. We find that while mode $m=0$ has a large maximum at zero frequency, all the other higher even m modes also have small maxima at zero frequency. As these even m spectra are pushed to the right, these small central maxima see more impedance from positive frequency than negative frequency. Since these small central maxima are near zero frequency where $\text{Re} Z_{\perp}$ is large, their effect may cancel out the opposite effect from the larger maxima which interact with the impedance at much larger frequency where $\text{Re} Z_{\perp}$ is smaller. This anomalous effect does not exist in some other longitudinal bunch distributions like $g_0(r) \propto (\tilde{r}^2 - r^2)^{-1/2}$, because the corresponding power spectra are $|j_m(\omega)|^2$ (spherical Bessel function) which vanish at zero frequency when $m>0$.

Table 6.16. Growth rates of transverse head-tail modes driven by the resistive wall impedance when $\chi \lesssim 2.3$.

Mode m	Form Factor	Growth Rate s^{-1}
0	-0.1495χ	-9.433ξ

1	+0.0600 χ	1.893 ξ
2	-0.0053 χ	-0.113 ξ
3	+0.0191 χ	0.301 ξ
4	+0.0003 χ	0.003 ξ
5	+0.0098 χ	0.103 ξ

The head-tail instabilities can be damped by the incoherent spread in betatron frequency. As mentioned in Section 6.7.7.3, a tune spread of $\Delta\nu_\beta = 0.0001$ is capable to damp a growth rate of 7.0 s^{-1} . Therefore, the monopole mode may not be damped if the storage ring runs at a few units of negative chromaticity. Running at positive chromaticity, however, the $m=0$ mode is stable, while the growth rates of other $m>0$ modes are small, if unstable. As an example, at $\xi=+10$ or $\chi\approx 6$, the linear approximation will no longer valid. From Figure 6.47, we see that both modes $m=0$ and $m=1$ are stable. With $F_1 \sim -0.1$, the growth rate for the $m=1$ mode is only $\sim 3.4 \text{ s}^{-1}$ which will be damped by a small tune spread easily.

6.7.9 Tevatron Dampers

The purpose of this document is to describe which techniques will be used to control coupled bunch instabilities in the Tevatron for Run II. This upgrade is necessary because of the increase in the number of bunches stored in the ring. As the number is increased from 6 bunches to 36 bunches, coupling from bunch to bunch is also increased providing a stronger mechanism for instabilities. Also, with the increase in beam current specified by the Run II parameters, all coupled bunch modes are potentially unstable.

Noise must be kept to a minimum in the system because the Tevatron acts as a storage ring. Excessive noise from the damper systems would cause slow emittance blowup and reduce luminosity. One way to reduce the noise of the damper system is to mold the working bandwidth tightly around the frequency spectrum that represents beam motion.

Because of the many potentially unstable modes and the necessary noise specification, it was decided to make 18 single mode dampers per plane. The noise from single mode dampers is much easier to control than equivalent wideband dampers used in other rings. In order to facilitate these upgrades, kickers and detectors need to be constructed and installed, processing equipment needs to be constructed and installed, and power amplifiers need to be purchased and installed.

The damper low level electronics will also be designed to provide a tune measurement of the protons and antiprotons.

6.7.9.1 Pickups & Kickers

Each of the detectors and kickers must be able to handle the bandwidth necessary to damp all modes. Although only half of the 53-MHz bandwidth is necessary to damp all modes, using the signal from the entire 53-MHz bandwidth helps signal/noise and doesn't involve any extra complications. The system will use the 53-MHz bandwidth around the 53-MHz carrier because amplifiers and detectors have a better response at these frequencies. The response of the pickups and kickers is shown in the plots below. The optimum length for the detectors and kickers is about 1m for the bandwidths we would like to operate.

The location of the pickups and kickers in the ring are also important. Ideally, only one pickup/kicker pair would be required for each plane and each direction. Betatron phase advance from pickup to kicker would be 90 degrees, and the separation between protons and antiprotons

would be a maximum. Changes in Tevatron tune make it impossible to maintain the 90 degrees advance, so it is necessary to create a virtual separation by combining the signal from two pickups which are approximately 90 degrees of phase advance apart. Thus we require a total of 4 pickups (2 horizontal and 2 vertical) and each stripline pickup provides signals for both protons and antiprotons

The plots below show that the best place to place the horizontal pickups are at D48 and E11. These locations have about a 60 degrees phase advance, a reasonable proton/antiproton separation, and large beta function values. These locations would be optimal for the vertical pickups as well except for the small beta functions. The small beta functions do not inhibit the performance of the dampers enough to require extra space elsewhere in the tunnel. If space is a premium, the pickups can be combined function horizontal/vertical, which would reduce the number of pickups needed to two.

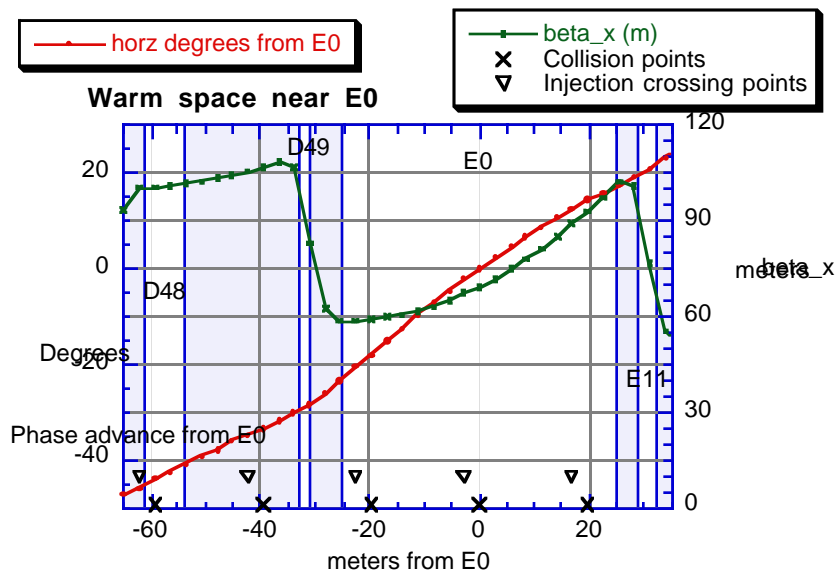


Figure 6.48. Horizontal phase advance.

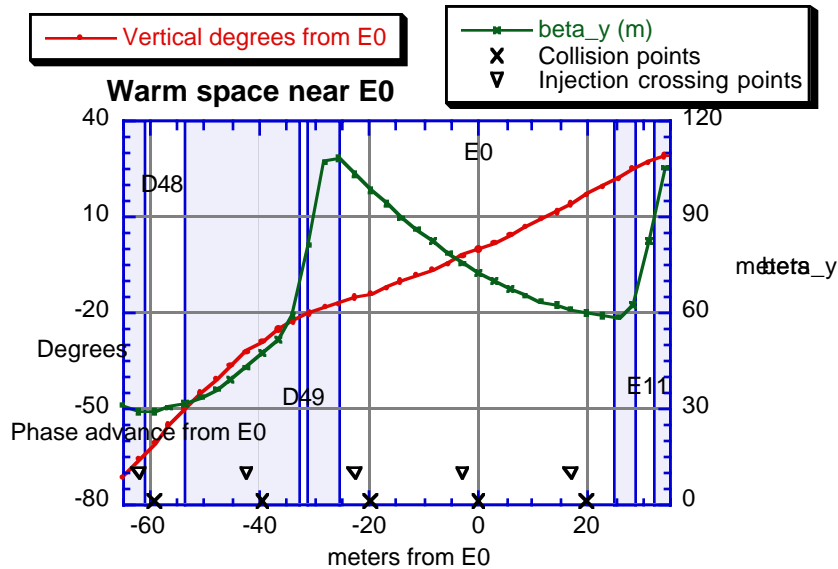


Figure 6.49. Vertical phase advance.

6.7.9.2 High Level Electronics

The power amplifiers, which drive the transverse kicker, must be linear over the range that the dampers will operate. There are many commercial solid state amplifiers that operate in the frequency range specified from the damper system. They come in power ranges from 200-5000 Watts. The amount of power required for the amplifiers is determined by the amount of injection oscillations and the necessary injection damping rate. It is assumed that the injection oscillations will saturate the amplifiers, and the power amplifiers must be strong enough to control instabilities during this saturation mode. The damping rate becomes less affected by proportional increases in power, while the cost goes up considerably. One-kilowatt amplifiers are optimal for this configuration when cost is taken into consideration, and this would lead to a saturated damping rate of 200 turns for an injection error of 1 mm. If a much greater damping rate is required at injection, the fast bump kicker should be utilized in the damper system at injection.

6.7.9.3 Low Level Electronics

The purpose of the low-level electronics is to process the signal from the stripline pickups and send the proper correction signal to the kickers. The first stage, the auto-zero circuit, consists of a very wide dynamic range filter that removes the effects of slow changes in orbit and RF phase. From the output of the auto-zero circuit, the signal is mixed down to base-band, filtered and sampled. The output of the sample and hold enters the processing circuits, which limit the bandwidth of the feedback to just around the frequencies of the instabilities. The processing circuits also provide the phase shift necessary to maintain negative feedback on the instabilities. Finally, in the case of the transverse circuits, the signal is mixed back up and sent to the power amplifiers, or in the case of the longitudinal circuits, the output is sent to the RF phase shifter.

The auto-zero circuit for the transverse system consists of a feedback loop that measures the effect slow variations in position from the pickup and cancels the variations with the common mode signal. One of the advantages of this technique is that it reduces all of the revolution harmonics of the beam, not just the fundamental RF frequency. The multiplier circuits that use this

technique are quite noisy, but because of the reduction of bandwidth through the processing circuits they do not contribute much noise to the kickers. The auto-zero circuit for the longitudinal dampers consists of a phase locked loop to the beam. Both techniques have been used and tested with the main ring dampers.

Transverse processing consists of two multipliers and a summer which take the signals from the two pickups to maintain the proper phase advance. The signal is mixed down again by a frequency equal to the revolution harmonic, closest to the coupled bunch mode frequency that needs to be damped. This signal will be created by a direct digital synthesizer, triggered at four times the RF frequency. The filter section is tuned to pass two betatron sidebands around half the revolution frequency. The signal is amplified and mixed back up with the frequency tuned to the coupled bunch mode and then enters a gate that deactivates damping on a particular bunch. Longitudinal processing will be very similar except that it needs to deal with both the upper and lower sidebands of the FM signal. Therefore, single sideband techniques are used for mixing, and the filters are tuned to the synchrotron frequencies instead of the betatron frequencies.

6.8 Beam-beam tune shift for 36×36 operations

For the 396 nsec bunch spacing, we have only gone through our calculations for the three fold symmetric case (36×36). The main goal here is to look at the differences between two different lattices. The first lattice, BD15, is the low-beta lattice we have used for Run IA and Run IB. The second lattice, JJ15C, is the dispersionless IR Lattice proposed for Run II.

The 396 nsec bunch spacing corresponds to 21 RF bucket (53 MHz) spacing. For 36×36 bunches, our filling scheme has 12 bunches with 396 nsec spacing followed by an abort gap of 2.6 μ sec. This is repeated 3 times for a three-fold symmetry. At the very end of this section, we will make a few comments on filling schemes that are not three fold symmetric.

With 396 nsec bunch spacing, the first crossing points on either side of the IP's are in the missing dipole at the 48 location and in the last dipole at the 11 location. These are far enough after the separators on either side of the IP's, so that we don't need a crossing angle at the IP's. However these first crossing points are still close enough to the separators so that the beams have less separation than is typical in the arcs. The first crossing points are a problem.

With 36×36, we only have 70 "parasitic crossings", much less than with the 132 nsec bunch spacing. However, most of the crossings in the arcs are not a problem. For the quantities we calculate, the main problems come from the first few crossing points around the IP's.

For our calculations, we use the parameters from Table 1.1. With our usual approximations and no crossing angles at the IP's, the bunch length has no effect on our calculations. The energy spread has some small effect.

Table 6.17 shows the planned separator configuration and settings for both the BD15 and the JJ15C lattices at 1 TeV. We are comfortable with separator settings as high as 4.24 MV/m. This corresponds to ± 106 kV on the plates across a gap of 5 cm. All the settings in Table 6.17 are below this limit.

The separator configuration shown in Table 6.17 is the configuration used for Runs IA and IB. That is, no separators have been moved or added. For Run II, both the rf system and the injection and extraction points will be near F0. To make more room there, we are considering moving the horizontal separator at F17 to D48. We have not gone through the detailed calculations for this, but this move would have only a small effect on the horizontal separation and we do not believe this would be a problem.

Table 6.17. Separator settings for 396 nsec bunch spacing ((bd15, jj15c2).pppp52).

Separators (# of modules)	BD15 Setting (MV/m)	JJ15C Setting (MV/m)
B11H (2)	4.162	4.214
B17H (4)	-2.814	-2.721
C49H (1)	3.049	2.039
D11H (2)	3.366	4.034
F17H (1)	-0.923	-1.388
A49H (1)	-4.018	-3.953
B11V (1)	-3.999	-3.727
C17V (4)	2.861	3.195
C49V (2)	-3.091	-3.995
D11V (1)	3.944	3.986
A17V (1)	-2.265	-2.639
A49V (2)	-3.205	-3.977

For the separator settings in Table 6.17, we first found the combination of separator settings that made closed three bumps between the IP's in each plane. We then scaled these combinations so that the strongest separator in each three bump was at 4.0 MV/m, just below our limit of 4.24 MV/m. Finally, we changed these settings slightly to compensate for the effects of the calculated beam-beam dipole kicks.

Unlike the 132 nsec case (see section 6.15.2), the signs for the different pieces of the separation bumps aren't very important. With no crossing angles, we don't have to be concerned about how the separation due to the arc helix combines with that from the crossing angle bumps. The beam-beam tune shifts don't depend on the signs of the separations between the beams. Apart from an overall sign, the beam-beam transverse coupling and the sum of the beam-beam dipole kicks only depend on the relative signs between the helices in the long arc and in the short arc. The coupling only depends on the product of the signs of the horizontal and the vertical separation bumps. The sum of the vertical beam-beam dipole kicks only depends on the relative signs of the long and short vertical separation bumps and similarly for the horizontal.

For both the BD15 and the JJ15C lattices, the horizontal separation in the short helix is not as large as we would like. For BD15, the short helix has peak horizontal separations of about 4.5 mm, whereas the other pieces of the helices (the vertical separations in the short helix and the horizontal and vertical separations in the long helix) have peak separations of about 5.5 mm. For JJ15C, the short helix has peak horizontal separations of about 3.0 mm, whereas the other pieces of the helices have peak separations of about 6.0 mm. The problem is that the horizontal phase advance between the B11 and the B17 horizontal separators is too close to π radians. As a result the effects from these two separators partially cancel through most of the arc. Although we would like to improve this, these separation schemes still appear to be acceptable.

Table 6.18 shows the bunch by bunch orbit differences for the antiprotons. The separations should be compared to the nominal beam size at the IP of 33.1 μm . The angular separations should be compared to the ratio of the transverse beam size and the bunch length. This is $(33.1 \mu\text{m})/(37.1 \text{ cm})=89.2 \mu\text{rad}$. On these scales, all the separations and angular separations in Table 6.18 look reasonably small. Also the values are nearly the same for the two lattices.

Table 6.18. Bunch by bunch orbit differences at the IP's

			B0		D0	
			horz	vert	horz	vert
BD15	pos (μm)	stnd dev	1.1	0.8	0.9	0.7
JJ15C	pos (μm)	stnd dev	0.9	0.6	1.1	0.4
BD15	angle (μrad)	stnd dev	7.5	2.4	1.3	6.2
JJ15C	angle (μrad)	stnd dev	7.4	2.5	0.9	5.3
BD15	pos (μm)	max – min	4.2	2.4	2.9	2.6
JJ15C	pos (μm)	max – min	2.7	2.0	3.4	1.5
BD15	angle (μrad)	max – min	22.0	7.7	4.9	18.2
JJ15C	angle (μrad)	max – min	21.6	7.7	3.0	16.4

For particles with zero betatron amplitudes in each of the bunches, we have also calculated the horizontal and vertical tune shifts and two transverse coupling components. The ranges in these are summarized in Table 6.19 and the horizontal and vertical tune shifts are also plotted as open circles in Figure 6.60 and Figure 6.61.

Table 6.19. Bunch by Bunch Zero Amplitude Tune and Coupling Differences

		horz tune	vert tune	coup cos	coup sin
BD15	stnd dev	.0020	.0019	.0001	.0003
JJ15C	stnd dev	.0012	.0014	.0002	.0006
BD15	max – min	.0079	.0078	.0004	.0009
JJ15C	max – min	.0052	.0054	.0007	.0019
BD15	max – min (A02–A11)	.0014	.0012	.0003	.0008
JJ15C	max – min (A02–A11)	.0010	.0012	.0006	.0018

The two transverse coupling components shown in Table 6.19 are the ones related to the resonance ($v_x - v_y$). These two components combine in quadrature to give the minimum tune split. Both the spreads in these components and in the resulting minimum tune splits look reasonably small for all the bunches. The coupling components for bunches A01 and A12 are close to those for the other bunches.

For the horizontal and the vertical tune shifts, the central ten antiproton bunches, A02 to A11, are tightly clustered together. This can be seen in the (max–min) in the last two lines of Table 6.19, where we have excluded A01 and A12. But the bunches on the edges of the trains, A01 and A12, are clearly separated from this cluster. This is reflected in the much larger (max–min) tune shifts in the middle two lines in Table 6.19. A01 is displaced vertically and A12 is displaced horizontally. This can be seen in Figure 6.60 and Figure 6.61.

The differences between the tune shifts of A01 and A12 and the rest of the bunches are due to the large tune shifts from the first crossing points on either side of the IP's. At these points, only A01 and A12 do not encounter protons.

At the first crossing point upstream of the IP's (upstream in the sense of the proton direction), the separation is mainly vertical, but the horizontal beam size is large. For BD15, at this point, the horizontal and vertical separations are about 0.5 mm and 1.1 mm, respectively and the horizontal and vertical beam sizes are 0.77 mm and 0.16 mm, respectively. As a consequence, this point contributes a large horizontal tune shift, about 0.0038. For JJ15C, at this point, the vertical separation is larger, about 1.5 mm (mainly due to higher settings for the A49 and the C49 vertical separators*) and the horizontal beta is significantly smaller, resulting in a smaller horizontal beam size, only about 0.62 mm. Both the larger vertical separation and the smaller horizontal beam size make similar contributions and together they reduce this point's horizontal tune shift to about 0.0021.

For the first crossing point downstream of the D0 interaction point, the situation is essentially the same except with horizontal and vertical interchanged. For the first crossing point downstream of the B0 interaction point, the settings of the B11 horizontal separator are similar for JJ15C and for BD15, so there is not as much of a reduction in the vertical tune shift for JJ15C. This point contributes a vertical tune shift of about 0.0027 in BD15 and about 0.0019 in JJ15C.

As a result of the smaller tune shifts from these first crossing points for JJ15C, the separation between the central cluster of bunches and either A01 or A12 is about 1/3 smaller in JJ15C than in BD15. This helps to make the particle distribution in the tune plane more compact for JJ15C than for BD15 and is a significant advantage for JJ15C.

* Ignoring the short horizontal separation bump, for BD15, the limiting separators are the vertical separators at B11 and D11 and the horizontal separator at A49. For JJ15C, the vertical β at the B11 and D11 vertical separators and the horizontal β at the A49 and C49 horizontal separators are about 25% larger than for BD15. This gives these separators a stronger effect for the same setting in JJ15C. Since these separators have a stronger effect, the separators on the other end of the bump have to be made stronger. Together, these give JJ15C more separation at the first crossing points. This is the largest contribution, but there are several other small effects.

As an example, for JJ15C compared to BD15, for the first crossing point upstream of the IP's, the vertical separator at the 49 location is about 25% stronger, the vertical β at these separators is smaller by about 10%, the vertical β at the first crossing point is about 17% larger, and the vertical phase advance between the vertical separator and the first crossing point is better, giving about 5% better efficiency. All together these give about 40% more vertical separation at this point for JJ15C than for BD15.

We also calculate the changes in the tune shifts as a function of a particle's betatron amplitudes. We look at a typical bunch in the middle of a train, A06.

Figure 6.50 and Figure 6.51 show the contributions from crossing points further than 28 half RF buckets from the IP's. These show the combined contributions from 66 proton crossings, but skip the effects from the IP's and the first crossing point on either side of the IP's. The contribution to the tune spread from the many crossing points in the arcs is small for both lattices. The tune spread in Figure 6.51 for JJ15C is slightly smaller than that in Figure 6.50 for BD15.

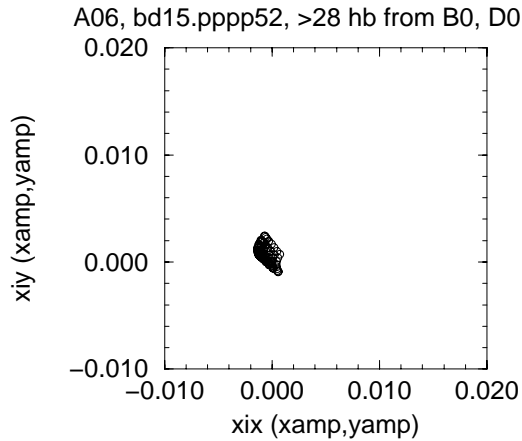


Figure 6.50. BD15, A06, Tune spread from crossing points >28 half buckets from IP's.

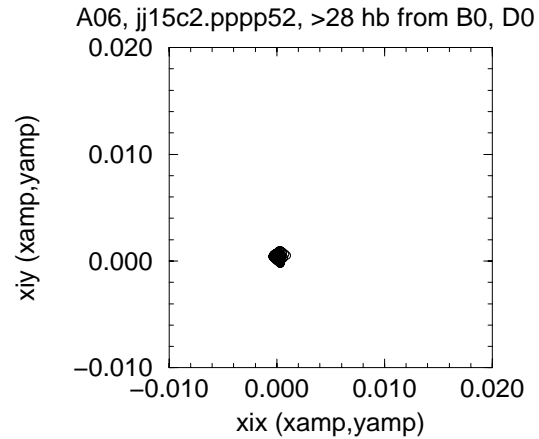


Figure 6.51. JJ15C, A06, Tune spread from crossing points >28 half buckets from IP's.

Figure 6.52 and Figure 6.53 show the contributions from all the crossing points *except* for B0 and D0, the two IP's. We've shown 2 and 3 σ_β contours in Figure 6.52. We did not show contours in Figure 6.53 because they wouldn't be visible. The differences between Figure 6.52 and Figure 6.50 and between Figure 6.53 and Figure 6.51 show the effects of the first crossing points on either side of the two IP's. The effects of these 4 crossing points are larger than the effects from the other 66 crossing points. For JJ15C, the tune spread in Figure 6.53 is still quite small. In Figure 6.52, the tune spread for BD15 is substantially larger than for JJ15C, though still much smaller than the 132 nsec cases. Earlier, for the first crossing points on either side of the IP's, we noted several advantages in the JJ15C lattice that reduced the tune shift for zero amplitude particles. These advantages also help to reduce the tune spread as a function of the particle's betatron amplitudes.

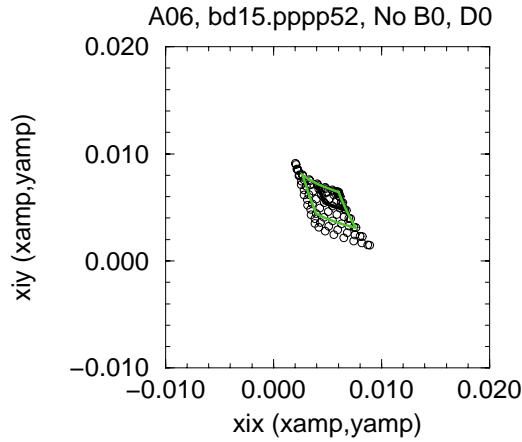


Figure 6.52. BD15, A06, Tune spread from all crossing points *except* B0 and D0.

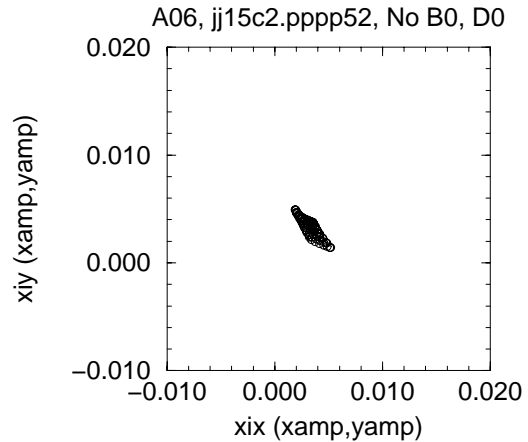


Figure 6.53. JJ15C, A06, Tune spread from all crossing points *except* B0 and D0.

The tune shifts shown in Figure 6.52 and Figure 6.53 have the same "sense" as the footprints from the IP's. In these figures, small amplitude particles are in the upper right corners. Particles with horizontal and vertical amplitudes of $(0, 4\sigma_{\beta y})$ are at the bottom right corners, particles with horizontal and vertical amplitudes of $(4\sigma_{\beta x}, 0)$ are at the upper left corners, and particles with horizontal and vertical amplitudes of $(4\sigma_{\beta x}, 4\sigma_{\beta y})$ are at the bottom left corners.

Figure 6.54 through Figure 6.57 show the same things except for bunches A01 and A12 rather than A06. In Figure 6.54 and Figure 6.56, the tune spread for these bunches for BD15 is much bigger than that in Figure 6.55 and Figure 6.57 for JJ15C. By coincidence, the spacing between crossing points with 396 nsec bunch spacing is almost exactly the cell length in the Tevatron. As it happens, A01 always encounters proton bunches at horizontally focusing locations, where β_x is large and β_y is small, and A12 always encounters proton bunches at vertically focusing locations, where β_y is large and β_x is small. As a result, for A01, the tune shifts are almost entirely horizontal and for A12 the tune shifts are almost entirely vertical.

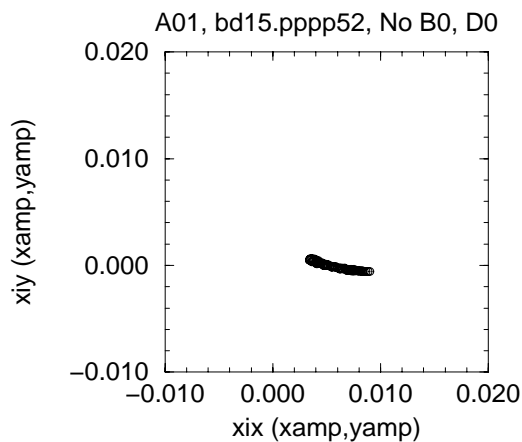


Figure 6.54. BD15, A01, Tune spread from all crossing points *except* B0 and D0, the main IP's.

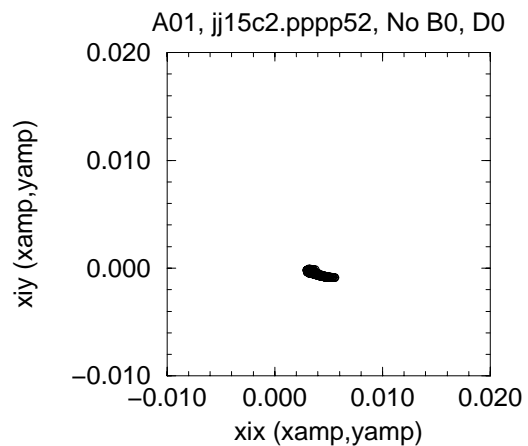


Figure 6.55. JJ15C, A01, Tune spread from all crossing points *except* B0 and D0, the main IP's.

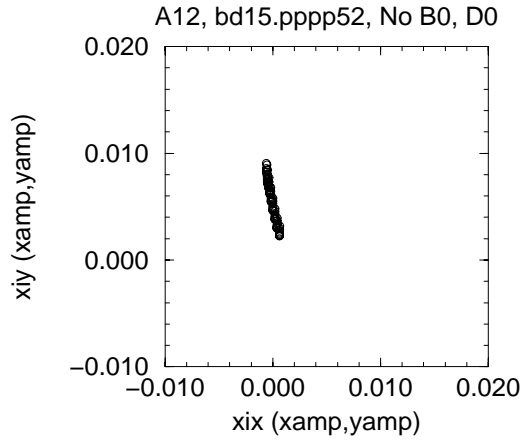


Figure 6.56. BD15, A12, Tune spread from all crossing points *except* B0 and D0, the main IP's.

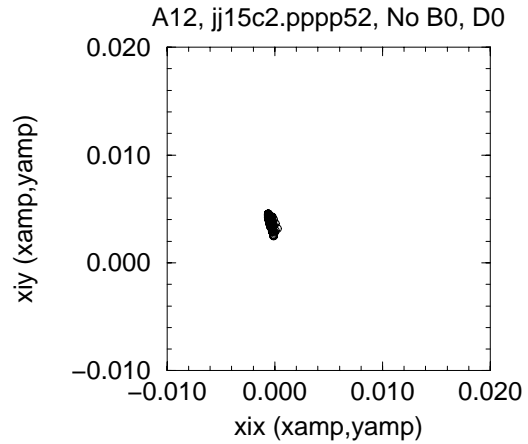


Figure 6.57. JJ15C, A12, Tune spread from all crossing points *except* B0 and D0, the main IP's.

Figure 6.58 and Figure 6.59 show the combined effects from all crossing points. These footprints aren't folded. They are pretty close to the usual shape for a head on beam-beam interaction with round beams.

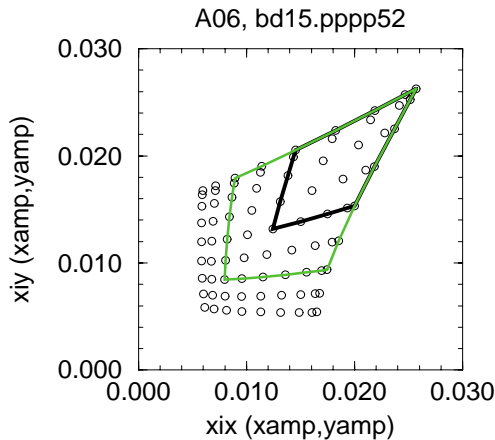


Figure 6.58. BD15, A06, Tune spread from all crossing points.

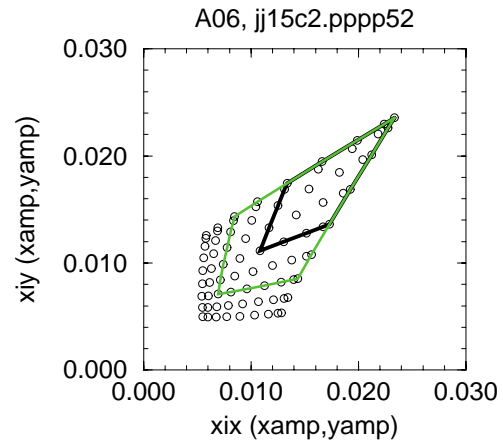


Figure 6.59. JJ15C, A06, Tune spread from all crossing points.

Figure 6.60 and Figure 6.61 show scatterplots of the combined tune footprints for all the bunches. The darker the points, the more particles that have those tunes. The open circles in these figures are the tune shifts for zero amplitude particles in each bunch. For both lattices, the zero amplitude particle tune shifts for A01 and for A12 are displaced vertically and horizontally, respectively, from the cluster of points for the other bunches. The separation between the zero amplitude tune shifts for A01 and A12 and the rest of the bunches significantly increases the amount of space taken up in the tune plane. This is smaller for JJ15C than for BD15, but is still a problem for both lattices.

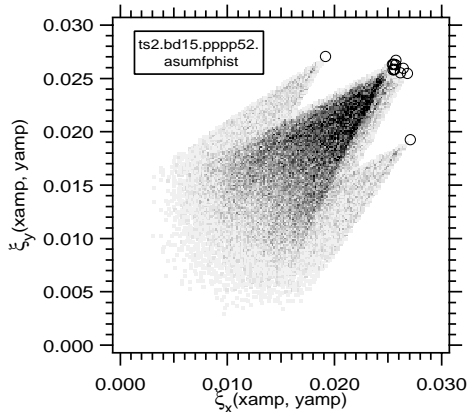


Figure 6.60. BD15, All bunches. Tune spread from all crossing points.

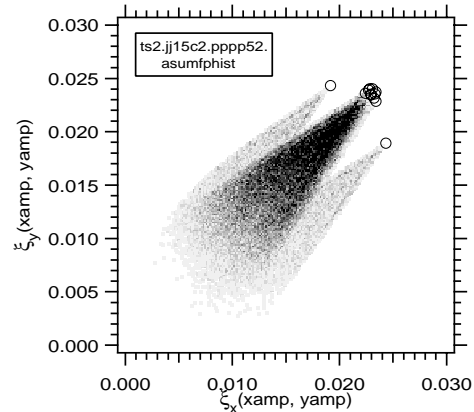


Figure 6.61. JJ15C, All bunches. Tune spread from all crossing points.

These scatterplots should be compared to the Figure 6.62 showing the resonances in the tune plane near our usual operating point of about (.585, .575). Neither the histogram for BD15 nor that for JJ15C fit nicely between the resonances. For BD15, we expect we would straddle the ($v_x=v_y$) line and the 7th and 9th order difference resonances. The distribution for JJ15C is smaller and, if we straddle the 7th and 9th order difference resonances, we can keep almost all the particles below the ($v_x=v_y$) line.

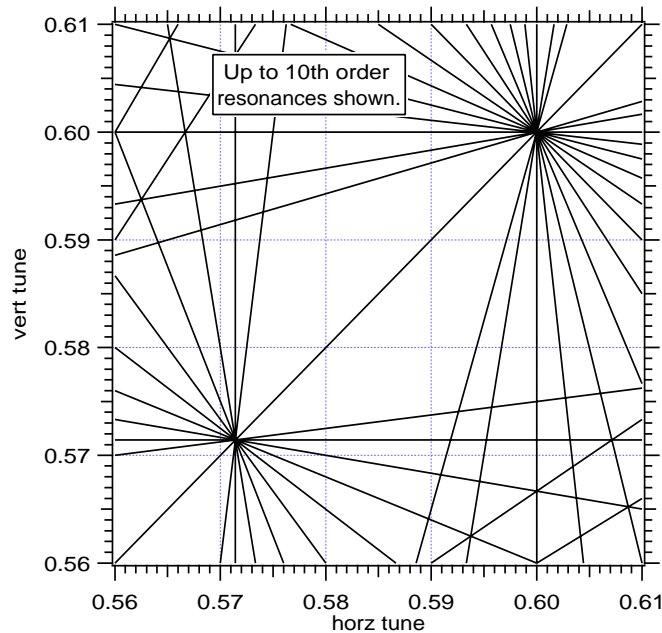


Figure 6.62. Tune plane near our usual operating point of about (.585, .575), showing resonances up to 10th order.

The effects of the first crossing points on either side of the IP's are smaller in the lattice JJ15C than in the lattice BD15. As a result, for JJ15C, the total tune spread due to all the parasitic crossings is smaller and the zero amplitude particle tune shifts for bunches A01 and A12 are closer to those of the other bunches. These two effects both reduce the amount of space taken up in the

tune plane for JJ15C. Mainly for these reasons, we plan to use the JJ15C lattice for Run II. We believe that the distribution for JJ15C is acceptable, but we still intend to try to improve it.

We can also consider filling schemes that are not three fold symmetric. Imagine a proton and an antiproton bunch colliding at B0. At this moment, there must be a proton bunch at F0, if we require that this antiproton bunch also collides with a proton bunch at D0. (Two thirds of a revolution later, the antiproton bunch will have gone counter-clockwise around the ring from B0 to F0 to D0 and the proton bunch that started from F0 will have gone clockwise around the ring from F0 to B0 to D0.) The proton bunches at B0 and F0 are separated by exactly one third of the ring or 371 RF buckets. 371 RF buckets is $53 \times (7 \text{ RF buckets})$, so for the 132 nsec (7 RF bucket) bunch spacing we could fill every 7th RF bucket between these two proton bunches. But for the 396 nsec (21 RF bucket) bunch spacing, we must leave a gap.

For the 396 nsec bunch spacing, we are considering a 46×41 filling scheme. The proton beam has one abort gap and two small gaps to fill out the thirds of the ring. We would have 17 proton bunches with a 396 nsec or 21 RF bucket spacing. The spacing to the next proton bunch is 35 RF buckets. This completes $1/3$ of the ring. The filling pattern for the second third of the ring is a repeat of the first third. The last third of the ring has the abort gap, so here there are only 12 proton bunches with the 21 RF bucket spacing, followed by the 2.6 μ sec abort gap. This gives a total of $(17+17+12)=46$ proton bunches. The filling scheme for the antiproton beam is very similar except it has two abort gaps and one small gap. This gives a total of $(12+12+17)=41$ antiproton bunches.

With this filling scheme, all the antiproton bunches will collide with proton bunches at both B0 and D0. All the proton bunches collide at least once with an antiproton bunch, but some protons collide with antiprotons at *both* B0 *and* D0 and others only collide with antiprotons at B0 *or* at D0. This difference between some of the proton bunches will make it more difficult to find conditions that are good for *all* the proton bunches.

In the 132 nsec case, one of the major advantages from the 140×121 case is that if an antiproton bunch does *not* see a proton bunch at, say, the first crossing point upstream of D0, then it *will* see a proton bunch at the first crossing point upstream of B0. Since these points are often similarly bad, this helps to reduce the difference between this bunch and the others by nearly a factor of two over the 90×90 case. However, for the 46×41 case, we *only* get this advantage for the last antiproton bunch at the ends of the 2 short trains of 12 antiproton bunches. For the 36×36 filling scheme, the biggest problem is from the first crossing points on either side of the IP's. For the 46×41 filling scheme, consider an antiproton bunch that does *not* see a proton bunch at the first crossing point upstream of D0 (upstream in the antiproton sense). Because of the short gap in the proton beam of 34 empty RF buckets to fill out the third of the ring, this antiproton bunch does *not* see a proton bunch at the first crossing point upstream of B0 either.

6.9 Beam Halo Scraping

The hardware, software, and procedures used for beam halo scraping in the Tevatron at the beginning of a colliding beam store must be improved for Run II in order to reduce the losses at B0 and D0 to a level the Collider experiments can tolerate. In addition, during Run 1b the typical scraping procedure took about 20 minutes at the beginning of each store -- sometimes much longer if there was an emittance blowup during acceleration, incorrect tunes, large orbit distortion, or some other anomalous condition. We are building an automated Tevatron beam collimation system that will scrape the beam halo at the beginning of each store quickly and in a systematic manner.

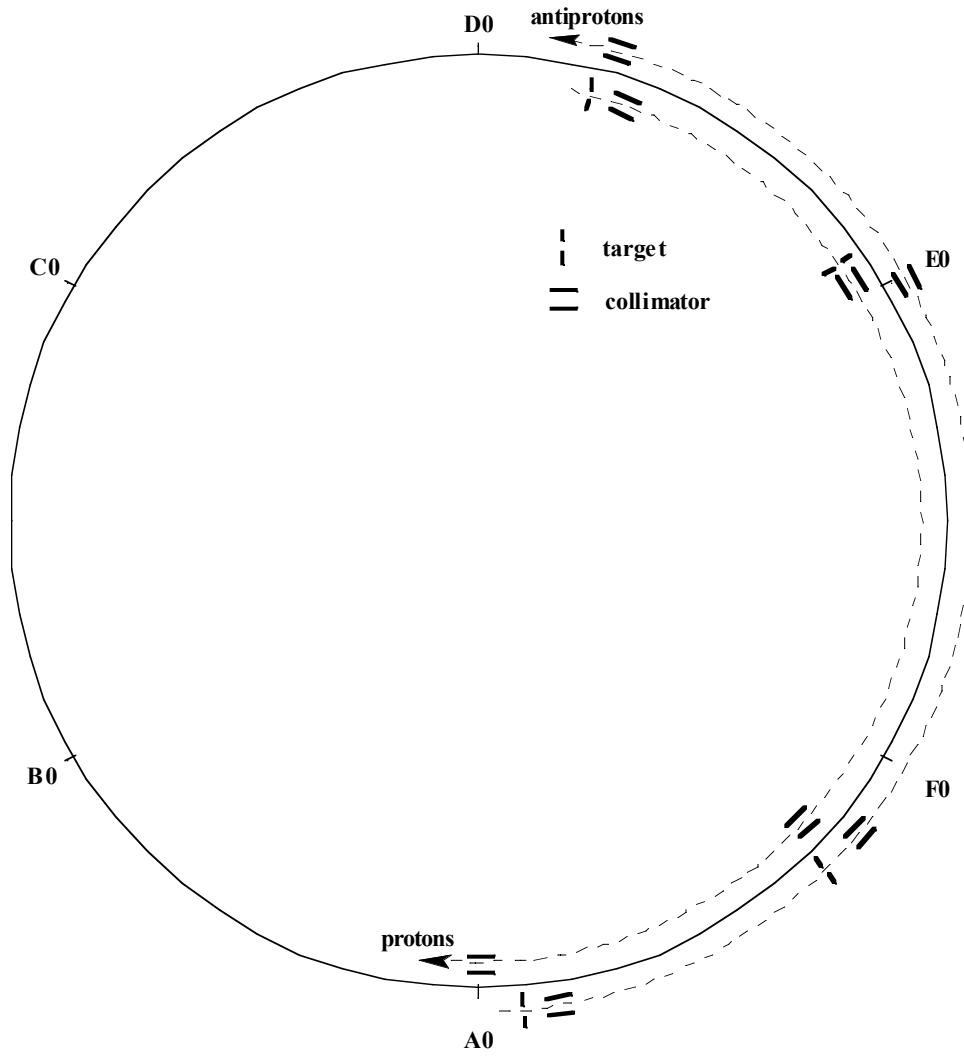


Figure 6.63. Schematic of collimator layout in the Tevatron for Run II

Currently there are 4 collimators in use in the Tevatron. At F49, A0, and F17 the collimators are stainless steel, 0.61m in length. At D17 the collimator is carbon steel 1.8m in length. Furthermore the collimator at A0 has two thin tungsten "lips" welded onto each end to act as targets. During Run 1b the collimators at D17 and F49 were used for the scraping proton halo, and the collimators at A0 and F49 were used for the scraping antiproton halo.

For Run II we will use a two-stage collimation system already pioneered at SPS²⁸ and HERA.²⁹ A target, consisting of a movable, narrow tungsten lip 5 mm thick, acts to scatter the particles in the beam halo. Secondary collimators, consisting of 1.5 m long stainless steel absorbers, are located at a suitable phase advance downstream of the target to intercept the scattered particles. The target is moved to about 5 to 6 σ of the beam axis to become the limiting aperture in the machine. The scattered particles are efficiently intercepted by the collimators placed at about 8 σ from the beam axis. Targets will be located at D17(1) and D49 to scatter protons with both vertical and horizontal large emittances. Collimators will be located downstream at D17(3), A0,

E0(1), and F17(2). For antiprotons, targets will be located at F17(3) and F49, with collimators downstream at F17(1), E0(2), F48 and D17(2). As shown in Figure 6.63, there will be a total of 4 targets and 8 collimators to be used for beam halo scraping. There is also 1 extra collimator to be placed at E0 for the proton removal system described in the proton removal section of this report. Table 6.20 lists the phase advances from target to collimator and the beta functions at each. In order to obtain suitable phase advances and proton/antiproton orbits, the 2 Tevatron tune quad circuits have been split into 6 separate circuits, and another 7 quads will be powered independently. Loss calculations have been done using the STRUCT³⁰ and MARS³¹ codes, to understand backgrounds at B0 and D0.

Table 6.20. Beta functions, phase advances from target, and beam separations at collimators

collimator	protons		antiprotons				beam separation	
	ϕ_x (deg) (mod 360)	ϕ_y (deg) (mod 360)	ϕ_x (deg) (mod 360)	ϕ_y (deg) (mod 360)	β_x (m)	β_y (m)	x (mm)	y (mm)
D17(1) target	0	0	326	354	87	34	4.41	1.80
D17(2)	6	12	320	342	63	47	3.41	2.82
D17(3)	8	14	318	340	58	52	3.18	3.06
D49 target	170	185	156	168	88	75	5.02	3.08
E0(1)	183	193	143	160	59	94	3.60	4.08
E0(2)	213	224	112	129	96	59	2.14	4.47
E0(3)	214	226	111	127	99	59	2.07	4.49
F17(1)	144	167	182	187	96	28	5.81	0.98
F17(2)	145	171	181	183	90	29	5.60	1.22
F17(3) target	151	184	175	170	64	41	4.74	2.19
F48	312	308	14	46	99	29	5.76	1.17
F49 target	326	354	0	0	179	40	7.74	1.59
A0	331	18			160	61	7.37	3.56

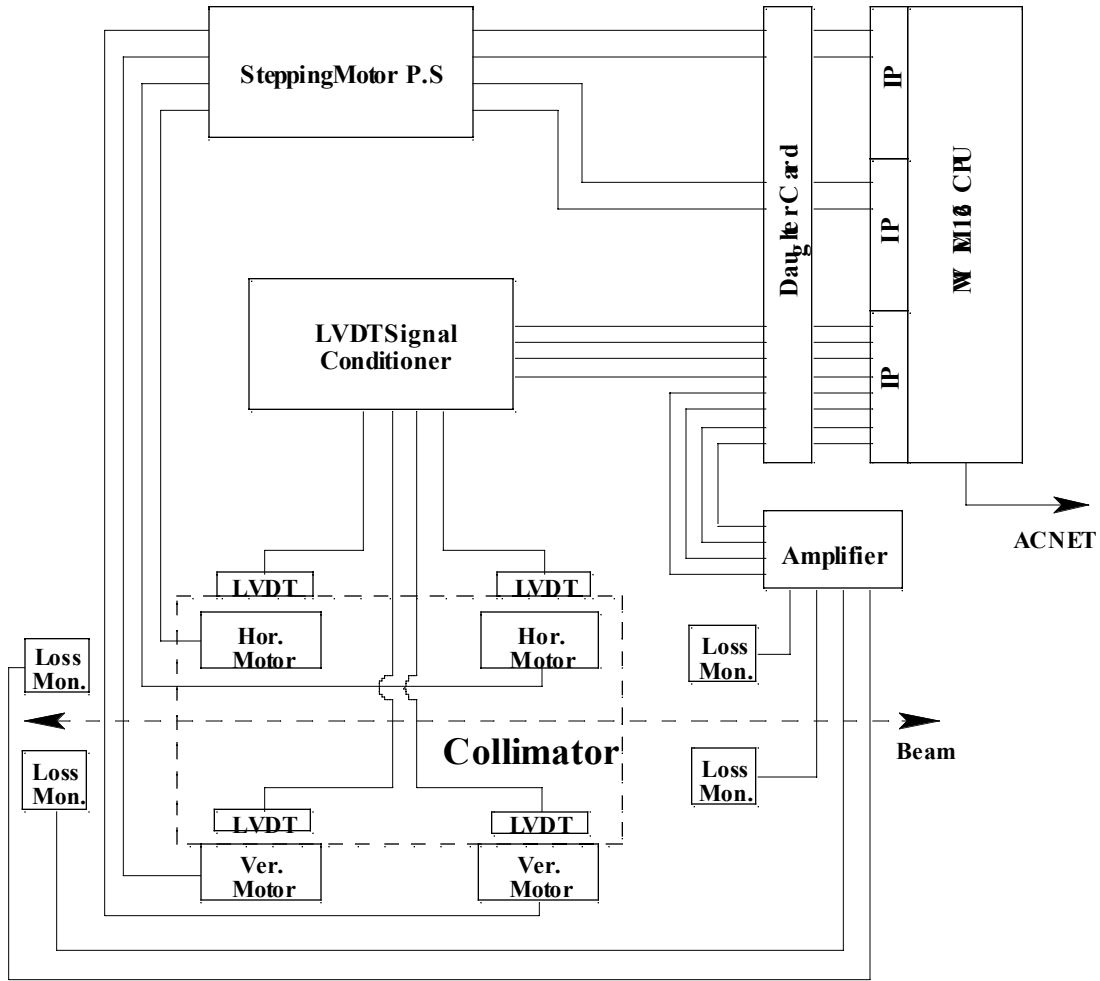


Figure 6.64. Block diagram of collimator control system

A block diagram of the controls for a single beam collimator is shown in Figure 6.64. Each collimator station will be controlled by an MVME162 processor running VXWORKS in a VME crate located in a nearby service building. Targets will have a single motor for vertical motion and a single motor for horizontal motion; collimators will have 2 motors in each dimension to control upstream and downstream motion independently. The stepping motors will run at 400 steps/turn, and will be geared so that the collimator can be moved ~1" in 13 seconds, which is approximately the distance from the full out position to the beam axis. This gearing will yield a minimum step size of .000125". Position readback is provided by LVDT's (Linear Variable Differential Transformer) – 4 per secondary collimator, 2 per primary collimator, and limit switches will protect the hardware from damage. Position readback will have an lsb of .00003', although the signal/noise ratio will limit position sensitivity to about .0005". Local fast feedback for the motion control, operating at a 720 Hz cycle in the CPU, will be provided by 4 standard TEV loss monitors -- 2 upstream and 2 downstream for redundancy. Stepping motors, loss monitors, and LVDT's will be interfaced to the CPU via 3 IP's (Industrial Packs), and cabling will be handled by a Fermilab-designed daughter board. Communication with ACNET will be via Ethernet. More than one system can be installed in a single VME crate. A prototype system has

been assembled and software is undergoing development using a prototype collimator stand in the lab.

The beam halo scraping sequence will be controlled by an application program that will initiate motion for each collimator and wait for completion status from that collimator before initiating the next collimator. It is envisioned that the entire beam halo scraping system will take approximately 5 minutes. In the simplest algorithm, a collimator will simply move into the beam until the local losses reach a certain level (scaled by beam intensity), then stop and inform the controlling application program of its completion. More complicated algorithms are being developed and can easily be handled within the 720 Hz feedback loop.

6.10 Antiproton Recycling from the Tevatron

6.10.1 Proton Removal

Once a store has been completed and we are ready to begin the next collider fill it is necessary to first decelerate the antiprotons in order to recycle them. Based on operational experience accelerating protons and antiprotons simultaneously, it is felt that a high antiproton deceleration efficiency will be operationally much easier if the protons are removed before the deceleration. Without the protons in the machine the long range beam-beam effects are no longer an issue and the helix can be collapsed to provide more aperture for the antiprotons which will have larger emittance at the end of the store.

Since it is impractical to use a kicker at 1 TeV to remove the protons without disturbing the antiprotons, the plan is to remove the protons by scraping them away with a collimator. The challenge will be to remove the 10^{13} protons in 2 minutes at 1 TeV without quenching the superconducting Tevatron magnets. The scraping process creates particle losses, which deposit energy in the superconducting magnets causing them to warm up and quench. To shield the superconducting magnets from the losses, a set of four Main Ring dipoles have been installed in the E0 straight section to form a double dogleg. The target collimator is located between the first and second magnets as shown in Figure 6.65. Since the orbit is not parallel to the Tev centerline at the location of this target, the neutral particles are pointed away from the superconducting magnets and the dogleg bends sweep away the negative particles and low energy positive particles.

Calculations of losses in the Tevatron magnets for such a scheme have been done and suggest it is possible to remove 1×10^{13} protons in 100 seconds. These calculations were done using a geometry similar to that shown in Figure 6.65 but with the double dogleg magnets located downstream and the space for the superconducting RF located upstream. The calculations used a target collimator located between the first and second MR magnets and a secondary collimator downstream of the fourth dogleg magnet. The secondary collimator was a rectangular aperture with height and width equal to 10 sigma of the proton beam width at collisions. With this geometry the loss calculations give a loss rate of 1.5 W/m in the superconducting magnets downstream of the collimator. Also in these calculations the MR magnets were assumed to operate near 4440 Amps and provide a bend angle of 2.8 mrad for the protons. The value of 4440A was chosen since this is the current of the TeV bus at 1 TeV and the initial idea was to run the MR magnets in series with the Tev bus.

Even though calculations suggest this scheme works, there is a technical problem with cooling the MR magnets running at a DC current of 4440A. The calculated temperature rise at this current is 95 degrees Fahrenheit with a 10 gpm flow rate of LCW. This results in magnet temperatures of an unacceptably high 200 degrees Fahrenheit. Also, running four B2 magnets at 4440A continuously would cost \$67,000 per year at 5.5 cents per kW-hr. Thus the choice was

made to operate the B2 magnets with an independent power supply. This allows the B2 magnets to be turned on only while performing the proton removal and allows the magnets to be run at a lower current. It was also decided to use the geometry in Figure 6.65 so the loss calculations will have to be repeated with the updated geometry although no significant change in the shielding effectiveness is expected with the new geometry.

To power the dogleg magnets an existing 500 kW Transrex power supply (5000A @ 100V Transrex model ISR2126-2) can be used with the four B2 magnets connected in series electrically. The maximum current is limited to about 3280A because of the 100V maximum power supply voltage and the total resistance of the magnet coils ($4 \times 7.2 \text{ m}\Omega$) and bus ($1.7 \text{ m}\Omega$). We should be able to run at 3280A with a ramp time of 10 sec ($L=4 \times 8 \text{ mH}$, so L/R is about 1 second). Operating the MR magnets at this current bends the beam by 2.3 mrad at 1 TeV and should provide sufficient bend to protect the superconducting magnets.

The power supply may or may not need a filter. The question is whether the ripple in the magnetic field will translate into too much orbit motion at the location of the scraper. Assuming a 20V peak-to-peak ripple at 720 Hz into a 28 m Ω load the current ripple is 0.10A, which is 1 part in 25,000 at 3280A. With a 2.3 mrad bend, the peak-to peak wobble of the beam position on the target collimator is 0.4 microns. This is smaller than the rms wobble from other sources.

The magnets are placed in parallel for the purposes of water cooling. At 3280A the power dissipation is 78 kW per magnet and with 10 gpm LCW flow the temperature rise is calculated to be 52 degrees Fahrenheit.

At the upstream end of E0, the helical orbit for the low beta lattice V3H15a puts the protons 1.8 mm to the radial inside and 2.2 mm vertical downward. (The antiprotons are at +1.8 mm horizontally and +2.2 mm vertically.) The beta functions at the location of the primary collimator are about 60 meters horizontally and 95 meters vertically. With these orbit separations and beta functions the protons can be scraped away completely by moving the primary collimator from the radial inside and still leave more than 220π mm-mrad for the antiproton beam.

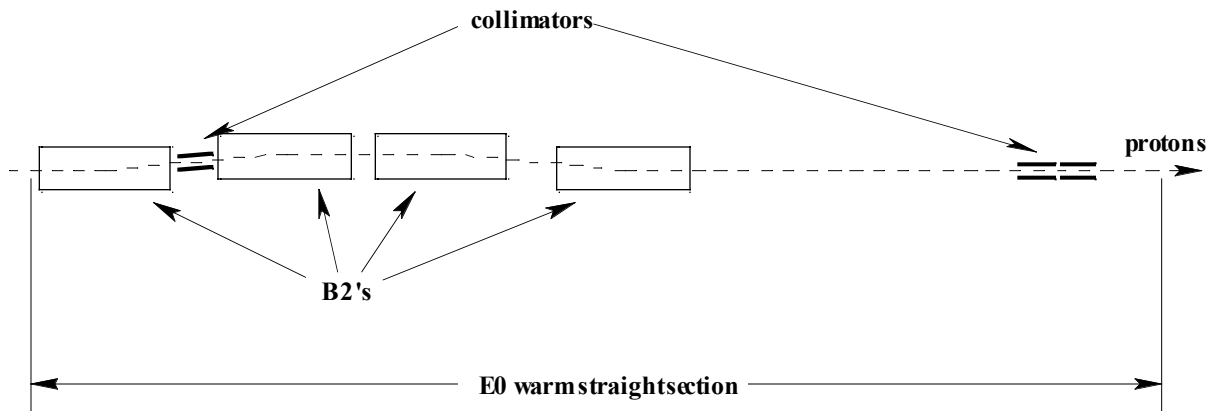


Figure 6.65. Sketch of the proton removal system at E0. Transverse scale is exaggerated. Space is left in this straight section for possible superconducting RF in the future.

6.10.2 Antiproton Deceleration

Part of the Run II plan for increasing the number of antiprotons available for collisions requires the Tevatron to recycle the antiprotons at the end of a Collider store by decelerating them from an energy of 1 TeV to 150 GeV for extraction into the Main Injector. While some tuning will be required to decelerate and extract antiprotons from the Tevatron, no fundamental problems are expected. The following outlines the scheme for deceleration of the beam in the Tevatron and subsequent transfer to the Main Injector.

Once the protons have been removed (see section 6.10.1), the electrostatic separators will be turned off and the β^* will be increased from its low beta value of 35 cm to the injection value of 170 cm. The sequence to accomplish this ("Recover From Low Beta") already exists, but is currently used only after beam has been removed from the machine. This step has been accomplished with beam under study conditions. The beam will be decelerated to 150 GeV. A new sequence will be created to accomplish the deceleration. There is a great amount of flexibility already built in to the power supply controllers (CAMAC cards). All the power supply controllers generate outputs that are the sum of 3 independent tables. Each sequence has its own group of 3 tables. This architecture makes it easy to have separate tables that function to correct the effects of hysteresis (if necessary) and persistent currents. The dipole corrector power supply controllers are being upgraded to the same type of controller as other Tevatron power supplies.

The ramp wave form used in Run I had a maximum rate of rise of 16 GeV/sec. This value was chosen so that acceleration could take place with a single RF cavity off. The deceleration waveform was a mirror image of that acceleration waveform. In Run II, the acceleration waveform may increase to 24 GeV/sec, but the deceleration portion of the ramp will remain at the slower 16 GeV/sec ramp rate. This ramp rate is slow enough that the one quadrant low beta power supplies can stay in regulation during the deceleration process.

The antiprotons will have to remain in the Tevatron at 150 GeV long enough for several transfers through the Main Injector to the Recycler. The number of transfers required will depend on the waveform of the proton injection kicker that is built. There will likely be nine transfers of four antiproton bunches to the Main Injector. The length of time that antiprotons must be stored on the Tevatron back porch is on the order of 10 minutes. Magnetic measurements of the dipoles would indicate that about 30 units of chromaticity drift would be expected during that time period. Experience with beam measurements has shown that less drift occurs on the front porch than would be predicted by the magnetic measurements.

Beam has been successfully decelerated from 800 GeV to 150 GeV during studies. The studies took place during a fixed target runs so the lattice, energy, and bunch structure was not representative of the collider run. Chromaticity drifts were measured on the 150 GeV porches. The drift on the back porch is dependent on the length of the preceding flattop. Typical chromaticity drifts on the back porch were on the order of 20 units in 15 minutes. The drift on the front porch is a function of both the length of the preceding flattop as well as the length of the preceding back porch. During previous collider runs, the Tevatron has compensated for about 25 units of chromaticity drift in the first half hour on the front porch. There will be less chromaticity drift on the front porch than in previous collider runs because of the presence of a back porch in Run II.

More magnetic measurements before the start of Run II could be used to establish the functional form of the chromaticity drifts with varying ramp histories. During the commissioning of the collider run, the drifts will have to be re-measured in the real machine to obtain the actual time constants of the chromaticity change.

During the previous collider run, the ramp history was made to be the same every store by cycling the ramp to full energy six times between each store. The front porch chromaticity drift was compensated for by playing a pre-defined table as a function of time on the front porch. In order to streamline shot setup in Run II, the six ramps will not be played between stores. This will necessitate the loading of new tables to compensate the chromaticity drifts every store. These tables will be a function of the recent history of the Tevatron ramp. Because of the new technique that will be used to control β^* in the Tevatron, the table used last run for compensation will not be available. Because of this, a second power supply controller will be used for the sextupole power supplies. The waveform to the power supplies will then be the summed output of the two controllers.

6.11 Instrumentation

The increased number of Tevatron bunches combined with a shorter injection cycle time leads to the necessity of upgrading the existing instrumentation. A side issue is the loss of available warm sections suitable for instrumentation, due both to the installation of new Run II hardware, and a new C0 collision region. This chapter lists the various devices used for beam diagnostics in the Tevatron and the plans for Run II upgrades. For the most part, these upgrades are directed at coping with the harsher operating conditions of the Tevatron, but some either add new capabilities and/or fix known problems diagnosed from earlier runs. Although this section primarily deals with the Tevatron, since it is the most challenging environment, similar instrumentation in the other machines will also be upgraded in due course. The last part of this chapter discusses the instrumentation problems for operations with more than 36 bunches.

6.11.1 Initial Run II 36×36

The major issue for the instrumentation in Run II will be the factor of six increase in the number of bunches, and yet only one tenth the time available to acquire, analyze, and report the results. Fortunately faster processors and judicious optimization of existing analysis software will enable the instrumentation to handle the increased data rate. A secondary topic is the directionality (or lack thereof) of the beam insertion pickups and how they will handle the shorter spacing in time between the proton and antiproton bunches.

6.11.1.1 Sampled Bunch Display (SBD), and Fast Bunch Integrator (FBI)

The SBD (fast oscilloscope and local CPU) and FBI (hardware integrator and interface) are primarily used to measure individual bunch intensities. Both rely upon a wall current monitor (with a bandwidth of 3 kHz to 6 GHz) as a pickup. The two systems are complementary in that the SBD provides precision (<2% absolute uncertainty) and the FBI provides speed. In addition the SBD calculates bunch lengths.

The non-directionality of the pickup complicates the bunch measurement when the proton and antiproton bunches overlap in time. A second wall current monitor (already available) could be located at another position to insure that the injection and collision cogging points are adequately covered. In any circumstance, the existing pickup must be moved to a new location to make way for a new Run II device. The SBD needs a two to three bucket separation in time between the proton and antiproton bunch for a clean analysis. The FBI is more critical since its measurement is done in hardware and requires a larger separation. It might be better if the FBI could be moved to a long stripline pickup (with appropriate front-end detector) to gain some directionality, although no

plans exist to do this at this time. The speed of the SBD during injection has been shown to be adequate (better than 3 Hz), while the FBI is basically “instantaneous”.

6.11.1.2 Flying Wires

The Flying Wire (FW) system provides precision transverse beam measurements. It is composed of one vertical, and two horizontal wires. The wire, a 30 micron diameter carbon filament, passes through the beam at 5 m/s creating a pion spray from the beam-carbon interactions. The proton and antiproton beams are measured simultaneously by dedicated (downstream and upstream respectively) scintillator paddles. The signals from each bunch are digitized on a turn by turn basis and stored in the digitizer’s memory. At the end of a fly, the data is read out and analyzed by a local CPU.

The crucial issue for the FW is the accelerator-complex injection cycle time since the Tevatron injection is the last step of this event. Time must be available for both the fly, the data acquisition, the analysis, and SDA (Shot Data Acquisition) readout. Assuming protons are injected before antiprotons and that at least 3 seconds are available between injections, the problem is well in hand. The reason for these requirements is that proton injection (2B Tclock event) is faster than antiproton injection (2A Tclock event). Since no antiproton analysis is necessary during proton injection, the FW analysis time is decreased a factor of two. The current estimate of Flying Wire Cycle time during proton injection (of the 36th bunch) is approximately 3 seconds from the 2B injection event - 0.6 s fly time, 1.4 s analysis time, 1.0 s Acnet and data readout / handling. The longer time available during antiproton injection easily allows the analysis of both beams.

Further speed optimizations (i.e. breaking the one system into three) would add to the costs and complexity of the system. Other more benign solutions would include reducing the amount of data and analysis done at injection. At this stage, these paths do not seem to be necessary, but they are left as options in case they are needed.

6.11.1.3 Sync Lite

Sync Lite is composed of two optical telescopes which image the synchrotron light from the proton and antiproton bunches. It provides a continuous precision on-line measurement of the transverse beam size. It takes data only when beam energy is greater than 800 GeV due to the intensity of the synchrotron light. Therefore its primary use is monitoring the beam size during a store.

Each bunch is handled individually giving a maximum cycle speed (ignoring analysis) of 2.2 seconds for all 72 bunches using a standard 30 frames/sec video camera and a single frame grabber. The data handling/analysis runs at speeds approaching 20 Hz/bunch on today’s machines (200 MHz). This gives a total cycle time of about 6 seconds for all proton and antiproton bunches. Only the period during the Low Beta Squeeze might prefer a faster rate, but at this time it doesn’t seem necessary to look for faster acquisition possibilities. However see the discussion below on the framing mode of streak cameras which offers the potential of faster acquisition.

Two possible upgrades are feasible. The bunch length and relative intensities could be measured (à la SBD) by using a fast photomultiplier tube (pmt) and oscilloscope. If a red sensitive pmt is used ($\lambda \geq 800$ nm), this system could work with energies as low as 300 GeV. A different upgrade would be the correlated measurement of both the transverse and longitudinal bunch sizes using a streak camera. The streak camera could potentially be used to study a single bunch on a turn-by-turn basis or a single turn of all bunches with one frame capture (30 ms) using the streak camera in “frame mode”.

The location of Sync Lite is problematic. The possibility exists that the C0 experiment may begin installation at the START of Collider Run II (when CDF and D0 detectors are rolled in). It isn't clear whether we will have a new location by that time scale. The section on >36x36 operation addresses this issue further.

6.11.1.4 Tevatron Ion Profile Monitor (TIPM)

The TIPM is a turn by turn transverse emittance monitor, which would be especially useful during beam injection. A prototype was installed in the Tevatron near the end of the 1997 Fixed Target Run and proved that the measurement is feasible. A major change planned for Run II (in all the IPM systems from the Booster to the Tevatron) is the collection of the electrons instead of the ions. This variant uses an external magnetic field (2 kG in Tevatron) to confine the electrons, allowing us to dispense with the need for bunch space charge corrections (a major difficulty with the ion collection mode). Since the electrons are collected in a time scale of 3-4 nsec, the proton and antiproton bunches can be separated by timing. However the existing preamplifiers have an integration time scale on the order of a microsecond and would need to be rebuilt with a shorter time constant. Separated orbits at the TIPM locations could also provide unique proton-antiproton identification, but as the available locations are extremely limited, it isn't clear whether this option is available.

6.11.1.5 Collision Point Monitor (CPM)

The CPM is a precision transverse and longitudinal collision point monitor at B0 and D0, which like the SBD uses an oscilloscope and local CPU. It finds the longitudinal collision position to 1.5 cm (rms), and transverse positions to 20 microns (statistical rms only) using the low-beta quadrupole bpm's. Unfortunately the time-delayed feed-through of the strong proton signal into the antiproton signal gives up to a 0.6 mm offset, rendering the transverse antiproton position measurement useless. This offset, in principle, can be removed by further on-line analysis. A working system could be quite valuable when we go to crossing angle operation.

Several hardware and software improvements would be beneficial. The actual replacement of the existing low beta quad bpm's with a new quad-pickup bpm (with a feed-through only on one end of each plate) would be highly desirable. This would greatly reduce the feed-through signal. Software could then easily eliminate any remaining feed-through. The slow cycle time (primarily due to averaging in the oscilloscope) limits the utility of the system during fast scans. We are actively seeking a faster system.

6.11.1.6 Beam Position Monitors (BPM)

The Tevatron BPM system measures beam position, and as a system provides diagnostics (closed orbit and turn-by-turn information). The primary issue for Run II is which bpm positions will give reliable antiproton measurements. The directionality of the bpm striplines is only 25 dB which allows the feed-through of high intensity proton signals to trigger the bpm digitizer when antiproton measurements are wanted. This was solved in Run Ib by slow gating of the intensity signal (the trigger to the digitizer). However the closer bunch spacing will probably render this solution inoperable. As one considers a future upgrade several issues come to the front. They include the front-end analog electronics (single bunch vs. batch processing and the intrinsic position resolution), digitizers and fast gating schemes, local diagnostics (turn-by-turn, fft,.....), and global diagnostics (turn-by-turn synchronization of entire bpm system which would aid lattice measurements). It is obvious that such a system could not be in place for the beginning of Run II. Two technologies are being developed now for the Antiproton Source and the Recycler BPM systems. Hopefully one of the two might be adopted for the Tevatron.

6.11.1.7 Beam Line Tuner (BLT)

The BLT makes a turn-by-turn measurement of a horizontal and vertical bpm to calculate the injection error. As a stand-alone system, it uses a more flexible hardware and software platform than the standard BPM system. Upgrades to this system include a better analog front end than the standard Tevatron RF module, and a faster cycle time (easily possible with a newer processor).

6.11.1.8 Loss Monitors

The standard ion chamber and log amp system will be available for Run II. In addition a new fast system of PIN diodes will be installed at selected location around the ring to monitor individual bunch turn by turn losses.

6.11.1.9 Bunch by Bunch Tune

A new active bunch by bunch tune measurement is being worked on. This system will extract the bunch tune by time gating and phase-locking on the excitation signal. An issue that remains is the pattern recognition of the horizontal and vertical tune lines to extract numerical values of the tune.

6.11.1.10 Luminosity Monitors

Online Luminosity Monitors calculate the luminosity provided to the experiments. Currently the CDF and D0 Luminosity Monitors are built, calibrated, and run by their respective experiments and made available to the Beams Division. They are expected to be operational for Run II. A Beams Division version uses the measurements of the beam to calculate the delivered luminosity. This is also expected to run as before. Currently the accelerator measurement disagrees with the CDF and D0 measurement by 30-40% with the disagreement changing over the length of a store. The comparison of the three may provide some useful insights on the lattice, the instrumentation, and perhaps the proton-antiproton cross-section

6.11.1.11 B0 IP Measurements

A collaboration between CDF and BD plans to place a spare horizontal and vertical FW in B0 collision region during Collider Commissioning in order to make relative measurements of beam size between interaction region and the locations of the Flying Wires and Sync Lite. This will aid our understanding of the lattice.

6.11.1.12 Control Room Display

The large number of bunches requires a graphical display of instrumentation measurements in order to be useful in the Control Room (and elsewhere). The standard techniques using Fast Time Plots and other ACNET utilities are assumed to work as before.

One solution is to implement this display using the standard console programming, which requires application programmers with C (or Java) skills.

A second solution is to make the display locally on the Instrumentation Platforms (which support it) and have it be available in via a standard web servers. A successful example of this is the "SBD On-line" which was implemented during the 96-97 Fixed Target Run. This can be done by the same person responsible for the Instrumentation Platform itself at almost no extra effort.

6.11.2 Instrumentation for 132 nsec Bunch Spacing

At this stage we should consider whether single bunch information is still useful (as opposed to multiple bunch measurements). To some extent this will be decided by the availability of faster CPU's, and by the ability of the hardware to separate the proton and antiproton bunches. The systems that are likely to be impacted are listed below.

6.11.2.1 Sampled Bunch Display (SBD), and Fast Bunch Integrator (FBI)

The non-directionality of the pickup becomes more critical, especially for the FBI. A directional Pickup (long stripline) might be a necessity for the FBI, and very desirable for the SBD. Narrower bunches will require a faster sampling scope for bunch length measurements (SBD). The bunch spacing will require some rework on the fast integrators of the FBI.

6.11.2.2 Flying Wires

The main issue with the Flying Wires will be the factor of three increase in the number of bunches. The shorter bunch spacing will require a rework of its integrators as they share a similar design as those of the FBI.

6.11.2.3 Sync Lite

At this stage we assume that the new C0 collision region is operational and that the current location (an approximately 3 m warm section near C11) is not available. A new warm location between two Tevatron dipoles (full or half-length) for proton and antiproton telescopes does not currently exist. In fact no other location in the Tevatron exists in which the downstream edge of a dipole opens into a warm region of at least 60 cm (necessary for the proton telescope). It might be possible to “steal” this space at C11 by keeping a 60 cm warm space between the existing dipole and a new 6m dipole which will replace the existing downstream 3m half dipole. Otherwise we would need to create such a space elsewhere in the ring either by “nudging” some existing magnets or building a new higher field (but shorter length) dipole magnet which could locally replace a standard dipole magnet.

Assuming that a solution to the physical problem can be found, then the speed of data acquisition could be improved by using a streak camera in “framing” mode - each bunch would appear as a separate image on the streak camera. The improvement would be dependent upon how many images could be stacked on the camera. The same streak cameras as mentioned before could be used.

6.11.2.4 Tevatron Ion Profile Monitor (TIPM)

If we wish to distinguish the individual bunches of protons and antiprotons, the preamplifiers would have to be rebuilt with very short time constants. A location where the orbits are clearly separated (if such a location exists) would offer the best solution.

6.11.2.5 Collision Position Monitor (CPM)

Hardware and software improvements to remove the proton feed-through signal are even more critical.

6.11.2.6 Beam Position Monitors (BPM)

The major question is whether reliable antiproton measurements can be made. It might be necessary to have an upgrade to the BPM system at this point.

6.12 Warm Straight Section Allocation.

As new ideas for Tevatron upgrades are being discussed an important topic is the availability of space in the warm straight sections. This chapter is a list of the warm space allocation during Run II. The list does not provide detail down to the inch scale but gives a listing of the devices installed in the Tevatron now and the plan for the start of Run II.

This list does not consider the devices needed for the insertion of a new collision point at C0, the devices needed for putting in a crossing angle for 132 nsec bunch spacing, electron beam beam-beam compensation, electron cooling, stochastic cooling, or optical stochastic cooling.

6.12.1 List of devices by functionality

6.12.1.1 Separators

Locations of separators for Run I

(This list does not include adding separators to provide a crossing angle for 132 nsec bunch spacing or to provide colliding beams at the C0 interaction point.)

Horizontal	Vertical
B11 (2)	B11 (1)
B17 (4)	C17 (4)
C49 (1)	C49 (2)
D11 (2)	D11 (1)
F17 (1)	A17 (1)
A49 (1)	A49 (2)

For Run II

The horizontal separator at F17 will be moved to D48.

6.12.1.2 Collimators

Locations of Collimators during Run I

A0 Horz/Vert

D17 Horz/Vert

F17 Horz/Vert

F49 Horz/Vert

E0 Horz/Vert (was never installed)

Location of Collimators during Run II

For beam halo scraping

D17 - one 5 mm Tungsten target

two opposing 1.5 meter long L-shaped collimators

F17 - one 5 mm Tungsten target

two opposing 1.5 meter long L-shaped collimators

For proton removal

E0 - one 1.5 meter long L-shaped collimator with tungsten wings.

two opposing 1.5 meter long L-shaped collimators

6.12.1.3 Dampers

6.12.1.3.1

dampers for Fixed target

one stripline pickup at F11 for longitudinal damper.

D

6.12.1.3.2

dampers Run II.

2 horizontal stripline pickups 1 at D48, 1 at E11

2 vertical stripline pickups 1 at D48, 1 at E11

2 horizontal kickers (proton and pbar). At E0

2 vertical kickers (proton and pbar). At E0

D

6.12.1.4 Instrumentation for Run II

Beam current monitor DCCT at E49
Flying wires E11(H/V), E17(H)
SBD Resistive wall monitor at E48
FBI Resistive wall monitor at F11
Sync Light Monitor - C11 half dipole space.
Shottky Detectors - 4 pickups at A17.
Tune Measurement System - Part of damper pickup system.
Ion Profile Monitor at A17.

6.12.1.5 Kickers for Run II

6.12.1.5.1

Injection Kickers

Proton injection kickers at F17
Pbar injection kicker at E48
Pbar injection bumper magnet at E48

I

6.12.1.5.2

Abort kickers

Proton and Pbar abort kickers at A0
Proton abort kickers at C0

A

6.12.1.6 Other

Electron Compression Experiment at F48.
Superconducting RF at E0 (damper kickers will have to be relocated)

6.12.2 List of devices by straight sections

6.12.2.1 A0

- (~2030 inches beam valve to beam valve)
Now and Run II.
458 inches of 5 Proton Abort Kickers.
318.5 inches of beam pipe.
45 inches of 2 BPMs for kicker scope trace.
390.25 inches of 2 abort blocks.
45 inches of 2 BPMs for kicker scope trace.
329 inches of beam pipe (with collimator at upstream end.)
444.5 inches of 5 Antiproton Abort Kickers.
Beam Halo collimators.

6.12.2.2 A17

- (464 7/16 inches between cold bypass)
(446.625" between beam valves.)
Now and Run II
~24" for ion pump
~19' for Ion Profile Monitor
~23.5" of beam pipe
(The above three items take up 66.5" of space total.)
50" Horizontal Schottky.

5" bellows.
50" Vertical Schottky.
33" Bumps and ion pump.
50" Horizontal Schottky.
5" bellows.
50" Vertical Schottky.
16.5" Vacuum port.
120.25" Vertical Separator.

6.12.2.3 A48

- (114 inches between cold bypass)
(104.875" between beam valves)
Now and Run II
Tokyo Pots

6.12.2.4 A49

- (~354 inches between cold bypass)
Now and Run II
Filled with 3 Separators (1 Horz, 2 Vert)

6.12.2.5 B0

- Detector.
Now and Run II

6.12.2.6 B11

- (~354 inches between cold bypass)
Now and Run II
Filled with 3 Separators (2 Horz, 1 Vert)

6.12.2.7 B17

- (462.5 inches between cold bypass)
(448.625" between beam valves.)
Now and Run II
Filled with 4 Horizontal separators.

6.12.2.8 B48

- (347" between beam valves)
Now and Start Run II
4 C0 Abort Kickers (or 3 C0 abort kickers and E853 Goniometer.)
Future
Used for C0 interaction region upgrade?
[Note: If C-magnets and Lambertsons are removed then the half-dipole downstream of B48 will have to be replaced by full length dipole and the length of this space is reduced.]

6.12.2.9 B49

- (~51 inches)
Now and Start Run II
Empty
Future

Used for C0 interaction region upgrade?

6.12.2.10 C0

- (~2043 inches, or ~52 meters)
Now and Start Run II
Lambertsons, Collimator, C-magnets.
- Future
C0 experiment.

6.12.2.11 C11

- (~122 inches)
Now and Start Run II
Special Cold Bypass. (No access to beam pipe.)
- Future
Used for C0 interaction upgrade?

6.12.2.12 C11 (half dipole space)

- (~105 inches)
Now and Start Run II
Proton and Pbar Sync Lite Monitor.
- Future
Space will disappear if half dipole upstream is replaced with a full-length dipole.

6.12.2.13 C17

- (~445 inches between cold bypass)
(445.375 inches between beam valves)
Now and Run II
4 Vertical separators. (Drawing shows only one separator but there are 4.)

6.12.2.14 C48

- (114.25 inches between cold bypass)
(105" between beam valves.)
Fixed Target
2 QXR quads and bucker magnet take up entire space.
- Run II
Empty

6.12.2.15 C49

- (??)
Now and Run II
Filled with 3 separators (1 Horz, 2 Vert)
Possibly roman pots if space is created by moving D0 low beta quads closer to D0.

6.12.2.16 D0

- Fixed Target
Extraction Septa and dogleg magnets.
- Run II
Detector, possibly with moved low beta quads

6.12.2.17 D11

- Now and Run II.

Filled with 3 separators (2 Horz, 1 Vert.)

Possibly roman pots if space is created by moving D0 low beta quads closer to D0.

6.12.2.18 D17

- (~ 445 inches between cold bypass)
(447" between beam valves.)

Now

22.875" beam pipe.

70" D17 collimator.

15" bellows.

35" fixed hole collimator.

224.625" beam pipe

64.5" fixed hole collimator.

15" bellows.

Run II

20" for 5 mm Tungsten target + bellows

283" space

72" (1.5 meter collimator + 12" for bellows)

72" (1.5 meter collimator + 12" for bellows)

6.12.2.19 D48

- (~230 inches between cold bypass)
(226.6" between beam valves)

Now

188.5" D48 kickers.

22.5" "Beam Detector" part of

15.5" beam pipe.

Run II

119" horizontal separator.

12.25" horizontal damper pickup.

12.25" vertical damper pickup.

6.12.2.20 D49

- (~62 inches.)

Now

Empty

Run II

Possibly a damper pickup.

6.12.2.21 E0

- (~2087 inches between quads, ~53 meters)
(~2058 inches between beam valves)

Now

Injection Lambertsons

Start Run II

Proton scraping and Dampers

239" for B2 magnet

14" space

72" (1.5 meters for collimator with tungsten wings plus 12" for bellows)
14" space
239" for B2 magnet
40" space
239" for B2 magnet
100" of space
239" for B2 magnet
20" of space
48.25" for proton horizontal damper kickers.
48.25" for proton vertical damper kickers.
48.25" for antiproton horizontal damper kickers.
48.25" for antiproton vertical damper kickers.
~505" of space.
72" (1.5 meters for collimator plus 12" for bellows)
72" (1.5 meters for collimator plus 12" for bellows)

2058" total

[Note: the damper kickers are located in between crossing points for 132 nsec bunch spacing.]

Future

Relocate damper kickers and install superconducting RF.

6.12.2.22 E11

- (~ 91 inches)

(91.25" between beam valves.)

Now

32.75" beam pipe.

25.75" of E11 Flying Wires.

32.75" beam pipe.

Run II

20.25" horizontal damper pickup.

25.75" of E11 Flying Wires.

20.25" vertical damper pickup.

6.12.2.23 E17

- (~ 458 inches between cold bypass)

(452.95" between beam valves.)

Now

2 proton injection kickers, E17 Flying Wires, and Pinger.

Run II

E17 Flying Wire.

Pinger.

6.12.2.24 E48

- (~232 inches between cold bypass)

Now

4 stochastic cooling tanks => Recycler.

36.75" Resistive wall monitor (used for SBD).

Run II

181.5" for two pbar injection kickers.

22.5" for beam detector.

6.12.2.25 E49

- (~50 inches)

Now and Run II

41.875" DCCT (Beam current monitor)

6.12.2.26 F0

- (~2055 inches)

Now

TeV RF.

Resistive wall monitor => Recycler.

12" Resistive Wall (FBI) => F11

66.5" Vertical Damper deflector => replaced with new kickers in Run II

66.5" Vertical Damper deflector => replaced with new kickers in Run II

Wide band cavity => Recycler.

45.75" Berkley Schottky Detector => not used in Run II.

50.75" Vertical Tune plate => Use damper pickups for tune measurements.

50.75" Horiz Tune plate => Use damper pickups for tune measurements.

Stochastic Cooling Tanks => Recycler.

54" Horizontal Damper deflector => replaced with new kickers in Run II

Run II

TeV RF and Injection Lambertsons.

6.12.2.27 F11

- (~91 inches)

Now

54" Horizontal Damper Deflector => replaced with new kickers in Run II

Fixed Target and Run II

36.75" Resistive Wall monitor used for SBD and FBI.

12.25" Stripline pickup for Tevatron longitudinal damper.

[Note: F11 is about 30 meters from F0 so F11 is midway between crossing points for both 396 nsec and 132 nsec bunch spacing.]

6.12.2.28 F17

- (458.75 inches between cold bypass.)

(450.5 inches between beam valves.)

Now

61.5" Horizontal Proton Detector => Replaced with new damper pickups

50.5" horizontal LLRF detector (rpos) => not used.

53.25" Collimator

61.5" Ver proton damper Detector => Replaced with new damper pickups.

119" Horizontal Separator

1999 Fixed Target Run

Proton injection kickers from E17. Two at 86" apiece.

Run II

20" (0.5 meter) for 5 mm tungsten target (including bellows)
240" Proton injection kickers.(5 magnets × 48 inches/magnet)
12" for 2 ion pumps.
60" (1.5 meter) L shaped collimator
+ 12" bellows
60" (1.5 meter) L shaped collimator
+ 12" bellows

416 inches total

6.12.2.29 F48

- (~233 inches between cold bypass.)
(224.5" between beam valves)
Fixed Target
2 QXR quads, bucker, scanning target, intensity monitor.
Run II
Electron Beam for Tune Compression Test

6.12.2.30 F49

- (??)
Now
collimators.
Run II
Empty

6.13 Operational Concerns

There will be many new features and changes to the way we operate for Run II. The major ones are :

- Integration of the Main Injector and the Recycler into operations
- Multi-batch coalescing
- Upgrade from 6 to 36 bunches per beam
- New antiproton injection line
- New injection kickers
- New damper systems
- A new family of feed down sextupoles
- 1 TeV Operation
- Luminosity Leveling
- New beam halo scraping system
- Greatly improved orbit stability at the Interaction Points
- Proton removal
- Deceleration
- Recycling antiprotons
- No 6 ramps at the end of a store to reset the remnant fields and return the magnets to a consistent hysteresis state

- Reduce the shot setup times to about 30 minutes
- Lattice Changes
- New Time Line Generator (New hardware, new software, and a new operating philosophy)
- Instrumentation Upgrades (These are described in another section.)
- Change from 160 cards to 460 cards for the Dipole Field Generators.

In addition to the changes for the initial portion of Run II, we are planning for 132 nsec bunch spacing and for a new high-energy physics experiment in the C0 straight section. Preparation for 132 nsec bunch spacing include

- Kicker upgrades
- Crossing angle and beam dynamics studies
- Moving or adding new separators to allow crossing angles at the IP's
-

Changes to the C0 straight section

- Removing the C0 abort
- Lattice modifications including new low beta quadrupoles
- Installing a new high energy physics detector
- Adding new separators as part of an integrated plan for providing collisions at B0, D0, and/or C0

Each of the changes and new features for Run II will require a substantial effort *both* in planning and preparation before we turn on *and* during the commissioning. We must not only make them work, we must also make them a part of operations. They must be robust and reliable, and, in many cases, we also have to work out procedures for how to tune them up when problems arise.

Most of the commissioning of the Main Injector and the Recycler and their integration with the other machines should take place before or during the fixed target run planned for 1999. In particular, this time will also be used to establish multi-batch coalescing of high intensity proton bunches. The Fixed Target start up, commissioning, and operations are considerable tasks in themselves and will require the time and effort of the same people who would otherwise be preparing for the collider run. During this time, we must be careful to balance our resources between commissioning, fixed target operations, and preparing for Run II.

When we turn on in Collider mode, we hope to have the framework in place for *all* the features and changes in our list. Many of these may only be rudimentary or "bare bones" versions, but this way we will be aware of problems with or conflicts between features early, we will quickly gain the use of the ones that turn out to be "easy", and we can start getting used to the new operating modes. This is an ambitious goal. We would not be surprised if one or two of the features have to be completely re-thought or re-worked from their original implementation. Even with a framework in place, each of the features will have to be tuned up and made to work well, both individually and in conjunction with the others. We doubt that we will have the resources to tackle all of these at once. Even if we did, it may still make sense to take on only a few at a time. Many of these will have effects on the others, effects that we must learn to recognize and

eventually understand. We must also be careful not to overwhelm ourselves with so many changes and projects that we can't tell if individual changes were beneficial. We expect that it may take a year or more before all the features in our list are working well. As documented in Fermilab Note TM-1970, Run IA took about 6 months to routinely achieve initial luminosities above $5 \times 10^{30}/(\text{cm}^2 \cdot \text{s})$. This was also about how long it took for Run IB, despite only a 7 month shutdown for the Linac Upgrade, the only major change between Runs IA and IB.

During start up and commissioning we can expect to be on rotating shifts for several months. This may be the case at the start of the fixed target run and will certainly be the case at the start of collider operations. We not only have to staff these shifts, we have to diagnose problems, plan ways to solve them, prepare studies, analyze and understand the data, document results, and revise operational procedures.

We want 2 people per Tevatron shift in the Control Room during the collider start up and commissioning. The Tevatron is a complicated machine. We believe it will take about 2 months for a new person to "learn the ropes" and gain a basic understanding of how and why the Tevatron works. After about 4-6 months, they can start to plan, conduct, and analyze studies. Of course, the time required depends strongly on the person's previous operational experience. After this training investment, it is important that these people continue to contribute to Tevatron operations. With commissioning and development of Run II expected to take about a year, we hope that the effort put into training in the first half will pay off in the second half.

We will require approximately a one-year investment from a *minimum* of 8 to 10 people full time. In both the Run IA and IB start-ups, this is about the number of people we had, but both of those start-ups ended with these people over-worked and burned out. From our list of changes and new features, Run II will have one of the harder, more prolonged start up and commissioning periods.

As one suggestion to try to avoid burnout, we should consider periods of several weeks when we temporarily stop doing studies and just try to run luminosity. This will hopefully allow some time for the physicists to "step back and look at the bigger picture" or, more specifically, to get out of the control room, analyze data, prepare future studies, and recuperate from rotating shifts. This will also allow some time for the operators to "catch up" with the changes made in studies and to again establish an idea of what is "normal".

Another complication for this start-up is that we have many new operators. The 14 Operators recently transferred from the Research Division have not directly experienced any Collider operations. Of the 13 Operator I and II's who have always worked from the Main Control Room, about 1/3 have seen less than 6 months of Collider operations and half have seen less than 1 year. We can expect to lose several more experienced operators between now and the start of Run II.

To summarize :

- 1) Present personnel resources aren't adequate. To be useful, additions should be involved full-time for *at least* 6 months to a year. Staffing rotating shifts is a large commitment, but a similar amount of work is required to prepare and analyze what happens on shift. It is essential that the people doing this are the same group of people who are on shift. Also during the fixed target run before Run II, many of the same people will be needed for fixed target start-up and operations and for preparations and planning for Run II. These needs will have to be balanced.

- 2) There is an enormous amount of work to be done and many changes to the way we operate. It will take months to get back to the performance levels from the end of Run IB.

- 3) Commissioning and changes to operation will continue for a long time, at least a year. At start-up, we hope to have the framework in place, at least to try all the new features. Some new

"features", such as luminosity leveling and 30 minute shot setup times, will not be present at the start. Others may be present but in a "rudimentary" form. After the initial period when we see what does and doesn't work, we must be prepared to decide which features or projects will get priority and which will be put on back burners. At this point, the number of available, trained, and knowledgeable people will be a major factor in how quickly these features are made to work.

4) Training will be an emphasis and a burden for at least the first 6 months. Training of operators and personnel could take about 10 to 20% of the time.

5) There will be times when we will want to take breaks from studies. However, even after the run has officially started, we will need studies periods, both to continue to commission "new features" and to prepare for Tev33. This should be a lab priority and we should consider regular scheduled studies periods. These are *in addition* to "operational studies" intended to tune up present operations.

6) There are several factors that likely will not be big problems in themselves but that will contribute to problems. Inexperience, training efforts, the new SDA, changes to instrumentation, difficulties in coping with the data from all 36 bunches, and increased complexity in orbit control will all sow confusion and make the diagnosis of underlying problems more difficult.

6.14 132 nsec Bunch Spacing

We plan to increase the number of antiproton bunches by decreasing the bunch spacing to 132 nsec. For fixed emittances, a fixed proton intensity per bunch, and a fixed number of antiprotons, the luminosity remains constant while the number of interactions per crossing decreases as the number of bunches is increased. However, as described in more detail below, we plan to introduce a crossing angle when the bunch spacing is reduced to 132 nsec. This effect reduces the luminosity as well as the number of interactions per crossing.

6.14.1 Kicker Considerations

Missing bunches (gaps) in the proton beam cause antiproton tune shifts that vary from bunch to bunch. A long gap is required to accommodate the rise time of the abort kickers and short gaps may be required if the proton kicker rise time is less than the bunch spacing. We plan to build the proton kicker so that the rise time can be increased to 132 nsec. The plan to initially achieve a kicker rise-time of 396 nsec and later upgrade it to 132 nsec was outlined in section 6.6.4.

It would be possible to decrease the antiproton kicker rise time to 132 nsec as well. However, there is less reason to do so since the proton shifts are smaller because of the lower antiproton intensities. The 140×121 bunch loading scheme described below assumes that both kickers have achieved a 132 nsec rise time while the 90×90 scheme assumes that neither kicker has been. With the 132 nsec rise time for the proton kicker but not the antiproton kicker, it would be possible to achieve a configuration similar to 140×121, but the antiproton beam would have an additional 10 missing bunches to accommodate the antiproton kicker rise time.

6.14.2 Beam-Beam Considerations

Over the last year, most of our work has concentrated on the case with 132 nsec bunch spacing, where we run with about 100 bunches in each beam. This report will also concentrate on that case. For the 132 nsec bunch spacing, we have *only* looked at the collision helix conditions. We have not yet looked at the injection helix or considered how we will make the transition from the injection to the collision helix.

For bunch spacing of 132 nsec (7 rf buckets at 53 MHz), the first crossing points on either side of the interaction points are in the Q2 element of the final focus quadrupole triplet, before the

first separator. The second crossing points are in the first dipole magnet, after the first separators, but close enough so that there is little separation between the beams. To avoid very strong beam-beam effects from these first crossing points (roughly of the same size as the beam-beam effects from the main interactions in the middle of the detectors), we must separate the beams. In order to separate them, we need a crossing angle at the interaction point. These crossing angles must be large enough to provide 3 to 5 σ of separation at the first crossing points. For our parameters, this gives half crossing angles of about ± 140 to ± 240 μrad . We choose to split this between the horizontal and the vertical planes, giving half angles of ± 100 to ± 170 μrad per plane.

These crossing angles have a significant effect on the overlap of the two beams at the main interaction points and hence on the luminosity. This is shown in Figure 6.66, of L/L_0 as a function of crossing half angle in each plane for the two bunch lengths.

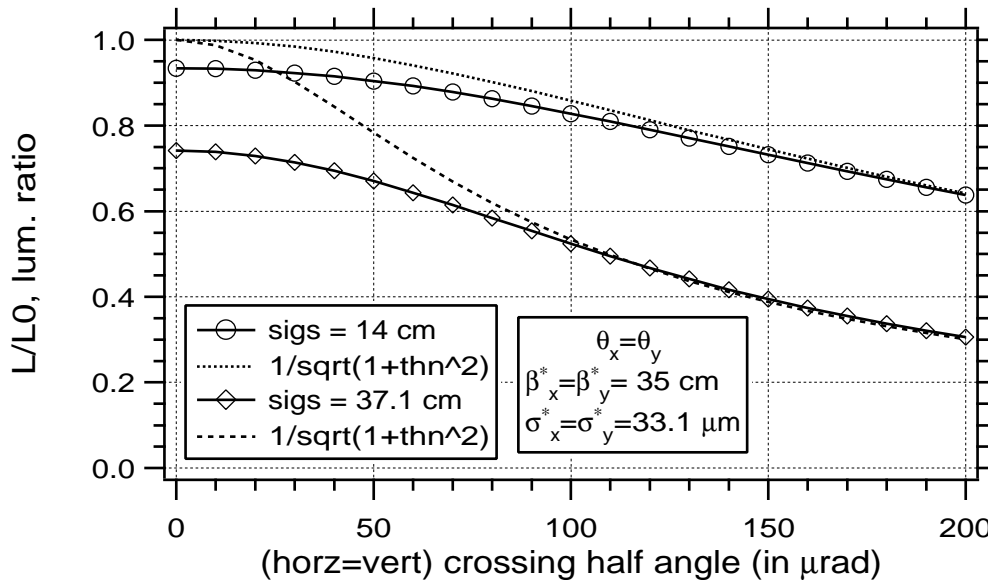


Figure 6.66. The dependence of luminosity (L/L_0) on the crossing half angle in each plane. The results for two bunch lengths (14 cm and 37 cm) are shown. The dotted lines show $(1 + \theta_N^2)^{-1/2}$, the approximation that ignores the hourglass effect, for the two bunch lengths.

The loss in luminosity due to the crossing angle is not small. For 14 cm bunch lengths and half crossing angles per plane of ± 136 μrad , the loss in luminosity is $(0.93 - 0.76)/(0.93) = 18\%$, where we have read the values from Figure 6.66. For 37 cm bunch lengths and half crossing angles per plane of ± 136 μrad , the loss in luminosity is $(0.74 - 0.43)/(0.74) = 42\%$.

In the lattice JJ15C (the lattice with zero dispersion in the interaction regions - see Run II lattice section of this report.), we have begun playing with the locations and the strengths of the separators to try to find configurations that give good separations and that have good beam-beam characteristics (that is, where the few, simple, beam-beam parameters we've been calculating are acceptable).

So far, we have only looked at different orbits for each bunch. Where the beams are separated, they give an average dipole kick to the opposing beam. For about 100 bunches per beam, we have to adjust the separator settings to compensate the effects of these dipole kicks. After the separators have been adjusted there are still small bunch to bunch orbit differences the tune

shifts and transverse coupling for zero amplitude particles for each bunch the tune shifts for particles with different transverse betatron amplitudes in each bunch.

These are fairly simple calculations. They begin to give us a handle on the severity of the beam-beam effects and can be useful for discriminating between various separation schemes, but they are far from a complete description of the dynamics. In addition to these, we need to calculate resonance strengths and widths and we will need to do some tracking studies to study the effects of both the main interaction points and the *many* near misses. (In particular, we are worried about the effects from synchro-betatron resonances due to the crossing angle at the main interaction points.)

One reason we have not begun these more advanced calculations is simply lack of time. But also, until we are fairly satisfied with the lattice and separator configurations, and these give good results for our simple tune shift and tune spread calculations, it doesn't make sense to go ahead with more detailed, complicated, questions.

6.14.2.1 Separator Configuration

In many ways the Tevatron is a highly constrained machine. The arcs are full of magnets, with no space available between the 17 and the 48 locations. The main quadrupoles are powered off the dipole bus and about the only quadrupoles that can be individually adjusted are the quadrupoles in the low beta inserts.

At present there are horizontal and vertical separators on either side of both interaction points (B0 and D0), at the 49 and 11 locations. There are also a horizontal and a vertical separator in each arc between the interaction points. This makes a total of 6 separators per plane, enough to make a closed bump for each arc in each plane. We depend on the lattice to make and keep the horizontal and vertical displacements $\pi/2$ out of phase with each other so that they form a helix and the beams are well separated everywhere in the arcs.

For the 132 nsec bunch spacing, we require crossing angles at the IP's. These "link" the helices in the two arcs. With 6 separators per plane, we can specify the separations and crossing angles at each of the 2 IP's and the sizes of the separation bumps in each the arcs.

In each plane, we tend to think in terms of the multipliers for 6 "closed bumps". The first 2 bumps are the separation bumps in the two arcs. These extend throughout the arc but end just before the IP's, producing no separation or angle between the beams at the two IP's. The next 2 bumps make only a separation and no angle at each of the IP's. The separators on either side of the IP's, at the 49 and 11 locations, are ideal for this and are essentially all that are used in these bumps. The last 2 bumps make only an angle and no separation at the IP's. Unlike the separation bumps, there is no such "nice, natural" set of separators for angle bumps across the IP's. These bumps extend well into the arcs and *have an effect on how well the beams are separated in the arcs.*

(In the arcs, our separations due to the arc helix are much larger than the separations due to the crossing angle bumps. There are several reasons that the arc helix must be larger :

- 1) The arc helix has an "inefficiency". Because the horizontal and vertical separations that make up the arc helix are not exactly $\pi/2$ out of phase everywhere in the arcs, the overall size must be larger so that there is adequate separation all through the arcs.
- 2) The crossing angle reduces the instantaneous luminosity. (See Figure 6.66.) This is a strong incentive to keep the crossing angles fairly small.
- 3) The crossing angle bumps are mainly needed for only the couple of crossing points on either side of the IP's. The arc helix must separate the beams at roughly 200 crossing points in the arcs. With so many more crossing points in the arcs, we want each of them to be weaker and so want more separation.

4) We appear to have both the aperture and the separator strength to make the arc helix large. At 900 GeV in the low beta lattice, we have not clearly seen any bad effects from increasing the size of the arc helix until we run out of separator strength.)

At the first crossing point on either side of the IP's, all the separation is from the crossing angle bumps. At the 2nd crossing points on either side of the IP's, the separation is mainly from the crossing angle bumps, but the "arc helix" has a small but significant effect. At the 3rd crossing points, the separation from the "arc helix" and the separation from the crossing angles bumps can be similar in size. For about the 4th crossing point and beyond, the separation from the arc helix dominates. Although at the 4th crossing point and beyond, how the arc helix and the crossing angle bumps combine still has a significant effect on the separation, the most important interference is at the 2nd and 3rd crossing points on either side of the IP's.

Basically we choose the size of the crossing angles so that the first couple of crossings aren't too bad. Also we have enough separator strength to make the separation in the arcs large enough so that the total tune shift and tune spread effects from all the crossing points in the arcs is quite small. But we still have trouble with the 2nd and 3rd crossings, the crossings in the transition region between where the angle bumps and the arc helix are important. The tune spreads still tend to be largely dominated by these points and the main IP's. (We will show some figures illustrating these points in the next section.)

We've been able to improve the separation at and the beam-beam effects from these points, but they are still not as good as we would like. It is important to keep in mind that the present scheme represents an existence proof of a separator configuration that we can put into the Tevatron and that appears to give reasonably good beam-beam behavior. This has *not* been "optimized". The present scheme is something we were playing with to start to get a feel for what the problems are and how we want to set up our separators. It is the result of a first pass at trying to develop a procedure to find good separation configurations, trying to develop good parameters for quick, easy, characterization of different configurations. The present scheme was never intended to be taken very seriously. We are confident that it can be improved. (In particular, we haven't even considered lattice modifications yet.) Despite this, it is our present "favorite" condition.

Table 6.21. Separator settings for 132 nsec bunch spacing (jj15c2(st, a12).pnpp3css.136nppp2).

Separators	90×90	140×121
(# of modules)	Setting (MV/m)	Setting (MV/m)
B11H (2)	-4.231	-4.182
B48H (4)	-3.766	-3.858
C49H (1)	-3.686	-3.647
D11H (2)	-2.532	-2.574
D48H (1)	-0.910	-2.006
A49H (1)	2.392	2.400
B11V (1)	3.022	3.092
C17V (4)	-2.403	-2.599
C49V (2)	2.350	2.351
D11V (1)	3.659	3.648
A17V (3)	2.901	3.463
A49V (2)	-4.474	-4.555

Table 6.21 shows the separator settings for the lattice JJ15C at 1 TeV for our "favorite" separator configurations, jj15c2(st, a12).pnpp3css.136nppp2. (The st refers to the 90×90 bunch settings, the a12 refers to the 140×121 bunch settings. We will describe these different filling schemes in the next section.) The slight differences in the settings for the two come from compensating slightly different sets of beam-beam dipole kicks.

We are comfortable with separator settings as high as 4.24 MV/m. This corresponds to ±106 kV on the plates across a gap of 5 cm. If we go much above that, the sparking rate increases rapidly. In Table 6.21, the only separator above this limit is the vertical separator at A49, which gets as high as 4.555 MV/m or ±114. kV on the plates. This is close to our limit and we feel it is acceptable if we have "strong" separator modules there. (Certain modules spark more than others.) If we cannot run this separator at this voltage without unacceptable sparking, we could bring it down to 4.24 MV/m by an 8% reduction in the size of the vertical separation bump in the short arc. There are several differences between the locations and numbers of separators shown in Table 6.21 and what was previously used in the Tevatron.

- We've moved 1 horizontal module from F17 to D48. Both the rf and the injection/extraction to the Main Injector will be near F0. Consequently, space near F0 will be very tight. We've moved this separator to try to free up some space near F0.

- We've added 2 more vertical modules at A17, for a total of 3 modules there. The vertical crossing angles at the IP's require a large kick from this location. To make this kick, while keeping the electric field under our limit of 4.24 MV/m, we had to add more modules. There is room for the additional modules if the Schottky detectors presently in the A17 straight section are moved.

- This does not use the 4 horizontal separator modules at B17. In the JJ15C lattice, the horizontal phase advance between the B11 and the B17 horizontal separators is $(0.92)(2\pi)$, making the effects of these separators very nearly degenerate. If we use both the B11 and B17 horizontal separators they both end up at high voltages. Instead of the B17 horizontal separators, we have used 4 horizontal separator modules at B48. Presently there is not enough room at B48 for 4 modules. If we really wanted to implement the separator configuration described above, we have a plan that would make room at B48.* (It may be possible to move the separators from B17 to B48,

* Presently the B48 straight section is occupied by the kickers for the C0 beam abort. This abort system will be removed for the Run II collider operations, freeing up not only the B48 straight, but also large portions of the C0 straight section presently occupied by lambertson magnets and C magnets for the abort. Without the kickers at B48, there is room for 2 separator modules. We propose the following plan to fit 4 modules into this space.

- 1) Move the B49 spool from the upstream to the downstream side of the quad C0U. (Upstream and downstream refer to the proton's direction.) This spool contains the VB49 Beam Position Monitor, the B49 horizontal and vertical steerings and the power leads.
- 2) Move the half dipole from the B48 straight to just after the B49 Quad. Part of this new location was previously occupied by the B49 spool. Without the half dipole in the B48 straight, there is room for 4 separator modules.
- 3) Replace the 3 lambertsons and the 2 C magnets in the C0 straight with one standard tevatron dipole running on the main bus. These 5 magnets contribute a kick of 8.483 mrad, slightly more than the standard dipole kick of 8.118 mrad. The remaining kick can be provided with 2 or 3 horizontal steering spools. These spools would run off their own dipole regulator, possibly one regulator per spool. In order to compensate the move of the half dipole, and to keep the tevatron closed, the bend center for the combination of this dipole and the spools should be 12.94 m upstream of C0. There's about 13.5 m

rather than building new modules. The B17 separators are presently used for the injection helix and we need to investigate whether the B48 location is acceptable from injection helix considerations.)

We could implement the separator configuration shown in Table 6.21 in the Tevatron. Several changes are required, more separator modules need to be built, some separators need to be moved, we'll need additional cold bypasses, etc. but we know how to do these things. Although it could be implemented, we doubt this is what we will actually use. We believe we can improve on this separator configuration both in terms of the beam-beam effects and in terms of the number of changes to the separators. We will continue to work on this.

6.14.2.2 Comparison of (90 90) and (140 121) Filling Schemes

The numbers refer to the number of proton and antiproton bunches respectively, so for example the 140×121 scheme has 140 proton bunches and 121 antiproton bunches.

The 90×90 filling scheme is three fold symmetric and has three abort gaps in each beam. Each third of the ring contains an abort gap of 2.6 μ sec and a train of 30 bunches. Each train is split into 3 sub-trains of 10 bunches each. Within a sub-train the bunches have a 132 nsec spacing. The sub-trains are separated in time by 396 nsec. This gap corresponds to the assumed rise time of the injection kicker. We have chosen to number the bunches in a train from 1 to 34. Bunches 11, 12, 23, and 24 are empty and correspond to the locations of the gaps for the injection kicker which separate the sub-trains.

The 140×121 filling scheme is not three-fold symmetric. It has one abort gap for the proton beam and two abort gaps in the antiproton beam. The "extra" abort gap in the antiproton beam ensures that all the antiproton bunches will see collisions at both the B0 and the D0 interaction regions. (If this were not the case, the antiproton bunches that see one or two collisions per turn would have very different beam dynamics and would take up more space in the tune plane.) The two abort gaps in the antiproton beam break it up into a short train of 34 bunches and a long train of 87 bunches. For this filling scheme, we assume new injection kickers with 132 nsec rise times, quick enough to inject adjacent bunches without leaving a gap.

In this scheme, all the antiproton bunches see collisions at both IP's, but the same is not true for the protons. This difference between some of the protons bunches will make it more difficult to find conditions that are good for *all* the protons bunches. However, we are less concerned about the protons than the antiprotons for two main reasons. First, the antiproton intensities will likely be significantly lower than the protons intensities, resulting in smaller differences between the proton

between this center point and the edge of the C0 upstream quad, which is plenty of space for these elements.

As a result of these dipole moves, between the B49 quad and the new bend center, that is between about 31 m to 13 m upstream of C0, the orbit moves radially out by a little less than 8 cm. The effect on the horizontal dispersion is negligible (about 1 mm at B0 and D0).

This plan should be considered an existence proof. It is a way we *could* do things, but this is probably *not* how we would *choose* to do things. In particular, we would prefer to remove the C0 abort lambertsons and C magnets and make up the bends by replacing the half dipoles at B48 and C11 with full dipoles. This would make C0 like the other straight sections. In this case, there would only be room for one separator module at B48. Rather than place any modules there, we would put them somewhere in the C0 straight section. We believe this is practical, but have not worked out the details.

bunches. Second, we consider protons to be "cheap". They do not have to be laboriously produced, captured, cooled, and accumulated like the antiprotons and the protons will be thrown away at the end of a store rather than recycled. We are willing to accept worse lifetimes for the protons than for the antiprotons.

The first few crossings near the IP's have the largest beam-beam tune shifts and couplings. Unlike the fairly weak effects of the crossings further into the arcs, the effects of these crossings are strong enough so that individually they can have a significant, easily seen effect on the beam-beam tune shifts of the antiprotons. Most of the antiproton bunches do see protons at these crossing points, but the antiproton bunches near the edges of the trains or sub-trains do not. The main benefit of the 140×121 case is that fewer antiprotons are on the edges of the trains and so the antiproton bunches are better concentrated in the tune plane. We will show this later in this section.

A minor benefit of the 140×121 case is that it gives 121 collisions per turn at each detector, about a third more than the 90×90 case. For the same luminosity, the number of interactions per crossing will be less for the 140×121 case.

These parameters were used for the calculations which follow :

- 1 TeV
- proton intensities of 270×10^9 /bunch
- antiproton intensities of 60×10^9 /bunch
- Transverse emittances of 20π mm-mrad (95%, normalized)
- Longitudinal emittances of 2 eV-sec
- Horizontal and vertical β^* of 35 cm
- Horizontal and vertical crossing angles of $\pm 136 \mu\text{rad}$
- bunch length of either 37 cm or 14 cm
- (σ_p/p) of 0.087×10^{-3}

The (σ_p/p) of 0.087×10^{-3} is not the correct value for the 14 cm bunch length. We assume that we will get the 14 cm bunch length using an rf upgrade with 15 MV of 212 MHz rf. With a longitudinal emittance of 2 eV-sec at 1. TeV, this gives a bunch length of 13.8 cm and a (σ_p/p) of 0.237×10^{-3} . In the next pass through these calculations, we will certainly correct this mistake.

We begin by looking at the bunch by bunch orbit differences. For each antiproton bunch we use an iterative procedure to calculate its separation and angular separation from the corresponding proton bunch at both interaction points. (In this calculation, we make the approximation that the bunch is short, so the bunch length has no effect here.) Table 6.22 shows two ways of parameterizing the range in these separations, the standard deviation of these separations and the difference (including sign) between the maximum separation and the minimum separation. The separations should be compared to the nominal beam size at the IP of 33.1 μm . The angular separations should be compared to the size of the full crossing angle of 272 μrad per plane.

Table 6.22. Bunch by bunch orbit differences at the IP's

			B0		D0	
			horz	vert	horz	vert
90×90	pos (μm)	stnd dev	2.9	3.2	1.2	1.2
140×121	pos (μm)	stnd dev	2.5	2.6	2.3	2.4
90×90	angle (μrad)	stnd dev	4.1	3.7	3.1	2.4
140×121	angle (μrad)	stnd dev	3.4	2.7	12.1	12.2
90×90	pos (μm)	max – min	10.4	11.4	4.7	4.6
140×121	pos (μm)	max – min	10.0	11.0	11.6	12.1
90×90	angle (μrad)	max – min	16.6	14.5	12.0	9.9
140×121	angle (μrad)	max – min	14.6	10.3	37.9	39.3

With two exceptions, all of these separations and angular separations look reasonably small and very similar for the 90×90 and the 140×121 cases. The two exceptions are the large horizontal and vertical angular separation at D0, for the 140×121 case. If we look more closely at these angular separations, we see that they are grouped in two well separated clusters. One cluster contains all the antiproton bunches in the short train and is centered on horizontal and vertical angular separations of 254. and 291. μrad, respectively. The other cluster contains all the antiproton bunches in the long train and is centered on horizontal and vertical angular separations of 280. and 265. μrad, respectively. The separation between these clusters is a concern, and we intend to both understand why it appears in this case and to reduce or eliminate it in future iterations.

For particles with zero betatron amplitudes in each of the bunches, we have also calculated the horizontal and vertical tune shifts and two transverse coupling components. The ranges in these are summarized in Table 6.23 and the horizontal and vertical tune shifts are also plotted as open circles in Figure 6.77 to Figure 6.80. Whether the bunch lengths are 14 cm or 37 cm makes very little difference in these ranges.

Table 6.23. Bunch by Bunch Zero Amplitude Tune and Coupling Differences

		horz tune	vert tune	coup cos	coup sin
90_90	stnd dev	.0029	.0024	.0014	.0026
140_121	stnd dev	.0010	.0011	.0007	.0011
90_90	max _ min	.0112	.0096	.0055	.0110
140_121	max _ min	.0065	.0072	.0048	.0054

The two transverse coupling components shown in Table 6.23 are the ones related to the resonance (x y). These two components combine in quadrature to give the minimum tune split, that is, the closest that the tunes can be brought together using the upright quad circuits only. If we can independently decouple both the proton and antiproton beams, we believe this beam-beam coupling is acceptable. If we decouple for the average antiproton bunch, the worst bunches will be

left with minimum tune splits of 0.0066 for the 90_90 case and 0.0035 for the 140_121 case. (This roughly corresponds to coupling components of half the (max _min) values in Table 6.23)

As expected, for both the tune shifts and the coupling components, the 140_121 case is more tightly clustered with fewer "outliers" than the 90_90 case. This shows in both the standard deviations and in the (maximum _minimum).

We have looked at the contribution of each of the crossing points to the tune shifts and coupling components. Much of the bunch by bunch differences shown in Table 6.23 are the effects of a few crossing points near the IP's.

The individual crossing points with the largest contributions to the tune shifts are the 2nd crossing points around B0 and D0. The 2nd crossing points upstream and downstream (in the proton sense) of D0 contribute _0.0023 to the horizontal and vertical tune shifts, respectively. The 2nd crossing points near B0 are not as bad, they only contribute _0.0011. (Due to our sign choices for the arc helices and the crossing angles, the 2nd crossing points near D0 have smaller separations than those near B0.)

For the coupling components, the individual crossing points with the largest contributions are the 1st and 2nd crossings around B0 and D0. As a result of the equal horizontal and vertical crossing angles, the 1st crossing points on either side of the IP's mainly affect the coupling, but not the tune shifts. For both the upstream and downstream points around D0, the 1st crossing point contributes about 0.0022 and the 2nd crossing point contributes about 0.0009 to the cos coupling component. We chose the signs of the crossing angles so that the points near B0 contribute similarly except with the opposite sign. As a result, for the 90_90 filling scheme, the coupling effects from these points from B0 and D0 largely cancel for all bunches. This trick doesn't work for the 140_121 filling scheme since it doesn't have 3 fold symmetry.

Table 6.23 shows results for zero amplitude particles. We are also concerned with the changes in the tune shifts as a function of a particle's betatron amplitudes. (Although we expect it will be significant, we have not yet tried to look at the effects of longitudinal oscillations, changes in the particle's energy and arrival time. In our calculations, the energy spreads are only used in the beam sizes for the opposing beam. Our test particles have no longitudinal oscillations.) We define a particle's betatron amplitude as (a_z ___ z) where we write a particle's betatron motion as

$$z_{\beta}(s) = (a_z \sigma_{\beta z}(s)) \cos \psi_z(s)$$

where z may stand for either x or y , denoting either horizontal or vertical motion, and $\sigma_{\beta z}$ is the beam size due to the betatron motion only. $\sigma_{\beta z}$ does not include the contribution to the beam sizes from the energy spread and the dispersion. With this definition and assuming linear motion, a_z is a constant around the ring.

* The three fold symmetry for the 90x90 case means that if a pbar bunch does not encounter a proton bunch at e.g. the first crossing upstream of D0, then it *will not* encounter a proton bunch at the first crossing upstream of B0. Since the coupling contributions of these two missed points are nearly equal and opposite, the coupling for this bunch will be nearly the same as for a bunch which does see proton bunches at these two points.

The opposite is true for the 140x121 case, that is, if a pbar bunch does not encounter a proton bunch at e.g. the first crossing upstream of D0, then it *will* encounter a proton bunch at the first crossing upstream of B0. For the 140x121 case, we do not get this nice cancellation. In spite of this, table yyy3 shows that the bunch to bunch coupling differences are still small for the 140x121 case. This suggests that this constraint on the signs of crossing angles may not be needed. We need to look into this.

We have typically calculated the tune shifts for particles with horizontal and vertical betatron amplitudes from 0 to $4 \sigma_{\beta_z}$ in amplitude steps of $0.5 \sigma_{\beta_z}$. This gives 9 values per plane or 81 points in total. We usually do these calculations for all the different antiproton bunches. Although we do these calculations for all bunches, we will begin by looking at the results for one "typical" bunch for each of the filling schemes.

As our typical bunch for the 90×90 case, we choose the bunch designated A17, which is both in the middle of a train and in the middle of a sub-train. For the 140×121 case, we choose the bunch designated A070, which is in the middle of the short train. These bunches will see the strong effects from encountering protons at the first few crossing points on either side of the IP's.

Figure 6.67 and Figure 6.68 show the contributions from the crossing points further than 4 crossing points (28 half rf buckets) from the IP's. For A17 and A070, these show the combined effects of 162 and 262 proton crossings, respectively. A070 has slightly more tune spread than A17, but for both of them, the tune spreads are very small.

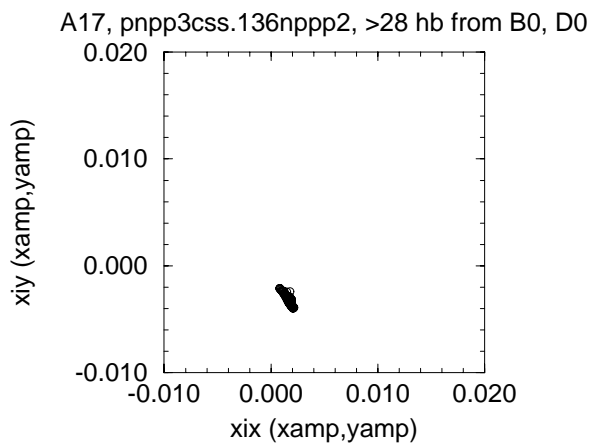


Figure 6.67. 90×90, A17, Tune spread from all crossing points *except* those within 4 crossings (28 half rf buckets) of the IP's.

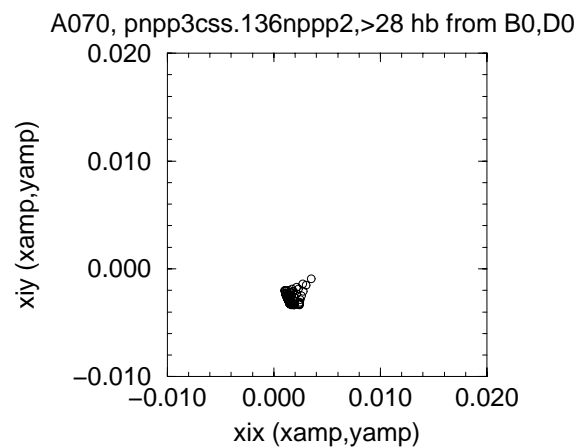


Figure 6.68. 140×121, A070, Tune spread from all crossing points *except* those within 4 crossings (28 half rf buckets) of the IP's.

Figure 6.69 and Figure 6.70 show the contributions from all the crossing points *except* for B0 and D0, the two interaction points. The differences between 4 and 2 and between 5 and 3 show the effects of the first 4 crossing points on either side of the two IP's. The effects from these 16 crossing points are much larger than the effects from the other 162 or 262 crossing points.

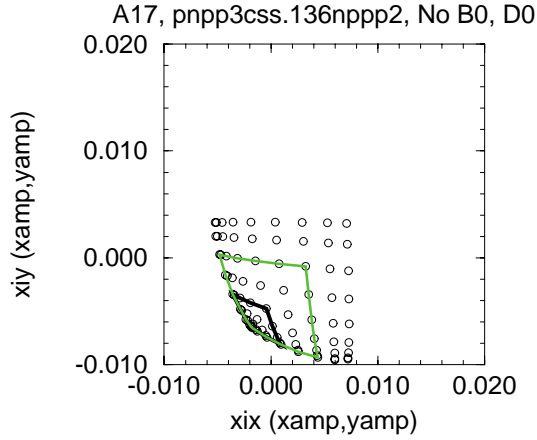


Figure 6.69. 90×90, A17, Tune spread from all crossing points *except* B0 and D0, the main IP's.

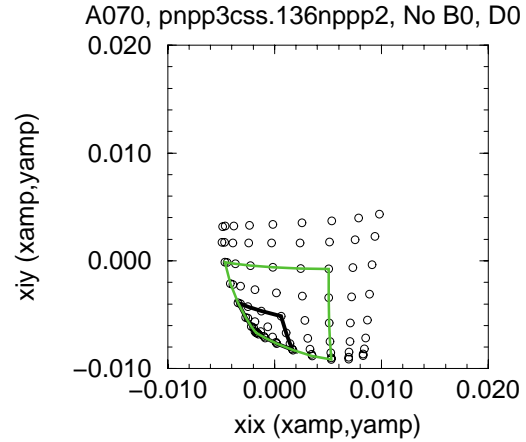


Figure 6.70. 140×121, A070, Tune spread from all crossing points *except* B0 and D0, the main IP's.

Since the tune spreads in Figure 6.69 and Figure 6.70 are dominated by the first few crossing points on either side of the IP's and since the effects of the many other crossing points further into the arcs are small, the tune spreads in Figure 6.67 to Figure 6.70 for the two different filling schemes are very similar. As was suggested earlier, the main difference between these two filling schemes is in the range for the different bunches. The tune shifts and spreads for a typical bunch near the middle of the (sub-)trains is very nearly the same in either scheme.

In Figure 6.69 and Figure 6.70, the heavy black lines connect the points corresponding to horizontal and vertical amplitudes of $(0,0)$, $(0,2\sigma_{\beta y})$, $(2\sigma_{\beta x},2\sigma_{\beta y})$, $(2\sigma_{\beta x},0)$ and back to $(0,0)$. Similarly the gray lines connect the points corresponding to horizontal and vertical amplitudes of $(0,0)$, $(0,3\sigma_{\beta y})$, $(3\sigma_{\beta x},3\sigma_{\beta y})$, $(3\sigma_{\beta x},0)$ and back to $(0,0)$. These lines help to show where the core and the tails of the beams are. In these figures, small amplitude particles are in the lower left corners. Particles with horizontal and vertical amplitudes of $(0, 4\sigma_{\beta y})$ are at the top left corners, particles with horizontal and vertical amplitudes of $(4\sigma_{\beta x}, 0)$ are at the bottom right corners, and particles with horizontal and vertical amplitudes of $(4\sigma_{\beta x}, 4\sigma_{\beta y})$ are at the top right corners. This is the opposite to the "footprint" from a head-on beam-beam interaction between oppositely charged beams,

The first three crossing points on either side of the IP's make the largest contributions to the tune spreads shown in Figure 6.69 and Figure 6.70. The ones upstream of the IP's contribute large horizontal tune spreads, those downstream contribute large vertical tune spreads. (Again, upstream and downstream are referenced to the proton direction.) This is a consequence of the optics. On the upstream side, the horizontal β is much larger than the vertical β at these three crossing points and vice versa for the downstream side.

The 1st crossing points upstream (downstream) of B0 and D0 each contribute about 0.0016 to the horizontal (vertical) tune spreads and about 0.0009 to the vertical (horizontal) tune spreads. The 2nd crossing points upstream (downstream) of B0 contribute about 0.0022 to the horizontal (vertical) tune spreads, while the 2nd crossing points near D0 contribute about 0.0032. Finally the 3rd crossing points upstream (downstream) of B0 and D0 each contribute about 0.0009 to the horizontal (vertical) tune spreads.

Although the first and third crossing points on either side of the IP's contribute very little tune shift for zero amplitude particles, they make large contributions to the tune spreads for particles with different betatron amplitudes.

Figure 6.71 and Figure 6.72 show the tune shifts due to *one* of the IP's. (Apart from the signs of the crossings angles, the two IP's are designed to be identical and so these figures are applicable to either B0 or D0.) Since these figures only show the effects of one of the two IP's, we've shown it at twice the scale to make it easier to compare with the other figures. The tune spread contributions from the first three crossings on either side of the IP's are similar in size to the contributions from the main IP's.

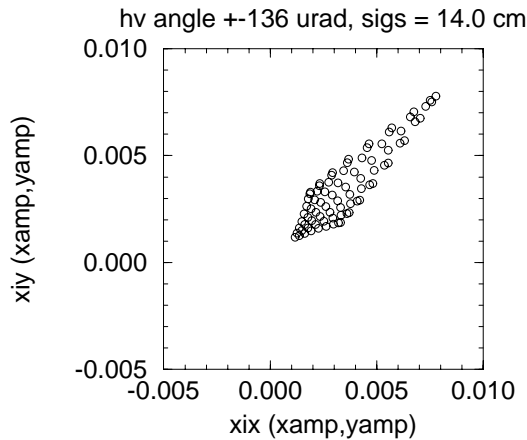


Figure 6.71. Tune spread from *one* of the main IP's. $\sigma_s=14$ cm.

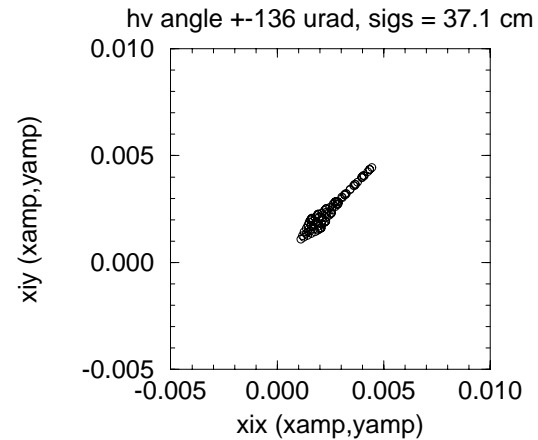


Figure 6.72. Tune spread from *one* of the main IP's. $\sigma_s=37$ cm.

If the beams collided head-on at the IP's with zero crossing angle, the horizontal and vertical tune shifts for small amplitude antiprotons would be 0.0099 from each IP. The crossing angle both reduces this small amplitude tune shift and distorts the shapes of the tune "footprints". In Figure 6.71, with a 14 cm bunch length, the small amplitude tune shift is 0.0078 and the distortion of the shape of the footprint is fairly small. In Figure 6.72, with a 37 cm bunch length, the small amplitude tune shift is down to 0.0044 and the distortion is more noticeable.

In Figure 6.71 and Figure 6.72, the small amplitude particles are at the top right, particles with zero horizontal amplitude and moderate vertical amplitudes are at the bottom right, particles with zero vertical amplitude and moderate horizontal amplitudes are at the top left, and particles with large horizontal and vertical amplitudes are at the bottom left. This is the opposite of where these particles are in the figures showing the tune spread from all the other crossing points, Figure 6.69 and Figure 6.70. The contributions to the tune spread from the IP's and from all the other crossing points will partially cancel. This is shown in Figure 6.73 through Figure 6.76.

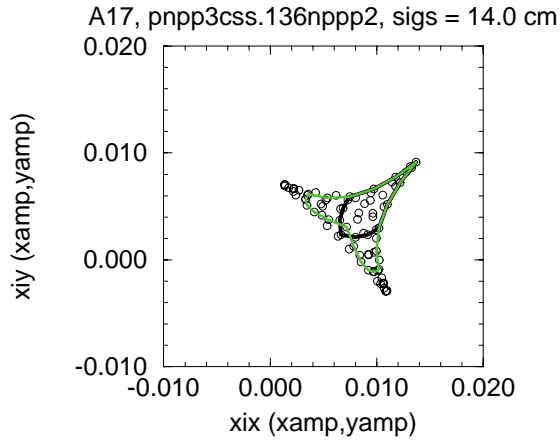


Figure 6.73. 90×90, A17, $\sigma_s=14$ cm. Tune spread from all crossing points.

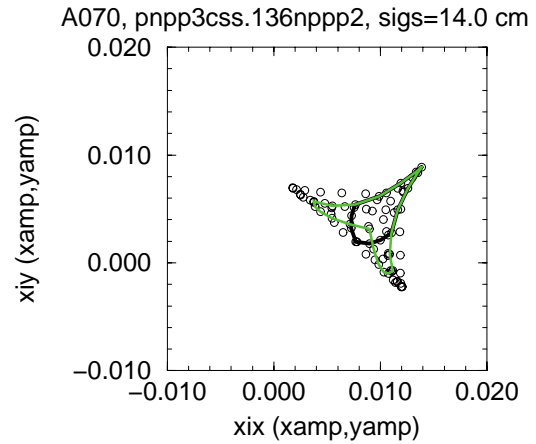


Figure 6.75. 140×121, A070, $\sigma_s=14$ cm. Tune spread from all crossing points.

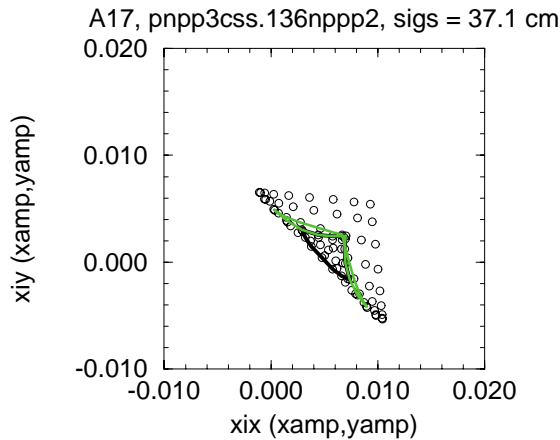


Figure 6.74. 90×90, A17, $\sigma_s=37$ cm. Tune spread from all crossing points.

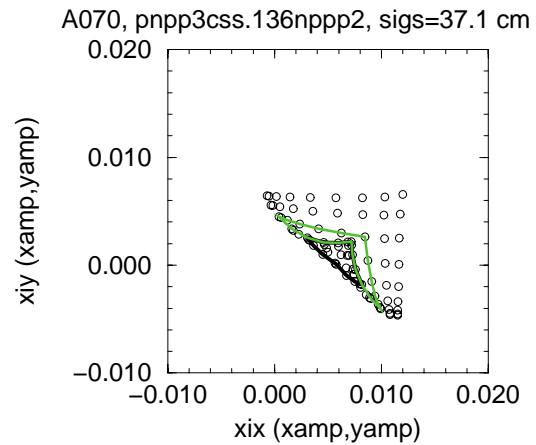


Figure 6.76 140×121, A070, $\sigma_s=37$ cm. Tune spread from all crossing points.

Figure 6.73 and Figure 6.74 show the tune spreads due to all the crossing points for the 90×90 case for 14 cm and 37 cm bunch lengths respectively. (For example, Figure 6.73 is Figure 6.69 plus twice Figure 6.71.) Similarly, Figure 6.75 and Figure 6.76 show the same things for the 140×121 case. Again for each bunch length, the figures for the 90×90 and the 140×121 cases are very similar.

In Figure 6.69 and Figure 6.70, for all the crossing points *except* B0 and D0, the points are more widely spaced for moderate to large amplitude particles, that is, the *change* in the tune shifts is larger for large amplitude particles than for small amplitude particles. The opposite is true for Figure 6.71 and Figure 6.72, for the IP's. As a consequence, all the footprints in Figure 6.73 to Figure 6.76 are folded.

As an example, for Figure 6.74, for the 90×90 case with a bunch length of 37 cm, we look at particles with equal horizontal and vertical amplitudes and consider increasing that amplitude from 0 to $4\sigma_{\beta z}$. Starting at 0 amplitude, the horizontal and vertical tune shifts decrease, reach a

local minimum at an amplitude of about $2\sigma_{\beta z}$, and then start to increase. At about $3\sigma_{\beta z}$, the tune shifts are about the same as they were for zero amplitude particles. They pass this and are continuing to rise at $4\sigma_{\beta z}$.

As a result of this folding, the extent of these footprints in the (+,+) direction* is smaller with the parasitic crossings than without them, particularly for the cases with bunch lengths of 37 cm. The extent in the (+,+) direction is also considerably less than would be the case with only two head-on beam-beam interactions at the IP's. However the width of the footprints in the (+,-) direction is mainly due to the parasitic crossings. In the (+,-) direction, the footprints in Figure 6.73 through Figure 6.76 are wider than either those from the IP's only or those if there were only two head-on beam-beam interactions at the IP's.

Now that we have some understanding of the tune footprint for a typical bunch, we'll look at how much space in the tune plane is taken up by the combined tune footprints for all the antiproton bunches.

Assuming Gaussian distributions of positions and angles for the particles in a bunch, we randomly generate betatron amplitudes for 5000 particles per bunch. Based on their betatron amplitudes, we interpolate between our calculated tune vs. amplitudes points to get the tune shifts for these particles. We then bin the particle tunes (bin size of 0.00015) and count the number of particles in each bin. The more particles in a bin the darker the point on the graph at that bin's location.

The 90×90 filling scheme has three fold symmetry, so all 3 trains see the same thing. We only need to show 30 bunches.

The 140×121 filling scheme has no symmetry. All the 121 antiproton bunches are slightly different. When we were doing the calculations for this case, we were short of time and so only calculated tune footprints for 64 representative bunches. We chose the 10 bunches at the start, in the middle, and at the end of each train. For the short train, this would have left out only 4 bunches, so we just did all the bunches in the short train. For the long train, this skips 57 bunches.

These histograms of the combined tune footprints are shown in Figure 6.77 through Figure 6.80 for the 90×90 and 140×121 cases and for bunch lengths of 14 and 37 cm. In these figures, the open circles are the tune shifts for zero amplitude particles in each bunch. The darkness of the gray scale indicates how many particles have those tunes.

* * If \vec{i} is a unit vector in the +x direction and \vec{j} is a unit vector in the +y direction, when we refer to the (+,+) direction, we mean the direction $(\vec{i} + \vec{j})$. Similarly when we refer to the (+,-) direction, we mean the direction $(\vec{i} - \vec{j})$.

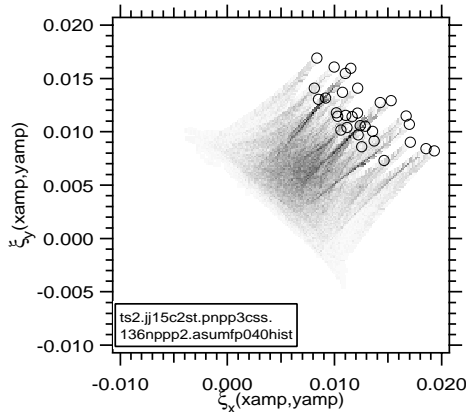


Figure 6.77 90×90, 14 cm, All bunches. Tune spread from all crossing points.

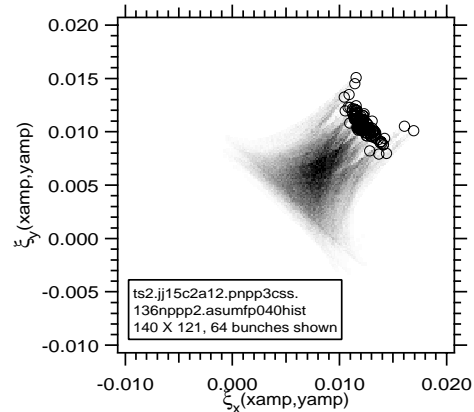


Figure 6.79. 140×121, 14 cm, 64 representative bunches. Tune spread from all crossing points.

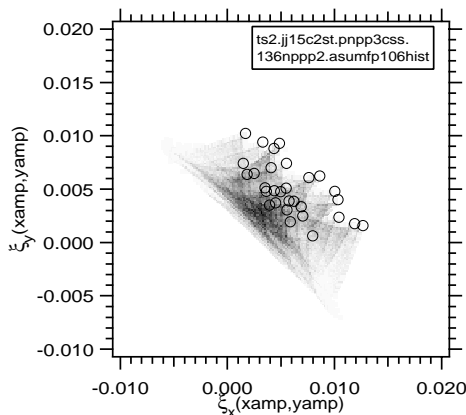


Figure 6.78. 90×90, 37.1 cm, All bunches. Tune spread from all crossing points.

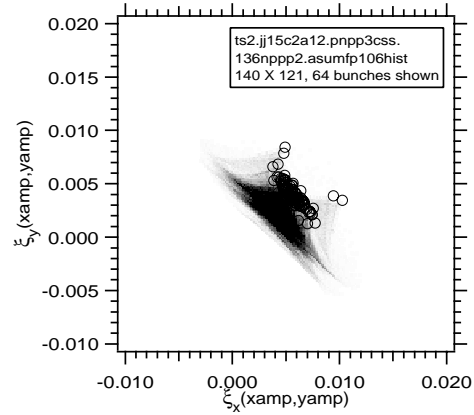


Figure 6.80. 140×121, 37.1 cm, 64 representative bunches. Tune spread from all crossing points.

The differences in the tune shifts for zero amplitude particles in each bunch make a significant contribution to the total space taken up in the tune plane. As noted earlier, these zero amplitude tune shifts are more tightly clustered for the 140 × 121 case than for the 90×90 case, resulting in the 140×121 case taking up less space in the tune plane.

In Figure 6.77 and Figure 6.78, the zero amplitude tune shifts for the 90×90 case appear to fall into an upper and a lower "tier", where each tier runs along the (+,-) direction and the upper tier is displaced from the lower tier by about (0.002,0.002). All the points in the upper tier correspond to bunches within 2 of the edges of the trains or sub-trains. Those at the front of the trains or sub-trains are at smaller horizontal tune shifts and larger vertical tune shifts and those at the back are at larger horizontal tune shifts and smaller vertical tune shifts. Of the lower tier, 4 of the points on the edges (the 3 points with the smallest horizontal tune shifts and the one point with the largest horizontal tune shift) are within 3 of the ends of the trains or sub-trains.

In Figure 6.79 and Figure 6.80, for the 140×121 case, the first two antiproton bunches in the short train are the two points with the largest vertical tune shifts (above the main cluster) and the last two bunches in the long train are the two points with the largest horizontal tune shift (to the

right of the main cluster). These are the bunches that do not see proton bunches at some of the first two crossing points on either side of D0. We are considering not filling these 4 bunches if they cause problems.

A great deal of the spread in the zero amplitude tune shifts for the 90×90 case is due to the bunches near the edges of the trains and sub-trains. The reduced number of edges for the 140×121 case (4 rather than 18) greatly reduces this spread.

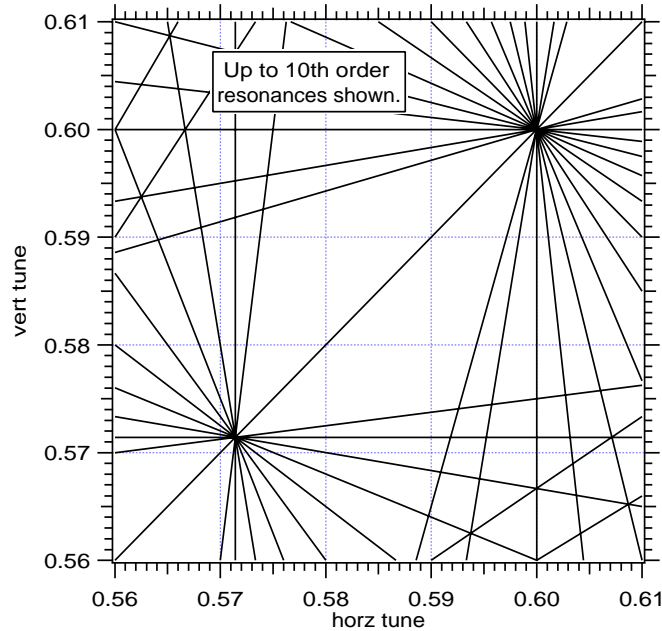


Figure 6.81. Tune plane near our usual operating point of about (.585, .575), showing resonances up to 10th order.

Figure 6.81 shows the tune plane near our usual operating point of about (.585, .575), just above the 4/7 and just below the 3/5. It shows the resonances up to 10th order. Lines with negative (positive) slopes represent sum (difference) resonances. Sum resonances are generally felt to be more destructive than difference resonances. The clear space is cut into two pieces by the line ($v_x=v_y$). This corresponds to the difference resonances ($v_x-v_y=0$), ($2v_x-2v_y=0$), ($3v_x-3v_y=0$), etc. The resulting two pieces of clear space have roughly the shape of right isosceles triangles whose equal sides have length of about .02 and whose hypotenuse has length of about .03. The shape of these regions gives more space in (+,+) direction than in (+,-) direction.

One important question is how well the tune plane space occupied by the antiprotons, as shown in Figure 6.77 through Figure 6.80, fits into the space between resonances shown in Figure 6.81.

The 90×90 cases shown in Figure 6.77 and Figure 6.78 don't quite fit between the resonances and must overlap several. The first few resonances which cut into the clear space and which the tune distributions overlap, are 7th and 9th order difference resonances. These *might* be weak enough so that this is acceptable. Alternatively, if we can straddle the line ($v_x=v_y$), this would effectively double the available space and the tune distribution would fit pretty well between the resonances. The problem is similar for both the 14 cm and the 37 cm bunch lengths, because the main problem for both is that the tune distributions are wide in the (+,-) direction. We feel that the 90×90 cases take up too much space in the tune plane and that this must be reduced.

The 140×121 cases shown in Figure 6.79 and Figure 6.80 are more compact in the (+,-) direction, primarily due to the reduced spread in the tune shifts for zero amplitude particles. These fit fairly well between the resonances. Also, we can get a little more margin if we leave out the 4 antiproton bunches separated from the main cluster.

Generally speaking, a smaller tune distribution is better. It fits better in the space between resonances and overlap fewer resonances. However, that our tune footprints pretty much fit within the clear space in the tune plane, does *not* guarantee that those resonances will not be a problem for us. (Very loosely speaking, this is analogous to the way that a small tune shift for zero amplitude particles from a certain crossing point does *not* guarantee that point will also contribute small tune spread for particles with a range of betatron amplitudes.) Alternatively just because a resonance crosses the tune distribution does not mean it will be a problem. That particular resonance may not be driven strongly by our non-linearities or the resonance may be weak for the particular amplitudes of the particles that are close to it in tune. (In our decision to only show up to 10th order resonances on Figure 6.81, we use this implicitly, assuming (or hoping) that resonances of greater than 10th order will not be major problems even if they do cross the tune distributions.)

It is encouraging that the 140×121 cases fit fairly well between the resonances in the tune plane. However this is by no means enough to claim that the beam-beam behavior will be acceptable. We have several general concerns about these schemes :

- 1) The first 3 crossing points on either side of the IP's contribute large tune spreads, suggesting a strong beam-beam effect driving strong non-linearities. The beams are separated at these points. For separated beams, the beam-beam interaction drives different resonances and the dependence of the resonance strengths and widths on a particle's betatron amplitudes is different. More families of resonances can be driven and certain resonances will be driven at much lower order. For example, the head-on beam-beam interaction can only drive even resonances, so the many resonances near 3/5 are only driven as 10th order resonances and the many resonances near 4/7 are only driven as 14th order resonances. With the beams separated, the beam-beam interaction can drive both odd and even resonances and can drive these as 5th and as 7th order resonances. This *may* increase the widths of these resonances, further reducing the available space in the tune plane.

- 2) The crossing angles at the IP's introduce another mechanism to drive synchro-betatron resonances. For our conditions, for bunch lengths of 37 cm and 14 cm, the synchrotron tunes at 1.0 TeV are 0.0007 and 0.0056, respectively. For 14 cm, the synchrotron tune is large enough so that if synchrotron side-bands appear off the betatron resonances, they will significantly reduce the clear space in the tune plane. This effect is much smaller for 37 cm bunch lengths.

- 3) The folds in the tune footprints (seen most clearly in Figure 6.73 through Figure 6.76 may worsen the effects of resonances near the beams. Typically, as a resonance increases the amplitude of a particle, the particle's tunes change, moving it off the resonance. With folds in the tune footprints, if the folds are oriented in the wrong direction, the particle's amplitudes may be able to change by larger amounts before the particle tune shifts away from the resonance.

- 4) For the 140×121 case, not all of the proton bunches collide with antiproton bunches at both B0 and D0. This causes differences between the proton bunches and it may be difficult to find conditions that are satisfactory for *all* the proton bunches. If the antiproton bunch intensities are low, maybe less than about 50×10^9 /bunch, we don't expect this to be too much of a problem. Additionally, with the beams in collision, we can reduce the chromaticities to values that would make the protons unstable if the beams were separated. This reduction in the chromaticity helps the

beam lifetimes and the background rates. If some of the proton bunches only collide once per turn, we may not be able to reduce the chromaticity as much, or we may have to rely on damper systems to keep these bunches stable.

There is still a great deal of work to be done, improving the separation schemes and extending our calculations, before we have a satisfactory plan. In the end, even after all our calculations, there will still be a large gap between what we can calculate and predict and the actual important parameters of the machine performance. While we may be able to use our calculations to avoid complete disasters, we cannot ensure good performance. The final test is always what happens in the machine.

6.15 High Temperature Superconducting Power Leads

Table 6.24 summarizes the helium usage by power leads in the Tevatron. The Table shows that in collider mode ~50 g/sec of helium flow goes into cooling these power leads. It is expected that this can be substantially reduced by replacing many existing leads with a new design incorporating high critical temperature superconductor.

The Technical Division has instituted an R&D program to develop such leads. Contracts have been let to two commercial vendors for prototype leads. A test setup is under construction with commissioning expected in September 1997. The prototype leads will be evaluated in October and November. It is anticipated that a Technical Division/Beams Division engineering team will then develop specific specifications for another round of lead development by one or both of the vendors. These next iteration leads will be tested, and if the specifications are successfully met, orders will be placed for production units. Production leads will be tested prior to installation.

Table 6.24 indicates that the 6-lead boxes for the low-beta insertion triplets have highest priority. This is because of access problems when the CDF and D0 detectors are rolled in and the in-tunnel shielding walls are in place. The two 6-lead boxes assigned to D0 are now out of the tunnel and readily accessible (because of the fixed target running configuration) as is the spare. The goal is to push this program forward so that this lead replacement can be accomplished by early 1999.

Table 6.24. TEVATRON POWER LEADS (TJP 17 February 1997)

Device	Replace- ment priority	Number of boxes installed	Number of leads	Lead size (kA)
Tevatron feed can	last	12	24	5
Power-spool (H-spool)	second	12	24	5
Safety leads, Correction leads, etc.	low	many	48 strings	0.1
6 Power lead box for triplet quads	first	4	24	6
P, L spools (for Q1, Q5 quads)	third	8	16	5 (or 6?)
J, K spools (with high-field quad)		4	8	5 (or 6?)
M, N spools (with 5-in-1 quad)		12	24	2
Barrier box (D0 only)		2	4	5
TOTAL RING FLOW				

Table 6.25. TEVATRON POWER LEADS (TJP 17 February 1997)

Device	Flow per lead (g/s) and [l/hr]*		Total flow for ring (g/s)	
	Power on	Power off	Fixed target	Collider
Tevatron feed can	0.32 [9.2]	0.16 [4.6]	7.68 [221]	7.68 [221]
Power-spool (H-spool)	0.42 [12.1]	0.25 [7.2]	10.08 [290]	10.08 [290]
Safety leads, Correction leads, etc.	0.11 [3.1] per string	0.11 [3.1] per string	5.51 [159]	5.51 [159]
6 Power lead box for triplet quads	0.42 [12.1]	0.25 [7.2]	2.94 [84.7]	10.08 [290]
P, L spools (for Q1, Q5 quads)	0.42 [12.1]	0.25 [7.2]	3.92 [113]	6.72 [194]
J, K spools (with high-field quad)	0.42 [12.1]	0.25 [7.2]	1.96 [56]	3.36 [97]
M, N spools (with 5-in-1 quad)	0.14 [4.0]	0.11 [3.1]	2.52 [73]	3.36 [97]
Barrier box (D0 only)	0.42 [12.1]	0.25 [7.2]	0.98 [28]	1.68 [48]
TOTAL RING FLOW			35.6 [1025]	48.5 [1397]

* Note: Flows are averages from old ring data and MTF data. Actual flows in the ring may be slightly different from this.

Comments on replacement priority:

1. 6 Power Lead Box accounts for about 21% of the total lead flow, about 6% of CHL capacity, in just 4 boxes. This fact plus accessibility during the next few years make it the best prospect for a lead upgrade.
2. Power-spools also account for about 21% of the total lead flow and are more accessible than feed cans, but there are 12 of them, hence they are second in priority on this list.
3. Feed cans are judged to be difficult to replace and in a bad location for HTS leads based on the cold-shock of cool-down. Hence, they are the worst place for HTS lead replacement.

6.16 Tev Spare Magnet Requirements

The Laboratory's Technical Division maintains facilities for the repair of all Tevatron magnets as well as for new construction. The installed magnets can be grouped into four classes:

1. Standard dipoles. There are approximately equal numbers of the TB and TC series as well as a few specials. In the factory a TC can be readily converted into a TB, but not vice versa. TD series are half length dipoles.
2. Standard quadrupoles. These include the arc quadrupoles of the TQ series as well as several kinds of straight section quadrupoles, which are similar to arc quadrupoles except in length. These are internally bussed as F-series (D-series), i.e., horizontally focusing (defocusing). In the factory F's can be readily converted to D's and vice versa.
3. Standard spool pieces. There are several series designated TSA,....,TSH which differ one from another in several ways including the number and kinds of nested weak corrector packages.
4. Low-beta insertion devices. These range from the large focusing triplet quadrupoles to specialized spool pieces.

6.16.1 Tevatron Dipoles

Table 6.26. List of standard TB and TC dipoles replaced in the Tevatron between 12 February 1990 and 1 August 1997 (no TD's were replaced).

Category of Repair		
	- Determined not to be faulted	N
	- Characterized as easily fixed	E
	- Characterized as a hard/expensive fix	H
	- Repair not yet characterized	U
	- Unfixable	X
	- Unsatisfactory quench performance	Q
1990	TB0340	E
	TB0823	U
	cold leak?	
1991	TB0297	E
	TC0496	X
1992	(none)	
1993	TB0453	N
	TB0568	N
	TB0662	Q

	TB0841	E
	TC0588	N
	TC0861	E
	TC0987	E
1994	TB0280	N
	TB0332	H
	TB0448	X
	TB0972	E
	TB1003	N
	TC0500	H
	TC0893	H

1995	TB0281	U	
	TB0340	E	
	TB0410	X (*)	
	TB0582	X	
	TC0555	E	
	TC0603	U	
(*) This is the "E" where we've found broken strands I'm treating this as unfixable, but we need to clean up the end first to be sure...			
1996	TB0214	Q	3/96 limiting quench C42
	TB0443	Q	3/96 on basis of MTF data, not tunnel experience
	TC0504	Q	4/96 limiting quench E24
	TC0508	X	6/96 blew up at C11, leads untied
	TC1052	U	8/96 limiting quench B18, but could be rag?
	TB1055	Q	3/96 on basis of MTF data, not tunnel experience
	TB1126	E	5/96
	TB1138	U	6/96 got sooted when adjacent dipole blew at C11
1997	TB0267	U	7/97 cold leak?
	TC0476	N	5/97 OK dipole taken out during E11 fault
	TC0509	H	5/97 Intermittent short D46, leads untied
	TC0525	Q	3/97 limiting quench E37
	TB0633	N	3/97 1 of 3 in tunnel hit by cart?
	TB0736	U	3/97 1 of 3 in tunnel hit by cart? prob "E"
	TC0790	U	7/97 cold leak?
	TB0958	Q	3/97 limiting quench C29
	TC1077	U	3/97 1 of 3 in tunnel hit by cart? prob "E"

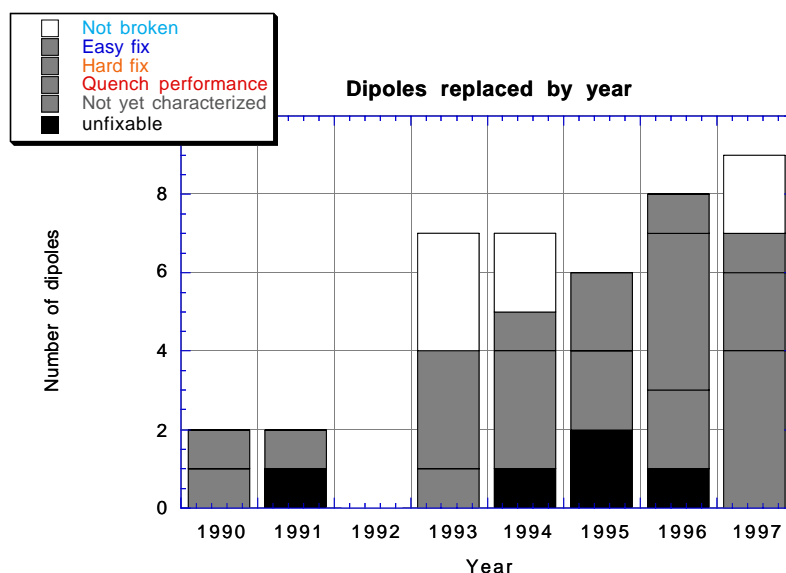


Figure 6.82. Number of Tevatron dipoles replaced by year

When a magnet problems forces suspension of operations, the imperative is to restore operations as quickly is possible. Often the faulted device is not unambiguously identified, and all possibly faulted devices are replaced at the same time. Later the removed devices are assessed above ground, and unfaulted devices listed in the available spares inventory. An example is the event of 15 May 1997, when four magnets were replaced, and later the quadrupole H8204D was identified as the only faulted device.

During the eight years of operating experience summarized in Table 6.26 on the average fewer than one dipole/year has faulted in a way that can not be repaired. This is an important point: Most faulted magnets can be repaired, and the size of the potential spares pool has not declined much during this period due to faults during operation. (Table 6.26 shows five magnets that are recognized as being unrepairable, but it is important to realize that until a magnet is actually worked on, surprises may occur. For example, TB0410 removed in 1995 was first classified as an easy repair, but, when the repair was attempted, broken strands in a lead were discovered .)

Table 6.27. Characterizes all standard TB, TC, and TD dipoles not in the unrepairable category as of 1 August 1997.

	TB	TC	TD
Installed during collider operations	395	377	2
Available spares	10	14	3
Potentially repairable	19	20	
Unsatisfactory quench performance?	6	5	

It can be seen that the number of available spares is large compared to the recent yearly replacement experience. It has been possible to maintain an adequate spares inventory while backlogging the hard/expensive fixes; many of those classified as hard fixes faulted prior to 1990. Because of competition from Main Injector work for skilled personnel, it is desirable to continue to

defer work on hard/expensive fixes until spring of 1998. Note that these fixes invariably require passage through Technical Division's cold test facility to confirm success of the repair, to reset the smart bolt/dumb bolt system in order to tune the normal and skew quadrupole components in the field, and to determine alignment data. Some magnets will prove to be unfixable and will have to be decommissioned.

In the future the spares pool needs to support these activities:

1. An "inspection" of selected Tevatron magnets will be made during the coming shutdown. The target is dipoles in which the lead ties may be absent or the leads subject to abrasion on sharp edges or where loose pieces could stick in Kautzky valves. Some problem magnets may be found and some may have broken superconductor strand that would lead to their decommissioning.
1. The warm up/cool down cycle is expected to show up many problems. During the coming shutdown some shuffling of magnets will occur in support of the 1 TeV program. The last full ring warm up/cool down cycle including substantial magnet interface work was in 1989 when the lead tie problem was last addressed. In that year 34 dipoles were replaced for a variety of reasons. Replacements directly traceable to the warm up/cool down cycle are difficult to isolate in this count. It is possible that this thermal cycle mechanical stressing plus the problems occurring during the interface work accounted for as many as 22 of the 34 dipole replacements.
1. The 1 TeV program relies mostly on shuffling magnets in the ring. During 900 GeV Run I collider mode operation, the Tevatron quenched at about 925 GeV equivalent. Reliable 1 TeV operation is thought to require raising the comparable quench performance number to at least 1030 GeV equivalent, about an 11 % increase in excitation current and a 21% increase in force levels in the dipoles and quadrupoles. So far 1010 GeV has been achieved, albeit for only a short period of time. Five dipoles designated "limiting quench" magnets have had to be replaced so far during the program. No dipole has faulted; one standard quadrupole has. Of these five dipoles two likely will have to be decommissioned. It is an open question whether the other three can operate satisfactorily if installed at the most cryogenically favorable locations in the ring. The same question exists concerning the other six magnets in the "unsatisfactory quench performance?" category. In-hand quench performance information supports changing out only a few additional dipoles during the upcoming shutdown; after 1 TeV tests resume toward the end of 1998 or early 1999 more changeouts are likely. But there is no way to know how many more dipoles will be decommissioned before reliable 1 TeV operation is achieved; a program total of 15 may not be an unrealistic estimate. The planned shuffling involves considerable interface work, not dissimilar to that done in 1989.
1. After reliable 1 TeV operation has been achieved, there will continue to be magnet faults. The optimistic view is that the experience of the past several years will continue: Many faults will be easy to repair, some will be hard/expensive to repair, and the occasional magnet (~1/year?) will have to be decommissioned.

The size of the spares pool necessary to support operations is open to debate. There are (at least) two significant issues: What is the worst kind of fault event (in terms resulting dipole changeouts), and can the previous replacement algorithm which involved "matching" magnet harmonics be relaxed to focus principally on quench performance? It is conjectured that a power system fault induced by, say, a lightning strike, could damage a half dozen magnets. The spares inventory needs to be able to accommodate two such events closely spaced in time. Such events are unlikely to damage only TB's or only TC's - there will be a mix of both. This scenario suggests

the minimum spares pools during operations should be 10 of each. If the changeout algorithm is relaxed, no increase is needed to provide for harmonics matching.

To summarize: there are now 74 (sum of TB's and TC's) dipoles that are ready potential spares. Addressing the 39 potentially repairable magnets may result in 3-8 being declared unrepairable. Excluding these and the 11 known (possibly) unsatisfactory quench performance magnets would reduce the 74 by 14-19, that is, to 60-55 by the fall of 1998. If the 1989 shut down experience is predictive and the inspection doesn't turn up too many magnets to be replaced, by that time the spares inventory will have to be built up to ~ 40 to provide for possible changeouts during the shutdown and cooldown and to have an adequate spares pool when operations resume. This will require resuming work on the hard fixes no later than spring of 1998 and repairing the changed out magnets in a timely way. By the fall of 1998, the number of unrepairable faulted magnets may have risen to 5-10. If subsequent 1 TeV commissioning identifies 8 of the 11 known questionable magnets plus another 15 to be decommissioned, the potential spares pool will still be in the 40-45 range, or twice the minimum required number of ready spares. So if the unrepairable fault rate during 1 TeV operations is comparable to that seen over the past eight years, it will be a while before new dipoles are needed.

There is no superconducting strand in-house. Obtaining cable with which to wind new coils is estimated to require 12 months. Other materials used in collared coil assemblies also need to be obtained; there would be a number of yokes and cryostats available from magnets decommissioned due to unacceptable quench performance. Here is a preliminary estimate: Eighteen to twenty-one months after the decision to proceed has been made, the first "new" dipole could be ready for cold testing. The reconstituted fabrication facility could have a second dipole ready two months later; and subsequent units could then be built at a rate of one per month. The team required for such an effort is estimated at 2.5 engineers, 1 designer, 2 tooling techs, 6-8 fabrication techs, and 0.5 QC specialist. To get the first magnet will require ~ \$ 400 K, the second ~ 200 K, and subsequent magnets ~ \$120 K each. It would not be sensible to plan to make fewer than ten, so this would be a ~ \$1.6 M undertaking. It must be emphasized that this schedule and cost estimate is merely an initial estimate, not the result of a detailed study.

6.16.2 Standard Tevatron Quadrupoles

A similar analysis made for the class of standard quadrupoles for the same time period cited for dipoles identifies only three arc quadrupole replacements. The involved magnets are all easy repairs. One was not faulted itself but was the recipient of a load of soot from a faulting adjacent dipole. During 1 TeV work a straight section quadrupole H8204D shorted internally; work is still in progress aimed at determining the cause of this fault. A N99 F quadrupole was removed at the same time, but is now known to be OK. Assuming that the H8204D situation is not the forerunner of more extensive problems, the spares situation shown in Table 6.28 is adequate for the foreseeable future.

Table 6.28. Characterizes Tevatron Quadrupoles.

	TQF	TQD	H25F	V25D	V32D	H82D	H82F	H90D	H90F	N99F
Installed during collider operations	90	90	1	1	3	3	3	1	1	8
Available spares	5	6	3	2	5	2	2	2	2	7

Potentially repairable	8	6	0	1	0	0	0	0	0	0
------------------------	---	---	---	---	---	---	---	---	---	---

Standard quadrupoles use the same cable as standard dipoles. If new quadrupoles were required, a similar effort and time scale would be required.

6.16.3 Tevatron Spool Pieces

The standard spools situation is shown in Table 6.29. During the 1990-1997 period one TSA, one TSB, one TSC, two TSD's, and two TSH's have been replaced. One H-spool was removed along with H8204D; it is now known that the quadrupole was the faulted unit. The situation for TSD's is complex: These spools have two nested weak correctors, referred to as "upstream" and "downstream". In 11 locations the downstream corrector is not powered. A "TSD-1" spool designates a D-spool purposely lacking a functional downstream corrector. So the two listed TSD-1 spares could be used in place of any of these 11, either when one of the 11 needed to be replaced or in order to free up a "complete" D-spool for use elsewhere.

Table 6.29. Characterization of Tevatron Spool Pieces

	TSA	TSB	TSB-1	TSC	TSD	TSD-1	TSE	TSF	TSG	TSH	TSH-1
Installed during collider operations	12	36	2	48	32	0	19	17	8	8	1
Available spares	3	4	1	6	2	3	2	4	3	4	1
Potentially repairable	2	3	0	8	5	0	2	14	2	5	0

The design of standard spools is such that many faults require a complete teardown of the spool in order to make repairs. Although there is some weak corrector wire in-house, repairing a spool with a failed corrector would probably be approached by cannibalizing another failed spool for its corrector. A problem with any spool teardown and reassembly is the lack of documentation.

6.16.4 Low Beta Quadrupoles

Table 6.30 shows low-beta devices. The number of spares was deliberately held low. Only one device—a TSP spool—has been changed out during this eight year period. However the Q3 on the A4 side of CDF has had both its heaters fail; it is scheduled for replacement during the coming shutdown. If the fault is deep within its cold mass, the cold mass will be replaced by the one existing Q3 "reserve" cold mass; this is the direct route to a spare. There is also now discussion about replacing a Q4 that has poor hi-pot performance. There is also a single reserve cold mass suitable for either a Q2 or Q4. The same cross-section cold mass is used in the T6 corrector in TSJ and TSK spools and in the Q1/Q5 quadrupole.

Table 6.30. Characterization of low beta quadrupoles.

	TSJ	TSK	TSL	TSM	TSN	TSP	TSR	N54 (Q1/Q5)	N13 (Q2)	N23 (Q3)	B13 (Q4)
Installed during collider operations	2	2	4	6	6	4	1	8	4	4	4
Available spares	1	1	1	2	2	1	1	1	1	1	1
potentially repairable	0	0	0	0	0	0	0	1	0	0	0

It has been long thought that the low-beta devices' cryostat faults could be repaired; there are no reserve cryostats. There is insufficient strand in house for building additional reserve cold masses of any kind.

6.17 C0 Collision Hall

The C0 Interaction Region project creates a facility where modest experiments and detector R&D may be undertaken at a potential third interaction point in the Tevatron collider. A FY98 project will provide an experimental area ± 40 feet along the beam and ± 8 feet transverse to the beam, along with a modest staging area, counting room facilities, and some minimal utilities. Future funding will be required to complete the outfitting of this facility for the installation of experiments, and for the low-beta focusing elements and electrostatic separators necessary to bring beams into collision at moderate luminosities.

The only part of this project well defined at this point is the civil construction of the collision hall and the assembly hall. This construction will take place during the Main Injector Shutdown in 1997-1998. Presently the C0 straight section in the Tevatron is a "normal" straight section that contains the C0 proton abort. After the civil construction is completed, the C0 abort and all of the Tevatron elements at C0 will be reinstalled. Eventually the C0 abort will be removed, so experimental apparatus may be placed in the C0 straight section. During collider operations, the A0 abort will be used for emergency removal of beam from the Tevatron.

There is no schedule for either the installation of an experiment at C0 nor the lattice modifications necessary to provide collisions at low beta. The schedule in Table 6.31 gives a plausible scenario, but it must be emphasized that plans for lattice modifications and experiments are at a most preliminary stage and no funding (other than the civil construction) has yet been approved.

There is a lot of work that needs to be done to specify the modifications to the lattice. These include a low beta at C0 lattice design, design and fabrication of low beta quadrupoles, and separator configurations to provide collisions at C0. The separator configuration is made more complicated by the shortage of warm space in the Tevatron and the necessity of providing collisions at B0 and D0 concurrently with collision at C0. Because of these limitations C0 may have to run with a crossing angle. It should also be noted that beam-beam interaction considerations suggest that colliding beams at C0 imply a reduction of luminosity at CDF and D0 by roughly 33%. The additional interaction point means there will be 3 places where the protons and antiprotons collide instead. The additional beam-beam tune shift from the extra crossing will require a reduction in proton intensity to keep the beam-beam tune shift within operational limits.

Thus the reduction of luminosity at CDF and D0. The situation is probably not this simple because of the tune shifts from the long range beam-beam interactions but a 33% reduction is about the right order of magnitude.

Table 6.31. Possible Schedule. This shows as a guess at a possible timing scenario for the shutdowns and detector installations. It should be emphasized that the funding and schedule has been determined only for the construction of the C0 Collision Hall. The rest of schedule depends on further funding and detector development.

Operations =====	Shutdown =====	Tevatron Configuration =====
FT ops (now)		Abort at C0. Extraction at D0
	MI installation C0 Exp Hall & Beam Enclosures	
Commission MI=>FT. Finish C0 external building with (minimal utilities)	C0 abort in.	D0 extraction in. CDF & D0 out.
	MI(FT) => MI(Collider)	
Commission MI=>collider		Abort at A0. C0 abort still in place. Remove D0 extraction. CDF & D0 low-Beta and separators installed. CDF & D0 out
	Roll-in CDF & D0	point A Abort at A0. CDF & D0 installed.
Operate CDF & D0 for 1 fb ⁻¹ each		CDF & D0 low-Beta and separators installed
Alternating 3 month exp. physics runs and relatively short 2-4 week shutdowns for detector maint. & repairs		
	Reconfigure for 36 => 99 bunches, (396 nsec => 132 nsec)	New separators Finite crossing angles. RF modifications

Operate CDF & D0
(indefinitely)
interspersing
M&D and operations

At Point A in the schedule (during the Fixed Target to Collider changeover) BTeV may want to install the SM3 spectrometer magnet in the C0 straight section. The questions concerning the installation of SM3 are:

- Will it be ready?
- Will funding be available?
- What about early soft-physics experiments?
- More importantly, since MI=>collider commissioning will have been accomplished with FT abort in place, pressure will be there to operate using the exact configuration that was just commissioned (In the long run, this is an untenable position since one could never make any changes or improve anything)

As the C0 lattice is modified to provide interactions and low beta at the C0 interaction point there are a number of possible configurations. The general ideas are listed below but more work is needed to establish the feasibility of some of these configurations.

- 1) Present FT abort configuration. Use existing lattice at C0 which has two half-dipoles, abort kickers, Lambertson magnets, C-magnets, pipes and bypasses This gives a beta = 70 meters
- 2) Convert to a normal long straight section. This involves replacing the two half-dipoles with two full-length TeV dipoles, remove abort kickers, abort Lambertsons, C-magnets, and Sync light instrumentation. This gives beta = 70 meters.
- 3) Improved optics with normal long straight section. Optimize luminosity and beam lifetime for operations with wire targets but without proton-antiproton collisions. Consider reducing beta to 10 - 20 meters.
- 4) Add SM3 analysis magnet (5.2 T-m, B=1.6 T) with compensating magnetic bends near the quadrupoles. This could be a horizontal or vertical 3-bump and has no effect on beta.
- 5) Proton-Antiproton collisions at C0. The separator configuration is not yet designed and is coupled to the problem of providing collisions at CDF and D0. Other options are:
 - a) Is it possible to have collisions without additional separators
 - b) Low luminosity collisions by turning OFF existing separators
 - c) New separators at C0:
 - i) No crossing angle. But is there enough room for separators?
Won't work with 132 nsec bunch spacing.
 - ii) Use only existing separators and live with a finite, non-adjustable angle and lose some luminosity.
 - iii) Finite adjustable angle for 132 nsec bunch spacing?
- 6) Low-Beta* insertion with compensation in superconducting spools. How low can we make beta*? (1-3 meters seems attainable - J. Johnstone) but still need a matched insert design. The technology for low beta magnets consists of several options
 - a) current technology from CDF & D0 insertions
 - b) current technology w/higher performance wire

- c) current technology w/cold compressors
- d) LHC technology with current refrigeration
- e) LHC technology with cold compressors
- f) LCH magnet and new refrigeration technology

6.18 Superconducting RF

6.18.1 Use of a Higher Frequency, higher voltage rf System

A high frequency, high voltage rf system can be used to produce short bunches in conjunction with or independently of the existing 53 MHz rf system. One possibility is to accelerate the beams and to bring them into collision with the high frequency system. This option is conceptually simple but places requirements on the rf power, tuning system, and voltage that would otherwise be less severe. An alternative is to use the 53 MHz system to accelerate the beams and to bring them into collision and to use the high frequency system only to shorten the bunches. The bunches can be shortened most easily by turning on the high frequency system adiabatically. Turning on the cavities would most likely be accomplished by slowly bringing the cavities into tune. The disadvantage of this method is that it will produce satellite bunches if the 53 MHz bunch length is longer than the period of the high frequency rf. This limitation could be overcome by rotating the bunches with the 53 MHz rf system. This method could eliminate the satellites, but it requires careful control of both systems and may provoke excessive beam loss through the long-range beam-beam interaction.

6.18.2 Effect of Crossing Angle and Bunch Length on Luminosity

We plan to use a crossing angle in the Tevatron to avoid deleterious effects from the parasitic crossings near the interaction region. Figure 6.83 shows the dependence of the luminosity as a function of crossing angle ($\theta_x = \theta_x$) for various bunch lengths. The nominal initial bunch length is 37 cm with the existing rf system and 14 cm with the high frequency rf system. The nominal crossing angle is 136 μ rad. **Table 6.24** gives a list of the parameters used to generate Figure 6.83.

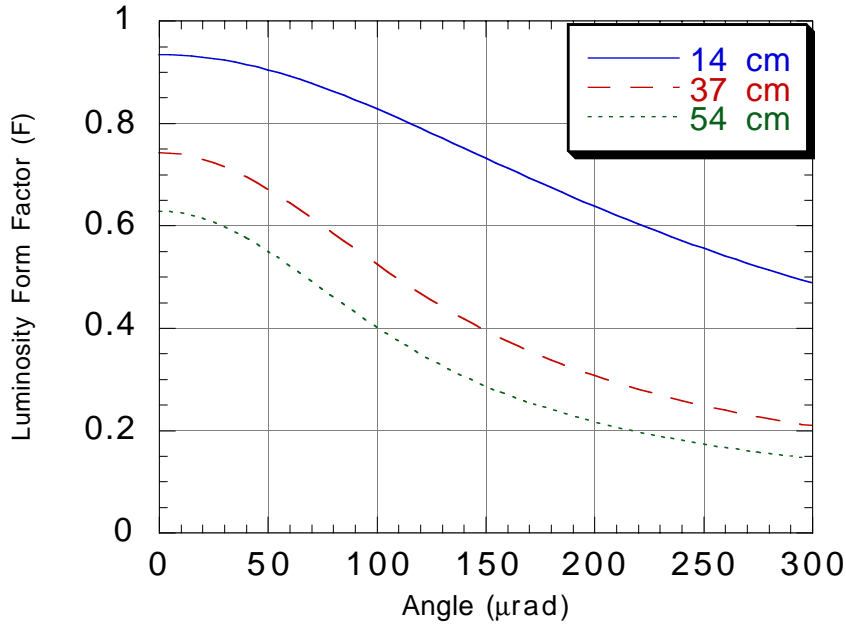


Figure 6.83. Luminosity form factor versus crossing angle for various bunch lengths. The nominal initial bunch length for Run II is 37 cm and a typical crossing angle is 136 μrad .

Table 6.32. List of parameters used in the luminosity comparison.

$\beta_x=\beta_y$	35	cm
$\epsilon_x=\epsilon_y$	20	π mm-mrad

6.18.3 Choice of Frequency and Voltage

The goal of the rf system is to reduce the bunch length by a factor of two while producing a bucket large enough to contain the beam. The bunch length is proportional to $1/\sqrt[4]{hV}$ where h is the harmonic number and V is the voltage. It is desirable to increase both the harmonic number and the voltage to reduce the bunch length. However, the bucket area is proportional to $\sqrt{V/h^3}$. In order to use the system to accelerate the beam the system must provide a bucket area greater than 2 eV-sec. Even if the system is not used for acceleration, the bucket at flattop must contain the beam emittance including the emittance growth from intrabeam scattering during the course of the store. A bucket area of 5 eV-sec at flattop is a reasonable minimum bucket area. The fact that higher gradients can be obtained at lower cost with high frequency biases the choice towards higher frequency, but the bucket area requirement suggests that $h=4452$ and $V=20$ MV is a reasonable choice. Superconducting rf is a good choice to generate the high gradients required

Table 6.33. Computed rf parameters for 20 MV at $h=4452$ in the Tevatron.

Parameter	150 GeV	1000 GeV	
Bucket Area	2.3	6.0	eV-sec
Bucket Height	388	995	MeV

6.18.4 Cavity Groups

It is desirable to have independent proton and antiproton rf systems. Two 10 MV cavities spaced by an odd multiple of quarter wavelengths phased to provide 20 MV to the proton beam will not effect antiprotons. A second pair of cavities will be phased to provide voltage to the antiproton beam while not affecting the protons. This technique is already used for the 53 MHz rf. Each cavity will consist of a group of 3 cells to generate the required 10 MV.

6.18.5 Cryogenic Requirements

The power lost in the cavity is small but significant because it must be removed at cryogenic temperatures. Specifying a minimum shunt impedance of $540 \text{ G}\Omega$ yields a maximum rf dissipation of 175 W in a single 10 MV rf cavity. The cavity R/Q will be approximately $180 \text{ }\Omega\text{T}$, so the Q must be greater than about 3.2×10^9 at 10 MV. The static heat load is specified to be less than 75 W per cavity, so the total cryogenic requirement for 4 cavities is 1000 W. This requirement can be satisfied by a standard Tevatron satellite refrigerator.

6.18.6 Power Amplifier

The general schematic of the power amplifier used for the purpose of estimating the power requirements is shown in Figure 6.84. The power is delivered from the power amplifier through a transmission line and a circulator. The transmission line is matched to the beam loaded cavity, and reflected power (if any) is absorbed by a load resistor.

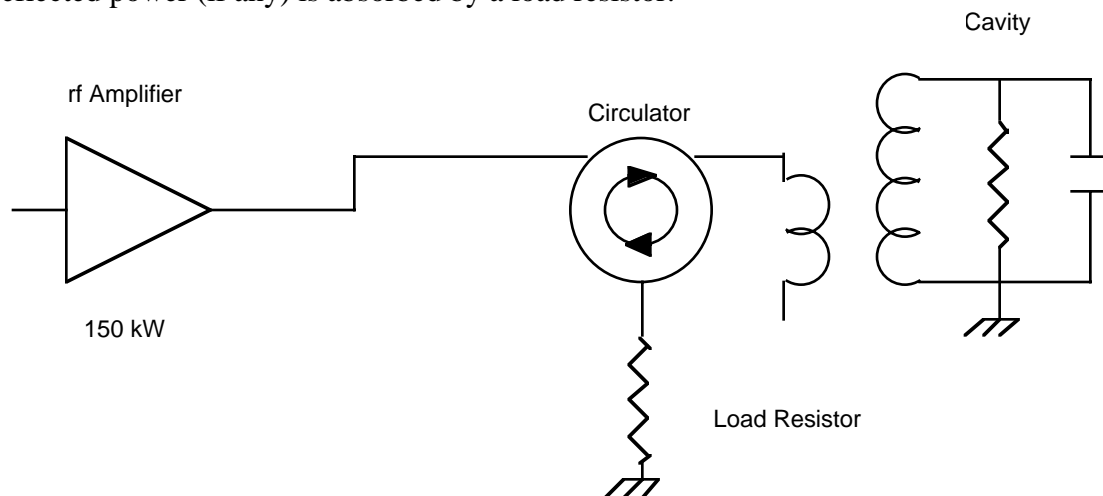


Figure 6.84. Schematic of rf amplifier and cavity system.

6.18.7 Steady State Beam Loading

A minimum rf power requirement is set by the acceleration rate. A maximum acceleration rate of 25 GeV/sec and a maximum (rf) beam current of 0.58 A (140 proton bunches of 27×10^{10} protons) results in a power requirement of 76 kW per cavity. The power requirement would be reduced by a slower ramp rate. We tentatively plan to cog the antiproton beam during acceleration so that it would be a reactive load on the proton cavities.

This Tevatron proton beam current represents a large beam loading that must be accounted for in the design of the system. The antiprotons also load the proton cavities, adding to the current

in one proton cavity and subtracting from it in the other. The maximum synchronous phase angle is 1.5° , so the beam loading is largely reactive. We plan to use the rf power amplifier output impedance to reduce the effective cavity shunt impedance by nearly a factor of 1000 to achieve a loaded Q of 5.6×10^6 . We also plan to detune the cavities to match the power amplifier to the beam load.

The cavity tune must be accurately controlled to avoid an excessive mismatch between the cavity and the load. Figure 6.85 shows the power requirements versus beam current for the beam being accelerated at the maximum synchronous phase angle (1.5°). Also shown are the power requirements in the presence of tuning errors of 8 Hz and 16 Hz. The 3 dB bandwidth of the loaded cavity is 19 Hz. The detuning angle at a (rf) beam current of 0.58 A is 89° .

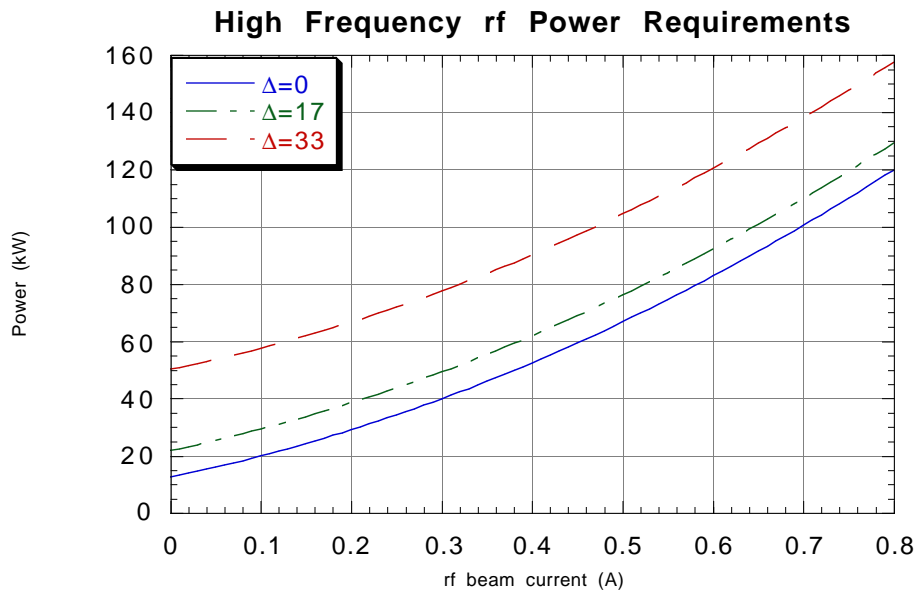


Figure 6.85. Power requirements of the high frequency rf system as a function of beam current for tuning errors of 0, 17, and 33 Hz.

6.18.8 Transient Beam Loading: Injection

When a new batch of protons is injected, the cavity tuning circuit responds slowly compared to the cavity filling time. The cavity voltage may be kept constant provided that the power amplifier can provide the necessary transient, namely:

$$\Delta P = V \Delta i_b / 8$$

Using $V=20$ MV and $\Delta i_b=0.58/12$ A (i.e., protons injected in 12 batches) we find a pulsed power requirement of 120 kW or 60 kW per cavity. This power requirement is similar to the power requirement for acceleration.

6.18.9 Transient Beam Loading: Collisions

The abort gap in the beam results in time varying beam loading. The power requirement to compensate for the transient beam loading is prohibitive. The effect of transient beam loading may be expressed as a phase shift after a beam gap of length τ_g is

$$\Delta\phi = \pi \frac{R f_{rf} \tau_g}{Q V}$$

Using $f=212$ MHz, $R/Q=720 \Omega$, $\tau_g=2.5 \mu\text{sec}$, and $V=20$ MV, we find a total phase shift of 2° . This distortion of the bunch spacing should be acceptable both at injection and during collisions.

6.18.10 Effect of Higher Frequency rf on Intrabeam Scattering

The higher frequency rf increases the momentum spread and drastically decreases the rate of growth of the longitudinal emittance as shown in Figure 6.86. The rate of transverse growth is slightly higher as shown in Figure 6.87.

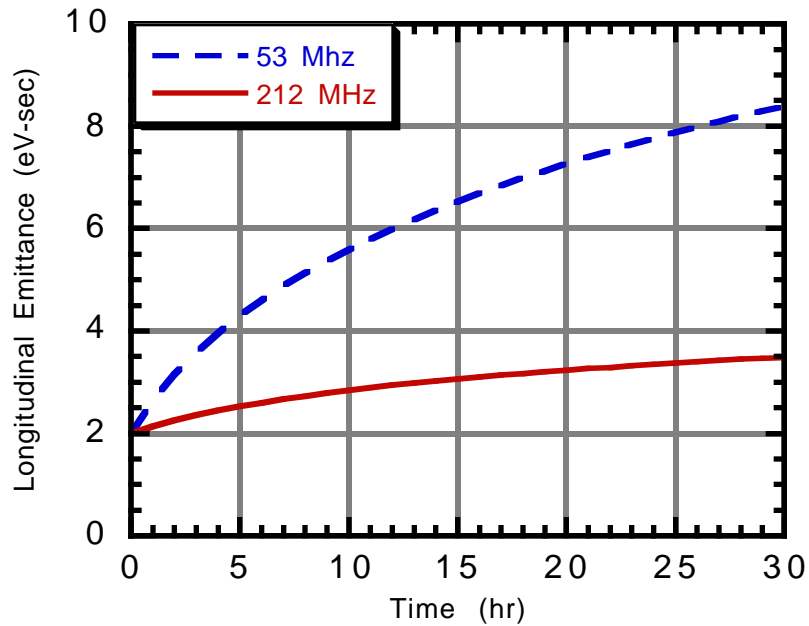


Figure 6.86. The evolution of the longitudinal emittance of a proton bunch during a store. The bunch has an initial intensity of 27×10^{10} , a longitudinal emittance of 2 eV-sec and a transverse emittance of 20π mm-mrad.

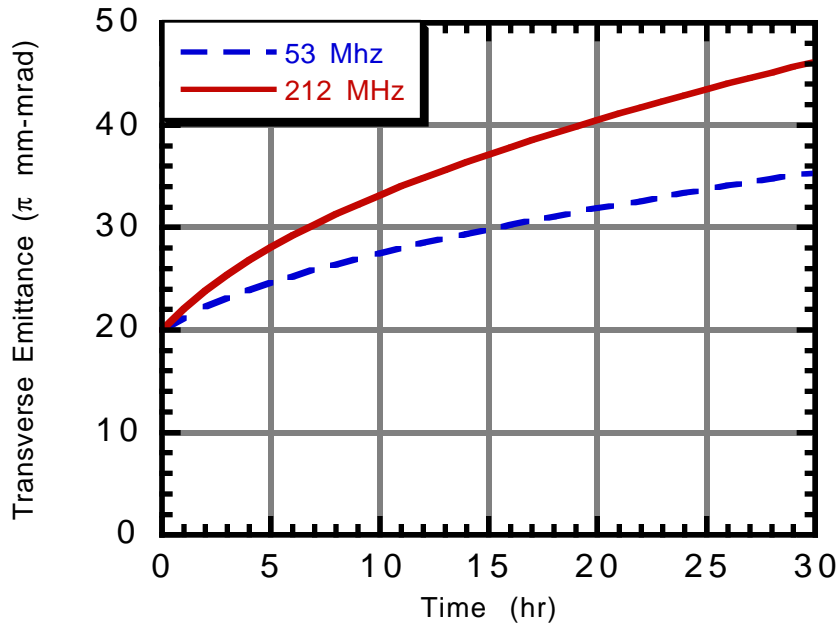


Figure 6.87. The evolution of the transverse emittance of a proton bunch during a store. The bunch has an initial intensity of 27×10^{10} , a longitudinal emittance of 2 eV-sec and a transverse emittance of 20p mm-mrad.

The effect of the higher frequency rf on integrated luminosity is shown in Figure 6.88.

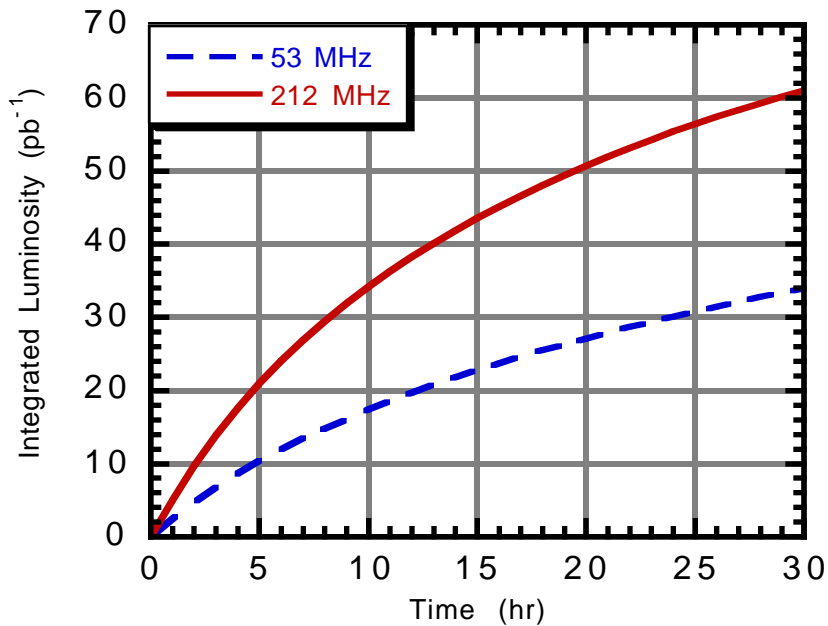


Figure 6.88. Integrated luminosity as a function of time in a store with and without the higher frequency rf system.

6.18.11 Power Loss in the Beam Pipe

The shorter bunches result in higher peak currents and, consequently, higher losses in the beam pipe. A second effect is the increased skin resistance for short bunches. The net effect is that the wall losses are increased by a factor of 4 when the bunches are shortened. The total loss is about 6 kW. This power is spread over the circumference of the Tevatron and would not be a concern except that it must be removed at cryogenic temperatures. This loss requires increased capacity in the Central Helium Liquifier (CHL).

6.18.12 Summary of Cavity Specifications

Table 6.34. High frequency rf system parameters

Antiproton Voltage (Max)	20	MV
Proton Voltage (Max)	20	MV
Harmonic number	4452	
Nominal Frequency	212.43	MHz
Tuning Range	± 4	kHz
Tuning Rate (Max)	0.5	kHz/sec
Acceleration Rate (Max)	25	GeV/sec
Synchronous Phase Angle	1.2	degrees
Available Longitudinal Space	~ 15	m
Number Proton Cavities	2	
Number of Antiproton Cavities	2	
Accelerating Voltage/cavity	10	MV
Cells per Cavity	3	
Cavity Length	2.5	m
Cavity Radius	0.7	m
Spacing Between Cavities ($\lambda/4$)	37.5	cm
Cavity Q at 10 MV (Min)	3.2×10^9	
R/Q	180	Ω
Accelerating Gradient	3.57	V/m
rf Power dissipation per cell (Max)	175	W
Static Heat Load (Max)	75	W
Beam Current (dc-typical)	0.3	A
Rf Power/cavity	150	kW
Loaded Q	5.5×10^6	
Detuning Angle (0.5 A)	88.9	degrees
Detuned Frequency (Δf @ 0.5 A)	953	Hz
Loaded 3 dB bandwidth	19	Hz

6.19 Speculative Ideas

6.19.1 Electron Compression of Beam-Beam Tune Shifts.

There are several dynamical issues caused by beam-beam forces from the interaction point and the many (~100) parasitic crossings. With a large number of bunches in the Tevatron the spread in tunes of the antiprotons, both as a function of particle amplitude and as a function of bunch number, can become large ($\Delta\nu$ about 0.025) causing antiprotons to lie on a resonance. An "electron compressor" is a device for reducing the tune spread by using an electron beam passing through the antiproton beam and acting as an electromagnetic lens which counteracts the beam-beam forces. A description of the "electron compressor" is given in the attached article by Vladimir Shiltsev.

The basic idea is to use electron guns with current of 1-2 Amps, energy of 10-20 kV, and about a 2 mm diameter to act as a defocusing lens on the antiprotons. By placing electron beams in the Tevatron which pass through the antiproton bunches at two locations (one with $\beta_x > \beta_y$ and one with $\beta_x < \beta_y$) it is possible to reduce the tune spread in the horizontal and vertical tune plane. By modulating the electron beam current to change the amount of focusing on a bunch by bunch basis it is possible to compress the tune footprint of the antiprotons by about a factor of 2.

The technology for building the electron compressor already exists and producing the electron beams is not expected to be difficult. There are a number of beam dynamics issues which need further understanding such as the effects of the electron beam on the protons, the stability of the electron beam current, and effects of higher order than the tune on the antiproton beam dynamics.

The technique is worthwhile pursuing. The electron beam tune compression project could be developed in several stages including the design and construction of the electron gun, installation to a single electron beam in the Tevatron as proof of principle and to study beam dynamics issues, and finally the installation of two electron beams to compensate for the beam-beam tune shifts.

6.19.2 Optical Stochastic Cooling

The introduction of the optical stochastic cooling offers the possibility of cooling bunched beam in less than ten minutes.^{32,33} Instead of radio frequency pick-ups and kickers, undulators are used to produce and receive signal of optical frequency which has a much larger bandwidth. In case of the Tevatron, it has been shown that the damping time of the transverse and longitudinal motion can be as short as 5 and 2.5 minutes, respectively (see Ref. 33). Recent study³⁴ shows that the optimal damping time for maximizing integrated luminosity is about 2 hours, resulting in a factor of 2.5 increase of the integrated luminosity of a 30 hour store (with other condition unchanged).

One of the key requirements of optical stochastic cooling is that the beam line connecting the two undulators has to be isochronous up to a fraction of the wavelength of the light emitted, which is about 0.1 μm for the Tevatron. A study done at LBL³⁵ demonstrates the feasibility of building such a beam line using presently available technology.

The possibility of implementing optical stochastic cooling has been studied for the past two weeks. Due to the need for two straight sections of 15 meters to accommodate the undulators, the section from D17 to E0 seems to be best suited for this purpose. The most realistic solution up to now results in a factor of 4 and 3 increase of β_x and β_y , respectively, which causes concern about the size of the beam at injection energy. No modification and relocation of the dipoles is required, while new quadrupoles have to be built to replace those currently used in the 12 standard cells.

Furthermore, several power supplies are needed. Given enough support, it seems that optical stochastic cooling may be possible in the Tevatron. However the modification of the Tevatron lattice would require considerable effort and cost. Since the Tevatron superconducting dipoles and quadrupoles are connected in series electrically running the quadrupoles with a different current would involve a complete rework of the Tevatron bus and the costs could be prohibitive.

6.19.3 Electron Cooling in the Tevatron

One possible method for increasing the integrated luminosity is to use electron cooling to preserve the brightness of the beams during the evolution of a store. Since this idea has already been investigated and the results published we merely give the reference here: Fermilab publication FN-657, **Electron Cooling in High Energy Colliders**, S.Y. Lee, P.Colestock, and K.Y. Ng, (1997).

Credits

M. Martens, Editor

J. Marriner, Editor

Contributors

G. Annala

P. Bagley

A. Braun

M. Church

A. Drozhdin

A. Hahn

R. Hanft

B. Hanna

J. Holt

P. Garbincius

G. Goderre

C. Jensen

J. Johnstone

T. Kobilarcik

M. McAshan

N. Mokhov

K.Y. Ng

S. Pruss

V. Shiltsev

J. Steimel

D. Quinell

W. Wan

D. Wildman

-
- ¹ V. Bharadwaj, *et al.*, TM-1970, unpublished.
- ² John Marriner, unpublished. Similar formulas appear in Edwards & Syphers book.
- ³ D. Finley, TNAL-TM-1646, (1989).
- ⁴ John Crawford, Summary of Run Ib stores, unpublished.
- ⁵ A. Piwinski, Proc. CERN Accel. School (1984)
- ⁶ L. R. Evans, Proc. 12th Int. Conf. on High-Energy Accelerators, (1983)
- ⁷ J. D. Bjorken and S. Mtingwa, Part. Accelerators, 13, (1983)
- ⁸ D. Finley, FNAL-TM-1646, (1989)
- ⁹ J. Wei, Proc. Workshop on Beam Cooling, Montreaux (1983)
- ¹⁰ Y. Mori, KEK-90-14 (1990)
- ¹¹ P. Bagley, "Beam-beam Tune Shifts for 36 bunch operations in the Tevatron, EPAC 96, Conf-96/340, October 1996.
- ¹² Main Injector Technical Design Report.
- ¹³ K.Y. Ng, Part. Accel. **16**, 63 (1984).
- ¹⁴ A.W. Chao, *Physics of Collective Beam Instabilities in High Energy Accelerators*, John Wiley & Sons, Inc., 1993, p. 70.
- ¹⁵ K.Y. Ng, Part. Accel. **23**, 93 (1988).
- ¹⁶ Y.H. Chin, *User's Guide for New ABCI Version 6.2 (Azimuthal Beam Cavity Interaction)*, LBL report LBL-33091 (UC-414), 1992.
- ¹⁷ *MAFIA User Guide*, DESY, LANL and KFA, May 3, 1988.
- ¹⁸ F.A. Harfoush and K.Y. Ng, Study of Separators using Numerical Simulations, Fermilab Report FN-536, 1990.
- ¹⁹ D. Sun, private communication.
- ²⁰ See, for example, K.L.F. Bane, P.B. Wilson, and T. Weiland, *AIP Proc. 127, Phys. of High Energy Accel.*, BNL/SUNY, 1983, p.875.
- ²¹ A. Hofmann, *Frontiers of Particle Beams*, Lecture notes in Phys., **296**, Springer-Verlag, 1986, p.99.
- ²² E. Keil and W. Schnell, CERN/ISR-TH/69-48, 1969.
- ²³ D. Boussard. CERN/PS-BI, 1972.
- ²⁴ F.J. Sacherer, IEEE Trans. Nuclear Sci. **NS 20**, 3, 825 (1973).
- ²⁵ D. Boussard and T. Linnecar, Proc. 2nd European Particle Accelerator Conference, Nice, 1990, edited by P. Marin and P. Mandrillon (Editions Frontieres, Gif-sur-Yvette Cedex, France, 1990), 1560.
- ²⁶ See for example, B. Zotter, *Theoretical Aspects of the Behaviour of Beams in Accelerators and Storage Rings*, Proc. First Course of Int. School of Part. Accel., Erice, Nov. 10-22, 1976, p.176.
- ²⁷ F.J. Sacherer, *Theoretical Aspects of the Behaviour of Beams in Accelerators and Storage Rings*, Proc. First Course of Int. School of Part. Accel., Erice, Nov. 10-22, 1976, p.198. F.J. Sacherer, *Methods for Computing Bunched-Beam Instabilities*, CERN Report CERN/SI-BR/72-5, 1972.
- ²⁸ P.J. Bryant, E. Klein, "The Design of Betatron and Momentum Collimation Systems", SL/92-40 (1992)
- ²⁹ M. Seidel, "The Proton Collimation System of HERA", DESY 94-103 (1994).
- ³⁰ IS Baishev, AI Drozhdin, NV Mokhov, "STRUCT Program User's Reference Manual", SSC-MAN-00034 (1994)
- ³¹ NV Mokhov, "The MARS Code System User's Guide, Version 13(95)", Fermilab-FN-628 (1995) HERA.
- ³² A. Mikhailichenko and M. Zolotarev, *Optical Stochastic Cooling*, Physical Review Letters, v.71, 25, 1993, p.4146
- ³³ M. Zolotarev and A. Zholents, Phys. Rev. E, **50**, (1994) .3087.
- ³⁴ A. Zholents and W. Wan, unpublished.

³⁵ S. Chattopadyay, C. Kim, D. Massoletti, W. Wan, A. Zholents and M. Zolotarev, LBL Lab Report, LBNL-39788.

7. Operating Scenarios*

7.1 36 x 36 Collider Operations

7.1.1 Shot Setup

Much of this scheme has been described elsewhere,¹ but it will be repeated here in more generality. This scenario is easily generalized to 109×144 operating scenarios (132 nsec bunch spacing). Table 7.1 shows the sequence of operations for each machine during future "shot setups". Shot setup starts at the end of a collider store (TCLK event \$CE) with proton removal from the Tevatron and proceeds through antiproton deceleration, transfer to the Recycler Ring (RR), reverse proton tune-up, proton loading, antiproton loading, acceleration, low beta squeeze and beam halo scraping. It ends with the commencement of the next store (TCLK event \$CB). During Run I, the average shot setup time was 202 minutes (including downtime). For Run II the goal is to reduce the optimum shot setup time to less than 40 minutes.

Protons are removed from the Tevatron by collimators in a dogleg insertion at E0. The collimators are first placed close to the beam, and then a local 3 bump is exercised, with feedback control, to move the beam into the collimators. The dogleg prevents beam losses from quenching superconducting magnets. Calculations suggest that this process can be done in 100 seconds. After the protons are removed the low beta regions are "unsqueezed", and the helix closed, in order to maximize the Tevatron aperture. Then all 36 antiproton bunches are decelerated to 150 GeV. At this point, the total RR antiproton stack will occupy approximately 1/4th of the RR azimuth between two rf barrier buckets.

A group of 4 antiproton bunches are transferred to the MI, after appropriate cogging, on MI \$20 cycles and decelerated to just above transition. The bunches, which are captured by the 53 MHz rf system, are adiabatically transferred to 2.5 MHz buckets and decelerated to 8 GeV (as described in section 5.x.x). The MI is appropriately clogged, and the 4 antiproton bunches are transferred to the RR into 2.5 MHz RF buckets. In the RR the 2.5 MHz is adiabatically decreased and the beam is captured between a pair of barrier buckets. The barrier buckets are then used to move the injected beam out of the way in preparation for the next injection. This process is repeated 9 times, with each new injected bunch being azimuthally merged with the previous injected bunches by combinations of rf barrier buckets. At the end of this process in the RR there is a "cold" bunch of antiprotons, occupying about 1/4 of the ring, and a "warm" bunch of freshly injected antiprotons occupying another portion of the ring.

At this stage beam lines for antiproton transfers can be tuned up with reverse protons on \$20 cycles (150 GeV) or \$2D cycles (8 GeV). This includes reverse proton transfers from the Tevatron to the MI via the A150 line and reverse proton transfers from the RR to the MI via the MI-22 line.

* Last revised on March 10, 1998.

Table 7.1. Shot setup timeline

Tevatron Sequence	MI Operations	RR Operations	time (min)
remove protons	\$29's for \bar{p} production; \$2B's for proton tune-up	cooling; possible transfers from antiproton source	5
unsqueeze, close helix, decelerate antiprotons to 150 GeV	\$29's for \bar{p} production; \$2B's for proton tune-up	prepare RR stack for \bar{p} injections	3
transfer 4 antiproton bunches to MI for deceleration to 8 GeV; repeat 9 times	inject, decelerate, extract 9 groups of 4 \bar{p} bunches; \$29's for \bar{p} production interleaved	Inject and stack 9 groups of 4 \bar{p} bunches	5
stop at 150 GeV			0
reverse proton tune-up	\$20's and \$2D's for 150 and 8 GeV reverse proton tune-up; \$29's for \bar{p} production interleaved	\$2D's for 8 GeV reverse proton tune-up	3
setup for injection	\$29's for \bar{p} production; \$2D's for 8 GeV reverse proton tune-up	\$2D's for 8 GeV reverse proton tune-up	2
inject protons (9 groups of 4 bunches)	inject, accelerate, and extract 9 groups of 4 proton bunches; \$29's for \bar{p} production interleaved	prepare stack for \bar{p} extraction	2
inject antiprotons (9 groups of 4 bunches)	inject, accelerate, and extract 9 groups of 4 proton bunches; possible \$29's for \bar{p} production interleaved	extract 9 groups of 4 \bar{p} bunches	5
accelerate, squeeze	\$29's for \bar{p} production	resume cooling; possible transfers from antiproton source	4
adjust tunes, correct orbit, scrape beam halo	\$29's for \bar{p} production	cooling; possible transfers from antiproton source	6

Protons are accelerated, coalesced, and injected into the Tevatron similar to current procedures, except that instead of single batch coalescing, 1 to 4 batches will be injected, accelerated, and coalesced simultaneously. Proton injection will thus require from 9 to 36 Main Injector cycles. Extraction of antiprotons from the RR and acceleration in the MI is essentially the reverse of injection. A group of antiprotons is separated from the "cold" antiprotons in the RR with barrier buckets. These are then bunched at 2.5 MHz, transferred to the MI, and accelerated to 25 GeV. These are then bunch rotated, captured by the 53 MHz RF, accelerated to 150 GeV, and transferred to the Tevatron. This process is repeated 9 times.

Once all the bunches are injected into the Tevatron, they are accelerated to 1 TeV, and collisions are initiated at CDF and D0 by squeezing and collision coggng. The acceleration ramp will be decreased from the current 80 seconds to perhaps 50 seconds. At this point the orbit and the tunes will be routinely corrected and the beam halo scraped by an automated collimation system using feedback from local loss monitors.

There is no provision for experimental "quiet time" in this scenario, and if the colliding beam experiments require it, the shot setup time will need to be increased by that much, since there is almost no time in which there is no beam in the Tevatron. In addition, there is no provision for ramping the Tevatron 6 times, as has been done in the past, so provision will have to be made to correct for persistent currents.

7.1.2 Accumulator to RR Antiproton Transfers

Antiprotons are stacked into the Accumulator in much the same way as in the past, except at a 1.5 second/pulse repetition rate. Depending on the cooling rate in the RR, after 1 to 4 hours the antiprotons are transferred to the RR via the AP3/AP1/MR remnant/MI partial turn/MI-22 line. The proposed AP-5 beam line will allow for direct transfer between the Accumulator and RR later in Run II. The mechanics of the transfer will be similar in both cases, however, the major disadvantage of the later transfer is that the AP1 line needs to be set up for 8 GeV before each transfer, which takes considerable time.

When the RR stack is cool enough, RF barrier buckets are used to form an azimuthal gap in the stack with enough space for injection of a 1.4 μ sec antiproton batch from the Accumulator. Stacking into the Accumulator is halted, and the core briefly cooled. An H=4 RF system accelerates the core to the extraction orbit. At the extraction orbit the Accumulator rf is phase-locked to the RR rf, kickers are fired synchronously with the RR aa marker, and a bucket-to-bucket transfer into the RR is obtained.

This scenario assumes that electron cooling in the RR has not yet been commissioned. In the present case, the RR will use stochastic cooling exclusively and Accumulator to RR transfers will take place every 1-4 hours. At a stacking rate of 20×10^{10} /hour, this corresponds to about $20\text{--}80 \times 10^{10}$ antiprotons/transfer. When electron cooling has been commissioned, the transfer rate between the Accumulator and RR may be significantly increased.

7.2 Beam Transfers and Synchronization

The coming reality of the Main Injector (MI), including a Recycler Ring in the same enclosure, presents new and unique demands for beam transfers and synchronization of those transfers. The Tevatron 10 MHz Time Clock (TCLK) and various beam synchronous clocks are envisioned to play continuing important roles for these transfers in conjunction with extant or new demands on the low level RF systems of the accelerators and storage rings.

The Tevatron Clock structure is sufficient to meet the new requirements. However, the Time Line Generator (TLG) hardware which is currently implemented in CAMAC, is being upgraded to a VME-based system. Existing TCLK events for the Main Ring are being reassigned to the Main Injector, with present definitions of events being adhered to in almost all cases in order to assure operational continuity. Current existing event assignments number 175 out of a potential 256, and this is being updated to 188 to encompass new scenarios: deceleration, RR operation, NUMI, and 120 GeV fixed target operation. Some events associated with obsolete scenarios are being deassigned, and this number is included in the above accounting.

There presently exist three beam synchronous clocks, each approximately 7.5 MHz (one seventh of the normal rf frequency), derived from the Tevatron proton, Tevatron antiproton, and Main Ring rf systems. These are called TVBS, APTVBS, and MRBS, respectively. MRBS will be reassigned to the Main Injector and will be referenced as MIBS. Events synchronous to the revolution frequency are coded onto each of these clocks and are always denoted by the hexadecimal code \$AA. A beam synchronous clock is being developed for the RR employing existing techniques and will be referred to as RRBS. Beam Transfers between machines are approximately driven by delays from particular TCLK events, or a combination of them. The actual transfers are initiated by uniquely coded beam synchronous events on particular beam synchronous clocks. These transfer events, which are encoded immediately subsequent to the revolution event, are detected and generally result in the generation of a TCLK event. This reflecting of beam synchronous transfer events in the Tevatron Clock has proven extremely useful for diagnostic purposes and this practice will be continued.

Some of the details of new (or modified) beam transfers and synchronization are described below for individual types of transfers. TCLK events are designated as \$nn (with a TLG subscript if they are sourced from the Time Line Generator), and beam synchronous events are denoted as \$nn subscripted with the relevant clock descriptor. Of particular note are the following additions and modifications to event usage: 1) addition of a new Booster reset event $\$0E_{\text{TLG}}$ dedicated to RR studies cycles; 2) reassignment of Booster reset event $\$19_{\text{TLG}}$ for NUMI

beam; 3) addition of a new MI reset event \$23_{TLG} dedicated to NUMI operation; 4) reassignment of MI reset event \$20_{TLG} for MI deceleration cycles.

7.2.1 Proton transfers from Tevatron to MI

This transfer is used to tune up the MI to Tevatron antiproton transfer line prior to antiproton transfers to the Tevatron, and it is accomplished in two steps. First, protons are injected into the Tevatron on a normal \$2B cycle (\$15_{TLG}, \$2B_{TLG}, \$4D_{TLG}). Second, protons are extracted from the Tevatron on either of the two cycles: \$2A_{TLG}, \$5D_{TLG} → \$D8_{MIBS} → \$55; or \$20_{TLG}, \$5D_{TLG} → \$D8_{MIBS} → \$55.

7.2.2 Antiproton deceleration

The following sequence of events is used to decelerate antiprotons from 1 TeV in the Tevatron to 8 GeV in the RR:

- Sequencer → \$ED (prepare RR stack for antiproton injection)
- Sequencer → \$6D or \$6E (start of ramp down in Tevatron)
- Sequencer → \$44 (start of ramp "back porch" in Tevatron)
- TLG → \$20_{TLG}, \$54_{TLG} → \$D6_{MIBS} → \$5F
- → \$D0 (prepare for deceleration in MI)
- → \$D1 (start deceleration in MI)
- → \$D2 (end deceleration in MI)
- → \$E0 → \$A0_{MIBS} (inject into RR).

7.2.3 NUMI operation

Six Booster batches are loaded into the MI, accelerated, and extracted to the NUMI beam line with the sequence \$19_{TLG}, \$19_{TLG}, \$19_{TLG}, \$19_{TLG}, \$19_{TLG}, \$19_{TLG}, \$23_{TLG}, \$A8_{TLG}. The MI can simultaneously serve NUMI and antiproton production by interleaving NUMI cycles with antiproton production cycles, or, slightly more efficiently, by replacing the first \$19_{TLG} in the above sequence with \$14_{TLG} and extracting the first Booster batch to the antiproton production target by careful placement of an \$80 in the timeline.

7.2.4 120 GeV Fixed Target operation

Similar to NUMI operation, this sequence is \$13_{TLG}, \$13_{TLG}, \$13_{TLG}, \$13_{TLG}, \$13_{TLG}, \$13_{TLG}, \$21_{TLG}, \$30_{TLG}, and it may also be combined with antiproton production cycles.

7.2.5 Inject decelerated antiprotons from the MI via the MI-22 transfer line

This sequence is \$20_{TLG}, \$54_{TLG}, \$E0 → \$A0_{MIBS}. MI cogging, RR rf manipulations, and the RR Lambertson bump are initiated by \$E0 or \$20_{TLG}. Extra time is required after the transfer to perform RR rf manipulations, which will be enforced by the TLG.

7.2.6 Inject antiprotons from Accumulator via AP5 line

This sequence is \$2D_{TLG}, \$E1_{TLG}, \$91_{TLG} → \$A1_{MIBS} → \$98. \$E1_{TLG} initiates Accumulator and RR rf manipulations, which take up to 20 seconds to complete. The reflected TCLK event \$98 is concurrent with the \$A1_{MIBS}. The \$91 is set to occur 0.5 sec before the transfer in keeping with all other Antiproton Source transfer scenarios. This same sequence can be used for transfers via AP3/AP1/MR remnant/MI/MI-22. The Accumulator extraction kicker is fired by \$A1_{MIBS}.

7.2.7 Inject protons from MI via MI-32 line

This transfer is used to inject protons into the RR for studies. The sequence is \$0E_{TLG}, \$2D_{TLG}, \$E2_{TLG} → \$A2_{MIBS}. MI cogging, RR rf manipulations, and the RR Lambertson bump are

initiated by $\$E2_{TLG}$. The MI-32 kickers are fired by $\$A2_{MIBS}$. If there is already an antiproton stack in the RR, $\$ED$ will need to be issued by the Sequencer prior to proton injections to prepare the antiproton stack.

7.2.8 Extract protons to MI via MI-22 line

This transfer is used to tune up the MI-22 line before injecting antiprotons into the RR. The sequence is $\$0E_{TLG}, \$2D_{TLG}, \$E2_{TLG} \rightarrow \$E3 \rightarrow \$A3_{MIBS}$. This cycle is generally concurrent with a proton injection cycle, and the timing delay for the generation of $\$E3$ is set so the proton beam circulates in the RR for approximately 100 turns. The MI-32 kickers are fired by $\$A3_{MIBS}$.

7.2.9 Extract antiprotons to MI via MI-32 line

This sequence is $\$2A_{TLG}, \$40_{TLG}, \$E4_{TLG} \rightarrow \$7A_{MIBS}$. MI cogging, RR rf manipulations, and the RR Lambertson bump are initiated by $\$E4_{TLG}$. MI-32 kickers are fired by $\$7A_{MIBS}$. If required, $\$EE$ will be issued by the Sequencer just prior to this cycle to prepare the RR stack for antiproton extractions.

7.2.10 Extract protons to the Accumulator via the AP5 line

This transfer is used to tune up the AP5 line prior to antiproton transfers. The sequence is $\$0E_{TLG}, \$2D_{TLG}, \$E2_{TLG} \rightarrow \$96 \rightarrow \$A6_{MIBS} \rightarrow \97 . The $\$96$ is referenced to the $\$E2$ with a delay such that beam circulates in the RR for about 100 turns before extraction to the Accumulator. The $\$96$ occurs 0.5 sec before beam transfer in keeping with all other Antiproton Source transfer scenarios. AP5 kickers are fired by $\$A6_{MIBS}$, and $\$97$ is concurrent with $\$A6_{MIBS}$. This same sequence can be used for transfers via AP3/AP1/MR remnant/MI/MI-22.

7.2.11 Extract protons via MI-40 (dump)

This sequence is $\$A5_{RRBS} \rightarrow \$F5$. The $\$A5_{RRBS}$ is sourced to a 377 timer module which can be fired by the Sequencer or by any suitable TCLK event. The $\$F5$ is concurrent with the transfer and is used for data collection.

7.2.12 Transfer Synchronization

Transfers between the MI and Tevatron are somewhat complicated by the different harmonic numbers of the Main Injector and Tevatron, being 588 and 1113 respectively. The following scheme will allow the full range of transfer possibilities. The 53 MHz RF is divided by 21 for each machine. This yields 53 rf/21 pulses (396 nsec spacing) for each Tevatron turn, and 28 rf/21 pulses for each MI turn. Before initiating transfer, the Tevatron is frequency matched to the MI, the phase difference is measured, and the Tevatron frequency is then phase shifted by less than one 53 MHz bucket to be phase locked to the MI. The Tevatron is then transfer clogged no more than ± 10 53 MHz buckets to align the RF/21 pulses to the MI. On each turn, the $\$AA_{MIBS}$ marker will then align with a different RF/21 pulse from the Tevatron, with the sequence repeating itself every .587 msec (53 MI turns). An MIBS event is issued with appropriate delay which takes into account the location of the beam (bucket number) in the first machine and the desired location of the beam in the second machine. All beam line kickers are referenced to this MIBS event. This scheme is easily extended to 132 nsec spacing.

In many cases, transfers into the RR from the MI will require placement of the beam at a specific longitudinal azimuthal in relation to beam already present in the RR. This will require "fast cogging" of the MI to align the RR beam gap and $\$AA_{MIBS}$ markers. This "fast cogging" can be done in the time between the start of the beam injection cycle and actual beam injection into the Booster—*i.e.*, when there is no beam in the MI. Since the MI and RR have the same revolution frequency, this is anticipated to be straightforward. Beam line kicker timing will be referenced to MIBS events.

Transfer synchronization from the Accumulator into the RR is described above in section 7.1.2. For transfers from the RR to the Accumulator, no cogging is required. The beam line kickers will be referenced to RRBS events.

7.3 Transverse and Longitudinal Emittance Budget

7.3.1 Antiprotons - Transverse

All transverse emittances in this section are stated as 95% normalized values, and are based on the assumption of beams which are both round and gaussian. Almost all of the emittances cited here are best measured in the vertical plane, and are assumed to be the same in the horizontal plane. Measurement of horizontal emittances requires correction for the effects of dispersion through use of lattice functions. However the uncertainties in the lattice functions and momentum spread tend to make this measurement less accurate.

In Table 7.2 below are listed typical values of the proton and antiproton emittances, as measured during Run Ib and as projected for Run II, at points taken throughout the acceleration chain. The antiproton value assumes essentially no change. With the upgrade of the stochastic cooling systems in the Debuncher from 2-4 GHz to 4-8 GHz and liquid helium temperatures, the cooling rate in the Debuncher is expected to dramatically increase. Even with an increase of the transverse aperture with modifications to the antiproton injection line (AP2), and a decrease in antiproton production cycle time from 2.4 seconds to 1.5 seconds, the transverse antiproton emittance coming out of the Debuncher is expected to decrease below Run Ib. During Run Ib the antiprotons were cooled in the Accumulator for a long period of time during each shot setup before extraction to the MR, resulting in a large decrease in emittance in the Accumulator. For Run II, only a few minutes will be allotted to cooling the beam after stacking is stopped and before the beam is transferred to the RR, and therefore the Accumulator will not contribute as much to cooling the beam transversally as in Run Ib. During stacking most of the transverse cooling power goes toward counteracting the transverse heating of the stack tail momentum cooling system.

Table 7.2. Transverse emittances through the accelerator chain

location	Protons		Antiprotons	
	Run Ib	Run II	Run Ib	Run II
Linac (400 MeV)	6	6	—	—
Booster (8 GeV)	12	15	—	—
Debuncher (inj-ext)	—	—	200-40	320-30
Accumulator (inj-ext)	—	—	40-8	33-10
RR	—	—	—	10
MR / MI (150 GeV)	14	18	12	12
Tevatron (1 TeV)	23	20	15	15

For stochastic cooling, the cooling rate is dependent on the number of particles -- more particles means slower cooling. Therefore the antiproton emittances are dependent on stack size in both the Accumulator and in the RR. However, the use of the RR to keep stacks from ever getting large in the Accumulator eliminates this effect in that machine, and the eventual use of electron cooling in the RR will eliminate the effect.

There has been an ongoing problem with emittance growth for the antiprotons in the AP3/AP1 beam line. During Run Ib much effort went into trying to solve this problem, with only limited success. The beam line model is not accurate enough to obtain a good beam line match, and, in addition, there are shot-to-shot variations which are not understood. This problem will be alleviated with the scenario of Run II, in which any emittance growth which has occurred during the transfer will be reversed by cooling in the RR. The eventual construction of an AP5 beam line will eliminate many of the transfer problems experienced in the past.

The transfer to the MI is through a very short beam line, so that emittance growth is expected to be small. Emittance growth during the MI acceleration, MI to Tevatron transfer, and Tevatron acceleration are expected to be similar to Run Ib, as indicated in Table 7.2

Emittance growth from RR to Tevatron during acceleration is expected to be 5π mm-mrad, and it is reasonable to expect the same emittance growth during the deceleration of antiprotons from 1 TeV to 8 GeV in the RR. At the end of a store, the antiproton emittance is expected to be about 20π mm-mrad. Therefore, we expect emittances of 25π mm mm-mrad for freshly injected decelerated antiprotons in the RR.

7.3.2 Protons - Transverse

The parameter list for Run II, Table 1.1, indicates a proton transverse emittance goal at collisions of 20π mm-mrad which is 3π mm -mrad (13%) lower than the Run Ib value. In terms of 2D phase space density, the proton value is increased by 34% from Run Ib. A major source of emittance growth for protons occurs in the Booster. This dilution is a topic deserving of study, and indeed the Booster Group has plans for such investigations. An ion profile monitor has led to the collection of a considerable amount of data, with growth seen throughout the acceleration cycle. There appear to be several separate mechanisms at work (large tune shifts at low energy, synchro-betatron coupling just above transition, and rf power supply noise have all been mentioned), but in truth neither those mechanisms nor the detailed calibration of the monitor is sufficiently well understood. The Run II operating scenario extrapolates from current Booster performance (see Table 2.2). This reasonable assumption may or may not be confirmed as that machine is operated at somewhat higher intensity.

This leaves stringent requirements on proton emittance growth in the MI and Tevatron. Whereas in Run Ib the overall proton emittance growth from Booster extraction to Tevatron flattop was 11π mm-mrad (92%), in Run II we are assuming we can keep the overall emittance growth to 5π mm-mrad (33%). This is an ambitious goal and will require well matched beam line optics, accurate beam line steering control, and careful control of beam dynamics during the acceleration cycles in the MI and Tevatron to prevent undue emittance growth. In addition to the MI itself, both transfer lines are new (Booster to MI, and MI to Tevatron), and one might optimistically assume that this will give an improvement in beam transfers. However, the multi-bunch injection schemes for protons and antiprotons place more severe requirements on the Tevatron injection kickers. In the Tevatron at 1 TeV it is planned to do both an orbit smooth and a tune correction at the beginning of every store. This was not routinely done during Run Ib. In addition, a generic injection tuning application program is being written which will archive all beam line changes during tune-up. This will in principle make it easier to track and diagnose beam transfer problems.

7.3.3 Antiprotons - Longitudinal

The operational mode of the accelerator complex for preparing antiproton beams for collision will be distinctly different in Run II than it was in Run Ib, therefore a direct comparison is difficult. The goal for the antiproton emittance is 2 eV-sec, which yields an rms bunch length at the beginning of a store of about 37 cm. In Run Ib the typical longitudinal emittance in the Tevatron at the start of a store was 3.5 eV-sec as measured by the SBD (Single Bunch Detector). This corresponds to a bunch length of 50 cm (at 900 GeV). In this section all longitudinal emittances are quoted as 95%.

The history of the antiproton longitudinal emittance during accelerator operations is the following. After bunch rotation in the Debuncher, the longitudinal emittance is 42.2 eV-sec ($\Delta p/p_{95\%}=.3\%$). After momentum cooling, just before transfer to the Accumulator, this becomes 23.9 eV-sec ($\Delta p/p_{95\%}=.17\%$). This was the case in Run Ib, and it will remain approximately the same for Run II (see section 3.3). The Accumulator stack tail and core cooling systems will be required to decrease this to less than 10 eV-sec before transfer to the RR. The RR momentum cooling system will cool a stack of 3.1×10^{10} recycled antiprotons to 54 eV-sec (>90%) after 8 hours of cooling. Divided by 36 this is 1.5 eV-sec per bunch, which allows for a 33% longitudinal emittance blowup on acceleration and transfer to the Tevatron.

During the antiproton deceleration cycle, the antiproton beam remaining at the end of an 8 hour store is expected to have a longitudinal emittance of about 3.5 eV-sec. The RR momentum cooling aperture of ± 20 MeV/c and the requirements of storing the “cold” antiproton beam and injecting new beam limit the tolerable longitudinal emittance at the RR to about 4 eV-sec.

7.3.4 Protons - Longitudinal

The goal for the proton bunch length at the beginning of a store is also (Table 1.1) 2.0 eV-sec. During Run Ib the proton longitudinal emittance at collisions was typically 3.8 eV-sec -- 10% larger than the antiproton longitudinal emittance. In Run Ib most of the proton emittance blowup came from trying to coalesce 11 53 MHz bunches at once in the MR. In Run II 5 proton bunches will be injected into the MI from the Booster, each with intensity 6×10^{10} and longitudinal emittance 0.1 eV-sec. We anticipate that acceleration and transition crossing will blow these up to 0.15 eV-sec before coalescing. ESME calculations show that coalescing will increase the longitudinal emittance from 0.75 eV-sec to 1.5 eV-sec, which allows for only a modest increase in emittance in the Tevatron. This scheme clearly requires coalescing to work well in the MI, and for the Booster beam emittance to be as small as possible, consistent with avoiding instabilities in the MI during transition crossing. It is quite possible that we will not be able to meet the transverse and longitudinal emittance goals simultaneously, and it may be possible to achieve low transverse emittance at the expense of longitudinal emittance by coalescing more low intensity bunches.

7.4 Instrumentation and Controls Requirements

7.4.1 Software

Numerous application programs are being modified or rewritten for Run II, either to accommodate new hardware (MI, RR,...) or to improve current operating procedures. Table 7.3 lists application programs currently planned to be modified or written for Run II. The tasks listed in this table range from a few hours of work to make minor changes in existing programs, to many months of work to rewrite large programs. A few of the more important items—SDA, TLG, Sequencer, TOP, and the injection closure program—are discussed in more detail below.

7.4.1.1 SDA

The Shot Data Acquisition program supporting collider operations, will undergo substantial changes before the next collider run. SDA collects megabytes of scalar and snapshot data during defined stages of shot setup for postmortem and shot improvement analysis. SDA's file structures and operations will migrate from the record management services of the VMS operating system to relational database tables with Standard Query Language, SQL, access. The database tables will be designed to remove the restrictions on the number of cases defining the collection of data. SQL access with join capability across shots will be exploited by the data logger plot package, and tools will be provided to export shot data to commercial applications. SDA's architecture will also change to support shortened shot setup times. SDA will have a new user input interface, likely run continuously, support a threaded database write facility, and

employ new methods of coupling to the collider Sequencer. Open Access front end clients, specialized data loggers, snapshot logging facilities, and other applications may also contribute to the population of these Shot Data tables, to complement or relieve traditional SDA collection responsibilities.

7.4.1.2 TLG

The old Time Line Generator (TLG) hardware will be rebuilt within a VME platform utilizing a finite state machine architecture. Many of the "kludges" added on to the system over the years will be eliminated and their function engineered into the basic hardware design. TCLK functionality will remain the same. However, the finite state machine architecture will allow for a more versatile user interface to the TLG hardware and more facile manipulation of timelines. The visible interface to the new timeline generator will be an application program that has some similarities to the current interface (D69). The new program will provide more automation in constructing timelines. Relevant information, such as ramp cycle lengths, will be supplied to the program via ACNET. The user will be able to specify new options in building timelines such as "packing" cycles or "spacing" cycles. The finite state machine will do the calculations for the actual time placement of the events, with the user specifying rules for *how* the events are triggered. The application program will be able to display timeline sequences in terms of the requested rules, or the actual event placement that will occur given the current machine parameters.

Table 7.3. Application programs for Run II

Category	Description
general	rewrite SDA -- Shot Data Acquisition
	rewrite SDA display (C1,C2)
	rewrite TLG -- Time Line Generator
	modify Sequencer
	miscellaneous modifications to D1,D6,D18,D20,D42,D59,D61,D68,D100,T61
	Sequencer aggregate development
	modify channel 13 display
Main Injector	ramp & tune (M2)
	PS control/status (M11,M12,M13,M17)
	LLRF display/control (M3,M5,M6,M73)
	MI orbit (M24,M25,M26,M55,M56,M128,M135))
	harmonic correctors (M27,M28,M33)
	transfer line steering (M57)
	BPM/BLM display/control/test (M37,M38,M39,M40,M46)
	BPM TBT (M126)
	Multiwire display (M53)
	Flying wire display (M47,M48,M49)
	HLRF status/control (M74,M77)
	LCW display and control (M105)
	Vacuum display and control (M106)
	lattice display (M131,M133)
	beam permit (M67)
	beam dampers

Tevatron	TOP -- Tevatron Orbit Program (C10)
	C49 -- TEV ramp modules
	tune measurement (GFSDA,)
	damper control
	modify T57 to accommodate Camac 160 upgrade
	36x36 beam parameters display
	modify flying wire program
	modify C23 -- ADC compare
	rewrite T106 -- lifetime plotting
	IP feedback
	TEV collimator control
Antiproton Source	modify P35 -- switch tree program
	rewrite P133 -- network analyzer display/control
	modify P134 -- delta kicker fitting
	modify P34 -- TWT status and control
	write new closed orbit program to accommodate Accumulator BPM upgrade
	modify P53 to accommodate new Accumulator lattice
	upgrade SEM grid display and control
	upgrade graphics programs for RF, stochastic cooling and diagnostics
Recycler	BPM control/display
	LLRF control/display
	Vacuum control/display
	stochastic cooling phase and gain measurement (like P133)
	TWT status and control (like P34)
	beam synch clock page (like T63)
	switch tree program (like P35)
	spectrum analyzer control/display (like P41,P42,P45,P112)
	tune and chromaticity measurement (like P43)
	beam lifetime/emittance monitor
	longitudinal emittance viewer (like P9)
	graphics programs for stochastic cooling, dampers, wide band pickups
	clearing electrode current monitoring (like P111)

Other features will be included to facilitate manipulation of timeline sequences. Booster study cycles will be handled outside the constraints of the saved timeline "files". They will be enabled, disabled, and adjusted in frequency via an ACNET parameter. The Sequencer will be able to trigger timeline sequences, with an option of loading a timeline sequence for repeat or for one shot play, for example.

7.4.1.3 Sequencer

The Sequencer will operate within the standard framework of console applications. It is envisioned that a single Sequencer instance will control the entire shot setup procedure, with the capability of multitasking to speed up the setup. It will make use of CLIB functionality and push for extensions to the current system where it appears necessary. The basic concepts used in the existing program will remain, with the design to extend and enhance features where needed. Old Sequencer modes and commands will not be ported, therefore new modes, aggregates, and commands will have to be constructed. This will allow for the enhancement of the command grammar—*i.e.*, which commands will be changed, consolidated, dropped, added, *etc.* Some features to be provided include the following: use of CLIB lock routines for more flexible aggregate and command edit and execution locks, a uniform and extended communications package (ACNET, tcp, udp/multicast) for programs used by the Sequencer; support for

scheduling (*viz.*, triggering aggregates on time-of-day or TCLK events), allowing for the Sequencer to be run in the background, support for copying and archiving Sequencer modes and aggregates, and more extensive edit protection. There will be streamlining of commands, specialized activity will be pushed to client applications and devices, a set of more general commands will be provided, commands will be stored in Sybase tables, user constructed "complex commands" will be supported, and conditional execution of commands will be supported.

7.4.1.4 TOP

The Tevatron Orbit smoothing Program (TOP) will be rewritten to support the new 460 function generator cards and to support the more complex operating scenarios of Run II. Both the three bump and least squares algorithms will be supported. The ability to make a three bump at a single location will also be supported. An attempt will be made to make this program much more user friendly than previous generations of this program so that it may be used routinely during shot setup.

7.4.1.5 Injection Closure

A single general purpose injection closure program is being written to service the Tevatron, MI, RR, and Antiproton Source Rings. Currently there are at least 5 application programs being used for injection closure (M56, M58, T120, T121, and P58). The new program will support both TBT mode and "first turn minus desired position" mode. It will have a manual mode, semi-automatic mode, and fully automatic mode. It will control BPM timers, set beam line devices, maintain a history of settings for trending studies, take input from either BPM's or a file, be callable from the Sequencer, have a built in learning capability (so it is model independent), have digital control, and have a variety of plotting options. This program is intended to greatly reduce the time required for reverse proton tune-up during shot setups.

7.4.2 Controls Upgrades

In addition to the topics mentioned above, there are other upgrades in progress which are worth noting.

1. The 160 ramp cards which drive the Tevatron correctors are being upgraded to 460 ramp modules in order to handle the increased complexity of operations.
2. The current GPIB/CAMAC interface (488/89 modules) in the Antiproton Source are being replaced by GPIB/Ethernet interfaces. The old CAMAC interfaces had some bugs which were never ironed out and which caused reliability problems. In addition, the new interfaces are faster, which is critical in some applications where megabytes of data are being read out. These interfaces are used for spectrum analyzers, network analyzers, oscilloscopes, DVM's, and miscellaneous other diagnostic equipment using the GPIB protocol.
3. A new generic MADC is being designed with the following features: 16 bits digitization, 100 kHz digitization rate, more channels available to the user, more general triggering capability, and more memory. These new MADC's will be installed first in areas requiring high throughput, such as F0.
4. A VME-based front end and new interface boards to the old vacuum controller (CIA) crates have been designed and are being installed in the MI. These systems solve the memory limitation problems of the existing CAMAC 170 modules. All vacuum crates in the Antiproton Source, Tevatron, and transfer lines will eventually be upgraded to this system.
5. A new Alarms system will be in place for Run II. The architecture utilizes daemon processes on local machines receiving alarms from a central processor through multicasting. This reduces the network bandwidth and central cpu cycles required to process alarms. An unlimited number of processes are able to connect with the local

daemon utilizing the tcp/ip network protocol. Alarm block information is being expanded to promote addition alarm display applications.

7.5 Main Injector Fixed-Target Operations

A major positive impact of the Fermilab Main Injector is that it will make available year-round 120 GeV fixed target beams. The fixed target program is beyond the scope of this handbook, but an outline of the strategy is given here because of its general interest and because it has some effect on Collider operation. The details are provided elsewhere.^{2,3} Design studies have demonstrated the feasibility of slow and fast spill resonant extraction at 120 GeV from the MI during collider operation. These beams will be directed at both the existing fixed target switchyard, as is detailed below, and at a new neutrino area located in the western part of the laboratory. A beam energy of 120 GeV is appropriate for two types of fixed target experiments of current interest: neutrino oscillations and kaon decays. The high cycle rate and beam intensity of the MI will allow detailed studies in both of these areas. Additionally, test beams will be available on a year-round basis. Beams of the MI energy are appropriate for testing and calibrating a variety of HEP equipment—wide angle parts of collider detectors, fixed target detectors and targets, and some segments of muon colliders. During the Tevatron Collider era test beams have only been available at Fermilab during fixed target runs, which have been years apart. Their essentially continuous availability will be a major improvement and will allow much more efficient utilization of that beam which is delivered to running experiments.

The Main Injector has been designed to execute a variety of cycle types in support of both collider and fixed target operation. Extraction may be single turn, as is appropriate for antiproton production, fast resonant (1 ms) for neutrino experiments, and slow resonant (1-sec) for other fixed target experiments and the test beams. In the original configuration the single turn and slow resonant extraction will take place at the MI-52 short straight section and the fast resonant extraction at MI-60. The fast beam is in support of the NuMI (Neutrinos at the Main Injector) program will deliver beam to the COSMOS and MINOS experiments. MINOS is a long baseline neutrino oscillation experiment with two detectors under design, one to reside in the Soudan mine in northern Minnesota and the other on site to provide a short baseline comparison.

A redesign has been made of the upstream portion of the fixed target Switchyard so that it can receive beam either from the Tevatron at 800 GeV or from the MI at 120 GeV; this design is shown schematically in Figure 7.4. A major design concern for 120 GeV SY operation is the apertures of electrostatic septa in light of the larger MI beam size compared to that of the Tevatron. Septa gaps must be small to provide sufficient electric fields at reasonable voltages for efficient operation at high energy, while at lower energy a larger gap is more appropriate. The feasibility of transporting MI beams with modifications to the SY optics has been demonstrated in computer simulations. One such change which is significant is the relocation of the FSEPs, the septa that split the Meson beam into separate lines.

Operationally it appears possible to run either NuMI or the Switchyard simultaneously with antiproton production for the collider program. In one scenario production cycles of 1.9 second length are alternated with those for SY, 2.9 seconds, or NuMI, also 1.9 seconds. A more aggressive scenario involves filling the MI with six Booster batches, of which one is destined for antiproton and the others to a fixed target region, thus combining both programs on the same cycles.

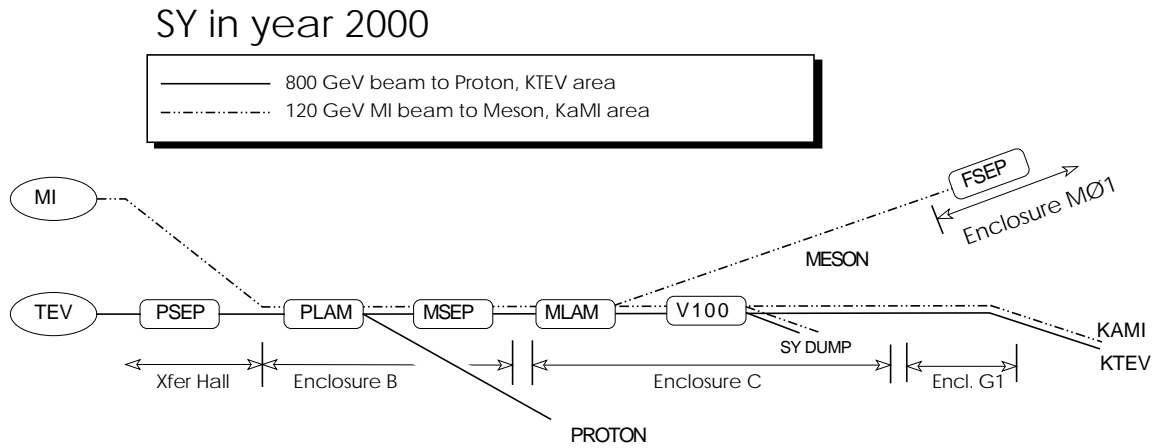


Figure 7.1. Schematic of the switch yard configuration allowing 120 GeV MI beams to be delivered to the meson area.

¹GP Jackson, "The Fermilab Recycler Ring Technical Design Report", Fermilab-TM-1991, 1996

²C. Brown, *et al.*, "Switchyard in the Main Injector Era Conceptual Design Report", Fermilab-TM-2014, 1997.

³D.A. Crane, *et al.*, "Status Report: Technical Design of Neutrino Beams for the Main Injector (NuMI)", Fermilab-TM-1946, 1995.